Doctoral Dissertation
博士論文

The Measurement of the Energy Spectrum and Depth of Maximum Shower Development of Ultra-High-Energy Cosmic Rays Collected by the Telescope Array with the Hybrid Trigger Mode
(テレスコープアレイ実験のハイブリッドトリガーモードを用いた超高エネルギー宇宙線のエネルギースペクトルとシャワー最大発達深さの測定)

A Dissertation Submitted for the Degree of Doctor of Philosophy
September 2022

令和４年９月博士（理学）申請
Department of Physics, Graduate School of Science,
The University of Tokyo
東京大学大学院理学系研究科物理学専攻

Heungsu Shin
申 興秀

Abstract

The Telescope Array (TA) experiment is the largest Ultra-High-Energy Cosmic Rays (UHECR) observatory in the Northern Hemisphere, which aims to investigate the origin of UHECR by observing the energy spectrum, mass composition, and anisotropy in arrival directions of UHECR. The TA experiment comprises 507 surface detectors (SD) and three fluorescence detector (FD) stations.

The FDs observe the longitudinal profile of an Extensive Air Shower (EAS) induced by UHECR, including the maximum shower depth ($\mathrm{X}_{\mathrm{max}}$), which is the observable related to the mass composition of UHECR. In contrast, the SDs observe the lateral distribution of the EAS on the ground. The EAS geometry and energy are reconstructed above $\sim 10^{17}$ eV using the FDs and above $10^{18.2}$ eV using the SDs.

By combining FD analysis with the data acquired by SDs, the hybrid analysis of the TA experiment yields higher energy and $\mathrm{X}_{\mathrm{max}}$ resolutions than the typical resolutions of the TA FD monocular analysis. However, due to the energy threshold of the TA SD array, the hybrid analysis was only possible above $10^{18.2}$ eV for the TA experiment.

To lower this energy threshold, the hybrid trigger system was implemented in the FD stations. The hybrid trigger system enables an SD sub-array to acquire data whenever the corresponding FD station detects an EAS-like event. This thesis presents UHECR observation data collected by the hybrid trigger mode of the TA experiment over 8.5 years of operation in the energy range from $10^{17.5}$ eV to $10^{19.5}$ eV.

The energy spectrum of UHECR measured in the TA hybrid trigger analysis is consistent with previous results obtained by other observation modes of the TA experiment. The lower limit of the energy spectrum measured in the conventional TA hybrid analysis is extended from $10^{18.2}$ eV to $10^{17.5}$ eV in the TA hybrid trigger analysis.

On the mass composition of UHECR, the Pierre Auger Observatory (PAO) reported a change in the $\mathrm{X}_{\mathrm{max}}$ elongation rate (the slope of $\mathrm{X}_{\mathrm{max}}$ as a function of energy) at $10^{18.32\pm0.03}$ eV. It indicates that the mass composition is the lightest at this energy. Therefore, it can be interpreted that the transition from the heavy composition to the light composition ends at this energy point ($10^{18.32\pm0.03}$ eV) when the energy increases from the 2nd Knee (the break in the energy spectrum at around 10^{17} eV). Since the PAO is located in the Southern Hemisphere, the TA and PAO mainly observe different skies. Therefore, it is essential to confirm the physics results independently.

The TA hybrid trigger analysis confirms the result from the PAO for the first time with the TA experiment. The break energy was obtained to be $10^{18.43\pm0.06}$ eV, which is compatible with the result from the PAO. The slopes of mass composition (<lnA>, mean logarithmic mass derived from $\mathrm{X}_{\mathrm{max}}$) measured in the TA hybrid trigger analysis below and above $10^{18.43\pm0.06}$ eV were -2.0±0.25 $\frac{d\mathrm{<lnA>}}{d\mathrm{Log}_{10}(\mathrm{E}_0/\mathrm{eV})}$ and +1.4±0.37 $\frac{d\mathrm{<lnA>}}{d\mathrm{Log}_{10}(\mathrm{E}_0/\mathrm{eV})}$, respectively. The chance probability of exceeding the difference between the two slopes described above (+3.4 $\frac{d\mathrm{<lnA>}}{d\mathrm{Log}_{10}(\mathrm{E}_0/\mathrm{eV})}$) for QGSJET-II-04 proton Monte Carlo (MC) simulations is less than 1×10^{-7} for 10^{7} trials, which corresponds to greater than 5.1σ.

The efficiency of the SD self-trigger in the TA experiment, previously estimated only by SD MC simulations and used to measure the energy spectrum by the TA SDs, was experimentally measured for the first time using the TA hybrid trigger analysis. The SD self-trigger efficiency measured in the TA hybrid trigger analysis is roughly consistent with that estimated by SD MC simulations and has an efficiency of approximately 100% above $10^{18.7}$ eV.

Acknowledgements

On pursuing my Ph.D. course in Japan, I received extensive assistance from many people I sincerely appreciate. Therefore, in this thesis, I express my appreciation to them here in a summary of my research. First, I must thank Professor Hiroyuki Sagawa, my research supervisor, for providing thoughtful and persistent support to my research. I was blessed with his attentive advice throughout my research, including developing this thesis. Never being limited to research-related subjects, Professor Sagawa also fully supported my status as an international student. It is safe to say that it is only possible to complete this thesis with all his assistance and resume my Ph.D. course after finishing my conscription in Korea. I sincerely appreciate him again. I want to thank Dr. Daisuke Ikeda. As a senior researcher, he did not hesitate to advise me throughout my research terms. I have learned from him how to conduct experiments, use experimental tools, and most importantly, the basics of the hybrid technique in analyzing extensive air showers. I want to show my appreciation to Professor Toshihiro Fujii as I have received various information about the TA experiment's FD from him. I have been pleased to have the weekly meetings with many researchers in the TA collaboration. I appreciate Professor Takashi Sako, Professor Shoichi Ogio, Professor Yoshiki Tsunesada, Professor Yuichiro Tameda, Dr. Takayuki Tomida, Professor Shigeharu Udo, Dr. Masahiro Takeda, Dr. Toshiyuki Nonaka, Dr. Eiji Kido, Dr. Kazumasa Kawata, and Dr. Takeshi Okuda for constantly providing valuable advice on my research. Writing this thesis was only possible upon many researchers' valuable works. I feel very grateful to Dr. Hisao Tokuno and Ms. Rie Ishimori for developing and implementing the hybrid trigger system. I want to show my gratitude to the students and researchers such as Dr. Anatoli Fedynitch, Dr. Yana Zhezher, Dr. Akimichi Taketa, Dr. Ryo Higuchi, Dr. Keitaro Fujita, Mr. Kozo Fujisue, Dr. Hitoshi Oshima, and Ms. Kaoru Takahashi for their pleasant communication on physics and research topics. Without the considerate support from the office of ICRR, I would not have been able to continue my study. I thank Ms. Takako Idomura and Ms. Atsuko Kitsugi for such valuable support. I need to make a particular mention of ICRR's University Research Administrator, Ms. Kumiko Sugimoto. Without her help, the integrity of my research life would have been compromised under the stressful situation with COVID-19. I also appreciate Professor Kimihiro Okumura's thoughtful help as my research mentor. I gratefully acknowledge that I have received valuable financial support from Monbukagakusho (MEXT) and the University of Tokyo, especially for ICRR Emergency Grant during COVID-19, which has been my consistent financial support. I appreciate Professor John N. Matthews, Mr. John A. Matthews, and Ms. Whitney Osborn for kindly reviewing the English expression of this thesis. Finally, I thank my precious family and friends, who are the greatest joy in my life.

The Telescope Array experiment is supported by the Japan Society for the Promotion of Science(JSPS) through Grants-in-Aid for Priority Area 431, for Specially Promoted Research JP21000002, for Scientific Research (S) JP19104006, for Specially Promoted Research JP15H05693, for Scientific Research (S) JP19H05607, for Scientific Research (S) JP15H05741, for Science Research (A) JP18H03705, for Young Scientists (A) JPH26707011, and for Fostering Joint International Research (B) JP19KK0074, by the joint research program of the Institute for Cosmic Ray Research (ICRR), The University of Tokyo; by the Pioneering Program of RIKEN for the Evolution of Matter in the Universe (r-EMU); by the U.S. National Science Foundation awards PHY-1607727, PHY-1712517, PHY-1806797, PHY-2012934, and PHY-2112904; by the National Research Foundation of Korea (2017K1A4A3015188, 2020R1A2C1008230, & 2020R1A2C2102800) ; by the Ministry of Science and Higher Education of the Russian Federation under the contract 075-15-2020-778, IISN project No. 4.4501.18, and Belgian Science Policy under IUAP VII/37 (ULB). This work was partially supported by the grants of The joint research program of the Institute for Space-Earth Environmental Research, Nagoya University and Inter-University Research Program of the Institute for Cosmic Ray Research of University of Tokyo. The foundations of Dr. Ezekiel R. and Edna Wattis Dumke, Willard L. Eccles, and George S. and Dolores Doré Eccles all helped with generous donations. The State of Utah supported the project through its Economic Development Board, and the University of Utah through the Office of the Vice President for Research. The experimental site became available through the cooperation of the Utah School and Institutional Trust Lands Administration (SITLA), U.S. Bureau of Land Management (BLM), and the U.S. Air Force. We appreciate the assistance of the State of Utah and Fillmore offices of the BLM in crafting the Plan of Development for the site. Patrick A. Shea assisted the collaboration with valuable advice and supported the collaboration ’ s efforts. The people and the officials of Millard County, Utah have been a source of steadfast and warm support for our work which we greatly appreciate. We are indebted to the Millard County Road Department for their efforts to maintain and clear the roads which get us to our sites. We gratefully acknowledge the contribution from the technical staffs of our home institutions. An allocation of computer time from the Center for High Performance Computing at the University of Utah is gratefully acknowledged. This work used ASGC (Academia Sinica Grid-computing Center) Distributed Cloud resources, which is supported by Academia Sinica.

Contents

List of Figures

List of Tables

Chapter 1

Introduction

1.1 Cosmic Rays

Since the early 20th century, research into the electric conductivity of air has led to the discovery of cosmic rays in 1912. These radiations from outer space have become a significant subject of physics research due to their extremely relativistic energy and constant availability [64]. Over the next two decades, significant progress was made in the study of cosmic rays, aided by advancements in experimental techniques such as the invention of the Geiger-Müller (GM) counter [65]. One of the most notable achievements during this era was the discovery of Extensive Air Showers (EAS), which are cascades of secondary particles induced by primary cosmic rays [66]. A more detailed and technical introduction to EAS is provided in Section 1.3.3. Another noteworthy accomplishment was the discovery of the new elementary particles now known as positrons (e^+) and muons (μ^-) [67][68]. Figure 1.1 on page 2 presents the observed energy spectra of cosmic rays, illustrating that their energies span more than 11 orders of magnitude.

1.2 Ultra-High-Energy Cosmic Rays

Following the discovery of EAS, significant theoretical and experimental research efforts were dedicated to understanding the nature of EAS and cosmic rays in the subsequent decades of the 1940s and 1950s. One notable research achievement was the development of an influential theory that explains the power-law energy spectrum observed for cosmic rays, attributing their acceleration to the magnetic field of molecular clouds in the interstellar space of the galaxy [69]. Through experimental investigations, cosmic rays with energies higher than 10^{17} eV were eventually discovered, leading to their classification as Ultra-High-Energy Cosmic Rays (UHECR) in this thesis. As illustrated in Figure 1.1 on page 2, the flux of cosmic rays decreases to less than 1 particle/m^2 per year above 10^{15} - 10^{16} eV. This characteristic makes it challenging to directly detect primary UHECR using satellite or balloon-borne detectors and to measure their dE/dX (direct measurements) with current instruments. Consequently, the viable method for observing UHECR using existing technologies is to measure the EAS induced by primary UHECR (indirect measurement). This section provides an overview of the history of UHECR observation through experimental techniques for EAS measurement, highlights contemporary UHECR observatories, and summarizes recent scientific findings.

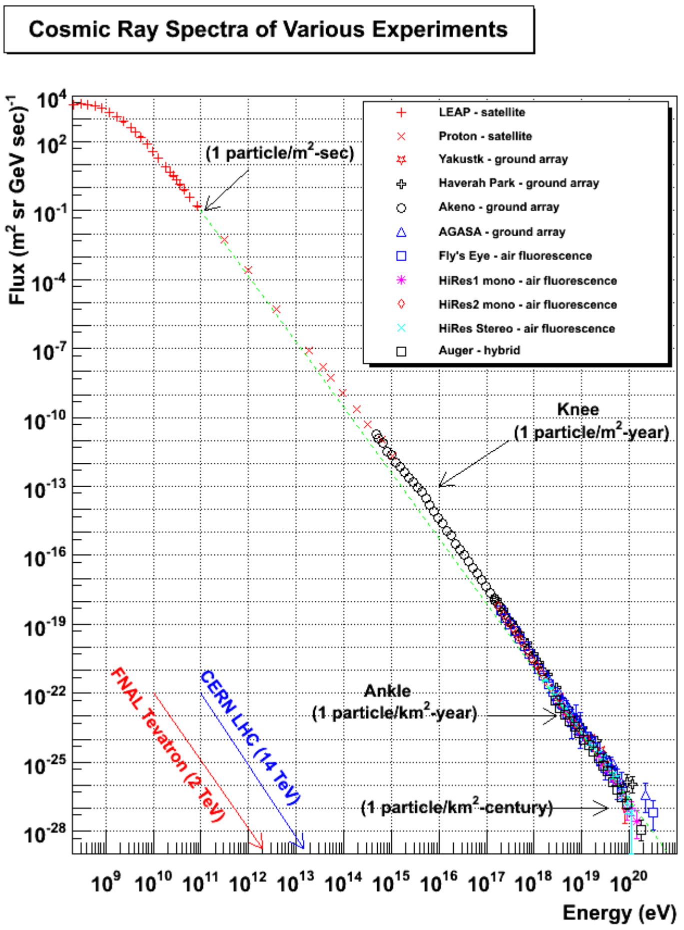

Figure 1.1: Energy spectra of cosmic rays [1]. A distinctive power law structure is shown.

1.2.1 Surface Particle Detection

In the 1950s, early attempts to detect EAS utilized arrays of GM counters at the surface level [70]. The particle density of an EAS could be estimated by counting the number of GM counters hit simultaneously. However, this method had limitations as it could not determine the arrival direction of the observed EAS, and the uncertainty in particle density increased with the size of the EAS.

During the early 1950s, two techniques were developed: density sampling and fast-timing techniques. The density sampling technique allowed for determining the core location of an observed EAS by sampling particle densities using an array of detectors. The fast-timing technique enabled the determination of the arrival direction of the EAS by analyzing the differences in particle hit timing among multiple detectors [71]. These techniques were successfully employed in the MIT-Agassiz experiment, which utilized scintillators and photomultiplier tubes (PMTs) for the first time in surface particle detection [72]. The MIT-Agassiz experiment reported the energy spectrum of cosmic rays up to 10^{18} eV, entering the energy range of UHECR [73]. The fundamental concepts of these techniques are still utilized in the analysis of contemporary UHECR observatories that employ arrays of surface detectors.

The first candidate for UHECR, with a primary energy of 10^{20} eV, was observed in 1962 by the Volcano Ranch experiment, which utilized an array of 19 surface detectors. This observation demonstrated that the energy spectrum of cosmic rays extends to 100 EeV [74]. In 1969, the Haverah Park experiment reported that the particle density at 500 m from the axis of an EAS is proportional to the primary energy of UHECR, regardless of mass composition and hadronic interaction models, within the margin of 12% [75]. Subsequent studies confirmed the validity of this technique when surface detectors predominantly observe the electromagnetic components rather than the muonic components of EAS. This technique, known as the energy estimator technique, is still employed by contemporary UHECR observatories that use arrays of surface detectors.

The spacing between surface detectors is initially determined based on the target energy range of the experiment. Subsequently, the challenge is to find the optimal energy estimator that minimizes discrepancies for different types of mass composition and hadronic interaction models, given the detector spacing and configuration [76].

One of the notable advantages of the surface particle detection technique is that it has approximately 100% duty cycle, so it allows gathering a more significant number of events than the photon detection technique, which is heavily affected by the weather and background light sources.

1.2.2 Photon Detection

Air Fluorescence

In the late 1950s, the potential use of Earth's atmosphere as a scintillator to detect EAS was explored that EAS can be detected by observing the isotropic air fluorescence light produced as the EAS particles traverse through the atmosphere [77]. Throughout the 1960s, significant efforts were devoted to establishing this new technique, leading to the development of an early air fluorescence yield model [57]. Moreover, a prototype of an air fluorescence telescope incorporating PMTs and optics was constructed [78]. The first observation of an EAS using the air fluorescence technique took place in 1968 [79].

One notable advantage of this technique is its ability to determine the depth of the maximum development of an EAS (X_{max}) by analyzing the longitudinal profile of the EAS. However, achieving accurate and precise measurements of X_{max} necessitates an accurate initial determination of the EAS geometry. Consequently, achieving a high level of accuracy and precision in determining the EAS geometry is crucial.

When an EAS is observed with only one air fluorescence detector, the EAS geometry is determined by analyzing the time differences in signal detection between PMTs on the detector plane. In the case of monocular observation, the precision of geometry determination is relatively low, leading to a lower resolution in determining the X_{max} of the EAS.

A way to improve this technique is a simultaneous observation of the same EAS by two air fluorescence detectors that are separated spatially. The Fly's Eye experiment adopts this technique of stereoscopic observation [80]. Another way to improve this technique is to simultaneously observe the same EAS by an air fluorescence detector and a surface detector array, called the hybrid technique. This hybrid technique is tested with the prototype of the High-Resolution Fly's Eye detector and the Michigan Muon Array (MIA), thus called the HiRes/MIA experiment [81]. Then it is adopted by most currently operating UHECR observatories [82][83].

More technical descriptions of air fluorescence emission from an EAS are provided in Section 1.3.4. Refer to Section 3.1 for further details about the above-mentioned techniques.

Cherenkov Radiation

About a decade after the discovery of Cherenkov radiation, the possibility of detecting Cherenkov radiation from an EAS was discussed [84]. In 1953, even before the detection of air fluorescence was established as an experimental technique, Cherenkov radiation from an EAS was successfully measured [85]. One of the early analyses that uses Cherenkov radiation from an EAS for determining a cosmic ray's primary energy and mass composition is the Cherenkov Lateral Distribution Function (CLDF) measurement [86].

Since Cherenkov radiation is highly directional, observation of Cherenkov radiation has a considerable advantage in pointing back to the source on the celestial sphere [87]. This advantage has led to the development of Imaging Atmospheric Cherenkov Telescope (IACT), which can track a possible source of gamma rays on the celestial sphere [88]. On the other hand, non-imaging Cherenkov detectors are expected to increase the detection area when deployed as an array similar to a surface particle detector array [6][7][89].

Traditionally, Cherenkov radiation is considered background in air fluorescence detection method due to its highly directional and extremely bright nature that make the determination of the geometry of an EAS more difficult. However, a technique that utilizes Cherenkov radiation and air fluorescence has been developed in the recent observation of cosmic rays for the energy above 10^{15} eV [90][91]. More technical descriptions of Cherenkov radiation from an EAS are provided in Section 1.3.4.

1.2.3 UHECR Observatories

Several UHECR observatories, in addition to the Telescope Array (TA) experiment, have played significant roles in advancing the understanding of UHECR properties and the development of detection techniques. Here, selected UHECR observatories and some of their notable results are briefly introduced.

KASCADE-Grande

The KArlsruhe Shower Core and Array DEtector(KASCADE) experiment was the UHECR observatory operated by the Karlsruhe Institute of Technology, which started observation in 1996 [2]. As its name suggests, one of the most notable features of the KASCADE experiment is a large hadron calorimeter with the dimensions of 20 m × 16 m × 4 m and a muon tracking detector covering 128 m^2 to track the hadronic and the muonic components of an EAS at the core. In addition, these detectors are surrounded by an e/γ surface detector array consisting of 252 detectors covering an area of 200 m × 200 m with a spacing of 13 m. With these three types of detectors, the KASCADE experiment aimed to measure each part of EAS separately and precisely: the hadronic part, the electromagnetic part, and the muonic part. The layout of the KASCADE experiment and the schematics of an e/γ surface detector is shown in Figure 1.2 on page 5.

The KASCADE-Grande experiment, which started observation in 2003, was an extended experiment of the KASCADE experiment that expanded the coverage area of the experiment to 700 m × 700 m by installing 37 more surface scintillation detectors with a spacing of 137 m [3]. The new scintillation detector for the KASCADE-Grande experiment had a sensitive area of 10 m^2 and

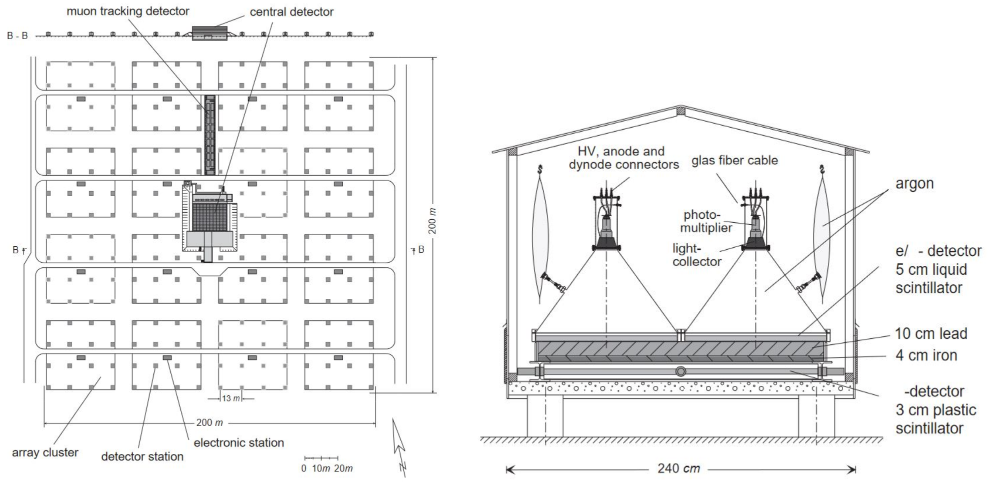

(a) Layout (b) e/γ detector

Figure 1.2: (a) Layout of the KASCADE experiment, showing its 200 m × 200 m array with a hadronic calorimeter and a muon tracking detector at the center. (b) Schematic diagram of an e/γ surface detector for the KASCADE experiment [2].

was developed initially for the EAS-TOP experiment [92]. The layout of the KASCADE-Grande experiment is shown in Figure 1.3 on page 5.

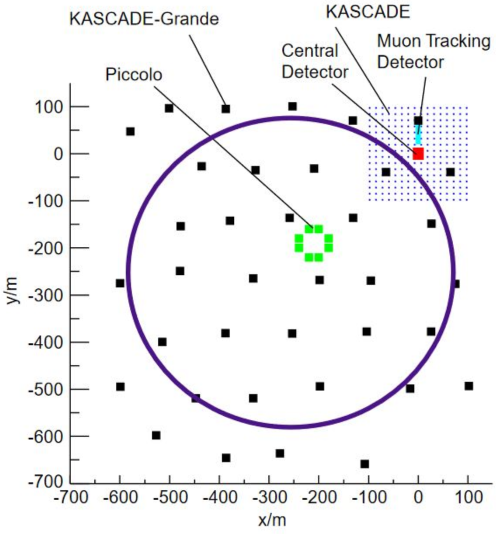

Figure 1.3: Layout of the KASCADE-Grande experiment [3]. The original KASCADE array is shown on the upper-right side.

With the expanded coverage area and the instruments mentioned above that can separate components of an EAS, the KASCADE-Grande experiment measured the energy spectrum of cosmic rays up to 10^{18} eV for two different groups: the electron-rich (lighter composition) group and the electron-poor (heavier composition) group. The result is shown in Figure 1.4 on page 6.

Tunka Experiment

The Tunka-133 array of the Tunka experiment is a non-imaging Cherenkov detector array of 175 detectors located at Tunka Valley, Russia. The array covering approximately 3 km^2 at an altitude of 675 m allows the experiment to measure

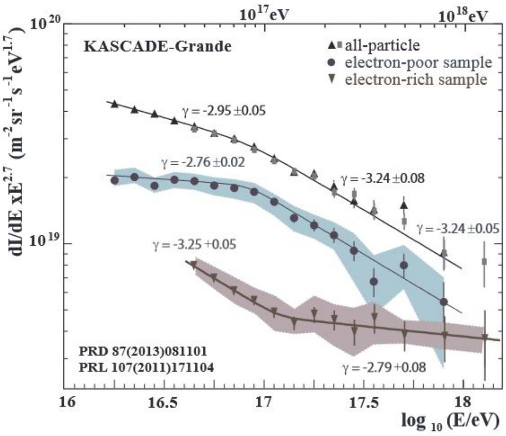

Figure 1.4: Energy spectrum of cosmic rays measured in the KASCADE-Grande experiment [4]. Spectral indices for all particles, the electron-poor group, and the electron-rich group are indicated. The break point for all particles is $10^{16.92}$ eV, the electron-poor group is $10^{16.92}$ eV, and the electron-rich group is $10^{17.08}$ eV.

the energy spectrum and the mass composition of cosmic rays in the energy range from 6×10^{15} eV to 10^{18} eV [5]. Figure 1.5 on page 6 shows the layout of the Tunka-133 array. The energy spectrum and the mass composition of cosmic rays reported by the Tunka experiment are shown in Figure 1.6 on page 7. The 2nd Knee is reported to be at 3×10^{17} eV by the experiment. It is also shown that the mass composition becomes lighter, from CNO (Carbon-Nitrogen-Oxygen) to helium, above the energy of 10^{17} eV.

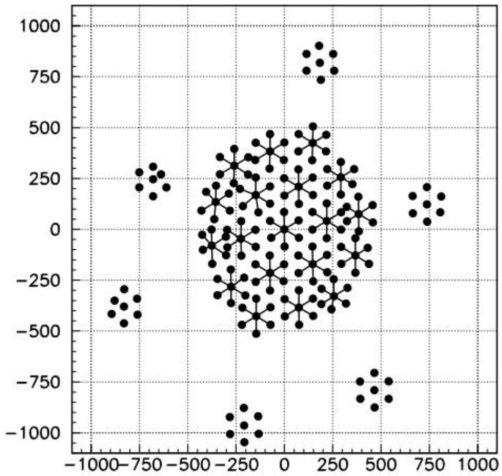

Figure 1.5: Layout of the Tunka-133 non-imaging Cherenkov detector array [5]. The detectors are grouped to form a hexagonal cluster of seven detectors. There are 25 clusters. The units for the vertical and horizontal axes are meters.

Yakutsk Experiment

The Yakutsk EAS array experiment in the Republic of Sakha, Russia, is one of the oldest cosmic ray observatories still operating [93]. The recent experiment setup consists of 120 surface detectors and three muon stations, approximately covering an area of 13 km^2. In addition to the scintillation detectors, 72 non-imaging Cherenkov detectors are installed. The Yakutsk experiment reported the

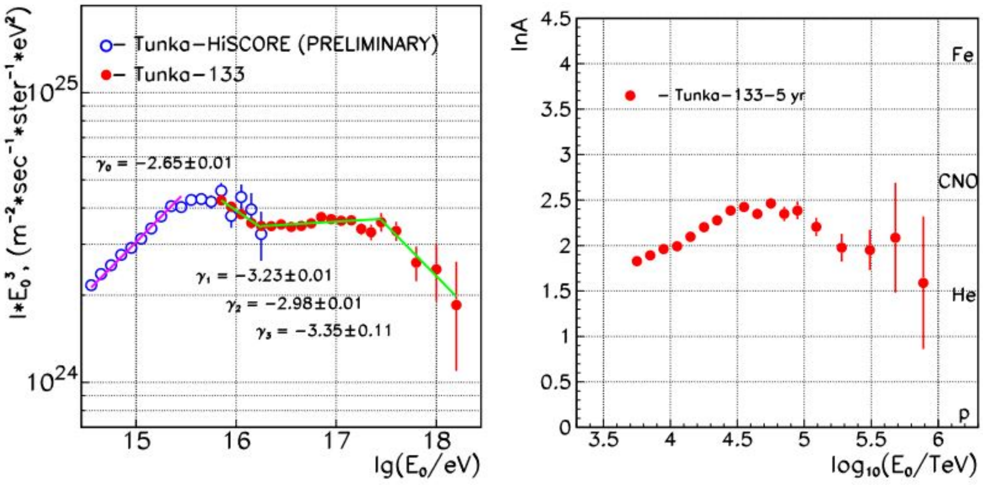

(a) Energy spectrum

(b) Mass composition

Figure 1.6: Result reported by the Tunka-133 array [6]. (a) Energy spectrum. (b) Mass composition in terms of mean logarithmic mass <lnA>.

energy spectrum and the mass composition of cosmic rays in the energy range from 10^{16} eV to 5.7×10^{19} eV [7]. Figure 1.7 on page 7 presents the recent layout of the experiment. The energy spectrum and the mass composition of cosmic rays reported by the Yakutsk experiment are shown in Figure 1.8 on page 8. Similar to the result of the Tunka experiment, the result also exhibits that the mass composition of cosmic rays becomes lighter from nitrogen above 10^{17} eV. Then the result indicates the transition from nitrogen to hydrogen ends around $10^{18.5}$ eV. Above this energy, the mass composition of UHECR again becomes heavier from hydrogen to helium, but the statistical error also becomes more significant.

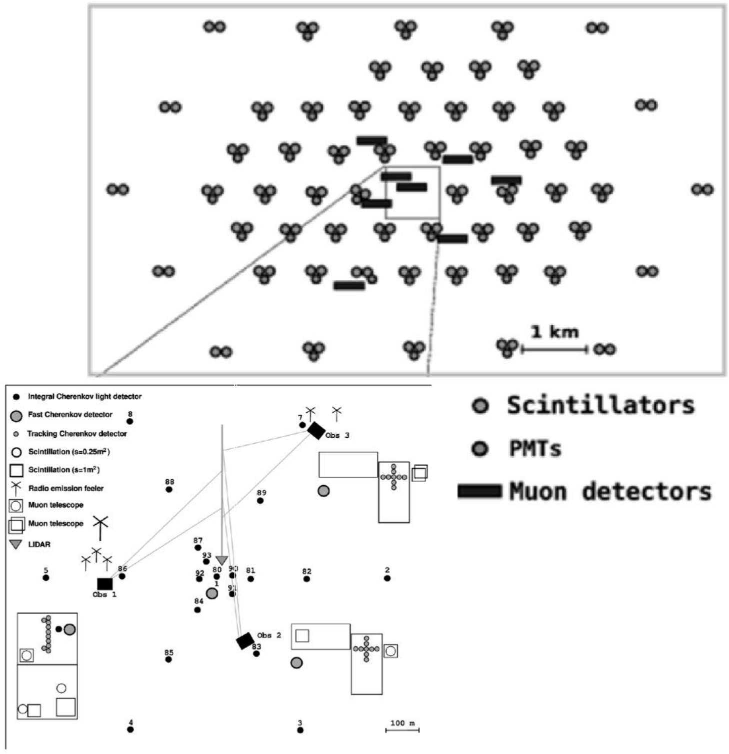

Figure 1.7: Recent layout of the Yakutsk EAS array [7].

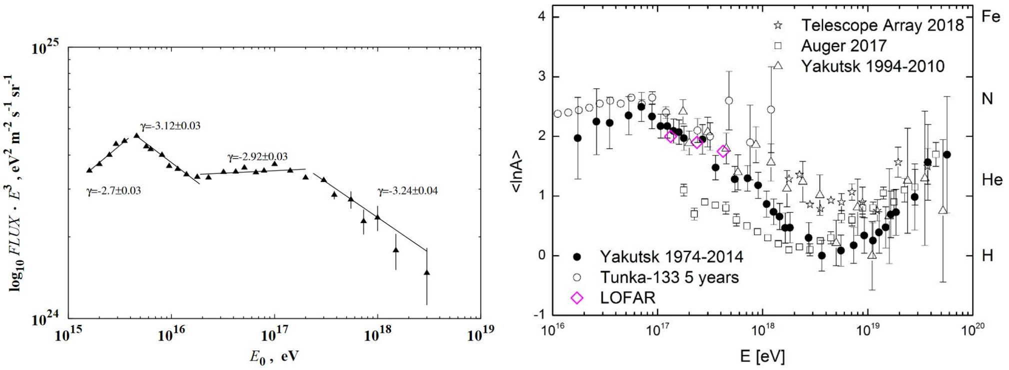

(a) Energy spectrum (b) Mass composition

Figure 1.8: Result reported by the Yakutsk experiment from 40-year operations [7][8]. (a) Energy spectrum. (b) Mass composition in terms of mean logarithmic mass <lnA>.

IceTop

IceTop is an array of ice Cherenkov surface detectors that is part of the IceCube Neutrino Observatory [9]. The array consists of 162 detectors, with a pair of detectors deployed next to each of the 81 strings of the IceCube Neutrino Observatory. Figure 1.9 on page 8 provides an overview of the IceTop array layout and the schematics of an IceTop detector.

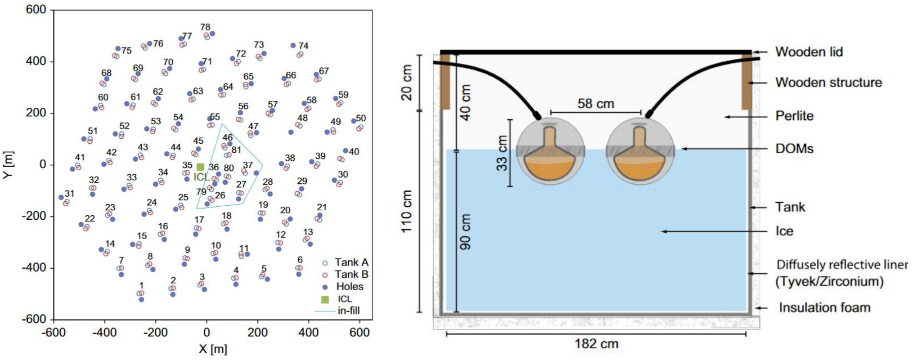

(a) IceTop layout (b) IceTop detector

Figure 1.9: (a) Deployment positions of the IceTop detectors. Two tanks are deployed as a pair. (b) Schematic diagram of an IceTop detector showing an ice-filled tank with two optical detector modules [9].

Situated at an altitude of 2,835 m, the 162 detectors of the IceTop array enable the measurement of the energy spectrum of cosmic rays ranging from $10^{15.5}$ eV to 10^{18} eV. The IceTop detectors, which are ice-filled tanks, can also estimate the mass composition of cosmic rays using only their surface detector setup. It is possible because the number of muons in an EAS is an observable that is sensitive to mass composition, as explained in Section 1.2.4. The energy spectrum and mass composition of cosmic rays, as reported by IceTop, are presented in Figure 1.10 on page 9.

The mass composition of cosmic rays around 10^{18}, as reported by the IceTop experiment, remains in the intermediate to heavy range, similar to CNO mass composition. However, this result contradicts the findings of other experiments, such as the Tunka and Yakutsk experiments, as depicted in Figure 1.6 and Figure

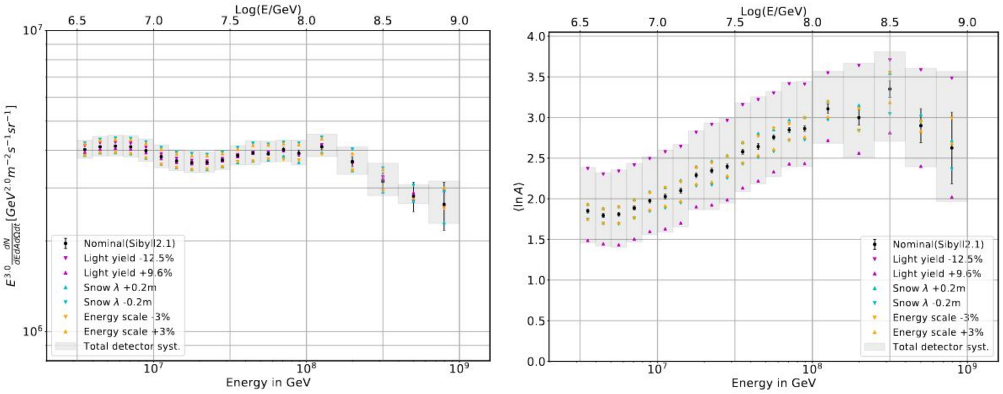

(a) Energy spectrum

(b) Mass composition

Figure 1.10: Result reported by the IceTop [10]. (a) Energy spectrum. (b) Mass composition in terms of mean logarithmic mass <lnA>.

1.8, respectively. There are a couple of potential explanations for this discrepancy.

One possible reason is the utilization of different hadronic interaction models in the IceTop experiment compared to those used in the other experiments. These models describe the interactions between cosmic rays and atmospheric particles, and variations in their implementation can lead to differences in the observed mass composition. Another potential reason for the discrepancy is the muon puzzle, which refers to a recently reported issue where the number of muons observed in EAS events is greater than the number predicted by simulations. This puzzle is further explained in Section 1.2.4.

These factors, namely the choice of hadronic interaction models and the muon puzzle, could contribute to the disparity in mass composition results between IceTop and other experiments. Further investigation and analysis are necessary to resolve these discrepancies and gain a deeper understanding of the mass composition of cosmic rays at around 10^{18} eV.

Pierre Auger Observatory

The Pierre Auger Observatory (PAO or Auger) is in the Southern Hemisphere in Provincia de Mendoza, Argentina. It is the largest UHECR observatory in the world. The observatory is situated at a mean altitude of ∼1,400 m, corresponding to an atmospheric overburden of ∼865 g/cm^2.

The observatory consists of 1,660 water Cherenkov surface detectors deployed with a spacing of 1,500 m over a ∼3,000 km^2 of area, which is surrounded by 24 normal-elevation and three high-elevation air fluorescence telescopes in four stations. Additionally, 61 water Cherenkov surface detectors with a spacing of 750 m are deployed to observe a lower energy range [12]. Figure 1.11 on page 10 shows the layout of the PAO and the two types of detectors making up the observatory: an air fluorescence detector station and a water Cherenkov detector.

The combined energy spectrum of cosmic rays measured in the PAO is shown in Figure 1.12 on page 10. The PAO reported five different spectral features over energy ranges broader than four orders of magnitude by combining results obtained by five different observation modes: vertical and inclined events detected by the 1,500 m-spacing surface array, events detected by the hybrid detectors, events detected by the 750 m-spacing surface array, and Fluorescence Detector (FD) events dominated by Cherenkov radiation. This combined energy spectrum

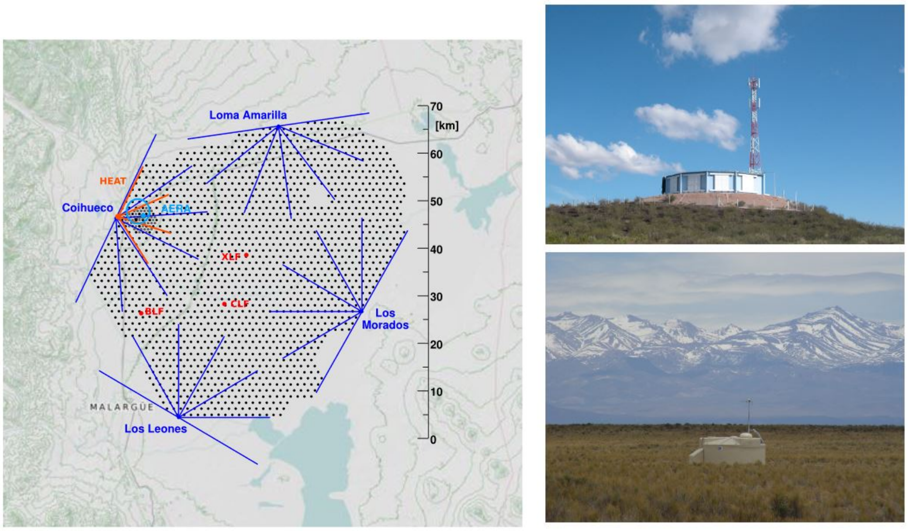

(a) Layout

(b) Detectors

Figure 1.11: (a) Layout of the PAO [11]. (b) Los Leones fluorescence detector station and a surface water Cherenkov detector for the PAO [12].

measured in the PAO fully covers the energy range of this thesis's analysis. The comparison of energy spectra of UHECR obtained by the PAO and this thesis's analysis is presented in Section 5.9.1.

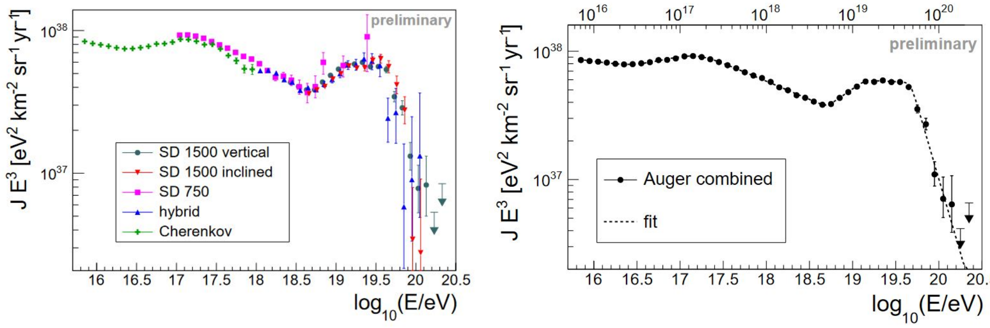

(a) Separated

(b) Combined

Figure 1.12: (a) Energy spectra of cosmic rays JE^3 measured in five different observation modes of the PAO. (b) Combined energy spectrum of cosmic rays JE^3 measured in the PAO using all five modes introduced in (a) [13]. A total of five spectral features are shown in the plot: the Low-Ankle at 2.8×10^{16} eV; the 2nd Knee at 1.58×10^{17} eV; the Ankle at 5.0×10^{18} eV; the Instep at 1.4×10^{19} eV; the Suppression at 4.7×10^{19} eV.

The result of the mass composition of UHECR in terms of mean logarithmic mass estimated by three different hadronic interaction models by the PAO is shown in Figure 1.13 on page 11. For all hadronic interaction models, it is reported that the mass composition becomes lighter in the energy range from $10^{17.2}$ eV to the break point around $10^{18.0}$ - $10^{18.5}$ eV. Then the mass composition becomes heavier for the energies above the break point.

The comparison of the mean logarithmic mass of UHECR obtained by the PAO and this thesis's analysis is presented in Section 5.9.2.

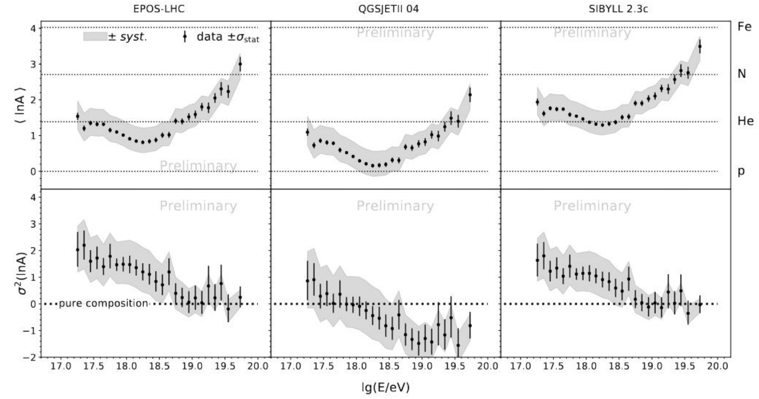

Figure 1.13: Means and variances of the logarithmic mass of UHECR measured in the PAO [14]. The upper row is for means and the lower row is for variances. The left column is the result obtained using the EPOS-LHC model [15], the center column uses the QGSJET-II-04 model [16], and the right column uses the Sibyll 2.3c model [17].

1.2.4 Recent Results

As mentioned in Section 1.2.1, it has been almost 60 years since the MIT-Agassiz experiment reported the energy spectrum of cosmic rays up to the extremely high energy of 10^{18} eV. Since then, numerous studies have been performed to clarify the nature of UHECR. This section provides an overview of recent research findings related to UHECR, focusing on the energy spectrum, mass composition, anisotropy in arrival directions, and the muon deficit in contemporary simulations of EAS.

Energy Spectrum

Figure 1.14 on page 12 presents the latest results of the energy spectrum of cosmic rays from several experiments. The spectrum exhibits three notable features: the Knee, the 2nd Knee, and the Ankle.

The astrophysical origin of the Knee feature is believed to be a change in the generation mechanism of UHECR. If the UHECR in this energy range originate within the Milky Way, the steepening observed around 10^{15} - 10^{16} eV can be explained by the proton acceleration limit of Galactic UHECR sources. Similarly, the steepening around 10^{17} eV (the 2nd Knee) may be attributed to the acceleration limit for heavy-nuclei like iron. The rigidity (R) of particles, which depends on their energy and atomic number, plays a crucial role in the acceleration and propagation of UHECR. It has been suggested that the acceleration limit for iron nuclei would occur at 26 times the energy corresponding to the Knee ($\rm E_{Knee}$) as proposed by Peters [94]. The KASCADE-Grande experiment reported a structure of the 2nd Knee in the UHECR energy spectrum and showed EAS caused by heavy nuclei accompanying this change [95]. These findings provide insights into the possible mechanisms and limits involved in the acceleration and propagation of UHECR at different energy ranges, shedding light on the astrophysical sources responsible for their generation.

The feature of the energy spectrum known as the Ankle has multiple theoretical explanations. One possibility is that it represents a transition from the lower-energy population of cosmic rays originating within the Milky Way to the higher-energy population originating from extragalactic sources [96]. Another explanation involves an energy loss process during propagation, specifically the

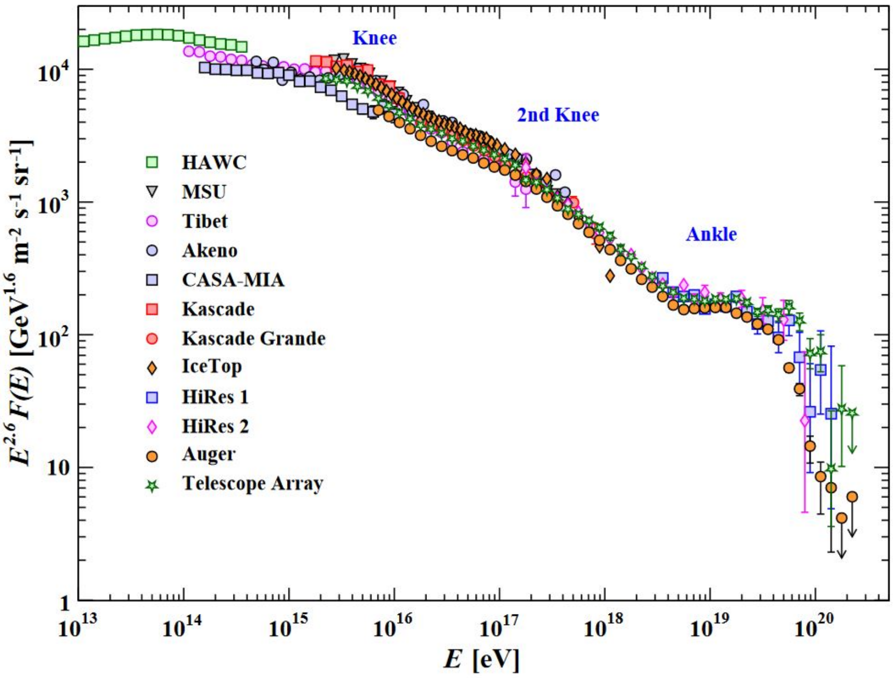

Figure 1.14: Recent results of the energy spectrum of cosmic rays F(E) reported by multiple experiments [18]. Spectra are multiplied by $E^{2.6}$ to demonstrate the changes in the structure. Three features in the spectra are shown: the Knee (steepening around 10^{15} - 10^{16} eV); the 2nd Knee (another steepening around 10^{17} eV); the Ankle (hardening around $10^{18.5}$ eV). The features are named after an analogy of a human leg.

pair production of an electron and a positron involving a proton UHECR and a Cosmic Microwave Background (CMB) photon [97]. Details of this process are described in Section 1.3.2. The mass composition of UHECR around the Ankle is believed to be proton dominant according to this scenario. However, the PAO has reported evidence of a mixed mass composition in the energy range from $10^{18.5}$ eV to $10^{19.0}$ eV, including nuclei with atomic mass $A > 4$ [98].

At the highest energy region, above approximately $10^{19.7}$ eV, the energy spectra of UHECR exhibit a rapid steepening referred to as the Suppression. Multiple experiments, including the HiRes experiment, the TA experiment, and the PAO, have reported this feature [48][99][100]. The origin of the Suppression can be explained by energy loss processes during propagation, such as the interaction of UHECR with CMB photons and the disintegration of UHECR nuclei. Section 1.3.2 provides further details on these processes. Additionally, the acceleration limit at the sources of UHECR is another possible explanation for the Suppression [101].

Figure 1.15 on page 13 displays the recent results of the UHECR energy spectrum above 10^{18} eV measured in the TA experiment and the PAO. The instrumentation and the specific results of the TA experiment are introduced in Section 2.2 and Section 2.3, respectively.

From Figure 1.15, it is shown from both measurements that there is another feature between the hardening of the Ankle and the rapid steepening of the Suppression [99][102]. This feature around $10^{19.2}$ eV is called the Instep by the PAO and the Shoulder by the TA experiment. Above the energy of this feature, it is shown that the spectral indices of the Suppression between the two experiments differ. This result might reflect the UHECR energy spectra difference between the Northern and Southern Hemisphere, as the TA experiment and the PAO mainly

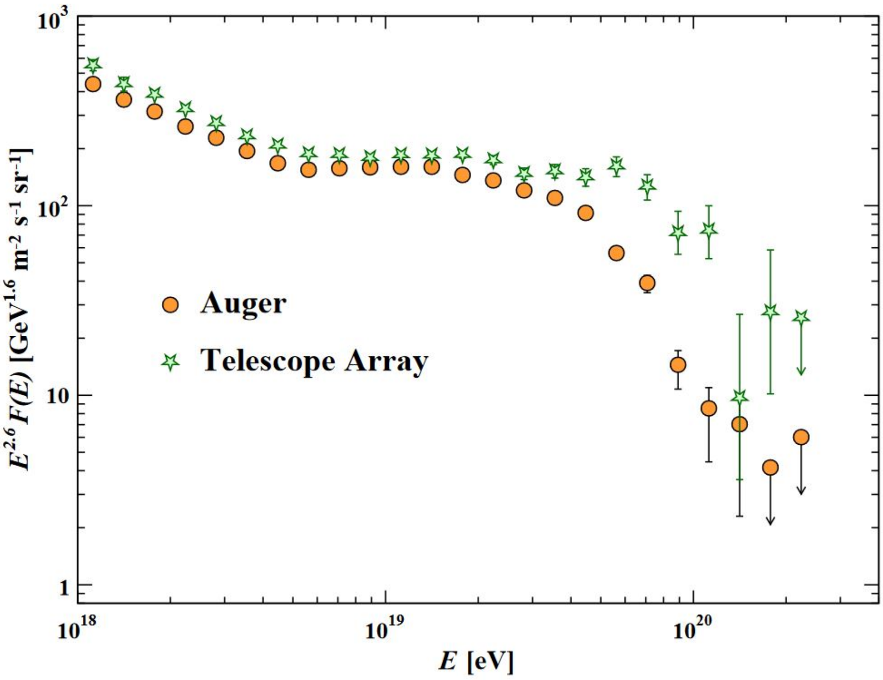

Figure 1.15: Recent results of UHECR energy spectrum above 10^{18} eV measured in the TA experiment and the PAO (Auger) [18]. The flux difference between both results corresponds to a 9% difference in energy scales [19].

cover the Northern and Southern Hemisphere, respectively. Since both experiments have reported anisotropies in arrival directions of UHECR independently, one of the most recent studies suggested the existence of a local astrophysical source of UHECR located in the Northern Hemisphere, which is only visible by the TA experiment. The study suggests that this scenario is favored at the 5.6σ level compared to the identical UHECR flux scenario for both experiments [103]. These findings contribute to the understanding of the energy distribution and characteristics of UHECR at extreme energies.

Mass Composition

To estimate the mass composition of UHECR, the observable X_{max} is commonly utilized in analyses. X_{max} represents the atmospheric depth at which the number of secondary particles in an EAS reaches its maximum. It is a sensitive observable that correlates with $\ln(E_0/A)$, where E_0 is the energy of the primary particle and A is its atomic mass. Furthermore, X_{max} is influenced by the interaction cross section of the primary UHECR with atmospheric molecules. A more detailed explanation of X_{max} and its technical aspects is provided in Section 1.3.3.

Figure 1.16 on page 14 displays the results of mean X_{max} measurements reported by several experiments. All the experiments in the plot employ photon detection technique to measure EAS, such as air fluorescence or Cherenkov radiation. As described in Section 1.2.2, the photon detection method allows for the measurement of the longitudinal development profile of an EAS, which is instrumental in determining X_{max} and analyzing the mass composition of UHECR.

From Figure 1.16, several transitions are found as the energy of cosmic rays increases. From the Knee ($\sim 10^{15-16}$ eV) to the 2nd Knee ($\sim 10^{17}$ eV), the observation data shift from a lighter, proton-like composition to a heavier, iron-like composition. This result is consistent with the difference in the Galactic accel-

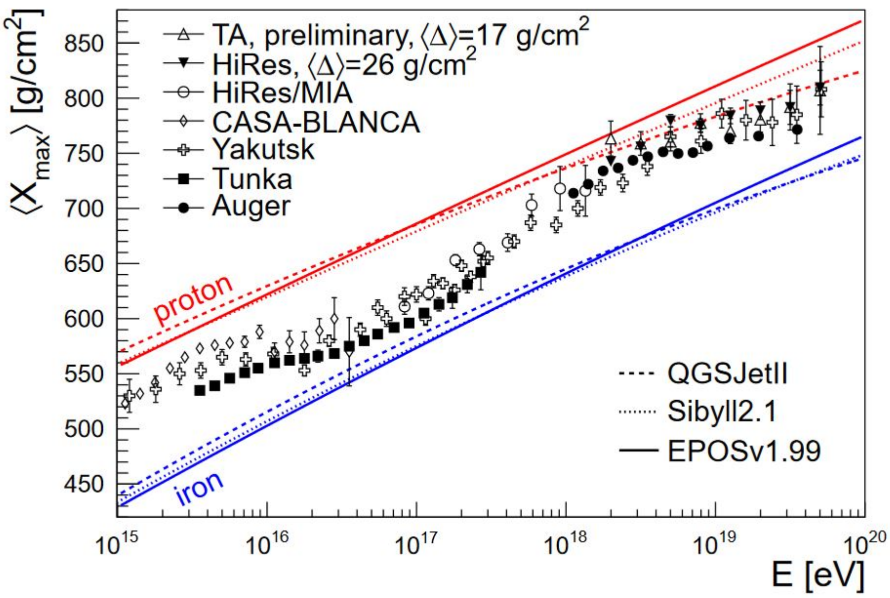

Figure 1.16: Mean $X_{\max}$ measured in multiple experiments compared with the results of proton and iron-nucleus EAS simulations in the energy range from the Knee to the highest [20]. The red lines indicate the proton EAS simulation with multiple hadronic interaction models—the blue lines for iron-nucleus.

eration limit for proton and iron-nucleus cosmic rays, as explained previously with the energy spectrum results. In the energy range from the 2nd Knee to approximately 10^{18} eV, the observation data shift back to a lighter, proton-like composition from a heavier, iron-like composition. This shift might indicate the increase of a lighter composition flux from a different source group, such as extragalactic sources.

The most recent results of the UHECR mass composition by multiple experiments are shown in Figure 1.17 on page 15. Instead of the mean $X_{\max}$, the mean logarithmic mass <lnA> is shown in Figure 1.17, which is calculated:

$$< \mathrm{lnA} >= \frac{X_{\max}^{\mathrm{obs}} - X_{\max}^{\mathrm{proton}}}{X_{\max}^{\mathrm{iron}} - X_{\max}^{\mathrm{proton}}} \cdot \mathrm{lnA}_{\mathrm{iron}}. \tag{1.1}$$

Figure 1.17 shows several features of the mass composition of UHECR. As shown in Figure 1.17 (a), the PAO reported that the mass composition of UHECR becomes lighter as energy increases from the 2nd Knee to $10^{18.32\pm0.03}$ eV, where the lightest mass composition is indicated. For the energy above $10^{18.32\pm0.03}$ eV, the mass composition becomes heavier to an intermediate composition as energy increases. The Yakutsk experiment reported a similar tendency in Figure 1.17 (b). The Yakutsk experiment results show that the mass composition of UHECR becomes lighter as energy increases from the 2nd Knee to the point around $10^{18.55}$ eV, where the lowest <lnA> value is indicated. Note that the Yakutsk experiment did not report the exact break energy. The mass composition is compatible with proton within the statistical errors in the energy from the point around $10^{18.55}$ eV to $\sim 10^{19}$ eV. For the energy above $\sim 10^{19}$ eV, the mass composition becomes heavier to an intermediate composition similar to the PAO's result.

Meanwhile, the most recent UHECR mass composition measurement by the TA experiment comes from the two independent observation modes: the TALE hybrid mode and the conventional TA hybrid mode, as shown in Figure 1.17 (c). The conventional TA hybrid mode is further explained in Section 3.1. Here, TALE

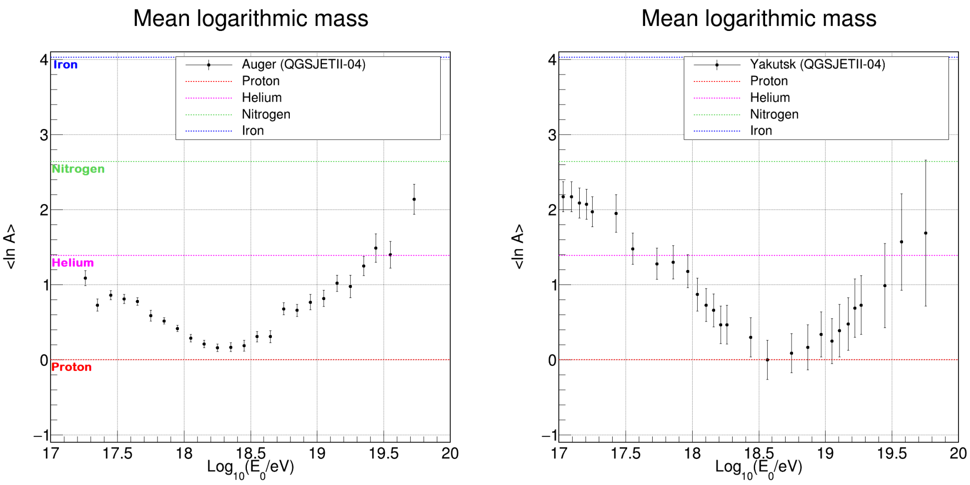

(a) PAO (b) Yakutsk

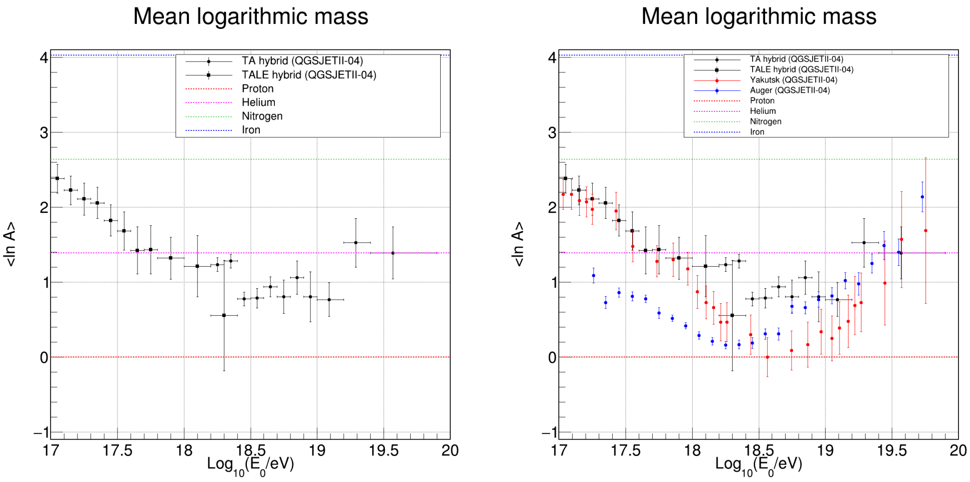

(c) TA (d) All

Figure 1.17: Mean logarithmic mass (<lnA>) of UHECR reported by multiple experiments. (a) The PAO [14]. (b) The Yakutsk experiment [7]. (c) The TA experiment with two observation modes: the Telescope Array Low-energy Extension (TALE) hybrid and the TA hybrid [21][22]. (d) All data. All results adopt the QGSJET-II-04 hadronic interaction model. The logarithmic mass of four pure elements: proton, helium, nitrogen, and iron are indicated with the colored dotted lines. Systematic uncertainties are not indicated.

stands for the Telescope Array Low-energy Extension and its instrumentation is introduced in Section 2.2.3. However, the limited event statistics of the TALE hybrid mode above 10^{18} eV make it challenging to understand the energy where the mass composition transition from the 2nd Knee ends as reported by the PAO ($10^{18.32}$ eV) and the energy point indicated by the result of Yakutsk experiment ($\sim 10^{18.55}$ eV).

This energy can be interpreted as the energy point where the transition from the heavier UHECR population at lower energies to the lighter UHECR population at higher energies is completed. In addition, the recent data-driven energy spectrum and mass composition combined model for cosmic rays named the Global Spline Fit (GSF) also shows such a transition [26]. Therefore, confirmation of this energy with the TA experiment independently from the results of the other experiments is of high importance for further study on the origin of

UHECR.

Anisotropy

Anisotropy in the arrival directions of UHECR has been a subject of investigation for many former and contemporary UHECR observatories. The presence of anisotropy could serve as solid evidence for the existence of astrophysical point sources of UHECR. Consequently, numerous studies have been conducted to search for anisotropy and establish correlations between UHECR and potential astrophysical sources.

The most recent result regarding the search for anisotropy in UHECR arrival directions reveals a dipole pattern for energies above 8×10^{18} eV, as reported by the PAO. This dipole, depicted in Figure 1.18 on page 16, exhibits an amplitude of 6.6%. The direction of the dipole suggests that UHECR with energies above 8×10^{18} eV originate from extragalactic sources, further supporting the notion of an extragalactic origin for these particles [23].

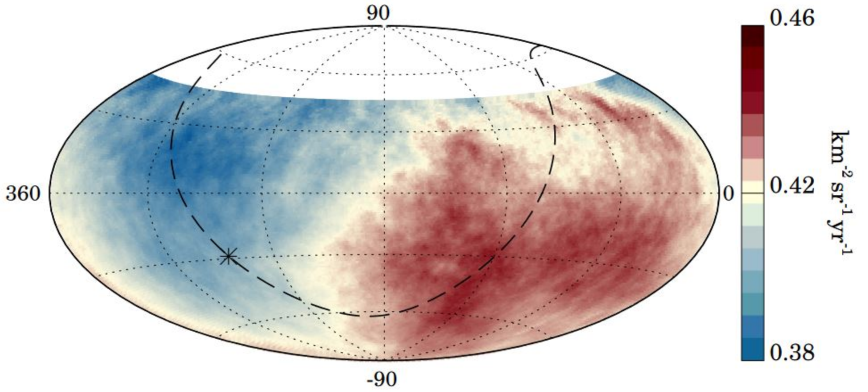

Figure 1.18: Equatorial coordinates sky map showing a flux of cosmic rays above 8 EeV measured in the PAO [23]. The asterisk indicates the Galactic center. The dashed line indicates the Galactic plane.

In addition to the dipole, investigations for structures with smaller angular scales have yielded several results. For instance, the TA experiment has reported an intermediate scale anisotropy in the arrival directions of UHECR above 57 EeV. The post-trial significance of this excess has been reported as 3.4σ for the initial five years of observation, as illustrated in Figure 1.19 on page 17. The updated post-trial significance with 12 years of observation stands at 3.2σ [104].

Muon Deficit in EAS Simulation (Muon Puzzle)

In addition to the X_{max} of an EAS, the number of muons of an EAS (N_μ) is a mass composition sensitive observable because the muons of an EAS are produced as an outcome of mesonic decays, as shown in Figure 1.23 on page 23, mainly with the channel of charged pion decays shown in Equation (1.11) on page 23. Therefore, the mean number of muons of an EAS is proportional to the primary particle's atomic mass A. See Section 1.3.3 for more detailed descriptions.

However, the PAO, by observing highly inclined EAS, reported that the numbers of muons of simulated EAS show deficits of 30% - 80% when compared to the observed EAS at the primary energy of 10^{19} eV depending on the hadronic interaction models [105]. A further study by the PAO reported that the numbers

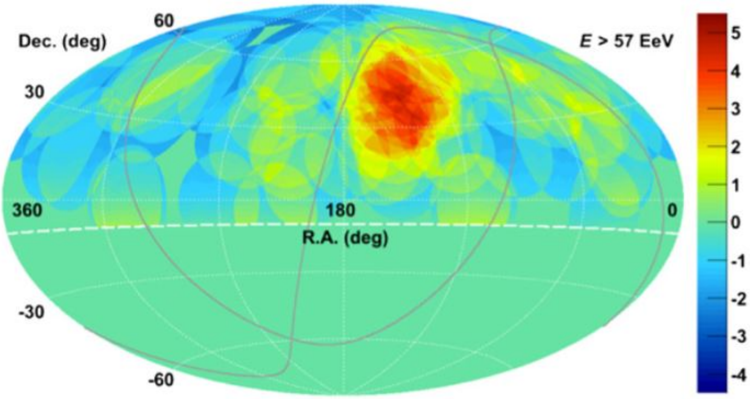

Figure 1.19: Equatorial coordinates sky map showing the significance of excess in arrival directions of UHECR above 57 EeV [24].

of muons of simulated EAS show deficits by measuring normally inclined EAS. When compared to the observed EAS at the primary energy of $10^{18.8}$ - $10^{19.2}$ eV, simulations with the EPOS-LHC hadronic interaction model show a deficit of 30% and simulations with the QGSJET-II-04 hadronic interaction model show a deficit of 60% [106].

By measuring highly inclined EAS, the TA experiment also reported a similar tendency of muon deficits in the EAS simulations using the pre-Large Hadron Collider (LHC) hadronic interaction model QGSJET-II-03 compared to the EAS observed by the surface detector array [107].

The following scale is introduced to quantify and compare the degrees of muon deficit reported by multiple experiments [25].

$$\mathrm{z} = \frac{\ln(\mathrm{N}_\mu) - \ln(\mathrm{N}_\mu^{\mathrm{proton}})}{\ln(\mathrm{N}_\mu^{\mathrm{iron}}) - \ln(\mathrm{N}_\mu^{\mathrm{proton}})}, \tag{1.2}$$

where $\ln(\mathrm{N}_\mu)$ is a logarithm of the estimated muon density measured in observed EAS, $\ln(\mathrm{N}_\mu^{\mathrm{proton}})$ is a logarithm of the estimated muon density measured by full proton EAS simulation, and $\ln(\mathrm{N}_\mu^{\mathrm{iron}})$ is a logarithm of the estimated muon density measured by full iron-nucleus EAS simulation. The z values calculated from the results of various experiments are plotted in Figure 1.20 on page 18.

It is shown in Figure 1.20 on page 18 that the mass composition of cosmic rays above 10^{17} eV measured using the z values is more compatible with iron-nucleus than proton UHECR or is even heavier than iron-nucleus in most experiments for the post-LHC hadronic interaction models. This significant discrepancy between the results expected from the $\mathrm{X}_{\mathrm{max}}$ and N_μ measurements indicates that an EAS simulation produces fewer muons than an actual EAS. The PAO recently updated the report using the measurement of the fluctuations in the number of muons of an EAS, reporting that the origin of the muon deficit is from a slight model-reality discrepancy at every stage of the development of an EAS, rather than from a model-reality discrepancy at the first interaction [108].

The muon puzzle shows the limitations of contemporary hadronic interaction models in explaining EAS. Therefore, a study regarding UHECR mass composition is better examined with multiple hadronic interaction models. It is also expected for the TA experiment to update the previous result with a post-LHC hadronic interaction model.

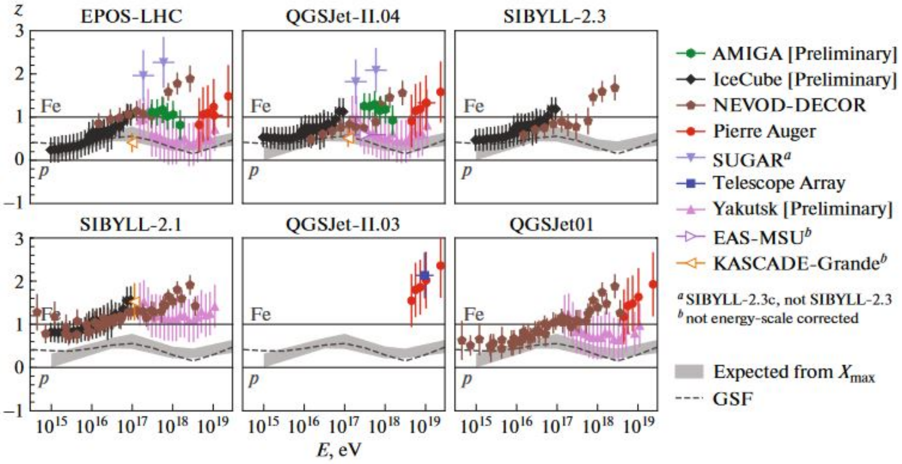

Figure 1.20: z values calculated as Equation (1.2) from the results reported by multiple experiments [25]. The upper row shows z values estimated using post-LHC hadronic interaction models. The lower row is for pre-LHC hadronic interaction models. The gray bands indicate the mass composition expected from $X_{\rm max}$ measurements. GSF is the Global Spline Fit model [26].

1.3 Physics of Ultra-High-Energy Cosmic Rays

The physics of UHECR remains largely unknown, particularly regarding their sources and the processes involved in their propagation. Despite this, physicists have put forward various estimations and models to understand the physics associated with UHECR. This section provides a general overview of the physics concepts relevant to UHECR.

1.3.1 UHECR Acceleration Models

In the study of UHECR, understanding their sources and acceleration mechanisms is a significant area of investigation. Two main approaches, Bottom-up and Top-down models, have been proposed to address this question.

Bottom-up models focus on explaining the sources of UHECR based on particle acceleration near celestial bodies with magnetic fields. These models explore scenarios where particles gain high energies through interactions with astrophysical objects, such as supernova remnants, active galactic nuclei, or pulsars. These sources are believed to have the conditions for particle acceleration to extremely high energies.

In contrast, Top-down models approach the question of UHECR sources from a different perspective. They propose that UHECR originate from exotic, high-energy processes or hypothetical particles with exceptionally high potential energy. These models consider scenarios where UHECR are produced through unknown physical processes associated with the decay or annihilation of supermassive particles or cosmic strings, for example.

Both Bottom-up and Top-down models contribute to understanding the sources and acceleration mechanisms of UHECR, providing different theoretical frameworks to explore the origin of these high-energy particles.

Bottom-up Models

Bottom-up models focus on explaining the sources of UHECR from the perspective of particle acceleration near celestial bodies that possess strong magnetic fields. These models assume the existence of cosmic particle accelerators, similar to particle accelerators such as the Tevatron. The Hillas plot, as shown in Figure 1.21 on page 19, illustrates the sizes of various celestial bodies that could serve as potential accelerators and their corresponding magnetic field strengths. The maximum energy to which particles are accelerated is limited by the size of the celestial body and the strength of its magnetic field. Equation (1.3) describes the upper limit of the acceleration energy based on these parameters.

$$\frac{\mathrm{E}_{\mathrm{max}}}{\mathrm{EeV}} = \beta \mathrm{Z}e(\frac{\mathrm{B}}{1\mu\mathrm{G}})(\frac{\mathrm{R}}{1\mathrm{kpc}}), \tag{1.3}$$

where Ze is the charge number of a particle, β is the ratio of the velocity of an accelerating shock wave to the speed of light, and B and R mean the magnitude of the magnetic field and the radius of a celestial body, respectively. The terms kpc and μG mean kiloparsec and microgauss, respectively.

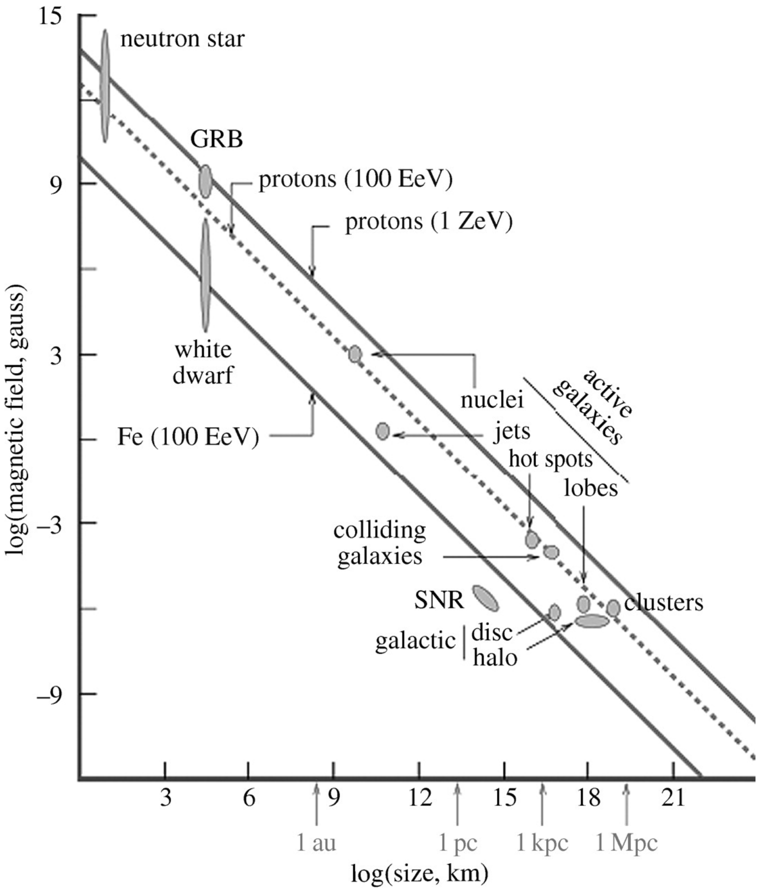

Figure 1.21: Sizes of various celestial bodies and their magnitudes of magnetic fields. The required values to accelerate cosmic rays up to the specific energies are also indicated [27].

According to Figure 1.21 on page 19, only a few candidates can accelerate particles to extremely high energy.

Top-down Models

On the other hand, Top-down models propose the existence of unknown substances or physical processes with extremely high energy that can produce UHECR. These models do not rely on cosmic particle accelerators but instead, hypothesize the presence of such high-energy substances. Examples include ultra-high-energy neutrinos [109], super heavy relic particles [110], and topological defects such as cosmic strings and magnetic monopoles [111]. However, these models often predict higher fluxes of gamma rays than hadrons, which constrain their validity because the observed gamma-ray flux sets strong limitations on these models [112].

1.3.2 Propagation of UHECR

The propagation of UHECR from extragalactic sources through the vast intergalactic space involves various physical processes. One important phenomenon predicted in the propagation of UHECR is the GZK limit, which is named after the physicists Greisen, Zatsepin, and Kuzmin, who first proposed it. The GZK limit predicts a cutoff in the UHECR flux due to interactions with low-energy photons of the Cosmic Microwave Background Radiation (CMBR) [113][114].

Photo-pion Production

One important process during the interaction between UHECR protons and CMB photons is photo-pion production. The CMBR, with a temperature of 2.7 K, consists of low-energy photons each carrying about 10^{-3} eV. However, due to the relativistic blueshift effect in the rest frame of UHECR, the energy of a CMB photon is significantly increased, reaching 100 MeV or higher depending on the energy of the UHECR. A UHECR proton colliding with a CMB photon can generate a Delta baryon (Δ) resonance state. This resonance state mostly decays into a pion and a nucleon [18]. There are two main decay modes for a Δ^+ [115]:

$$\begin{aligned} p + \gamma_{\mathrm{CMB}} &\longrightarrow \Delta^+(1232) \longrightarrow \pi^+ + n \ \ (1/3 \text{ of all cases}), \\ p + \gamma_{\mathrm{CMB}} &\longrightarrow \Delta^+(1232) \longrightarrow \pi^0 + p \ \ (2/3 \text{ of all cases}). \end{aligned} \tag{1.4}$$

The center of mass energy $\sqrt{\mathrm{s}}$ must be higher than the sum of proton and pion masses to expect this process. The square of the center of mass energy for a proton and a photon collision in the laboratory frame follows Equation (1.5):

$$s = \mathrm{m}_{\mathrm{proton}}^2 + 2\mathrm{E}_{\mathrm{proton}}\epsilon(1 - \cos(\theta)), \tag{1.5}$$

where ϵ is the energy of γ_{CMB} in order of 10^{-3} eV. θ is the collision angle between UHECR and γ_{CMB} where a head-on collision indicates $\cos(\theta)$ = -1. From these conditions, the minimum energy required for a proton UHECR is calculated in Equation (1.6):

$$\mathrm{E}_{\mathrm{proton}} = \frac{\mathrm{m}_{\mathrm{pion}}}{4\epsilon}(2\mathrm{m}_{\mathrm{proton}} + \mathrm{m}_{\mathrm{pion}}) \simeq 10^{20}\mathrm{eV}. \tag{1.6}$$

Particle accelerator experiments have well established the cross section of this process. The highest cross-section value is about 500 μb at the mass of the Delta resonance referred to in Equation (1.4) [116]. Various numerical studies have also estimated the energy loss length. For a proton UHECR, the energy loss length becomes an order of 10 Mpc (megaparsecs), working as the main effect causing the GZK-cutoff. Figure 1.22 on page 21 indicates its effect on the propagation of UHECR.

These photo-pion production processes play a crucial role in the energy loss and attenuation of UHECR as they propagate through the intergalactic medium, ultimately leading to the GZK cutoff in the UHECR flux.

Photo-disintegration

For heavier nuclei in Ultra-High-Energy Cosmic Rays (UHECR), there is an additional energy loss process known as photo-disintegration. This process occurs when a nucleus UHECR interacts with a photon from the Cosmic Microwave Background (CMB) or the Extragalactic Background Light (EBL), which is the emission from extragalactic sources in the energy range from 10^{-3} eV to 10 eV [117].

In photo-disintegration, a heavy nucleus UHECR absorbs a photon and emits one or more nucleons. The equation can represent the interaction:

$$\mathrm{Z} + \gamma_{\mathrm{CMB\ or\ EBL}} \longrightarrow (\mathrm{Z} - n\mathrm{N}) + n\mathrm{N}, \tag{1.7}$$

Here, Z represents the heavy nucleus UHECR, n is the number of nucleons the nucleus loses, and N is the emitted nucleon after disintegration. Photo-disintegration occurs when the center of mass energy of the collision between the heavy nucleus UHECR and the photon is equal to or greater than the threshold of the Giant Dipole Resonance (GDR) of the nucleus.

The GDR refers to the peak of cross sections in nuclei when they absorb photons. It arises from the collective motion of nucleons in the nucleus, where protons move in one direction while neutrons move in the opposite direction [118]. The GDR threshold for photons in the rest frame of the nucleus is approximately 10 MeV to 30 MeV [119].

Figure 1.22 on page 21 illustrates that iron nuclei with an energy of 10^{20} eV have a similar energy loss length to protons.

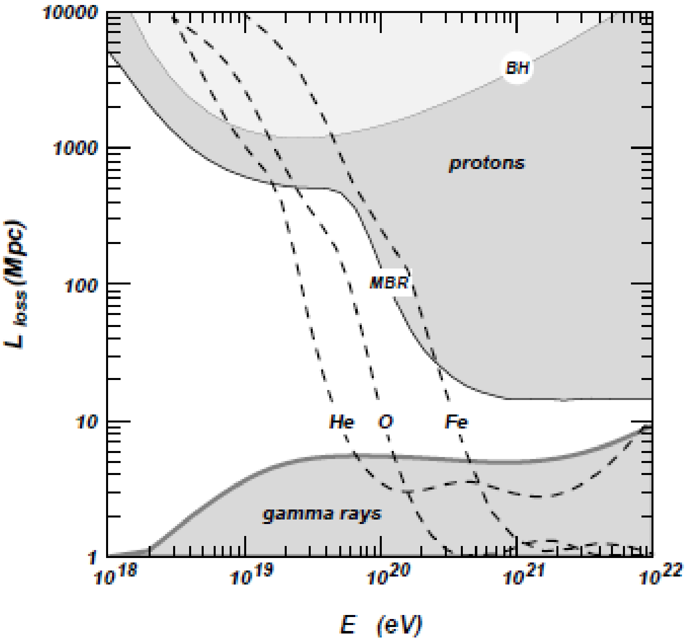

Figure 1.22: Energy loss lengths of proton UHECR, nuclei UHECR, and gamma rays over a broad range of energy [28]. The energy loss lengths of proton UHECR show the contributions from two processes: e^+e^- pair-production labeled as BH and interaction with CMBR photons labeled as MBR. The energy loss lengths of nuclei UHECR are indicated with broken lines. The energy loss lengths of gamma rays are also shown. Adiabatic loss due to the expansion of the universe itself is not considered.

Pair Production

UHECR can also lose energy through e^+e^- pair production when interacting with CMB photons. This process resembles the classic pair-production process for gamma ray photons in a nuclear field.

$$p + \gamma_{\text{CMB}} \longrightarrow e^+ + e^- + p. \tag{1.8}$$

The average energy loss length is calculated with the inverse of the product of the interaction cross section and the CMB photon density. For example, the energy loss length calculated for a 10^{19} eV proton UHECR is about 1 Gpc (gigaparsec), as shown in Figure 1.22 on page 21. Therefore, the effect of e^+e^- pair production is less significant in estimating astrophysical sources of UHECR. However, the pair production cross section is a quadratic function of the charge of the nucleus $\text{Z}e$ [120]. Therefore, e^+e^- pair production becomes an integral part of propagation loss when the composition of UHECR is a heavier nucleus.

Adiabatic Loss

Another energy loss mechanism for UHECR is adiabatic loss, resulting from the cosmological redshift and the expansion of the universe. The energy loss length due to this effect is calculated using the speed of light in vacuum (c_0) and the Hubble constant (H_0) [18]. The calculated energy loss length is approximately 4 Gpc [121].

The equation for calculating the energy loss length is:

$$\frac{c_0}{\text{H}_0} = 1.372 \times 10^{26} \ \text{m} \simeq 4,440 \ \text{Mpc}. \tag{1.9}$$

1.3.3 Extensive Air Showers

Regarding the observation of UHECR, as mentioned earlier, directly detecting primary cosmic rays with energies above 10^{15} eV is challenging due to their low flux, which is less than 1 particle per square meter per year. Therefore, the feasible approach is to observe the cascade of secondary cosmic rays triggered by the initial interaction between a primary cosmic ray and a nucleus in the Earth's atmosphere. This cascade of secondary cosmic rays is known as an EAS.

The initial stage of an EAS involves secondary hadronic particles such as protons, neutrons, $\pi^\pm$ (pions), π^0 (neutral pions), and $\text{K}^\pm$ (kaons). These secondary particles undergo interactions with other nuclei in the atmosphere, leading to an increase in their numbers and the development of the EAS.

Among the secondary particles, the decay of a π^0 into two gamma rays (γ) is represented as follows:

$$\pi^0 \longrightarrow \gamma + \gamma. \tag{1.10}$$

The two gamma rays generated by a decay process of a π^0 in the early stage of an EAS have energies high enough to start electron-positron pair productions by interacting with atmospheric nuclei. The generated electrons and positrons can also produce gamma rays via Bremsstrahlung or pair annihilation. The cycle of the above processes results in an electromagnetic cascade as compared to a hadronic cascade. Both electromagnetic and hadronic cascades account for most of an EAS started by a primary UHECR.

Muons become a distinguished part of the secondary particles in an EAS. Muons are an outcome mainly of a charged pion decay in a hadronic cascade, as shown below:

$$\pi^{\pm} \longrightarrow \mu^{\pm} + \nu_{\mu}(\overline{\nu_{\mu}}). \tag{1.11}$$

The following process is the decay of a muon into an electron or a positron with two neutrinos, as shown below:

$$\mu^{\pm} \longrightarrow e^{\pm} + \nu_{e}(\overline{\nu_{e}}) + \overline{\nu_{\mu}}(\nu_{\mu}). \tag{1.12}$$

However, for the following reasons, most muons from an EAS can reach ground level without becoming a part of an electromagnetic cascade.

1. A muon's relatively longer mean lifetime of 2.2 × 10^{-6} s [18].
2. The lower interaction rate of a muon with atmospheric nuclei.

Figure 1.23 on page 23 shows a simplified diagram of an EAS. It clearly shows that the EAS has three parts: hadronic, electromagnetic, and muonic.

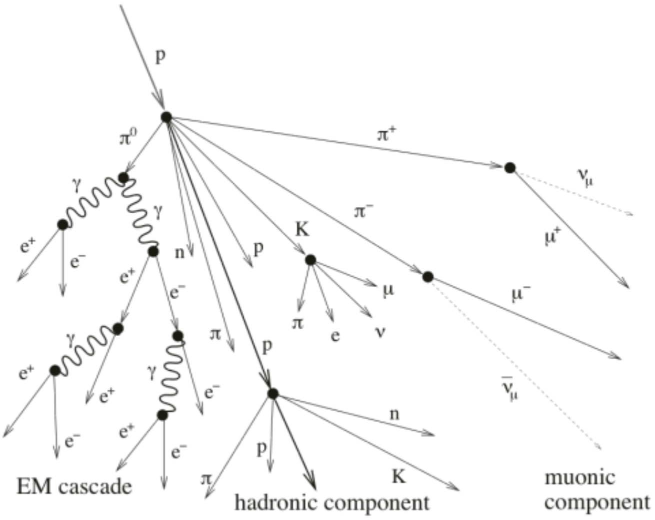

Figure 1.23: Simplified diagram of a UHECR-induced extensive air shower [29]. The primary cosmic ray is assumed to be a proton. Each electromagnetic part (EM cascade), hadronic part, and muonic part of the EAS are shown.

Longitudinal Development

During the early stage of an EAS, the number of secondary particles in the cascade rapidly increases as the energy of each individual secondary particle decreases. However, a threshold energy called the critical energy (E_c) plays an essential role in the development of the EAS. In air, the critical energy is approximately 80 MeV.

The critical energy marks a transition point in the EAS development. Below this energy, the electromagnetic component of the EAS stops growing in number, and the dominant energy loss process shifts from electron Bremsstrahlung to ionization. The critical energy is associated with the balance between the energy loss rate due to ionization and the energy loss rate due to Bremsstrahlung.

As the energy of individual particles in the cascade drops below the critical energy, the energy loss rate by ionization increases and eventually becomes comparable to the energy loss rate due to electron Bremsstrahlung. At this point, ionization becomes the dominant energy loss process in the cascade.

This shift in dominant energy loss mechanisms below the critical energy has important implications for the longitudinal development of the EAS and the energy distribution of the particles within the shower.

This development of an EAS along the depth of the atmosphere through which the EAS passes is called the longitudinal development of an EAS. For the electromagnetic part, Heitler's simplified model presents a simple way to estimate a longitudinal particle distribution of an EAS by adopting a perfect binary tree of a particle cascade [122]. At each step, one of two processes takes place in this model, as shown below:

$$\begin{aligned} e^- &\longrightarrow \gamma + e^-, \\ \gamma &\longrightarrow e^- + e^+. \end{aligned} \tag{1.13}$$

The simplified interaction step length (d) is formulated from the radiation length λ_r as shown in Equation (1.14), which is approximately 37 g/cm^2 in air.

$$\mathrm{d} = \lambda_\mathrm{r} \ln 2. \tag{1.14}$$

By ignoring the energy dependence of the cross section of the processes and the energy loss due to collision, an individual particle's energy after n-th interaction is calculated as $\mathrm{E}_0/2^n$. E_0 is the energy of a particle that initiated the electromagnetic cascade. Since the number of particles increases until the individual particle's energy reaches the critical energy, the maximum number of particles in a cascade (N_max) is calculated as below:

$$\mathrm{N}_\mathrm{max} = \frac{\mathrm{E}_0}{\mathrm{E}_c}. \tag{1.15}$$

From N_max, the atmospheric depth at which the number of secondary particles of an EAS reaches the maximum (X_max) is calculated as below:

$$\mathrm{X}_\mathrm{max} = \mathrm{X}_0 + \lambda_\mathrm{r} \ln(\mathrm{N}_\mathrm{max}), \tag{1.16}$$

where X_0 is the atmospheric depth at the start point of the cascade. Then the change of X_max as a function of energy E_0 is defined below:

$$\mathrm{D}_{10} = \frac{d\mathrm{X}_\mathrm{max}}{d \log_{10} \mathrm{E}_0} = 2.3\lambda_\mathrm{r}. \tag{1.17}$$

This change rate of X_max, D_{10} is traditionally referred to as an elongation rate based on the study by Linsley in 1977 [123]. The following approximation is used in usual cases to get the number of secondary particles in an EAS as a function of atmospheric depth:

$$\mathrm{N}_e(t) \sim \frac{0.31}{\sqrt{y}} e^{t(1-1.5\ln(s))}, \tag{1.18}$$

where $y = \ln(\mathrm{E}_0/\mathrm{E}_c)$. The aging parameter s is $3t/(t+2y)$. t indicates the atmospheric depth the EAS penetrated in a unit of the radiation length (λ_r) in air.

The method widely adopted in analyses for recent UHECR experiments to describe the numbers of particles in the longitudinal development of an EAS is a function proposed by Gaisser and Hillas in 1977 [124]. The Gaisser and Hillas (G-H) function is shown below:

$$\mathrm{N}_e(\mathrm{X}) = e^{\frac{\mathrm{X}_{\mathrm{max}}-\mathrm{X}}{\lambda}} \times \mathrm{N}_{\mathrm{max}}(\frac{\mathrm{X}-\mathrm{X}_0}{\mathrm{X}_{\mathrm{max}}-\mathrm{X}_0})^{\frac{\mathrm{X}_{\mathrm{max}}-\mathrm{X}_0}{\lambda}}. \tag{1.19}$$

The definitions of $\mathrm{N}_{\mathrm{max}}$, $\mathrm{X}_{\mathrm{max}}$, and X_0 are the same as in Heitler's simplified model described above. λ is a parameter describing the attenuation length of the longitudinal distribution. The commonly used value for the attenuation length is 70 g/cm^2. The exact value is used in the analysis of the hybrid trigger mode of the TA experiment, as described further in Section 4.2.3.

Lateral Development

The lateral development of an EAS refers to the spread of particles in the perpendicular direction to the shower axis. The shower axis is essentially the virtual axis along which the EAS develops, and it is approximately aligned with the incident direction of the primary UHECR.

In lateral development, one key parameter of interest is the particle density distribution around the shower core (EAS core), which is the point where the shower axis intersects the ground level. To approximate this distribution for the electromagnetic component of the EAS, the Nishimura-Kamata-Greisen (NKG) function is commonly used [125][126]. This function allows for an estimation of the charged particle density (ρ_e) as a function of the radial distance (R) from the shower core and the aging parameter (s), as calculated below.

$$\rho_e(\mathrm{R,s}) = \mathrm{C}(s)\frac{\mathrm{N}_e}{\mathrm{R}_m^2}(\frac{\mathrm{R}}{\mathrm{R}_m})^{s-2.0}(1+\frac{\mathrm{R}}{\mathrm{R}_m})^{s-4.5}, \tag{1.20}$$

where R is the distance from the position of the shower axis and N_e is the number of all charged particles. R_m indicates the Molière radius, which is a characteristic constant for a given material describing its electromagnetic interaction properties. R_m of a given material is estimated using the radiation length and the atomic number of the material. s is the aging parameter also used in Equation (1.18). Finally, C(s) is the normalization factor, which is calculated with gamma functions as described below:

$$\mathrm{C}(s) = \frac{\Gamma(4.5-s)}{2\pi\Gamma(s)\Gamma(4.5-2s)}. \tag{1.21}$$

1.3.4 Photon Emission from Extensive Air Showers

Air Fluorescence

Air fluorescence is an important phenomenon in observing EAS induced by UHECR. When a charged particle traverses through the atmosphere, it loses energy by exciting electrons in the material it passes through. Optically transparent materials emit a fraction of this deposited energy as scintillation light. In the case of an EAS, which involves a vast number of charged particles, a fraction of their energies is deposited in the atmosphere and emitted as fluorescence light, known as air fluorescence.

Research efforts on air fluorescence have revealed that the dominant component of this light comes from excited nitrogen molecules, which constitute about 78% of the Earth's atmosphere. The fluorescence light emitted by excited nitrogen molecules has wavelengths primarily in the ultraviolet (UV) region, ranging from 300 nm to 400 nm, approximately. Different research collaborations have measured the wavelength spectra of nitrogen fluorescence, as shown in Figure 1.24 on page 26. These measurements help characterize the properties of air fluorescence and are essential for UHECR observatories utilizing this technique to detect and study cosmic rays.

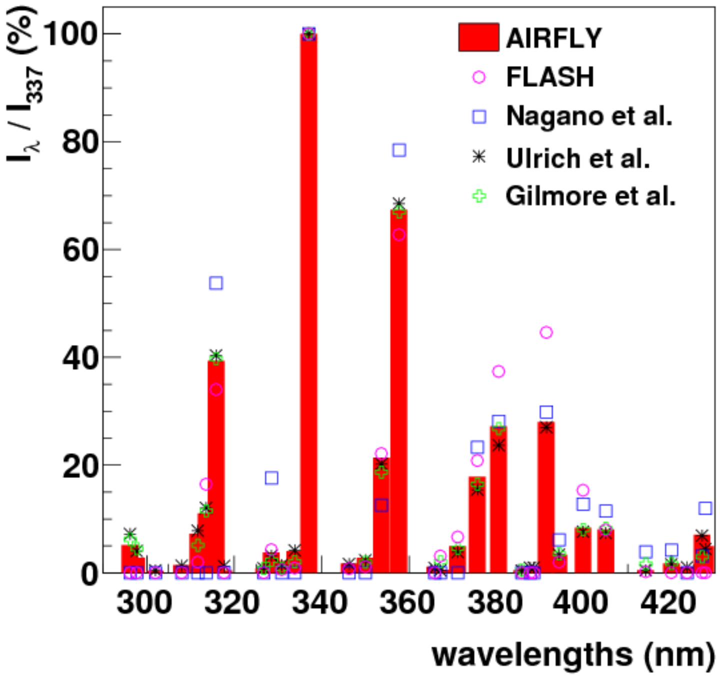

Figure 1.24: Wavelength spectra of nitrogen fluorescence measured in various research collaborations [30]. Fluorescence intensities are normalized to the intensity at 337 nm, the wavelength at which the results of all collaborations showed the highest intensity.

Establishing a robust fluorescence yield model is essential to analyze an EAS accurately using the air fluorescence detection technique. The research collaborations in Figure 1.24 on page 26 have measured fluorescence yields using charged particles of various energies.

Cherenkov Radiation

Cherenkov radiation is emitted when a charged particle moves through an optically transparent medium at a velocity higher than the speed of light in that medium [127]. The angle between the direction of motion of the charged particle and the wavefront of Cherenkov radiation is given by the formula:

$$\theta = \arccos(\frac{c_0}{n \cdot v}), \tag{1.22}$$

where c_0 is the speed of light in a vacuum, n is the refractive index of the medium, and v is the velocity of the particle in the medium. For example, in the atmosphere at 1 atm pressure with a refractive index of approximately 1.00029, a particle moving at the speed of light would have a radiation angle of 1.4° approximately. However, the refractive index depends on the altitude of actual EAS. Below formula gives the refractive index for various heights:

$$n(h) = 1 + 0.000283 \frac{\rho_{\text{air}}(h)}{\rho_{\text{air}}(0)}, \tag{1.23}$$

where $\rho_{\mathrm{air}}(h)$ is the density of air at the altitude h. At a typical altitude of 10 km, the radiation angle becomes 0.8° approximately. To emit Cherenkov radiation in air at this altitude, a charged particle must have a Lorentz factor γ greater than 72, corresponding to an electron energy about 37 MeV [128].

The number of Cherenkov radiation photons emitted per unit length of the charged particle's path and per unit wavelength λ is calculated using the formula:

$$\frac{d^2\mathrm{N}}{dxd\lambda} = \frac{2\pi\alpha\mathrm{Z}^2}{\lambda^2}(1 - \frac{c^2}{n^2v^2}), \tag{1.24}$$

where α is the fine structure constant, Z is the charge number of the particle, and c is the speed of light.

Although Cherenkov radiation is highly directional, it can contribute to background noise in air fluorescence technique to detect EAS due to the following reasons:

1. The lateral development of an EAS leads to a broadening of the actual radiation angle of Cherenkov radiation emitted from the shower.

2. Cherenkov photons are scattered in the atmosphere.

Figure 1.25 on page 27 shows the numbers of simulated photons injected into the FD of the TA experiment. It demonstrates that photons generated by Cherenkov radiation dominate in an EAS with a specific geometry. Section 4.2.4 describes a method to improve the quality of reconstructing EAS by rejecting the Cherenkov radiation background.

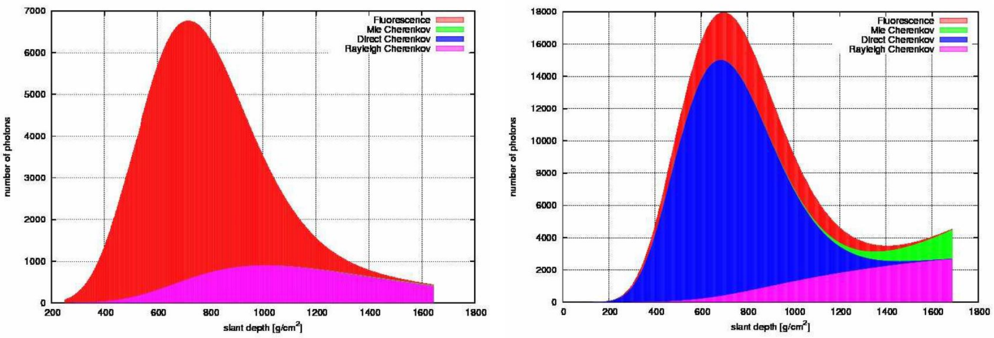

(a) Nominal

(b) Cherenkov dominated

Figure 1.25: Numbers of photons injected into the TA FD telescope in an early Monte Carlo (MC) simulation study [31]. The red region indicates the contributions from air fluorescence. The blue, green, and magenta regions indicate the contributions from Cherenkov radiation. (a) EAS is going across the Field Of View (FOV) of the FD telescope. (b) EAS is heading toward the FD telescope, which shows significant contamination by Cherenkov radiation.

1.3.5 Propagation of Light in the Atmosphere

In the propagation of light in the atmosphere, the photons produced from an EAS undergo various physical processes before reaching the photon detectors of observatories. The dominant effect in this propagation is Rayleigh scattering, which occurs when light interacts with molecules in the atmosphere. The ratio of incident light I_0 to scattered light I_s in Rayleigh scattering is given by the formula:

$$\frac{\mathrm{I}_s}{\mathrm{I}_0} = \frac{8\pi^4 \mathrm{N}\alpha(1+\cos^2\theta)}{\lambda^4 r^2}, \tag{1.25}$$

here, N represents the number of scattered particles, α is the polarization rate, θ is the scattering angle, λ is the wavelength of the incident light, and r is the distance between the point of scattering and the point of observation.

Rayleigh scattering applies when the size of the scattering particle (such as air molecules) is smaller than the wavelength of light. The size parameter x, which characterizes the scattering particle size, is defined as:

$$x = \frac{2\pi r}{\lambda}, \tag{1.26}$$

where r is the characteristic radius of a scattering particle. Rayleigh scattering occurs when $x \ll 1$. However, when the size parameter approaches to 1 ($x \approx 1$), a different type of scattering, called aerosol scattering or Mie scattering, must be considered. Aerosol scattering typically occurs due to colloidal particles. The transmittances of light for both Rayleigh scattering ($\mathrm{T_R}$) and aerosol scattering ($\mathrm{T_A}$) are calculated as follows:

$$\ln \mathrm{T_R} = -\frac{\mathrm{X_t}}{\mathrm{X_R}}\left(\frac{400}{\lambda(\mathrm{nm})}\right)^4, \tag{1.27}$$

$$\ln \mathrm{T_A} = \frac{h_m}{l_m \cos\theta}\left(e^{\frac{-h_1}{h_m}} - e^{\frac{-h_2}{h_m}}\right)\frac{\lambda_m}{\lambda}, \tag{1.28}$$

$\mathrm{X_t}$ is the slant depth, measured in g/cm^2, that the light from the EAS has penetrated through. $\mathrm{X_r}$ is the radiation length of Rayleigh scattering, which is 2,974 g/cm^2 at a wavelength of 400 nm.

For aerosol scattering, h_m is the scale height of the aerosol distribution, where the aerosol density is assumed to decrease exponentially above this height. l_m is the horizontal mean free path of aerosol scattering at the wavelength λ_m. h_1 and h_2 are the heights of the scattering point and the photon detector, respectively. Typical values used in the analysis of the TA experiment are $h_m = 1$ km, $l_m = 25$ km, and $\lambda_m = 360$ nm [21].

The transmittance of Rayleigh scattering is calculated relatively quickly based on atmospheric density, which is correlated with temperature and air pressure. However, the transmittance of aerosol scattering depends on the distribution of colloidal particles in the atmosphere, which is more random and challenging to model precisely. Therefore, a dedicated calibration device or monitoring system, such as the Central Laser Facility (CLF) used in the TA experiment, is essential for analyzing data collected by air fluorescence detectors. The CLF is described in more detail in Section 2.2.1.

Chapter 2

The Telescope Array Experiment

The Telescope Array (TA) experiment is the largest Ultra-High-Energy Cosmic Rays (UHECR) observatory in the Northern Hemisphere, situated in Millard County, Utah, United States [82]. It is an international collaboration involving over 100 scientists from various countries, including Japan, the United States, Russia, South Korea, Slovenia, and Belgium. The primary goal of the TA experiment is to study UHECR and their properties.

The TA experiment consists of multiple detectors, including three Fluorescence Detector (FD) stations and 507 Surface Detectors (SD) [45][129]. These detectors enable using two independent detection methods: air fluorescence and surface particle detection, as shown in Figure 2.1 on page 29.

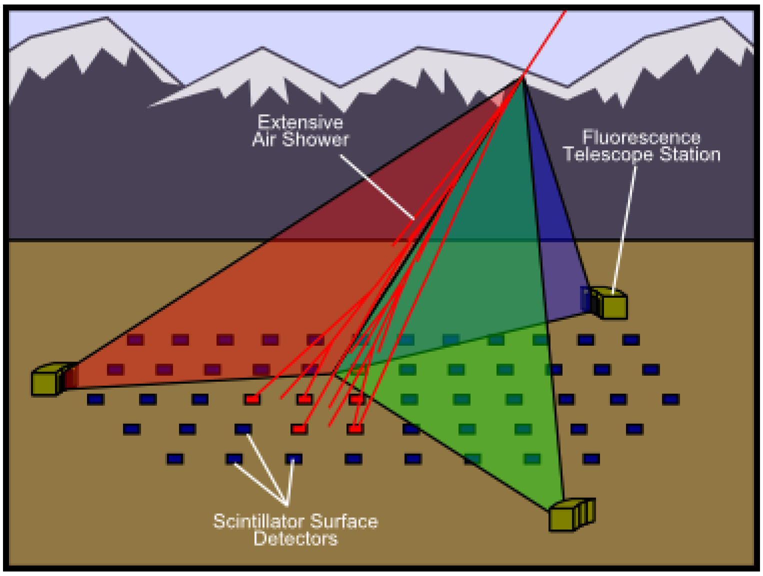

Figure 2.1: Conceptual diagram of the hybrid detection principle [32]. Both fluorescence detectors and surface detectors are shown.

The air fluorescence detection method relies on observing the fluorescence light emitted by nitrogen molecules in the atmosphere when they are excited by the passage of Extensive Air Showers (EAS). The FD stations are equipped with telescopes that capture and measure this fluorescence emission to determine the energy and other characteristics of the incoming cosmic rays.

The surface particle detection method involves a network of surface detectors spread over a large area. These detectors are sensitive to the secondary particles produced when UHECR interact with the Earth's atmosphere. Valuable information about the primary cosmic rays is obtained by measuring the distribution and properties of these particles at the ground level.

The TA experiment has been conducting regular observations since 2008, accumulating more than ten years of data. Combining air fluorescence and surface particle detection provides a comprehensive and complementary approach to studying UHECR, helping scientists better understand the origin and nature of these high-energy particles.

2.1 Background of the TA Experiment

The motivation for the TA experiment stems from the need to reconcile conflicting results observed by previous UHECR observatories, namely the Fly's Eye experiment and the Akeno Giant Air Shower Array (AGASA) experiment.

The Fly's Eye experiment reported an energy spectrum that did not contradict the expected suppression model [96]. In contrast, the AGASA experiment observed an extension of the energy spectrum beyond the hypothesized Greisen-Zatsepin-Kuzmin (GZK) cutoff [130]. Figure 2.2 on page 30 illustrates the UHECR energy spectra measured in the AGASA experiment and the HiRes experiment, which is a successor to the Fly's Eye experiment.

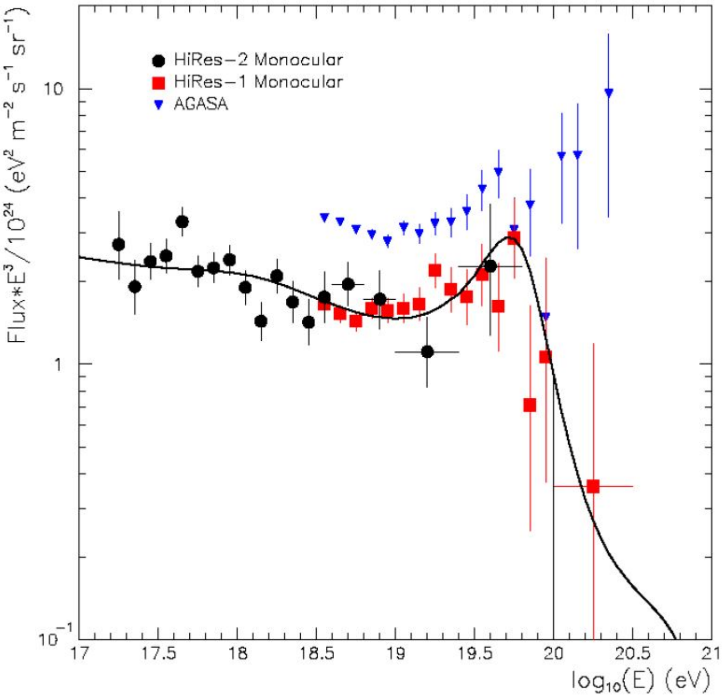

Figure 2.2: UHECR energy spectra reported by the HiRes experiment and the AGASA experiment [33], displaying a difference between the two results at the highest energy.

The Fly's Eye and HiRes experiments relied solely on air fluorescence detection with two spatially separated FD stations [80]. On the other hand, the AGASA experiment employed only surface particle detection with 111 SDs [131]. Furthermore, the limited event statistics, particularly at the highest energies also made it challenging to reach a definitive conclusion.

To address and resolve the discrepancies, physicists recognized the need for a large-scale UHECR observatory with a hybrid detection technique. This motivation led to the development of the TA experiment in the desert region of central Utah, characterized by a high rate of clear sky and minimal artificial light contamination. The experiment site is located near 39° North latitude and 113°

West longitude, with an average elevation of approximately 1,400 m above sea level, corresponding to an atmospheric depth of about 860 g/cm^2. The layout of the observatory is depicted in Figure 2.3 on page 31.

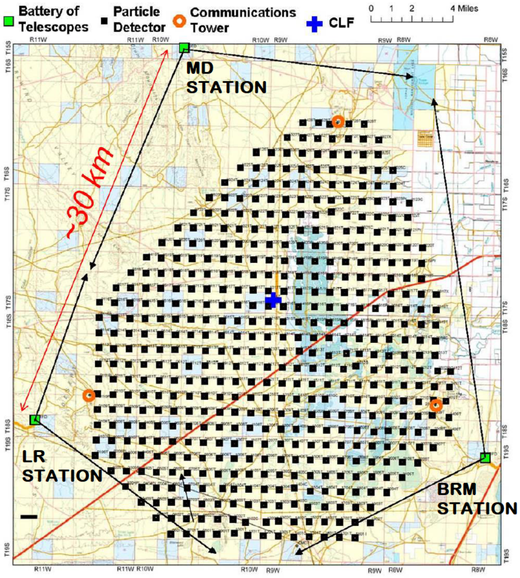

Figure 2.3: Layout of the TA experiment site [34]. The black squares indicate the surface detectors, and the orange open circles indicate the three SD communication towers. The green squares indicate the fluorescence detector stations. The blue cross in the middle of the SD array indicates the Central Laser Facility (CLF). The black arrows from fluorescence detector stations represent their azimuthal extent of the field of view.

The TA experiment comprises three air FD stations: Middle Drum (MD), Black Rock Mesa (BRM), and Long Ridge (LR). The BRM and LR stations each have 12 air fluorescence telescopes, while the MD station has 14 telescopes. In addition, 507 SDs are deployed on a square grid with a spacing of 1.2 km, covering an area of approximately 700 km^2. The combination of FD and SD allows for a hybrid detection approach, providing a comprehensive view of UHECR events and enabling more accurate measurements of their energies, arrival directions, and other properties.

2.2 Detectors of the TA Experiment

2.2.1 Fluorescence Detector

The air fluorescence detectors of the TA experiment are installed at the three stations, as stated above. This section is dedicated to the instrumentation of the BRM and LR stations since the fluorescence detectors of the MD station are refurbished from the detectors of the former HiRes experiment. Each of these two FD stations is designed to cover 108° in azimuth and 3° to 33° in elevation to record the tracks of air fluorescence generated by an EAS. An FD telescope comprises the optics, the main photomultiplier tube (PMT) camera, and the dedicated Data AcQuisition (DAQ) system. The photographs of the FD stations and FD telescopes are shown in Figure 2.4 on page 32.

Optics

The composite mirrors with a spherical surface are central to the BRM and LR station optics. Each camera's 3.3 m diameter of optics consists of 18 segments of

Figure 2.4: The FD stations of the TA experiment [35]. The upper photograph shows the BRM station and a pair of FD telescopes designed to cover lower and upper elevations of the sky. The lower photograph shows the MD station and a pair of FD telescopes covering the sky's lower and upper elevations. Showing the BRM station and the MD station have different instruments.

hexagonal mirrors. The Full Width at Half Maximum (FWHM) of the spot size of the optics is designed to be ∼ 30 mm, which is smaller than the opposite side distance (distance across flats) of 60 mm for a hexagonal PMT. Each hexagonal mirror is made of Tempax glass with the surface coated by anodized aluminum. A hexagonal mirror has 660 mm of diagonal length with a thickness of 11 mm and the curvature radius is 6,067±40 mm. The mirror's reflectance is above 80% in the wavelength range from 350 nm to 400 nm. This optics allows a PMT to have a Field Of View (FOV) of $1^\circ \times 1^\circ$. In ordinary cases, the reflectances of all mirrors in FD stations are measured every three months. In addition, all mirrors are cleaned once a year because specks of dust and stains on the mirror surface affect the reflectance of a mirror.

Camera

At the focal surface of the optics described above is the main camera. The main camera is made of an array of PMTs. Each array of PMTs includes $16 \times 16 = 256$ PMTs. The model number of PMT is R9508, manufactured by Hamamatsu Photonics with a hexagonal-shaped photocathode. Each PMT has an Ultraviolet (UV) band-pass filter (BG3; Schott Advanced Optics) attached to its photocathode surface to cut the amount of background light from the night sky. The detailed transmittance profile of the Schott BG3 UV band-pass filter is described in Figure 2.5 on page 33.

Figure 2.6 on page 33 is a view of a PMT for the BRM and LR stations. The 16×16 array of PMTs is installed in a protective box to keep PMTs from

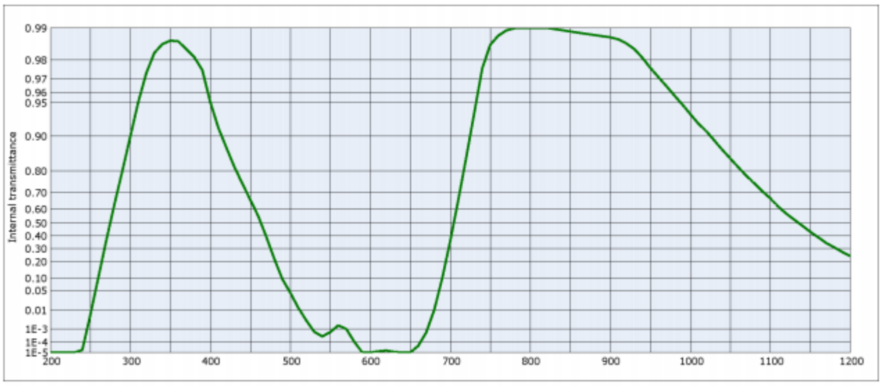

Figure 2.5: Transmittance profile of Schott BG3 filter. The horizontal axis represents the wavelength of light in nanometers. The vertical axis represents transmittance. BG3 filter has transmittance greater than 90% in the wavelength range from 300 nm to 400 nm, which accounts for the majority of nitrogen fluorescence spectrum, as shown in Figure 1.24 on page 26.

contamination by environmental factors. Figure 2.7 on page 34 shows an array of PMTs installed in a protective box for the BRM and LR stations before getting attached to a telescope structure. The front of a protective box is an opening made of a UV-transmitting methacrylic resin sheet (PARAGLAS UV00; Kuraray Co., Ltd), which is for all weather. The detailed transmittance profile of Kuraray PARAGLAS UV00 is described in Figure 2.8 on page 34.

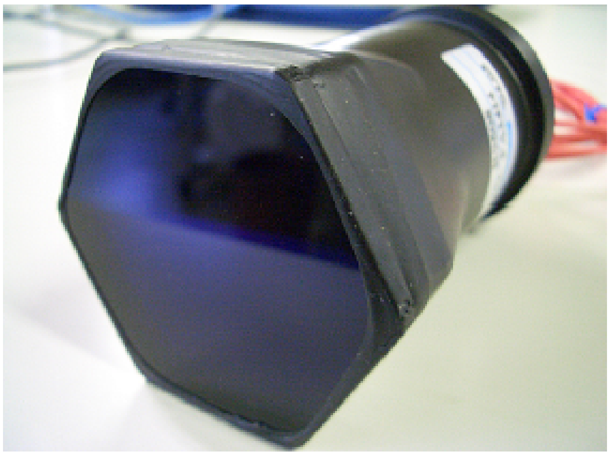

Figure 2.6: PMT for the FDs of the BRM and LR stations with BG3 filter attached on the photocathode surface [36]. Its hexagonal shape makes it easy to build a honeycomb-shaped array.

DAQ Electronics

On the DAQ part of the BRM and LR stations, the electric current signals from PMTs are amplified by a pre-amplifier with a gain of 5 first. Then the combined gain of a PMT is tuned to be $4{\times}10^6$ by controlling the voltage applied to each PMT. After amplification, the signals are processed by three kinds of VME (Versa Module Europa) bus standard DAQ modules: Signal Digitizer and Finder (SDF), Track Finder (TF), and Central Trigger Distributor (CTD) [33].

An SDF module has the main amplifier and a Flash Analog to Digital Converter (FADC) with the first-level trigger logic circuits. Each SDF module has

Figure 2.7: FD camera assembled for the BRM and LR stations [36]. An array made of 256 PMTs is contained in a protective box. The box has a UV transmitting window.

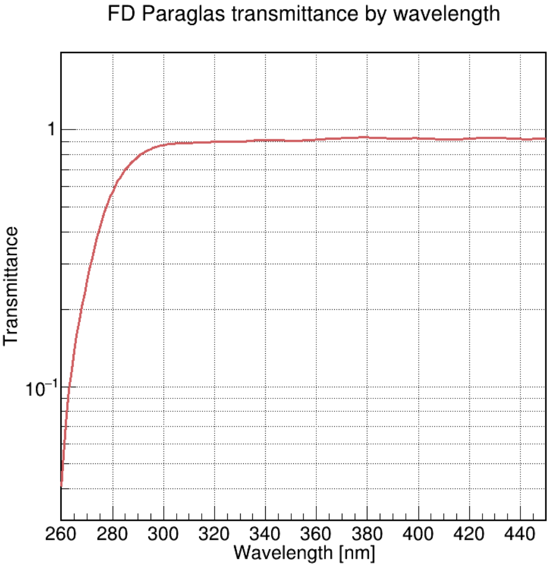

Figure 2.8: Transmittance profile of Kuraray PARAGLAS UV00. PARAGLAS UV00 has more than 85% of transmittance in the wavelength range from 300 nm to 400 nm.

16 inputs, and 16 SDF modules work for one camera, as there are 256 PMTs for each camera. The FADC of SDF has a 12 bits digitizing ability with a 40 MHz sampling rate. An SDF module first integrates four sampled data into a single bin, so each integrated bin becomes 100 ns long, and then sets a 12.8 μs long signal finding window. If a unit of this finding window has a signal that exceeds a threshold set by operators, a first-level trigger is issued from an SDF module. Then the first-level trigger is passed onto a TF module.

The TF module for each camera then judges if a spatial track meets the condition for issuing a second-level trigger. The judgment is made by collecting all first-level triggers from 16 SDF modules installed for each camera. If a TF module finds a spatial track, a second-level trigger is passed onto the CTD module.

There is only one CTD module for each FD station. By collecting all second-level triggers from 12 TF modules representing each camera, the CTD module judges to issue the final level trigger to the event record system of an FD station. A CTD module has a clock generator, an initializer, and a Global Positioning System (GPS) module. A simple diagram is shown in Figure 2.9 on page 35 to introduce the general structure of the DAQ system of the BRM and LR stations.

The additional features of the DAQ system of the BRM and LR stations are the detector dead time and airplane veto. To process the event data and become ready to be triggered again, an FD station cannot be triggered within a specific period from a trigger. This insensitive period is called dead time and occupies about 10% of FD operation time with a median dead time of 30 ms per trigger. A CTD module can record the dead time that is vital in calculating the on-time of the FD station, which is explained in Section 5.3. Meanwhile, the sky above the TA experiment site is air routes; it is reported that strobe flashers equipped on airplanes cause a burst of triggers during the early operation of the BRM and LR stations. Airplane veto is implemented to avoid this problem by suspending triggers temporarily when an FD station receives airplane-like signals. This intentionally insensitive time also is added up to an FD station's dead time [37].

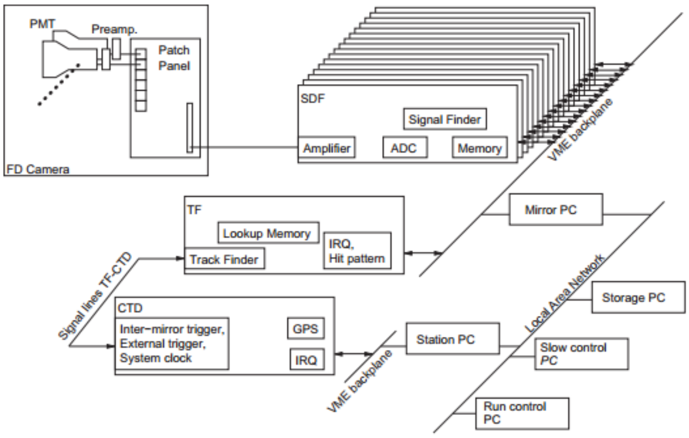

Figure 2.9: Schematic diagram of the DAQ system of a TA FD [37].

Calibration

To make the measurement of an EAS as precise as possible, it is required to study the systematic uncertainties in the observation data obtained by FDs. These studies include the absolute calibration for PMTs used in FD telescopes, the on-site optics calibration, and the atmospheric condition monitoring. As a part of such studies, a dedicated photometric calibration system for the BRM and LR stations is developed for absolute calibration at the laboratory. The system is called Calibration using RAYleigh Scattering (CRAYS). The CRAYS adopts an N_2 laser system with 337 nm wavelength as its source of light, and the laser is optically guided into the N_2 filled chamber and is scattered inside. A PMT for the BRM and LR stations is set to the chamber only to receive the Rayleigh scattered light from the source.

Since CRAYS has a calibrated energy probe to monitor the intensity of the incident laser and the cross section of Rayleigh scattering is well studied, it can precisely estimate the intensity of light entering a PMT. This feature allows the CRAYS to calibrate the response of PMTs with a systematic uncertainty of approximately 7.2% [38]. This absolute calibration by the CRAYS is done every three PMTs in each camera. A diagram of the CRAYS device is shown in Figure 2.10 on page 36. PMTs are attached to the cylindrical chamber to receive only the calibrated light from the source.

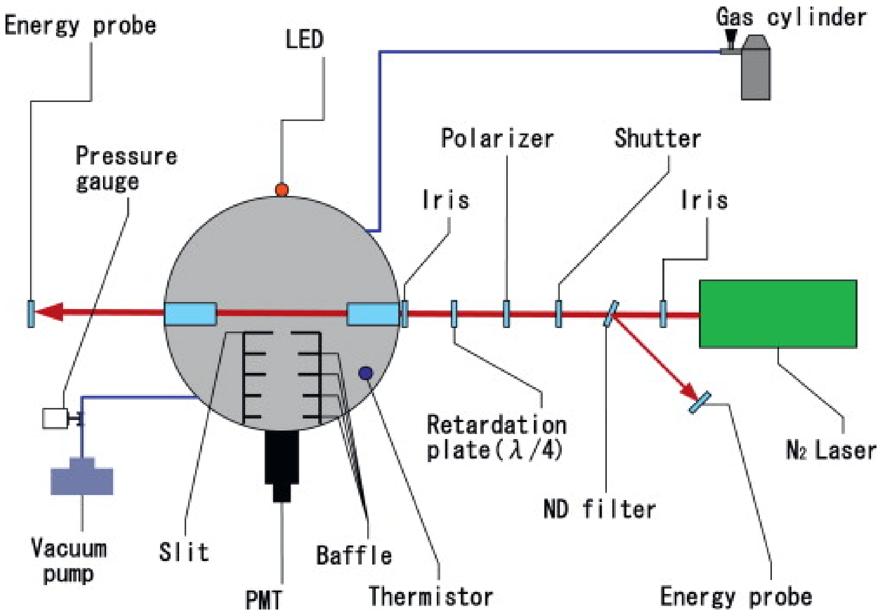

Figure 2.10: Schematic diagram of the CRAYS system [38]. The gray shaded areas indicate the scattering chamber. The red arrows indicate the paths of the laser beam. Baffles are shown between the chamber and the output port for a PMT. Baffles are needed to ensure only Rayleigh scattered light enters a PMT.

Since the results of absolute calibration made in the laboratory of the Institute for Cosmic Ray Research (ICRR) of the University of Tokyo can be altered by temperature, humidity, long-term effect, and even during the transportation to the experiment site at Utah from ICRR, a stable light source is required to be attached to monitor the response of absolutely calibrated PMTs to track the change in the calibration results. For the BRM and LR stations, Yttrium Aluminum Perovskite (YAP) is adopted to play this role as a stable radioactive light source consisting of $YAlO_3$:Ce scintillator and 50 bq of ^{241}Am α source. Each YAP module is embedded in the BG3 filter of the PMT, which is absolutely calibrated using the CRAYS in the laboratory. By tracking the electric signals of these calibrated PMTs caused by $\sim$50 Hz and 40 ns width UV pulses of a peak wavelength at 350 nm produced from YAP, the gain change of PMTs was monitored [39]. A photograph of YAP embedded in the BG3 filter is shown in Figure 2.11 on page 37.

Other 253 PMTs in a camera, which the CRAYS does not absolutely calibrate in the laboratory, are relatively calibrated using a Xenon flasher. As shown in Figure 2.4 on page 32, there is no mirror segment at the center of the composite mirror optics of the telescope. A Xenon flasher equipped with a diffuser is placed in this region of the optics for each camera. The uniform light from the Xenon flasher illuminates all 256 PMTs, including the three absolutely calibrated PMTs. The responses of PMTs from this light source are set to be the standard for the DAQ system to adjust the gains of all PMTs, so they can show a similar value of gain whether they are absolutely calibrated or not.

Although the optics for an FD camera is designed to have a 30 mm or a smaller spot size as described above, 2-dimensional fluctuations in sensitivity exist for all

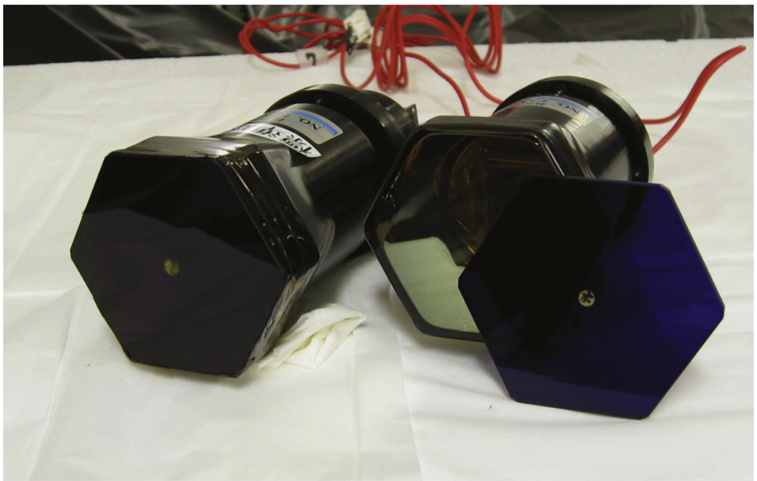

Figure 2.11: BG3 filter embedded with YAP and a PMT with a YAP embedded BG3 filter attached on its photocathode surface [39].

PMTs. Therefore, an XY-scanning device was developed to track this effect quantitatively. As the device is designed to be attached to the whole FD camera, it can scan the map of sensitivity for the camera by measuring its response from the monochromatic light of 365 nm wavelength emitted from a UV Light Emitting Diode (LED) light source. The spot size of light at the photocathode surface of a PMT is measured to be 3.83 mm, defined as the diameter of a circle containing 90% of the total light intensity. The intensity of a single pulse is adjusted to produce approximately 1,000 photoelectrons [40]. Finally, the scanning results are applied to compare the simulated and observed signals. Photographs of the XY-scanning device are shown in Figure 2.12 on page 37.

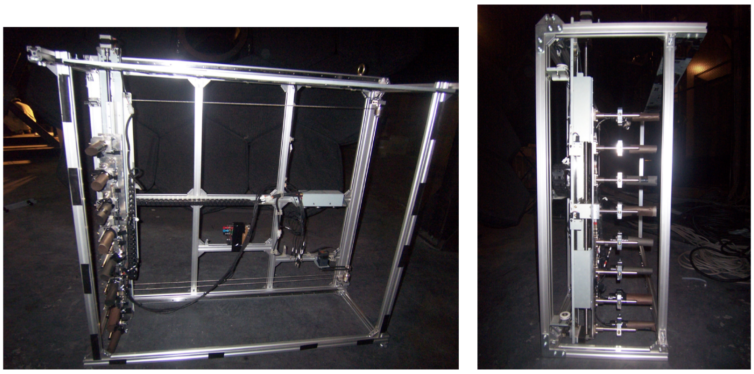

Figure 2.12: XY-scanning device developed for calibrating PMTs in the BRM and LR stations [40].

The relatively new method for on-site optics calibration adopted by the TA experiment is a flying light source called Opt-copter. As its name (Optics + Octocopter) suggests, the Opt-copter is a multirotor module equipped with a stable UV light source. By flying around the FOV of FD telescopes and flashing UV light at the designated positions, the Opt-copter is expected to perform the precise calibration of the pointing directions of the FD telescope of the TA experiment. The data collected by the Opt-copter is currently being analyzed [41][132]. Figure 2.13 on page 38 shows a photograph of the Opt-copter.

As well as the detector itself, constant monitoring of atmospheric conditions is required to measure the photons from EAS accurately. Typically, the photons

Figure 2.13: The multirotor module Opt-copter developed for calibrating FDs of the TA experiment [41].

travel through kilometers of air before reaching the telescope. The TA experiment has a set of atmosphere monitoring systems. As one of them, weather monitoring by human eyes has been performed since the beginning of the FD operation. The protocol for checking cloud coverage by human eyes is called the WEAT code (Weather code). A more detailed explanation of WEAT code is described in Section 5.1. Also, three Charge Coupled Device (CCD) fish-eye cameras were installed at the Central Laser Facility (CLF) site, the BRM station, and the LR station to monitor the weather and cloud coverage by tracking the night-time motion of stars. The system checks if stars are seen at the expected positions without being blocked by a cloud [133]. Figure 2.14 on page 38 shows an image taken by a CCD fish-eye camera. In the image, stars and cloud coverage are shown.

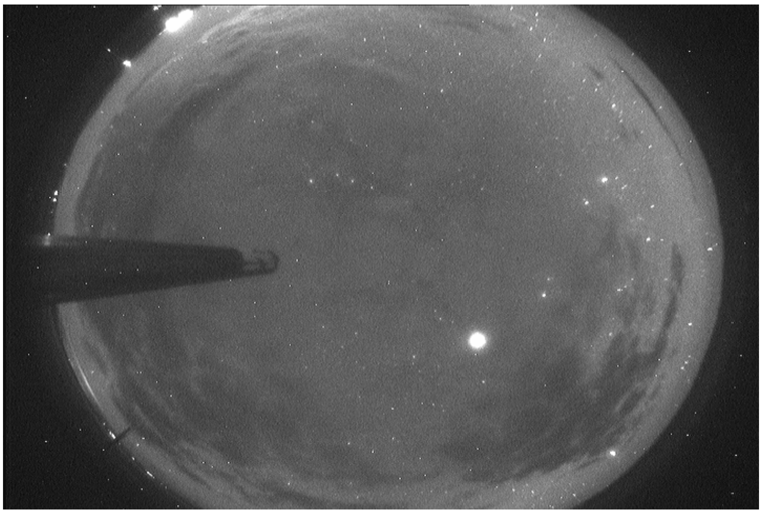

Figure 2.14: CCD fish-eye camera image taken on March 13th, 2015, at the rooftop of the BRM station. The dark shadows in the image indicate the position of clouds.

The CLF is the main atmospheric monitoring system for the TA experiment. Since the CLF is located at the center of the TA experiment site, approximately 21 km equidistant from all FD stations, it is possible to estimate the effect of aerosols in the atmosphere on all FD stations. The light source of CLF is an

Nd:YAG laser module that generates UV light wavelength of 355 nm [134]. The CLF vertically shoots UV laser pulses twice per hour when any FD of the TA experiment is running. Each shooting set consists of 300 pulses with a frequency of 10 Hz. Observation of laser pulses by the FD telescopes provides the profiles of an aerosol layer that causes aerosol scattering of light from EAS [42]. The photographs of the CLF are shown in Figure 2.15 on page 39.

(a) Exterior of CLF

(b) Optics of CLF

Figure 2.15: CLF instruments [42]. (a) Exterior of CLF container. (b) Optics of CLF.

The Electron Light Source (ELS) is a compact on-site Linear Accelerator (LINAC) installed about 100 m in front of the BRM station. This facility is expected to reproduce what occurs in an EAS using high-energy electron beams. Since the luminosity and the energy of an accelerated beam are measured precisely, the amount of air fluorescence from this bunch of accelerated electrons can be estimated. By comparing this result to observation data, the end-to-end calibration for the entire system of an FD can be performed [43]. The maximum acceleration energy the ELS achieves is 40 MeV for each electron. The schematic diagram of the ELS system is shown in Figure 2.16 on page 39. The method to filter out EAS-like signals generated by vertical particle cascade from the ELS in the operation of the TA hybrid trigger mode is introduced in Section 3.2.

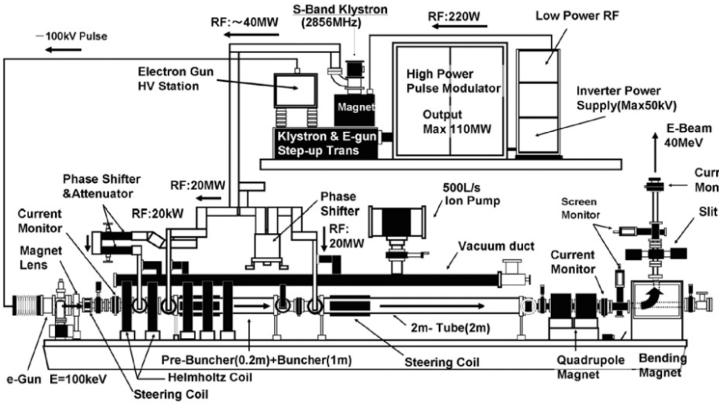

Figure 2.16: Schematic diagram of the ELS, the on-site LINAC of the TA experiment [43].

2.2.2 Surface Detector

The TA experiment utilizes a scintillator-based SD. Each SD consists of two layers of plastic scintillators, each measuring 3 $m^2 \times 12$ mm, separated by a 1-mm-thick stainless steel plate. The surface of the plastic scintillator has grooves at regular intervals of 20 mm, where Wavelength Shifting Fibers (WLSF) are placed. The WLSFs used in the TA experiment are the Y-11 type manufactured by Kuraray Co., Ltd. These fibers transmit light and illuminate the photocathode surface of the PMTs (9124SA; Electron Tubes Ltd.). Each SD is equipped with two PMTs, with one PMT detecting light from the upper layer and the other from the lower layer. To minimize background noise from environmental ionizing radiation, signals from the SD are processed only when there is a coincidence of signals from both layers of the scintillators [45]. The internal structure of the SD is seen in Figure 2.17 on page 40.

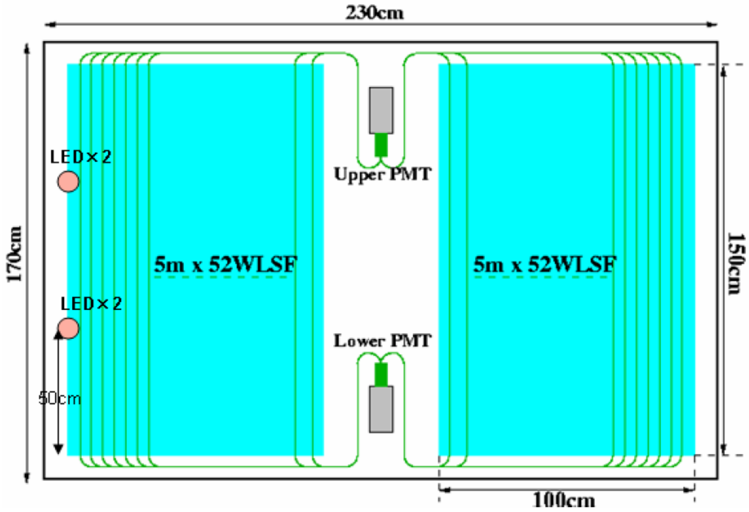

Figure 2.17: Schematic diagram of the internal structure of the SD of the TA experiment [44]. The blue rectangles represent plastic scintillators. The green lines represent WLSFs. The WLSFs from each layer are bundled and attached to one of the two PMTs.

The performance of an SD is designed to yield approximately 25 photoelectrons per single Minimum Ionizing Particle (MIP) passing through a scintillator layer. The position dependence of the signal intensity is estimated to be 20% [51]. Two LEDs are incorporated to track the linearity of the signals from the PMTs. Power for operating an SD is provided by a 120 W solar power module, a charge controller, and a battery, enabling the detector to be self-sustaining. The DAQ system of an SD includes a -3dB low-pass filter with a cutoff frequency of 9.7 MHz to extend the waveform of signals, a 12-bit signal digitizing FADC with a sampling rate of 50 MHz, and a Field Programmable Gate Array (FPGA) module with the trigger logic implemented. The SD electronics are enclosed in a protective box with a heat sink. This protective box is housed within a cooler box (insulated box) together with the battery system. A photograph of an SD in operation at the TA experiment site is shown in Figure 2.18 on page 41.

The SDs in the TA experiment are classified based on the communication towers they connect to via a 2.4 GHz wireless Local Area Network (LAN). The TA experiment's SD array is divided into three virtual regions known as sub-arrays, corresponding to the three communication towers: Smelter Knolls (SK), Black Rock (BR), and Long Ridge (LR). The analysis regarding sub-arrays is described in Section 4.2.4. Each operating SD in the array communicates with

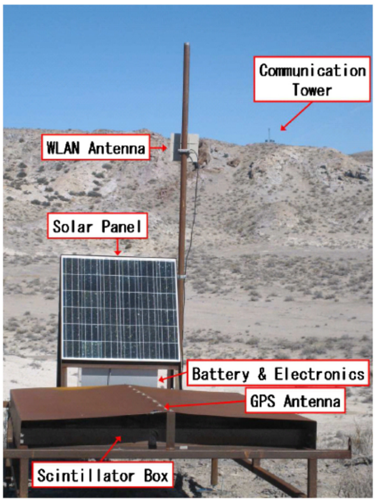

Figure 2.18: SD of the TA experiment [45]. Each part of an SD is indicated. A communication tower above the hill is seen behind the detector.

one of the three towers. The SD array trigger system is closely tied to these communication towers. When an energetic particle produces scintillation light inside an SD, the light is converted into electric current signals by a pair of PMTs. An FADC module digitizes these electric signals, and the digitized waveforms are used to make trigger decisions. There are three types of triggers used in the SD operation [44]:

1. Level-0 trigger

   The sum of 8 bins of digitized waveform signals is continuously compared to the previous 8 bins to make a Level-0 trigger decision. If there is a coincidence between both scintillator layers, and the difference between the two buffered values exceeds the threshold of 0.3 MIPs (roughly 8 photoelectrons), a Level-0 trigger is issued. As a result, data from 128 bins are recorded, starting from 35 bins before the trigger judgment. The Level-0 trigger rate is approximately 700 Hz.

2. Level-1 trigger

   The Level-1 trigger uses the same logic and judgment method as the Level-0 trigger but with a higher threshold of 3.0 MIPs. The data recording method for the Level-1 trigger is the same as in the Level-0 trigger. The Level-1 trigger rate is approximately 40 Hz.

3. Level-2 trigger

   The Level-2 trigger is different from the Level-0 and Level-1 triggers. A communication tower issues a Level-2 trigger to all SDs belonging to its sub-array. The communication tower checks the Level-0 and Level-1 trigger information sent at a frequency of 1 Hz from all operating SDs in its sub-array. If three or more adjacent SDs have a Level-1 trigger within an 8 μs scanning window, the communication tower issues a Level-2 trigger, collecting information on all SDs that exhibit Level-0 or Level-1 triggers.

Furthermore, to address the efficiency decrease near the boundaries of each sub-array, a special type of Level-2 trigger called the boundary trigger was implemented on all three communication towers [135]. The SK communication tower communicates with the BR and LR communication towers and looks up their Level-1 and Level-2 trigger information on boundary SDs. If the Level-2 trigger condition is met in multiple sub-arrays, the SK communication tower issues a boundary trigger to the corresponding sub-array's tower to initiate DAQ.

In summary, the SDs in the TA experiment consist of two layers of plastic scintillators separated by a stainless steel plate. Each layer has WLSFs that transmit light to PMTs. The signals from the SD are processed based on coincidences in both scintillator layers and triggers are issued at different levels depending on the signal characteristics. The SDs are operated independently through communication towers, and a boundary trigger system is implemented to maintain efficiency near the sub-array boundaries.

2.2.3 Extension of the TA Experiment

The TA experiment has undergone several expansions to further its scientific capabilities and extend its reach to different energy ranges, enabling a more comprehensive study of cosmic rays. Here are the key expansions:

Telescope Array Low-energy Extension

Telescope Array Low-energy Extension (TALE) is an extension of the TA experiment that focuses on exploring cosmic rays in the energy range from the Knee to approximately $10^{18.4}$ eV, expanding the analyzable energy range of the TA experiment towards lower energies [136]. TALE features a high-elevation fluorescence detector station with ten telescopes constructed adjacent to the MD station, as shown in Figure 2.19 on page 42.

Figure 2.19: Photograph of the TALE FD station, which is built next to the MD station [21].

TALE is also designed to have a hybrid feature similar to the TA experiment. The SD array of TALE follows the FOV of the TALE FD. The spacing of the SD array varies, with 40 SDs located close to the TALE FD station having a spacing of 400 m and the remaining 40 SDs located farther from the TALE FD station having a spacing of 600 m. This arrangement results in an effective area of approximately 20 km^2 for the entire SD array. The detector layout of the TALE is shown in Figure 2.20 on page 43.

TALE-infill

TALE-infill is a project within the TALE that aims to lower the energy threshold of detection to around 1 PeV. This feature is achieved by deploying a denser

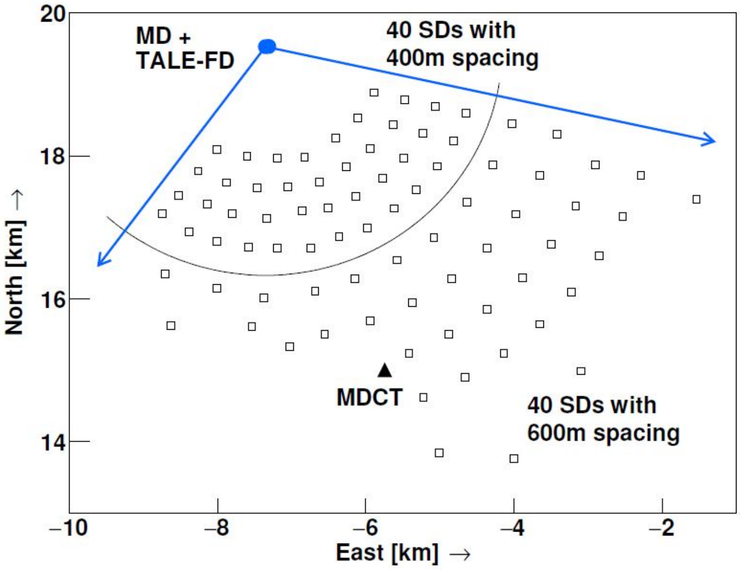

Figure 2.20: Layout of the TALE [21]. The open black squares indicate the surface detectors. The black triangle indicates the SD communication tower. The blue circle indicates the fluorescence detector station. The blue arrows from the fluorescence detector station represent its azimuthal extent of the FOV.

surface detector array with a narrower spacing of 100 m [137]. By increasing the density of detectors, TALE-Infill enhances the sensitivity to lower energy cosmic rays.

Non-Imaging CHErenkov array

Non-Imaging CHErenkov array (NICHE) is another expansion of the TA experiment designed to study cosmic rays in the energy range from 10^{16} eV to 10^{18} eV [89]. The NICHE SD array consists of 14 Cherenkov radiation detectors deployed over a 300 m × 300 m of area, which falls within the FOV of the TALE and MD FD stations. The detector spacing of the NICHE array is set at 100 m. Unlike FDs in the TA experiment that observe the longitudinal development of an EAS, NICHE focuses on the lateral development of an EAS. By measuring the time difference of Cherenkov radiation photons arriving at the detectors, it is possible to estimate the longitudinal development of the EAS using the Cherenkov Lateral Distribution Function (CLDF) technique. Figure 2.21 on page 44 shows the layout of the NICHE array and the Cherenkov radiation detector developed for the NICHE.

TA×4

The TA×4, officially approved in 2015, aims to quadruple the TA experiment [138]. In 2019, the TA×4 SD array was expanded to 2.5 times the size of the original TA SD array. In addition, two more FD stations were installed using refurbished detectors from the HiRes experiment, allowing for more comprehensive observations. The TA×4 experiment has started regular observation, and initial analysis results have been reported [47][139]. Figure 2.22 on page 45 shows the layout of the TA×4.

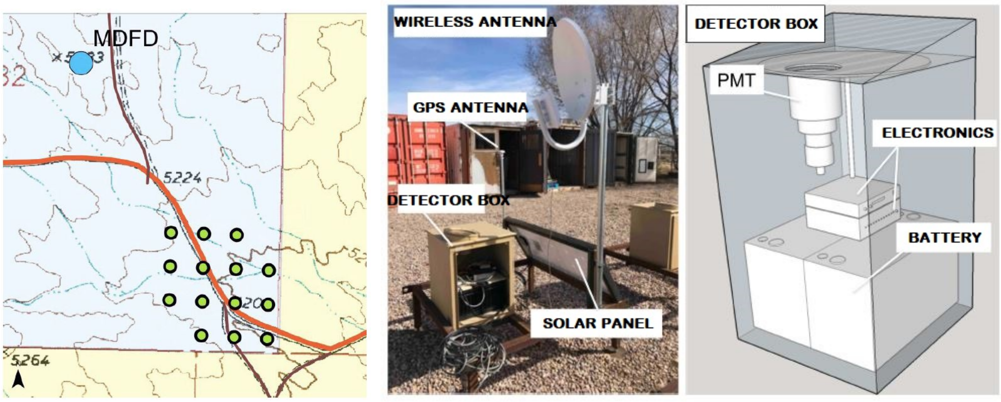

(a) Layout

(b) NICHE detector

Figure 2.21: (a) Layout of the NICHE experiment, showing its 300 m × 300 m array with 14 surface detectors with 100 m spacing. The blue circle indicates the MD station and the green circles indicate the NICHE detectors. (b) Photograph and schematic diagram of a NICHE detector [46].

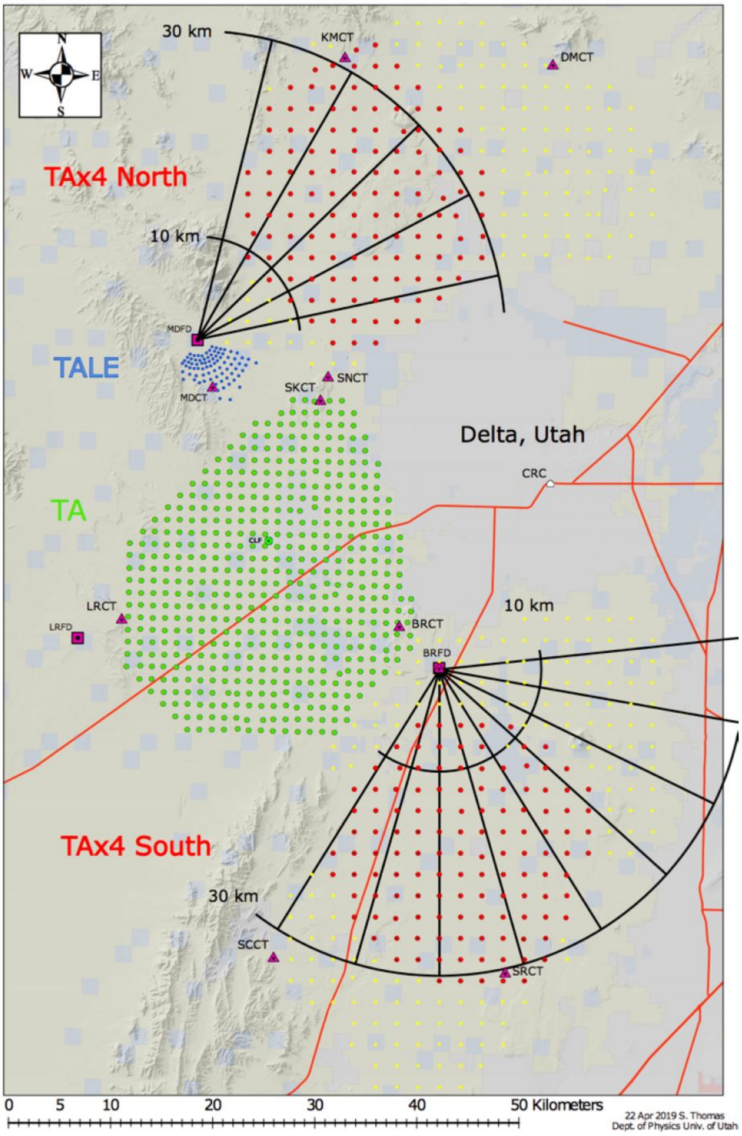

Figure 2.22: Layout of the TA×4 experiment [47]. The area expanded from the original TA experiment is shown. The SD array of the TA×4 experiment is divided into two regions: TA×4 North and TA×4 South. The red circles indicate the newly deployed SDs of the TA×4 experiment. The yellow circles indicate the locations of SDs that have not been deployed yet. The black lines from FD stations represent the azimuthal extent of the FOV.

2.3 Introduction to the Results of the TA Experiment

The TA experiment aims to uncover the unknown characteristics of UHECR. One of the primary goals was to experimentally confirm the existence of the Suppression phenomenon in the energy spectrum of UHECR. This goal was motivated by the discrepancies observed in previous UHECR observatories' results. The TA experiment has reported the energy spectra of UHECR using multiple observation modes, including the FD monocular mode, TALE FD monocular mode, SD mode, and conventional hybrid modes [50][63][90][140][141][142]. The details of the conventional hybrid modes are described in Section 3.1. The energy spectrum measured in the SD observation mode of the TA experiment exhibits a suppression of flux at the highest energy region, which is consistent with both the GZK-cutoff and acceleration limits, as shown in Figure 2.23 on page 46.

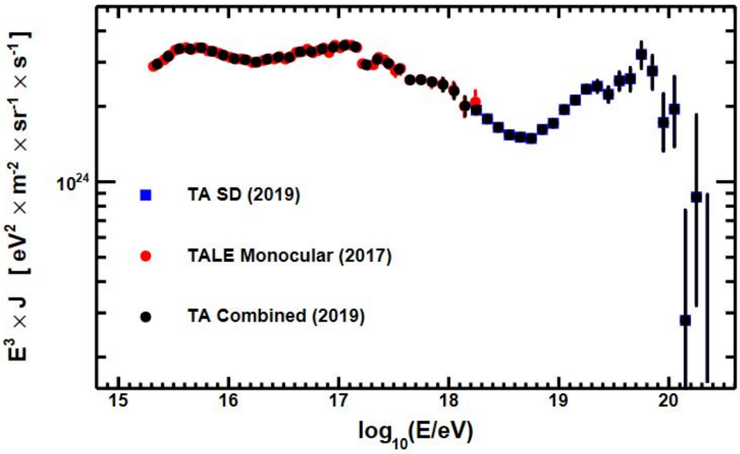

Figure 2.23: Combined energy spectrum measured in two observation modes of the TA experiment: TALE FD monocular and TA SD [48].

Another significant achievement expected from the TA experiment is the estimation of the mass composition of UHECR. By measuring the depth of maximum shower development of EAS, known as $X_{\max}$, the TA experiment has reported the results of UHECR mass composition analyses using various observation modes, including conventional TA hybrid modes, TA FD monocular mode, TALE FD monocular mode, and TALE hybrid mode [21][22][143][144][145]. The mean $X_{\max}$ as a function of primary energy, referred to as $X_{\max}$ elongations, have been analyzed for multiple observation modes. The results are shown in Figure 2.24 on page 47, depicting the $X_{\max}$ elongations.

Figure 2.24 on page 47 shows the results of mass composition analyses performed by the TA experiment in the energy range from $\sim 10^{17}$ eV to $\sim 10^{20}$ eV. Notably, the TALE hybrid mode analysis reported the change in mass composition for the energy higher than $10^{17.1\pm0.1}$ eV, which is around the 2nd Knee. Specifically, the elongation rate of the observed data above the $10^{17.1\pm0.1}$ eV (92 ± 10 g/cm^2/decade) is higher than the elongation rates of the proton Monte Carlo (MC) simulation (61 ± 4 g/cm^2/decade) and the iron-nucleus MC simulation (48 ± 3 g/cm^2/decade). This result indicates that the mass composition becomes lighter as the energy increases for this energy range [21].

Furthermore, the conventional TA hybrid mode analysis for the BRM and LR stations tested several pure mass composition MC simulations with observed $X_{\max}$ distributions in the energy range from $10^{18.2}$ eV to approximately 10^{20} eV. The analysis found that the elongation rate of the observed data is 56.8 ± 5.3

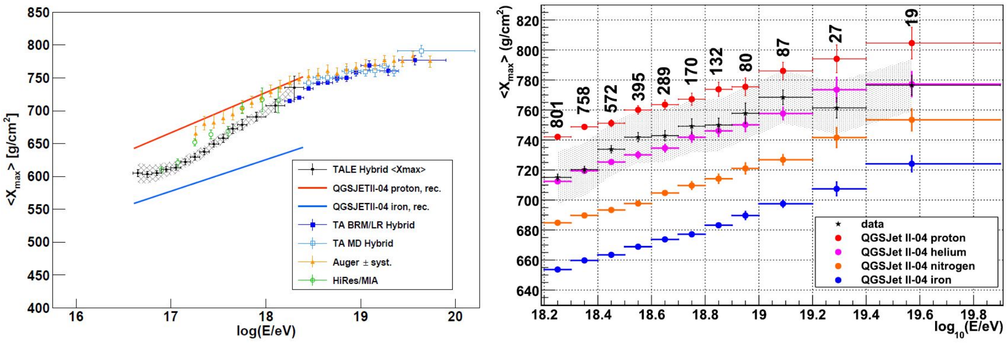

(a) TALE hybrid mode

(b) Conventional TA hybrid mode (BRM/LR)

Figure 2.24: (a) X_{max} elongations measured in several observation modes of the TA experiment: the TALE hybrid mode and the two conventional TA hybrid modes (BRM/LR and MD) [21]. The results from the PAO and HiRes/MIA are also plotted. (b) X_{max} elongation measured in the conventional hybrid mode (BRM/LR) [22].

g/cm^2/decade [22].

The discrepancy in elongation rates between the TALE hybrid mode (92±10 g/cm^2/decade) and the conventional TA hybrid mode for BRM/LR (56.8±5.3 g/cm^2/decade) suggests the existence of an energy point where the reported change in mass composition by the TALE hybrid mode is completed. However, its precise determination is challenging with the TALE hybrid mode and the conventional TA hybrid mode since the energy point is at the transition between the two observation modes.

It is worth noting that the TA experiment has also reported evidence of intermediate-scale anisotropy in the arrival directions of UHECR with energies above $\sim 10^{19.7}$ eV. This anisotropy is referred to as the Hotspot, located near the constellation of Ursa Major, as shown in Figure 1.19 on page 17 [24].

Chapter 3

Hybrid Trigger Mode of the Telescope Array Experiment

The hybrid trigger mode of the Telescope Array (TA) experiment is designed to collect data from both the Fluorescence Detector (FD) stations and the Surface Detector (SD) array simultaneously. The TA hybrid trigger system was implemented in October 2010 as an external trigger system, where the FD station issues a trigger to its corresponding SD sub-array. When an FD station detects an Extensive Air Shower (EAS)-like event, it sends trigger information to the corresponding SD communication towers.

Upon receiving a hybrid trigger from an FD station, the SD communication tower issues a Level-2 trigger. Since the TA hybrid trigger includes the information on the center timestamp and the width of the waveform scan window, the Data AcQuisition (DAQ) system can collect the SD data of the target SD sub-array for the corresponding time.

It is important to note that the hybrid trigger system implemented in the Middle Drum (MD) FD station differs from the hybrid trigger systems implemented in the Black Rock Mesa (BRM) and Long Ridge (LR) FD stations in terms of the energy threshold. The main reason for this difference is the distance between the MD station and its corresponding sub-array, the Smelter Knolls (SK) array. The distance between the MD station and the SK array is greater than the distances between the BRM station and the Black Rock (BR) array and between the LR station and the Long Ridge (LR) array. Therefore, in this thesis, only the hybrid trigger system implemented at the BRM and LR stations is described, and only the analysis results obtained from these stations' hybrid trigger systems are presented.

3.1 Motivation of the Hybrid Trigger Mode

As mentioned in Chapter 2, the important feature of the TA experiment is that it adopts two independent methods in observing UHECR-induced EAS: the air fluorescence detection technique and the surface particle detection technique. However, mainly due to the difference in the observation principle between the two techniques, the apertures of the two observation modes differ by the primary energy of UHECR. For example, Figure 3.1 on page 49 shows the apertures of the FD monocular observation mode and the SD observation mode as a function of the primary energy of UHECR.

Figure 3.1 on page 49 shows that the apertures of the FD monocular observation mode and the SD observation mode differ in the lower energy range ($<10^{19}$ eV). For example, at 10^{18} eV, the aperture of the FD monocular observation mode is about 400 km^{2}sr while the aperture of the SD observation mode is about

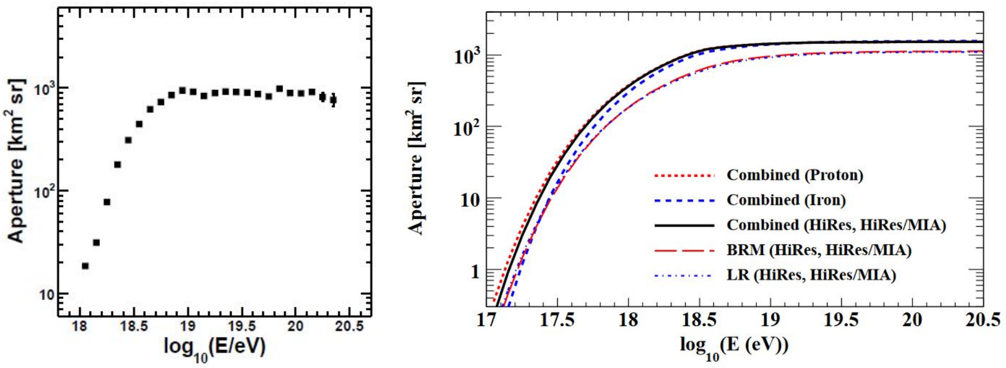

(a) SD mode

(b) FD monocular mode

Figure 3.1: (a) Aperture of SD observation mode of the TA experiment [49]. (b) Aperture of FD monocular observation mode of the TA experiment [50]. The black line indicates the combined aperture of the BRM and LR stations estimated using the mass composition reported by HiRes and HiRes/MIA experiment.

20 km^{2}sr. This difference is the main reason why the analyzable energy range of the FD monocular observation mode is an order of magnitude more expansive than that of the SD observation mode ($\geq 10^{17.2}$ eV for the FD monocular mode, $\geq 10^{18.2}$ eV for the SD mode) [50][140].

However, as explained in Section 1.2.2, the FD monocular observation mode of the TA experiment has relatively low accuracy in determining the geometry of an EAS. The typical reconstruction resolution of UHECR arrival directions of the TA FD monocular observation mode is 7.4° [31]. In contrast, the SD observation mode is 1.5° [49].

In the TA experiment, there have been two approaches to improve the accuracy of the FD monocular observation mode in determining EAS geometry: the FD stereoscopic observation mode and the conventional hybrid mode. Below is a brief introduction to the FD stereoscopic observation mode and the conventional hybrid mode.

1. FD stereoscopic observation mode

   Unlike the FD monocular observation mode, which analyzes the data observed by a single FD station, the FD stereoscopic observation mode is based on the simultaneous observation of the same EAS by two or more FD stations that are spatially separated as shown in the left panel of Figure 3.2 on page 50.

   If two FD stations observe the same EAS, the intersection line of two Shower Detector Planes (SDPs) determines the shower axis of the EAS with high accuracy. The typical reconstruction resolution of EAS arrival directions of the FD stereoscopic observation modes of the TA experiment is 1.6° [34]. If three FD stations observe the same EAS, an algorithm selects the best pair of sites [146].

   However, an EAS must be bright enough for the FD stereoscopic observation mode because the EAS needs to be observed by two FD stations separated by ∼35 km. Therefore, the analyzable energy range of the FD stereoscopic observation mode is significantly narrower than that of the FD monocular observation mode ($\geq 10^{18.4}$ eV) [146].

2. Conventional hybrid observation mode

Another approach to improve the FD monocular observation mode is a simultaneous observation of the same EAS by a single FD station and the SD array, which is called the conventional hybrid observation mode. The term “conventional” emphasizes the old hybrid observation mode compared to the new hybrid trigger observation mode presented in this thesis.

In the conventional hybrid mode, the SD array provides the FD monocular observation mode with the detection information about an EAS. As shown in the right panel of Figure 3.2 on page 50, the reconstruction procedure can determine the impact timing and position of an EAS at the ground level precisely. This results in an increased geometric reconstruction accuracy, which is 0.9° in terms of the typical reconstruction resolution of UHECR arrival directions [63].

However, since the FD stations and the SD array of the TA experiment are operated independently, the conventional hybrid observation can only utilize observation data separately obtained by the SD array and the FD stations. Therefore, the analyzable energy range of the conventional hybrid observation mode is equal to that of the SD observation mode ($\geq 10^{18.2}$ eV).

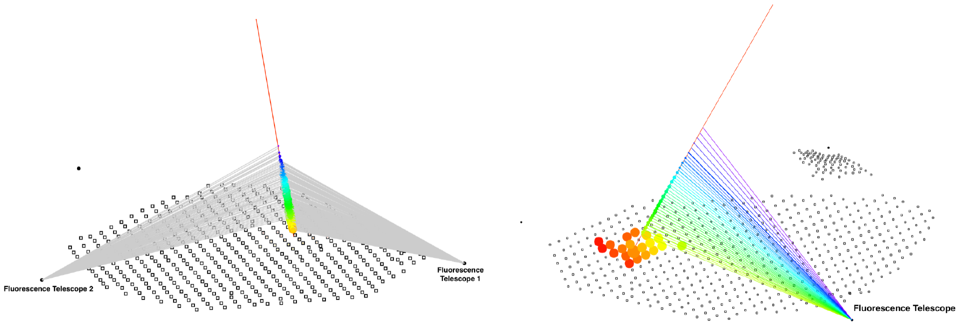

Figure 3.2: (Left) Visualization of stereoscopic observation using two FD stations. (Right) Hybrid observation using an FD station and an SD array [21].

While three or more adjacent SDs with energy deposit greater than 3 Minimum Ionizing Particles (MIPs) are required for the SD array to be triggered as described in Section 2.2.2, former simulation studies reported that more than 85% of simulated proton and iron-nucleus EAS in the energy range above $10^{17.5}$ eV deposit energy greater than 3 MIPs to at least one SD [147]. This study result indicates that it is possible to analyze EAS with a hybrid technique in the energy range from $10^{17.5}$ eV to $10^{18.2}$ eV by implementing a unique trigger system that prompts the SD array to perform DAQ in coincidence with the trigger system of the FD stations. As a result, better reconstruction resolutions in the energy range from $10^{17.5}$ eV to $10^{18.2}$ eV are expected. With this motivation, a hybrid trigger system is developed and implemented as an external trigger system for an SD array issued by an FD station.

3.2 Hybrid Trigger Algorithm

The hybrid trigger algorithm of the TA experiment was developed with two critical requirements:

1. The Flash Analog to Digital Converter (FADC) waveform scan required by a hybrid trigger for an SD must be completed within 16 seconds because each SD holds waveform information for only 16 seconds.

2. The rate of hybrid trigger issued by an FD station must be less than 0.2 Hz considering the limitation in communication speed between an SD communication tower and the SDs belonging to the sub-array.

To achieve the first requirement, the time window for SD waveform data collection was adjusted. During the development stage, four different time windows were considered: ±32 μs, ±64 μs, ±96 μs, and ±128 μs. The expected waveform data for each SD was calculated based on the typical Level-0 trigger rate, around 700 Hz. For example, for a time window of ±64 μs, approximately 0.0896 waveform data per SD were expected (700 Hz $\times$ 128 μs $= 0.0896$). With 191 SDs in the LR sub-array (the largest sub-array), the total number of waveform data in a ±64 μs time window would be $0.0896 \times 191 = 17.1$.

The time required for a communication tower to acquire one waveform data was estimated to be around 40 ms [135]. Thus, the time needed to acquire 17.1 waveform data would be 17.1×40 ms $\simeq 684$ ms. Since a communication tower spends approximately 100 ms collecting waveforms from SDs in its 1-second DAQ cycle [34], the collection time would be around 7 seconds. Therefore, even with a ±128 μs time window, the waveform scan could technically be completed within 16 seconds, but this would limit the maximum rate of the hybrid trigger.

In the actual hybrid trigger setup, a ±64 μs is adopted as the search window width, and the time offset is set to -35 μs. These values were determined based on early survey observations [34].

Regarding the second requirement, it is not possible to issue a hybrid trigger for all triggered events in an FD station since the typical trigger rate of an FD station is about 2 - 3 Hz during stable operation [31]. Therefore, the TA hybrid trigger system must filter out non-EAS events to decrease the trigger rate by one order of magnitude. Several candidates for non-EAS events that could issue FD triggers include calibration light sources (e.g., Xenon flashers), a vertical laser shooting from CLF (Central Laser Facility), a vertical particle cascade from ELS (Electron Light Source), and continuous light contamination from artificial sources. It is also considered that a single muon passing through the array of Photomultiplier tubes (PMTs) in an FD camera or passing near an FD camera can generate a spatial track of the signal.

The criteria for issuing hybrid triggers implemented in the BRM and LR stations are as follows:

1. The number of triggered PMTs in an FD camera must be ≤ 250.
    - This condition filters out events caused by Xenon flashers or other noise from artificial light sources illuminating the entire FD camera surface, such as a beam of light from a car's headlight near an FD station.
2. No PMT in an FD camera should have an FADC value exceeding 3σ for 51.2 μs.
    - This condition filters out artificial light that accidentally enters the FD cameras and rejects false signals caused by noisy or malfunctioning PMTs. The period of 51.2 μs is equivalent to four times the FD signal finding window and is equal to the full DAQ length of the FD cameras at the BRM and LR stations.
3. Five or more PMTs are required to make a group defined explicitly by the trigger algorithm.

    - This condition filters out signals with short spatial tracks that are difficult to perform geometric reconstruction on due to limited information on the signal detection timing difference between PMTs. A group is defined by spatially and temporally neighboring triggered PMTs. Spatially neighboring PMTs are defined based on adjacency, calculated using the PMT numbers in an FD camera. Temporally neighboring PMTs are defined by having signal peak bins less than 20 bins apart, corresponding to 2 μs.

4. The time interval between the earliest signal peak bin and the latest signal peak bin among the triggered PMTs must be separated by more than 8 bins.
    - This condition filters out non-EAS-related spatial tracks caused by single muons traversing through a PMT array or passing near an FD camera, producing a track of Cherenkov radiation bright enough to trigger an FD station. The period of 8 bins is equivalent to 800 ns.

By implementing these criteria, the TA hybrid trigger system effectively filters out non-EAS events and reduces the trigger rate to an acceptable level, allowing for the collecting of relevant data for the hybrid analysis in the TA experiment.

The above four criteria examine each FD camera's data obtained at an FD station. Whenever the data of an FD camera meet all criteria, they are flagged as a hybrid trigger camera. If there are one or more flagged FD cameras, a hybrid trigger is issued finally.

The on-site test result of the TA hybrid trigger system reported that the rate of the TA hybrid trigger mode with the above judge criteria was ≤ 0.01 Hz, which was sufficiently lower than the initial requirement of ≤ 0.2 Hz [34]. In addition, the TA hybrid trigger system allows any FD operator to set a veto period. As a default setting, the 1 minute at HH:00 and 1 minute at HH:30 are set to be veto periods in time with the schedule of CLF vertical laser shooting. A sample veto setting for the TA hybrid trigger system is shown in Figure 3.3 on page 53. Every veto information is considered in the on-time calculation of the TA hybrid trigger analysis, as described in Section 5.3.

Still, an unexpected surge in the rate of the TA hybrid trigger mode might occur and disrupt the stable SD operation. To prevent such an occasion, a real-time trigger rate limitation is also implemented. Hybrid triggers can only be issued 2 seconds after the last hybrid trigger and 20 seconds after the fifth hybrid trigger from the last.

Implementing the TA hybrid trigger system is expected to affect the dead time of the DAQ at the FD station. It is found that the effect of the TA hybrid trigger on the dead time at an FD station is smaller than the fluctuation of a typical dead time at an FD station [34].

It should be emphasized that there are two exceptions in the operation of the TA hybrid trigger system where a hybrid trigger system does not perform the collection of SD waveform data. The first type of exception is called Timeout. The Timeout means that the central timestamp of the waveform scan by the TA hybrid trigger request is outside the 16-second limit described in the earlier part of this section. This exception might occur when the time synchronization between an FD station and its corresponding sub-array is lost or when the data communication between an FD station and its corresponding sub-array is highly unstable. The observation period with Timeout exception is excluded from the on-time of the TA hybrid trigger mode as described in Section 5.3.

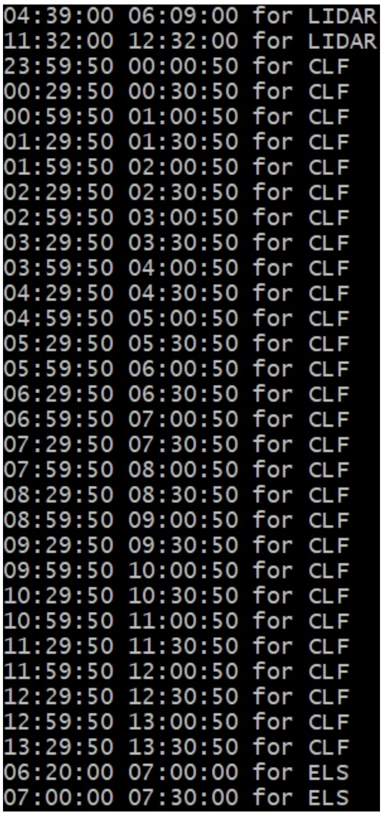

```
04:39:00 06:09:00 for LIDAR
11:32:00 12:32:00 for LIDAR
23:59:50 00:00:50 for CLF
00:29:50 00:30:50 for CLF
00:59:50 01:00:50 for CLF
01:29:50 01:30:50 for CLF
01:59:50 02:00:50 for CLF
02:29:50 02:30:50 for CLF
02:59:50 03:00:50 for CLF
03:29:50 03:30:50 for CLF
03:59:50 04:00:50 for CLF
04:29:50 04:30:50 for CLF
04:59:50 05:00:50 for CLF
05:29:50 05:30:50 for CLF
05:59:50 06:00:50 for CLF
06:29:50 06:30:50 for CLF
06:59:50 07:00:50 for CLF
07:29:50 07:30:50 for CLF
07:59:50 08:00:50 for CLF
08:29:50 08:30:50 for CLF
08:59:50 09:00:50 for CLF
09:29:50 09:30:50 for CLF
09:59:50 10:00:50 for CLF
10:29:50 10:30:50 for CLF
10:59:50 11:00:50 for CLF
11:29:50 11:30:50 for CLF
11:59:50 12:00:50 for CLF
12:29:50 12:30:50 for CLF
12:59:50 13:00:50 for CLF
13:29:50 13:30:50 for CLF
06:20:00 07:00:00 for ELS
07:00:00 07:30:00 for ELS
```

Figure 3.3: The time setting of the TA hybrid trigger veto at the BRM station on March 9th, 2011. The timestamp is in Coordinated Universal Time (UTC). The veto period for CLF vertical laser shootings is shown as 1 minute. Other than the CLF, veto periods were set for the LIght Detection And Ranging (LIDAR) and ELS operations on this date.

The other type of exception is called Cancel. Cancel means that the SD self-trigger already performed DAQ within a time range of ±8 μs from the center timestamp of the waveform scan request by the TA hybrid trigger system. Since the self-trigger efficiency of an SD array is approximately 1 above the primary energy of 10^{19} eV [49], the SD self-trigger system can almost always acquire EAS observation data above this energy. Therefore, in this thesis, all SD observation data acquired by the BR sub-array and the LR sub-array, which coincide with the timestamp of the hybrid trigger, are analyzed regardless of the types of the trigger, i.e., the hybrid trigger and the SD self-trigger.

3.3 Extensive Air Showers Reconstruction Principle

The TA hybrid trigger reconstruction method uses the observation data from an FD as a calorimetric measurement of the energy of a primary UHECR by tracking its longitudinal development. Then spatiotemporal information on when and where an EAS hits the ground level is added from the observation data obtained by an SD.

The main part of EAS reconstruction is divided into two stages. The first stage is geometric reconstruction, which involves the SDP, the distance between the FD station and the core position ($\mathrm{R_{CORE}}$), and the angle of the shower axis inside the SDP (ψ angle). The next stage is longitudinal reconstruction, where the profile of longitudinal development of the EAS is determined by parameters such as calorimetric energy $\mathrm{E_{cal}}$ and depth of maximum shower development

X_{max}.

In geometric reconstruction, the timing of the arrival of an EAS on the ground level ($\mathrm{T}_{\mathrm{CORE}}$) can precisely be estimated using the SD data that collected the energy deposit by particles originating from the EAS. The expected detection timing ($\mathrm{T}_{\mathrm{EXP},i,j}$) of the i-th PMT of the FD and the j-th SD is calculated using the following equation:

$$\mathrm{T}_{\mathrm{EXP},i,j} = \mathrm{T}_{\mathrm{CORE},j} + \frac{\sin\psi - \sin\alpha_i}{c_0 \sin(\psi + \alpha_i)} \mathrm{R}_{\mathrm{CORE}}, \tag{3.1}$$

where c_0 is the speed of light in vacuum, α_i is the elevation angle of the i-th PMT in the SDP, $\mathrm{R}_{\mathrm{CORE}}$ and ψ are the same as explained above. $\mathrm{T}_{\mathrm{CORE},j}$ is the timing of the EAS reaching the ground and is estimated from the position and detection timing of the j-th selected SD using the following equation:

$$\begin{aligned} \mathrm{T}_{\mathrm{CORE},j} &= \mathrm{T}'_{\mathrm{SD},j} + \frac{\cos\psi}{c_0}(\mathrm{R}_{\mathrm{CORE}} - \mathrm{R}_{\mathrm{SD},j}), \\ \mathrm{T}'_{\mathrm{SD},j} &= \mathrm{T}_{\mathrm{SD},j} + \frac{1}{c_0}(\vec{\mathrm{P}'}_{\mathrm{SD},j} - \vec{\mathrm{P}}_{\mathrm{SD},j}) \cdot \vec{\mathrm{P}}, \end{aligned} \tag{3.2}$$

where $\vec{\mathrm{P}}_{\mathrm{SD},j}$ is the position vector of the j-th selected SD. $\mathrm{T}_{\mathrm{SD},j}$ is the timing at which the j-th selected SD receives the signals. $\vec{\mathrm{P}'}_{\mathrm{SD},j}$ is the position vector of the j-th selected SD projected on the SDP. $\mathrm{T'}_{\mathrm{SD},j}$ is the timing when the j-th selected SD receives the signals whose position is projected on the SDP. $\vec{\mathrm{P}}$ is the vector of the shower axis, indicating the up-going direction. The simplified diagram of the geometric relationship of the parameters is shown in Figure 3.4 on page 54.

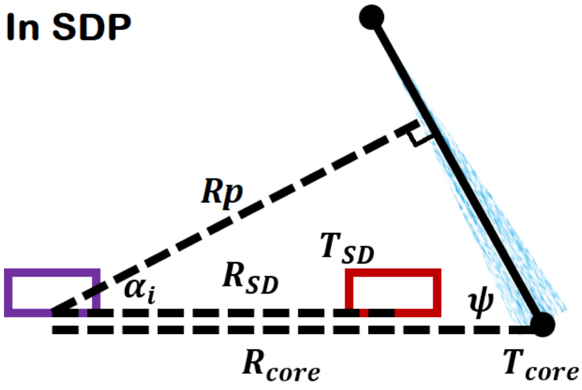

Figure 3.4: Simplified diagram showing several geometry parameters used in the reconstruction of EAS. The purple rectangle represents an FD station, the red rectangle represents an SD, and the long blue triangle represents an EAS. All angles indicated in this plot are with respect to the SDP.

Since the SDP is determined by using the FOV of multiple PMTs that detected the signals from an EAS, $\mathrm{R}_{\mathrm{CORE}}$ and ψ angle in the determined SDP are estimated by searching for the j-th selected SD that minimizes χ^2_j, which is calculated using the following equation:

$$\chi^2_j = \sum_i \frac{(\mathrm{T}_{\mathrm{EXP},i,j} - \mathrm{T}_i)^2}{\sigma^2_{\mathrm{T}_i}}, \tag{3.3}$$

where T_i is the timing of the signal at the i-th PMT and $\sigma^2_{\mathrm{T}_i}$ is the square of its error. The j-th SD that gives the least χ^2_j is called the anchor SD.

In the longitudinal reconstruction, the Inverse Monte Carlo (IMC) method is adopted [148]. With the geometry determined at the earlier stage of reconstruction, the IMC session generates multiple EAS in a reduced form of the Gaisser and Hillas (G-H) function introduced in Equation (1.19) where $\mathrm{N}_{\mathrm{max}}$ is fixed to be 1. X_0 and λ are also fixed to be specific values. Then $\mathrm{X}_{\mathrm{max}}$ is put as a free parameter. For each trial of $\mathrm{X}_{\mathrm{max}}$, the likelihood is calculated as Equation (3.4):

$$\text{Likelihood} = \sum_i n_{\mathrm{OBS},i} \times \log \frac{n_{\mathrm{EXP},i}(\mathrm{X}_{\mathrm{max}})}{\sum_i n_{\mathrm{EXP},i}(\mathrm{X}_{\mathrm{max}})}, \tag{3.4}$$

where $n_{\mathrm{OBS},i}$ is the number of photoelectrons detected by the i-th PMT and $n_{\mathrm{EXP},i}(\mathrm{X}_{\mathrm{max}})$ is the number of photoelectrons expected by the i-th PMT at a tested $\mathrm{X}_{\mathrm{max}}$ value in the IMC trial. The IMC session tries multiple $\mathrm{X}_{\mathrm{max}}$ values until it reaches the $\mathrm{X}_{\mathrm{max}}$ that gives the maximum likelihood value. After the $\mathrm{X}_{\mathrm{max}}$ that gives the maximum likelihood is determined, the shower size parameter $\mathrm{N}_{\mathrm{max}}$ is estimated by the following equation:

$$\mathrm{N}_{\mathrm{max}} = \frac{\sum_i n_{\mathrm{OBS},i}}{\sum_i n_{\mathrm{EXP},i}}. \tag{3.5}$$

After the IMC session determined $\mathrm{N}_{\mathrm{max}}$ and $\mathrm{X}_{\mathrm{max}}$ yielding the maximum likelihood value, the number of electromagnetic particles $\mathrm{N}_e(\mathrm{X})$ of the EAS as a function of atmospheric depth X is estimated. The energy deposit of the EAS at an atmospheric depth X is a multiplication of the number of particles $\mathrm{N}_e(\mathrm{X})$ and the critical energy E_c described in Section 1.3.3.

Finally, the sum of electromagnetic energy deposits made by the EAS, namely the calorimetric energy of the EAS ($\mathrm{E}_{\mathrm{cal}}$), is estimated by integrating all energy deposits made in the integrated depths of the atmosphere as shown in the following equation:

$$\mathrm{E}_{\mathrm{cal}} = \int_{\mathrm{X}_0}^{\infty} \mathcal{E}(\mathrm{X}) d\mathrm{X}, \tag{3.6}$$

where $\mathcal{E}(\mathrm{X})$ is the energy deposit at the atmospheric depth X. Since the actual EAS contains not only the electromagnetic cascade but also muons and other particles that do not contribute to the electromagnetic cascade, $\mathrm{E}_{\mathrm{cal}}$ is always smaller than the actual energy E_0 of the primary UHECR because $\mathrm{E}_{\mathrm{cal}}$ misses the energy carried away by this kind of particles. Thus this difference (E_0 - $\mathrm{E}_{\mathrm{cal}}$) is commonly referred to as the missing energy. E_0 is calculated from $\mathrm{E}_{\mathrm{cal}}$ by estimating the ratio of $\mathrm{E}_0/\mathrm{E}_{\mathrm{cal}}$ in the target energy range and a primary composition. Estimating the missing energy can only be performed by studying the result of the Monte Carlo (MC) simulation, which is described further in Section 4.2.3.

The principle of EAS reconstruction by the hybrid technique is explained in this section. However, to apply this reconstruction principle to the raw observation data obtained by the hybrid detectors of the TA experiment, a further process is necessary to select a set of FD PMTs that received signals from the EAS. Then the process also requires determining the signal timing parameters such as T_i for the signal timing of the i-th selected FD PMT, $\sigma^2_{\mathrm{T}_i}$ for its squared error, and $\mathrm{T}_{\mathrm{SD},j}$ for the signal timing of the j-th SD. The signal intensity parameters are required to be determined as well, such as $n_{\mathrm{OBS},i}$ for the number of photoelectrons detected by the i-th FD PMT and the energy deposit recorded by the j-th SD in a unit of Minimum Ionizing Particle (MIP). These processes are described in Section 4.2.

3.4 Observation Status

The TA hybrid trigger system started on October 8th, 2010, and had been operating for about 9.5 years by March 2020. However, the operation of the BRM and LR stations had been suspended since March 2020 due to the COVID-19 pandemic. In November 2021, the investigation to resume the operation of the BRM and LR stations was performed and the first post-pandemic operation was performed in June 2022.

The sample EAS event collected by the TA hybrid trigger mode is shown in Figure 3.5 on page 56.

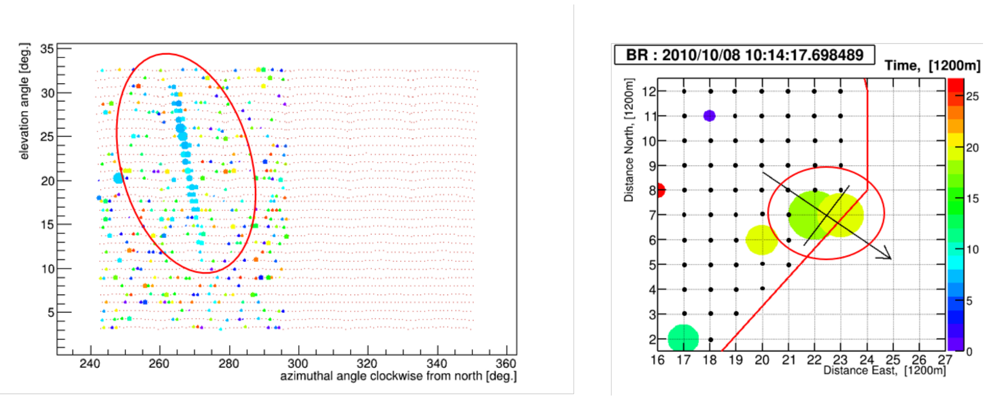

Figure 3.5: Sample EAS event visualized by both SD and FD event displays. (Left) The FD event display. (Right) The SD event display. The red ovals emphasize the event signal parts. The size and color of the markers represent the amplitude and timing of the signals, respectively.

Figure 3.5 on page 56 shows that this sample event has only two adjacent SDs with signals, which means that this event does not meet the decision criteria of the SD Level-2 trigger, as described in Section 2.2.2. Thus this event can only be triggered by the TA hybrid trigger system. This event is successfully reconstructed by the method described in Section 3.3. The primary energy (E_0) and X_{max} of this event are reconstructed to be 0.3 EeV and 769 g/cm^2, respectively. However, the event is not included in the observation dataset described in Section 5.1 due to the weather cut described in Section 5.1.

Chapter 4

Monte Carlo Simulation Studies

The Extensive Air Shower (EAS) simulation framework with the actual detector setup of the Telescope Array (TA) experiment, including responses from Data AcQuisition (DAQ) electronics, is fundamental in evaluating the performance of detectors of the TA experiment for Ultra-High-Energy Cosmic Ray (UHECR)-induced EAS. This performance information consists of the aperture of detectors, the bias and resolution in the reconstruction of EAS, and the evaluation of missing energy. This chapter describes the Monte Carlo (MC) simulation and reconstruction framework developed for the TA hybrid trigger mode.

4.1 Details of MC Simulation

As a simulation framework for the TA hybrid trigger mode, Cosmic Ray Simulations for KAscade (CORSIKA) version 7.3500 is adopted as the simulation code library for particle cascades in EAS [149]. For a model to simulate hadronic interactions in EAS, QGSJET-II-04 is used for the higher energy region above 80 GeV [16]. Below 80 GeV, FLUktuierende KAskade (FLUKA) is used [150]. In addition, EGS4 (Electron Gamma Shower) is adopted to simulate the electromagnetic components of EAS [151]. The lateral extent of the electromagnetic components of EAS is estimated using the Nishimura-Kamata-Greisen (NKG) function, which is explained in Section 1.3.3.

Since the maximum number of particles N_{max} in a simulated EAS is substantial, especially for an EAS with E_0 greater than $10^{19.0}$ eV, the computation for simulation is highly time and Central Processing Unit (CPU) resource consuming. For this reason, the thinning technique with a factor of 10^{-6} is adopted to save the simulation time and CPU resources. The thinning technique reduces the number of particles that need to be tracked by making a randomly selected particle carry the weight of all particles produced at the same time window [152]. Such a thinned EAS is then dethinned to recover the information on each particle at the ground level [153].

To simulate signal responses of a Surface Detector (SD) to an EAS, the physical and structural details of the SD are implemented using the simulation framework Geant4 (GEometry ANd Tracking) [154]. In addition, the energy deposit by background particles to an SD is also implemented in the simulation using the typical trigger rate of an SD and the observed spectrum of energy deposit for an SD. An SD's physical and structural model is visualized in Figure 4.1 on page 58.

Secondly, a simulation of signal responses of a Fluorescence Detector (FD) station to the same EAS, which is simulated in the previous SD simulation stage, is performed. By looking up the longitudinal development profile of the simulated

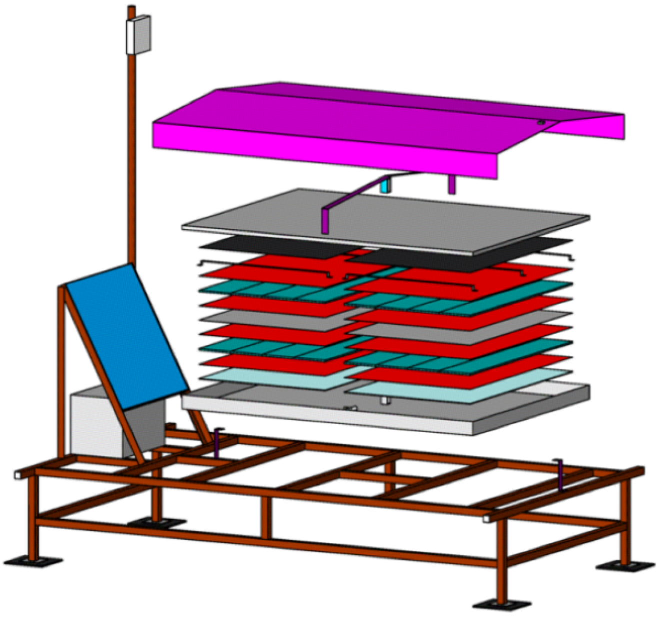

Figure 4.1: Visualized Geant4 model of a TA SD [51].

EAS that contains the information on the number of particles and the energy deposits with 1 g/cm^2 step size, it is possible to estimate the intensity of air fluorescence and Cherenkov radiation from the simulated EAS. To estimate the intensity of air fluorescence yield, the total yield measured in the Kakimoto model [56] is adopted with the spectrum of air fluorescence photons reported by the FLuorescence in Air from SHowers (FLASH) experiment [61].

For atmospheric parameters such as pressure and temperature, the data prepared by the Global Data Assimilation System (GDAS) are adopted [155]. The GDAS database, operated by National Oceanic and Atmospheric Administration (NOAA), provides atmospheric profiles of 23 vertical layers with pressure ranging from 20 to 1,000 hPa every three hours. Each vertical layer contains altitude, temperature, and dew point at the given pressure. The database has a total of $360 \times 180 = 65{,}160$ points, representing each longitude and latitude of the Earth in a 1-degree grid. The GDAS dataset for the point (39N, 113W), which is the closest point to the site of the TA experiment, is adopted for the atmospheric parameters to be used in the EAS simulation.

The measurement of aerosol is made by the LIght Detection And Ranging (LIDAR) system described in Section 2.2.1. The averaged Vertical Aerosol Optical Depth (VAOD) value is estimated to be 0.034, which is adopted in the EAS simulation [156]. The simulation model for a ray-tracing session inside an FD station structure is also generated and visualized in Figure 4.2 on page 59.

The other conditions in generating a set of MC simulated EAS for the TA hybrid trigger mode are summarized in Table 4.1 on page 59. Note that the period is 8.5 years, from October 2010 to June 2019, when the FD calibration data were available. This simulation period equals the observation period described in Chapter 5.

Table 4.1 on page 59 shows that the MC set has 31 bins of primary energy for each composition. It should be emphasized that each energy bin has 400 MC simulated proton EAS and 301 MC simulated iron-nucleus EAS generated by the CORSIKA framework. For each EAS simulated by the CORSIKA framework,

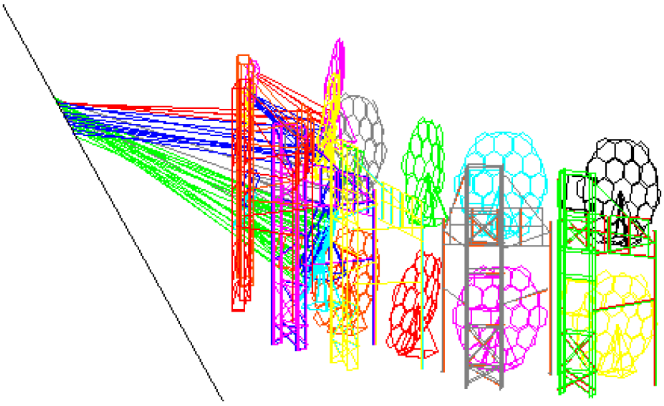

Figure 4.2: Structure model visualizing the ray-tracing inside the Black Rock Mesa (BRM) FD station [35].

Table 4.1: Summary of conditions generating a set of MC simulations for the TA hybrid trigger mode. A total of 31 energy bins exist in the energy range of $17.0 \leq \mathrm{Log_{10}E_{thr.}} \leq 20.0$ with 0.1-decade energy bins.

MC generation condition	Parameters
Composition	Proton, Iron-nucleus
Primary energy in $\mathrm{Log_{10}E_{thrown}}$ (eV)	17.0 to 20.0
θ Zenith (deg)	0 to 70
ϕ Azimuth (deg)	Uniformly random in 0 to 360
EAS core position:condition 1	Random inside 25 km radius from CLF
EAS core position:condition 2	Refer to Table 4.3
Atmospheric model	GDAS
Period	~8.5 years
Hadronic interaction model	QGSJET-II-04, FLUKA

65 to 2,000 iterations of detector simulations are made with a random EAS core position and a random ϕ (Azimuth) value. The number of iterations varies by the primary energy of an EAS. The iteration number by primary energy is described in Table 4.2 on page 59.

Table 4.2: Number of detector simulations using a single CORSIKA-generated EAS.

Primary energy (eV)	Iteration number
$10^{17.0}$ - $10^{17.5}$	2,000
$10^{17.6}$	1,500
$10^{17.7}$	490
$10^{17.8}$	300
$10^{17.9}$	190
$10^{18.0}$ - $10^{18.2}$	125
$10^{18.3}$ - $10^{20.0}$	65

As described in Table 4.1 on page 59, there are two conditions for an EAS core position. In addition to the conventional distance limit from Central Laser Facility (CLF) (Condition 1), a distance limit from an FD station (Condition 2) is introduced to save CPU time in the simulation for the TA hybrid trigger mode.

The simulated event must satisfy both EAS core position Conditions 1 and 2. It should be noted that Condition 2 varies with the primary energy of EAS. The details are described in Table 4.3 on page 60.

Table 4.3: Maximum distance between any FD station and an EAS core position for a given primary energy.

Primary energy (eV)	Maximum distance (km)
$10^{17.0}$ - $10^{17.4}$	12
$10^{17.5}$	13
$10^{17.6}$	14
$10^{17.7}$	16
$10^{17.8}$	17
$10^{17.9}$	18
$10^{18.0}$	19
$10^{18.1}$	22
$10^{18.2}$	23
$10^{18.3}$ - $10^{20.0}$	24

Since the EAS core position condition is modified from the usual circular condition, effective geometric areas vary by the primary energy of a shower. This effect is described in Section 4.3. The EAS core position distributions for all proton-simulated and iron-simulated events are plotted in Figure 4.3 on page 60. Additionally, the EAS core position distributions for three energy ranges, $17.0 \leq \mathrm{Log}_{10}(\mathrm{E}_{\mathrm{thrown}}/\mathrm{eV}) < 18.0$, $18.0 \leq \mathrm{Log}_{10}(\mathrm{E}_{\mathrm{thrown}}/\mathrm{eV}) < 19.0$, and $19.0 \leq \mathrm{Log}_{10}(\mathrm{E}_{\mathrm{thrown}}/\mathrm{eV}) \leq 20.0$ are plotted in Figure 4.4 on page 61. It is shown that the EAS core positions follow the conditions listed in Table 4.1 on page 59.

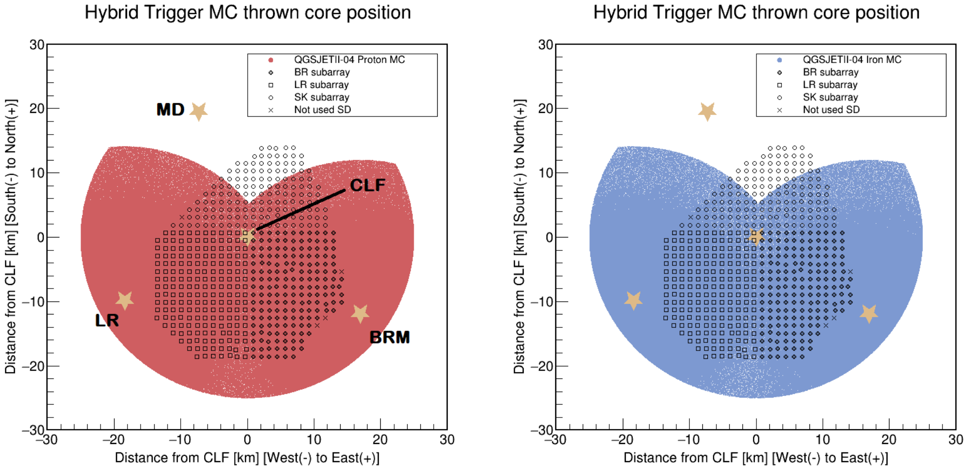

(a) Proton MC

(b) Iron-nucleus MC

Figure 4.3: (a) Distribution of EAS core positions of all proton simulated events. (b) Distribution of EAS core positions of all iron-nucleus simulated events. The position of CLF is set to be (0,0). Star markers represent the Middle Drum (MD) station, the BRM station, the Long Ridge (LR) station, and the CLF.

As displayed in Figure 4.3, the shapes of EAS core position distributions are not circular because of a condition regarding the maximum distance from FD stations described in Table 4.3. The θ (Zenith) distribution of all CORSIKA-generated EAS: 400 × 31 = 12,400 proton-simulated and 301 × 31 = 9,331 iron-

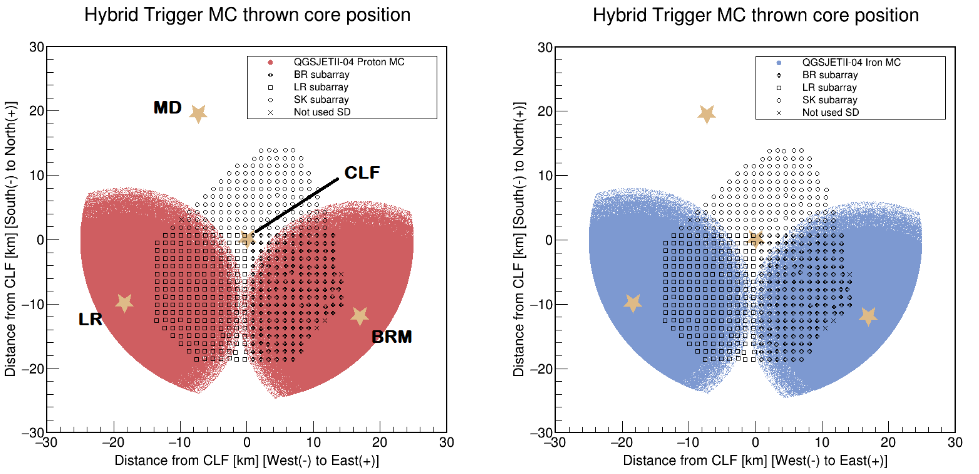

(a) Proton MC $17.0 \leq \mathrm{Log}_{10}(\mathrm{E}_{\mathrm{thr.}}/\mathrm{eV}) < 18.0$ (b) Iron-nucleus MC $17.0 \leq \mathrm{Log}_{10}(\mathrm{E}_{\mathrm{thr.}}/\mathrm{eV}) < 18.0$

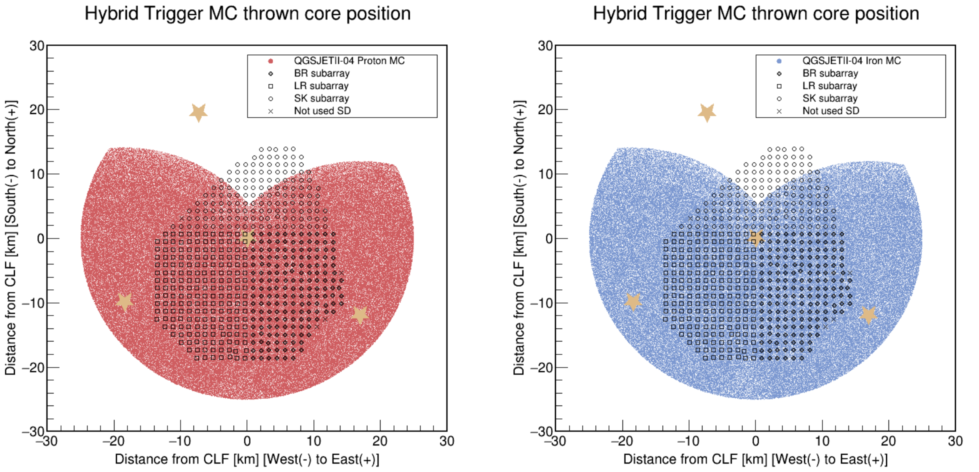

(c) Proton MC $18.0 \leq \mathrm{Log}_{10}(\mathrm{E}_{\mathrm{thr.}}/\mathrm{eV}) < 19.0$ (d) Iron-nucleus MC $18.0 \leq \mathrm{Log}_{10}(\mathrm{E}_{\mathrm{thr.}}/\mathrm{eV}) < 19.0$

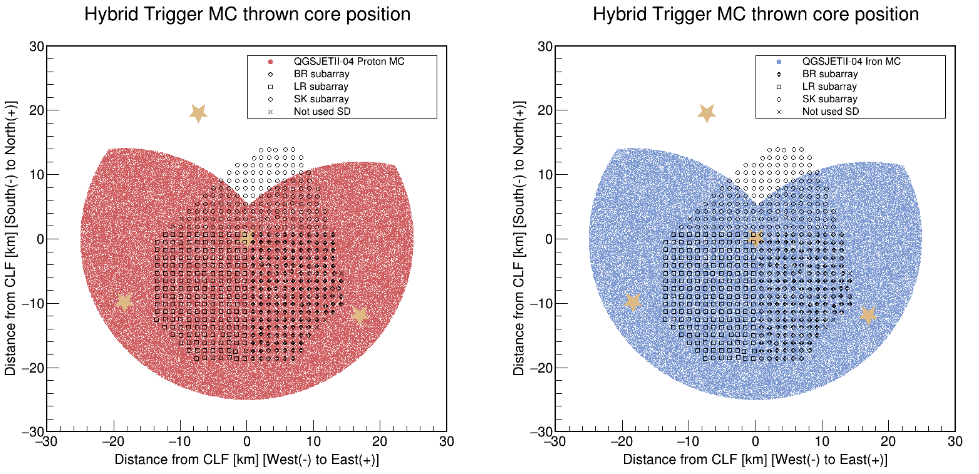

(e) Proton MC $19.0 \leq \mathrm{Log}_{10}(\mathrm{E}_{\mathrm{thr.}}/\mathrm{eV}) \leq 20.0$ (f) Iron-nucleus MC $19.0 \leq \mathrm{Log}_{10}(\mathrm{E}_{\mathrm{thr.}}/\mathrm{eV}) \leq 20.0$

Figure 4.4: Distributions of EAS core positions of proton and iron-nucleus simulated events. Shown in three different energy ranges.

simulated EAS are shown in Figure 4.5 on page 62 together with the ϕ (Azimuth) distribution of all simulated proton and iron simulated EAS after the complete iterations.

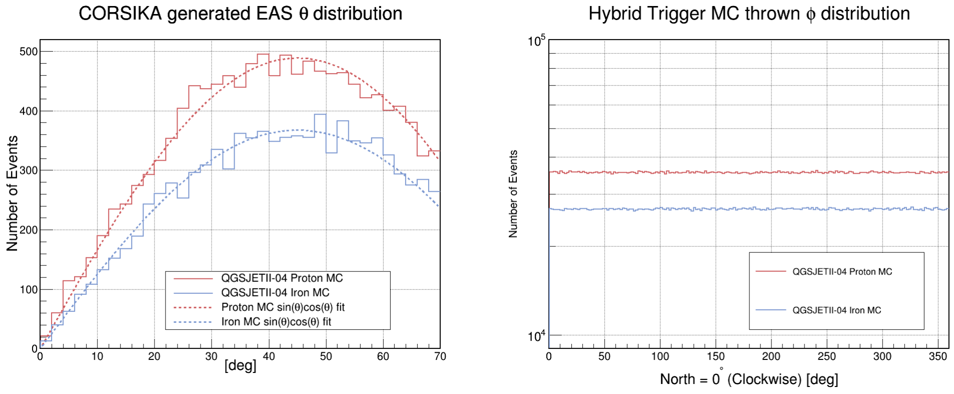

(a) Zenith

(b) Azimuth

Figure 4.5: (a) Zenith angle θ distribution of CORSIKA-generated EAS. (b) Azimuth angle ϕ distribution of simulated EAS after the iterations.

The number of events increases until θ reaches the peak at 45° and then decreases as displayed in Figure 4.5 (a) on page 62. The shown distributions are fitted by a trigonometric function of ($p[0] \times \sin(\theta) \times \cos(\theta)$, where $p[0] =$ constant), which is a typical fitting function for a θ distribution in the actual SD observation mode. When particles arrive on the Earth uniformly, the spherical segment increases with $\sin(\theta)$ while the effective area of a detector decreases with $\cos(\theta)$.

It is confirmed that the ϕ values for all simulated EAS are uniformly distributed from Figure 4.5 (b) on page 62. The difference in the number of events between proton and iron-nucleus MC is caused by the difference in the number of CORSIKA-generated EAS (400 EAS per each energy bin for proton MC and 301 EAS for iron-nucleus MC), as described above.

Then the mean values of $\mathrm{X}_{\mathrm{max}}$ distributions ($<\mathrm{X}_{\mathrm{max}}>$) of CORSIKA-generated EAS are shown in the upper part of Figure 4.6 on page 63. The standard deviations of $\mathrm{X}_{\mathrm{max}}$ distributions (($\sigma(\mathrm{X}_{\mathrm{max}})$)) are also plotted in the lower part of Figure 4.6. Although not analyzed in this thesis, the $<\mathrm{X}_{\mathrm{max}}>$ and $\sigma(\mathrm{X}_{\mathrm{max}})$ estimated by the different hadronic interaction models EPOS-LHC [15] and QGSJET-II-03 [157] are shown in Figure 4.6 as well to show the effects on $\mathrm{X}_{\mathrm{max}}$ when using the different hadronic interaction model.

In Figure 4.6 on page 63, it is exhibited that the mean $\mathrm{X}_{\mathrm{max}}$ values increase as the primary energy increases from 685 g/cm^2 to 850 g/cm^2 for the proton MC simulation and 585 g/cm^2 to 750 g/cm^2 for the iron-nucleus MC simulation. It should be noted that the proton MC simulation shows an atmospheric depth of approximately 100 g/cm^2 deeper in mean $\mathrm{X}_{\mathrm{max}}$ than the iron-nucleus MC simulation. The standard deviations of $\mathrm{X}_{\mathrm{max}}$ distributions slightly decrease as the primary energy increases. For the proton MC simulation, the standard deviations range from 55 g/cm^2 to 85 g/cm^2. The standard deviations of the iron-nucleus MC range from 20 g/cm^2 to 30 g/cm^2.

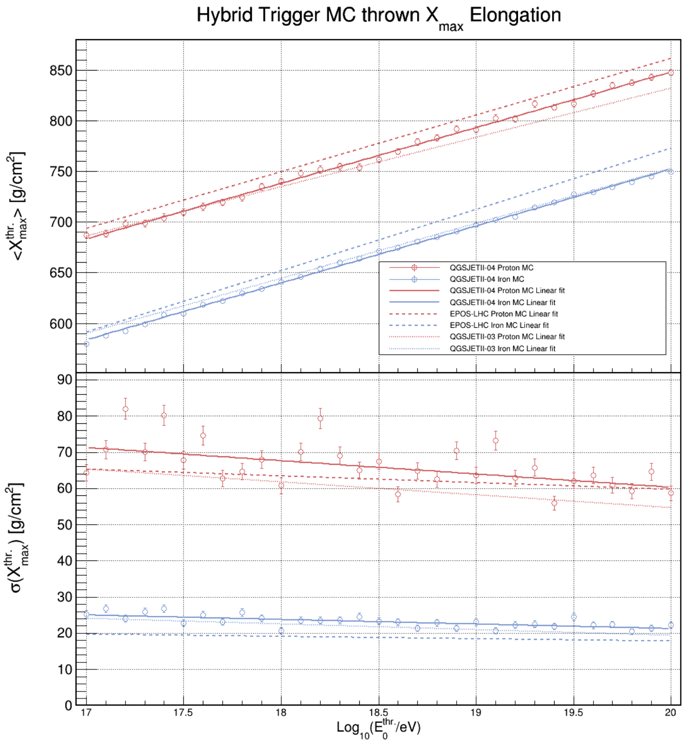

Figure 4.6: Upper part shows the mean $X_{\max}$ of CORSIKA-generated EAS as a function of primary energy. Error bars represent the standard errors (the standard deviation divided by $\sqrt{(\text{the number of events})}$). The solid lines represent the results of linear fittings. Lower part shows the $\sigma(X_{\max})$ (standard deviation of $X_{\max}$). Error bars represent the standard deviation divided by $\sqrt{(2 \times \text{the number of events})}$. The dashed lines and the dotted lines represent the linear fittings of the results obtained by the different hadronic interaction models EPOS-LHC and QGSJET-II-03.

4.2 Reconstruction Condition

The detailed procedure to reconstruct an EAS event in the TA hybrid trigger mode is described in Section 3.3 using Equations (3.1) through (3.6). However, to reconstruct the EAS event from the actual raw observation data, an extra process is needed to determine a set of SDs and a set of FD Photomultiplier tubes (PMTs) to be used in the reconstruction procedure and the timing and intensity parameters for the above equations. This process, called pre-reconstruction, is described in the following subsections.

4.2.1 SD Pre-reconstruction

In this stage, the Flash Analog to Digital Converter (FADC) waveform data acquired from all triggered SDs are scanned to determine the energy deposit and signal timing. The first rising time in a waveform is set to be the signal timing of an SD to detect the leading edge of the waveform caused by an EAS. Since the waveform pedestal level and its standard deviation σ_{ped} are monitored at 10-minute intervals, the rising time of the waveform is calculated from these parameters. In this analysis, the first time bin that recorded a signal greater than $3\times\sigma_{\text{ped}}$ from the pedestal level is determined to be the rising time.

The total energy deposit in the SD is calculated from the same parameters. First, signal regions are determined to estimate the total energy deposit in an SD. Signal regions are defined by the start-time-bin where the signal exceeds or becomes equal to $3\times\sigma_{\mathrm{ped}}$ from the pedestal level and the end-time-bin where the signal falls below or becomes equal to $3\times\sigma_{\mathrm{ped}}$ from the pedestal level.

After integrating all signal regions with their corresponding start-time-bin and end-time-bin, the total energy deposit in an SD is obtained in a unit of Minimum Ionizing Particle (MIP) by multiplying the conversion factor. With the energy deposits and signal timings of all triggered SDs determined, the following selection procedure is applied to determine the candidates for an anchor SD.

1. Energy deposit threshold for an anchor SD: above 3 MIPs.

   Since the geometric reconstruction of an EAS with the TA hybrid trigger mode only considers the signal timing information and the position information provided by one selected SD, inaccuracy in geometric reconstruction might be introduced by selecting an anchor SD triggered by particles from a non-EAS event.

   By selecting the Level-1 trigger ($>$ 3 MIPs) as an energy deposit threshold instead of the Level-0 trigger ($>$ 0.3 MIPs), it is possible to reduce the probability of choosing an anchor SD that is related to a non-EAS event. This chance probability is reduced to an order of magnitude lower level as the typical Level-0 trigger rate is approximately 700 Hz. The typical Level-1 trigger rate is approximately 40 Hz, as described in Section 2.2.2.

2. Shower Detector Plane (SDP) distance threshold for an anchor SD: $<$ 1.5 km.

   Although the probability of selecting a non-EAS-related SD is reduced with the above selection, non-EAS-related SDs with energy deposits above 3 MIPs remain in the set of candidates for an anchor SD. To remove such SDs from the candidates, the SDP distance threshold is introduced.

   First, the initial SDP is estimated using the same method as FD monocular analysis. This process results in a reference line for this selection, which is the intersection line of the ground and the initial SDP. Then, any SD separated from the reference line by 1.5 km or farther is removed from the set of candidates for an anchor SD.

   Since the spacing of the TA SD is 1.2 km, 1.5 km is sufficient to select the set of candidates for an anchor SD. This selection allows only SDs near the shower axis to be selected as an anchor SD, rejecting SDs too far from the EAS.

4.2.2 FD Pre-reconstruction

The FD pre-reconstruction consists of four stages of PMT selection procedures that perform a selection of PMTs to be used in the reconstruction and the determination of signal timing and intensity for each selected PMT. Each stage is described below.

1st Selection: Signal Search with the Triangle Filter

The waveform is a common term to refer to FADC counts plotted by each time bin. Since a waveform with signals from an EAS typically exhibits a triangular shape, the dedicated triangle filter scans the waveform and then determines the peak p and its width w that gives the maximum value of significance $\sigma_{(w,p)}$, which is calculated using the following equation:

$$\sigma_{(w,p)} = \frac{\sum_{i=p-w}^{p+w} \mathrm{F_{sub}}(i)\mathrm{W}(i)}{\sum_{i=p-w}^{p+w} \mathrm{P_{rms}}(i)\mathrm{W}(i)}, \tag{4.1}$$

where W_i is the weight of the i-th waveform bin equals to $w - |p - i|$. $\mathrm{F_{sub}}$(i) means the value of the i-th waveform bin subtracted by the pedestal and $\mathrm{P_{rms}}$ means the fluctuation in the pedestal. A conceptual diagram of the triangle filter is shown in Figure 4.7 on page 65.

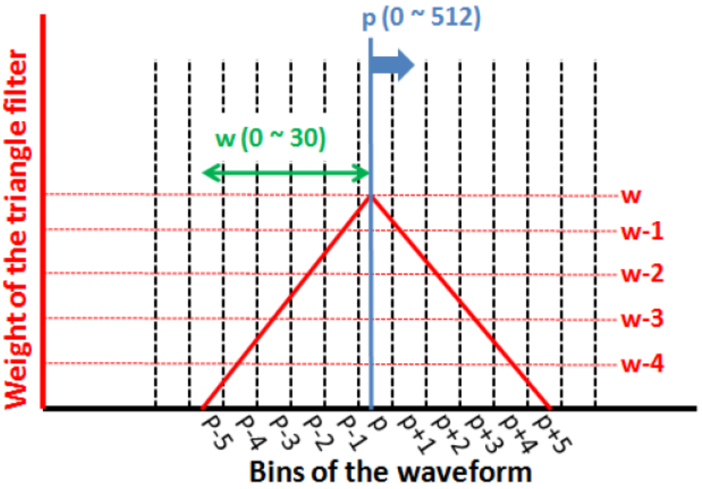

Figure 4.7: Conceptual diagram of the triangle filter to determine the maximum significance $\sigma_{(w,p)}$, peak, and width in the waveform of a PMT [52]. The filter scans all 512 bins to find the peak p and the width w in the range from 0 to 30 bins. As a result, a pair of (w,p) that yields the maximum significance $\sigma_{(w,p)}$ is determined.

After p and w are determined at the maximum significance, the PMT signal timing T and its squared error σ_{T}^2 are formulated as in Equations (4.2) and (4.3). The 100 ns in the equations indicates the bin width at the 10 MHz sampling rate of FADC.

$$\mathrm{T} = 100\mathrm{ns} \cdot \frac{\sum_{i=p-w}^{p+w} \mathrm{F_{sub}}(i) \times i}{\sum_{i=p-w}^{p+w} \mathrm{F_{sub}}(i)}. \tag{4.2}$$

$$\sigma_{\mathrm{T}}^2 = 100\mathrm{ns} \cdot \frac{\sum_{i=p-w}^{p+w} \mathrm{F_{sub}}(i)(\mathrm{T} - i)^2}{\sum_{i=p-w}^{p+w} \mathrm{F_{sub}}(i)}. \tag{4.3}$$

Next, the integration window must be determined to estimate the number of photoelectrons received by a PMT. The integration window is defined by start-time-bin and end-time-bin.

In this analysis, the start-time-bin (startBin) is the first bin before the peak bin that shows an FADC value lower than the pedestal, $\mathrm{F_{sub}}(i) < 0$. The end-time-bin (endBin) is the first bin after the peak bin that shows an FADC value lower than the pedestal, $\mathrm{F_{sub}}(i) < 0$.

The peak bin here is determined by the triangle filter described earlier. Then the number of photoelectrons ($\mathrm{N_{p.e.}}$) received by a PMT is calculated as shown in Equation (4.4), where g is the conversion factor between the FADC value and the number of photoelectrons, which is measured using the detector calibration.

$$N_{\mathrm{p.e.}} = \sum_{i=\mathrm{startBin}}^{\mathrm{endBin}} \mathrm{F_{sub}}(i) \times g. \tag{4.4}$$

After all required parameters are calculated, the selection procedure filters out the PMTs that showed lower significance $\sigma_{(w,p)}$ in the triangle fittings. A significance greater than 6σ is required for each PMT to be selected.

2nd Selection: Linear Structure Search with Hough Transform

Noisy PMTs should be mostly filtered out in the first selection, but the first selection does not filter out the PMTs with large background. Since the longitudinal development of an EAS occurs along its shower axis, the air fluorescence from an EAS generates a linear track on FD cameras. With this principle, the second selection can filter out irrelevant PMTs by selecting only PMTs with signals in a possible shower track contained in a linear structure, which is determined by Hough transform [158]. A line in an $x - y$ space is parameterized using (ρ,ω) by Hough transform as in Equation (4.5):

$$\rho = x\cos(\omega) + y\sin(\omega). \tag{4.5}$$

In the resulting $\rho - \omega$ space called Hough space, a group of all lines going through a particular point (x_i,y_i) in the $x - y$ space forms a curved line, meaning that a single data point in the $x - y$ space corresponds to a single curved line in the Hough space. Therefore, to find a line that goes through all data points, one needs to determine the point of intersection for all curved lines in the Hough space. The conceptual diagram of Hough transform is shown in Figure 4.8 on page 66.

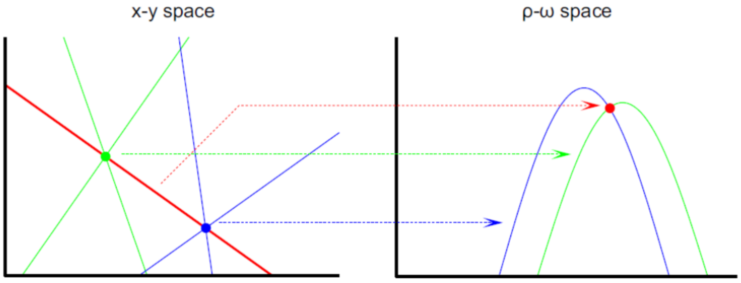

Figure 4.8: Conceptual diagram of a simple Hough transform [52]. All lines passing through the green data point in an $x - y$ space are transformed into the green curved line in a $\rho - \omega$ space. All lines passing through the blue data point in the $x - y$ space also form the blue curved line in the $\rho - \omega$ space. The red line passing through the green and blue data points in the $x - y$ space is indicated as the red point in the $\rho - \omega$ space.

Now the linear track on FD cameras by an EAS is determined, the separation angle β_i of the i-th PMT from the linear track is calculated as below:

$$\cos(\beta_i) = \vec{n_i} \cdot n_{(\vec{proj},i)}, \tag{4.6}$$

where $\vec{n_i}$ is the direction vector of the i-th PMT and $n_{(\vec{proj},i)}$ is the projection vector onto the determined linear track. Since the lateral widths of EAS tracks vary by their geometry, the threshold for β to reject spatially separated PMTs also varies. In this analysis, β values of all PMTs are filled in a histogram with a bin width of 1 degree. Then the threshold is set to the smallest β with zero entries in the histogram. Any PMT showing a degree of separation above the threshold is rejected in this selection. Figure 4.9 on page 67 shows a sample shower track with the determined linear track and the histogram of β.

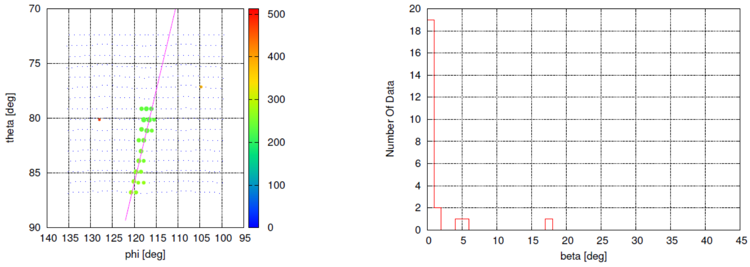

Figure 4.9: (Left) The purple line indicates the determined linear track from the sample shower track. (Right) Histogram of calculated β [35]. The threshold is set to be 2 degrees since it is the first bin from the 0 degrees bin that has no entry. The PMTs showing β above 4 degrees are rejected.

3rd Selection: Timing Sequence Search with the Timing-elevation Angle Fit

Even after two previous stages of selection, noisy PMTs with significant background in the vicinity of the selected linear structure might remain. Since a PMT's signal timing T and its squared error σ_{T}^2 are determined using Equations (4.2) and (4.3), it is possible to compare the signal timing T with the expected signal timing $\mathrm{T}_{\mathrm{exp}}$ estimated using Equation (4.7). Note that Equation (4.7) is similar to Equation (3.1), which estimates the expected signal timing with the data acquired by an SD.

$$\mathrm{T}_{\mathrm{exp},i} = \mathrm{T}^* + \frac{\sin\psi - \sin\alpha_i}{c_0 \sin(\psi + \alpha_i)} \mathrm{R}^*, \tag{4.7}$$

where $\mathrm{T}_{\mathrm{exp},i}$ is the expected signal timing at the i-th PMT; T^* is the signal timing at the center of the shower track; c_0 is the speed of light in vacuum; ψ is the angle of the shower axis inside the SDP; R^* is the distance from the FD to the track center, which is shown in Figure 4.10 on page 67.

Now the observed signal timing T and the expected signal timing $\mathrm{T}_{\mathrm{exp}}$ are estimated for all PMTs. The residual time $\Delta\mathrm{T}$ is also calculated with the difference between observed and expected signal timing values. In this analysis, $\Delta\mathrm{T}$ values of all PMTs are filled in a histogram with a bin width of 1 μs. Then the threshold is set to be the first bin from the 0 μs bin, which shows no entry for the histogram. The PMTs showing residual time above the threshold are rejected in this selection. Figure 4.10 on page 67 shows a sample shower track with the geometric parameters and a result of timing-elevation angle fit.

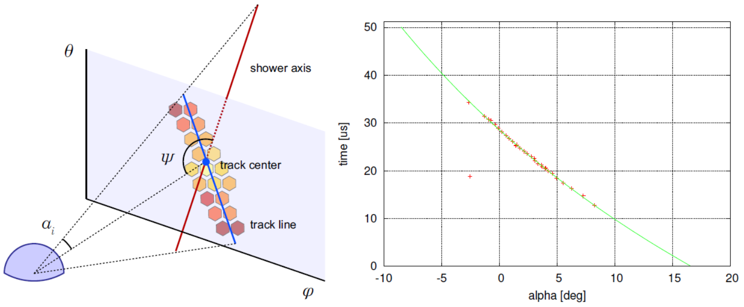

Figure 4.10: (Left) Conceptual diagram of several geometric parameters used in the timing-elevation angle fit. (Right) The green curve obtained from the fit represents the expected signal timings, while the red crosses represent the observed signal timings [35]. The data point near (-2.5,19) on the right panel is rejected.

4th Selection: Sweeping for Small Signals with a Lowered Threshold and a Performance of Pre-geometry Reconstruction

Although the previous three stages of PMT selection choose only PMTs with signals above 6σ of significance estimated in the first selection, this final selection stage sweeps signals regardless of the significance threshold.

First, the timing-elevation angle function $f(\alpha_i)$ is obtained by the fitting described in Equation (3.1) with the set of PMTs that pass all previous selection procedures. The set of PMTs that pass this selection is called GOOD PMTs. Then the timing difference R_i, χ_i^2, and the separation angle β_i from the SDP for the i-th PMT are calculated as in the following equations, including the PMTs rejected by the previous stages:

$$\mathrm{R}_i = |f(\alpha_i) - \mathrm{T}_i|, \tag{4.8}$$

$$\chi_i^2 = (\frac{\mathrm{R}_i}{\sigma_{\mathrm{T}_i}})^2, \tag{4.9}$$

$$\beta_i = \arcsin(\vec{n_i} \cdot n_{\mathrm{N}\vec{\mathrm{S}}\mathrm{DP}}), \tag{4.10}$$

where α_i is the elevation angle of the i-th PMT projected onto the SDP; $f(\alpha_i)$ is the fitted signal timing at a specific elevation angle α_i; T_i and σ_{T_i} are the i-th PMT's signal timing and its error, respectively, estimated by Equations (4.2) and (4.3) in the first selection procedure; $\vec{n_i}$ is the direction vector of the i-th PMT; $n_{\mathrm{N}\vec{\mathrm{S}}\mathrm{DP}}$ is the normal vector of the SDP. With the three obtained parameters, all PMTs are tested to see if they meet the criterion called SOFT and then the criterion called HARD, described in Table 4.4 on page 68.

Table 4.4: Two types of criteria for selecting PMTs for the fourth selection.

Parameter	SOFT	HARD
R_i	$< 1.2\ \mu$s	$< 0.8\ \mu$s
χ_i^2	< 20	< 15
β_i	$< 4°$	$< 2°$

Specifically, the PMTs that satisfy the SOFT criterion are tested again with the linear fitting of elevation angle and signal timing with the GOOD PMTs within the separation angle less than 5° and the timing difference less than 5 μs. If the residual time R_{lin}, the number of PMTs N_{lin}, and the χ_{lin}^2 of the linear fitting satisfy the conditions described in Table 4.5 on page 69, then the PMT is added to the GOOD PMTs. If the set of GOOD PMTs is updated during the procedure, the selection procedure starts over from the beginning. This iteration terminates when there is no more PMT to add or remove from the set of GOOD PMTs. After the test with the SOFT criterion is finished, the test with the HARD criterion is initiated. The PMTs that meet the HARD criterion are tested with the same method described above and the iteration continues until there is no more PMT to add or remove from the set of GOOD PMTs.

4.2.3 Other Parameters and Missing Energy

After the PMT selection procedure is cleared, it is necessary to fix additional free parameters for the longitudinal reconstruction of an EAS, as described in Section 3.3.

Table 4.5: Linear fitting conditions for a PMT to be added to the GOOD PMTs. Any PMT must meet all three conditions to be added.

Parameter	Condition
R_{lin}	$\leq 0.6\ \mu$s
N_{lin}	≥ 3
χ^2_{lin}	≤ 150

1. X_0: -60 g/cm^2.

   X_0 is a free parameter of the Gaisser and Hillas (G-H) function used in the longitudinal reconstruction. Here, -60 g/cm^2 is chosen according to the previous hybrid analysis performed by the TA experiment [22].

2. λ: 70 g/cm^2.

   λ is another free parameter of the G-H function used in the longitudinal reconstruction. Here, 70 g/cm^2 is chosen according to the previous hybrid analysis performed by the TA experiment [22].

As mentioned in the later part of Section 3.3, the EAS reconstruction procedure only gives E_{cal} as it is based on the calorimetric energy estimation of electromagnetic cascades in an EAS. Therefore, the method to obtain E_0 from E_{cal} is implemented in the TA hybrid trigger shower reconstruction procedure by referring to the ratio of E_0/E_{cal} for each composition and simulated energy.

Since the longitudinal development profiles of EAS generated by CORSIKA are recorded for each 1 g/cm^2 of atmospheric depth, the energy deposit of the EAS by charged particles can be plotted by slant depths. By fitting the G-H function with fixed values of X_0 and λ to the energy deposit of the EAS generated by CORSIKA for each step of slant depth with the fitting range feasible with the Field Of View (FOV) of the FD cameras, it is possible to estimate the E_{cal} for the thrown simulated energy of the EAS generated by CORSIKA.

Since there are 400 and 301 EAS events for proton and iron-nucleus in each 0.1-decade energy bin, respectively, the mean values of reciprocal of E_0/E_{cal} for each energy bin are plotted in Figure 4.11 (a) on page 70. In this analysis, missing energy estimation is performed using the QGSJET-II-04 proton MC simulation, as indicated by the red arrow in Figure 4.11 (a).

The reconstruction in this analysis adopts the QGSJET-II-04 proton's missing energy ratio E_{cal}/E_0, which is represented by red open squares in Figure 4.11 (a) on page 70. The uncertainties caused by the composition fraction are added to the total uncertainty in the energy reconstruction, described in Section 5.7.5. The data plotted in Figure 4.11 (a) on page 70 are plotted in another way by putting the QGSJET-II-04 proton ratio as 1 to see the differences between models and compositions, as shown in Figure 4.11 (b) on page 70. The largest discrepancy in the ratio E_{cal}/E_0 estimated using the QGSJET-II-04 proton and iron-nucleus MC is approximately 1.09 at the lowest energy of 10^{17} eV. The discrepancy between the two compositions decreases as the primary energy of UHECR increases.

4.2.4 Quality Cut

After the EAS reconstruction is completed, a judgment is made on whether to use the reconstruction result in the analysis. This procedure is called the quality cut. As its name suggests, this procedure minimizes the biases and maintains good

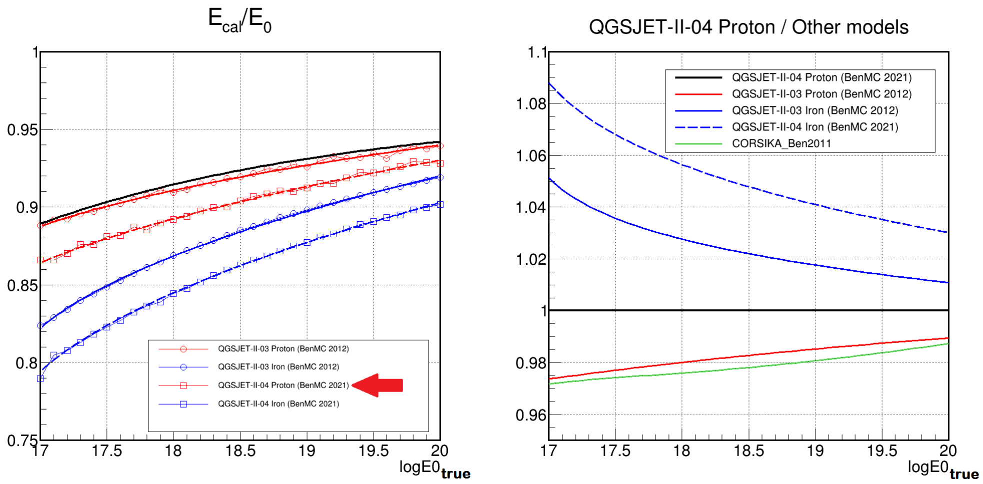

(a) E_{cal}/E_0

(b) Models comparison

Figure 4.11: (a) E_{cal}/E_0 calculated using various sets of CORSIKA-simulated EAS using different hadronic interaction models and mass compositions. The open squares represent the ratio estimated using the QGSJET-II-04 and the open circles represent the ratio estimated using the QGSJET-II-03. The red markers indicate the proton MC and the blue markers indicate the iron-nucleus MC. The results of curve fittings are also shown. (b) Same data as in (a), but the data points of the QGSJET-II-04 proton MC simulation are placed as 1 to see the discrepancy between hadronic interaction models and mass compositions.

resolutions in reconstruction while maximizing the statistical size of reconstructed events. The conditions for the quality cut in this analysis are described in Table 4.6 on page 70.

Table 4.6: Conditions for the quality cut and criteria for each element.

Condition	Criterion
Number of selected PMTs	> 20 PMTs
Spatial length of track	$> 15°$
θ (Zenith)	$< 55°$
Minimum viewing angle	$> 20°$
X_{max} bracketing	$X_{start} < X_{max} < X_{end}$
Fiducial volume	$X_{start} < 550$ g/cm^2 and $X_{end} > 850$ g/cm^2
Reconstructed energy	$17.5 \leq \text{Log}_{10}(E_{rec.}/\text{eV}) < 19.5$
Core position 1	Inside the corresponding sub-array
Core position 2	> 100 m separation from the array border

Each condition for the quality cut in this analysis is explained further below. It must be noted that there is an extra process in the quality cut procedure regarding the stereoscopic events. When the EAS has a favorable incident geometry and is bright enough, the same EAS event can trigger both BRM and LR stations. In this case, the reconstruction and the quality cut procedures for the EAS event are performed independently from the data acquired at each station. Suppose the event is successfully reconstructed and passes the quality cut with the data independently acquired at both stations. In that case, the result from the station that received more photoelectrons from the EAS is adopted and the result from the other station is rejected.

1. Number of selected PMTs

   This condition relates to the spatial track length of the reconstructed event. An EAS with a shorter track is difficult to reconstruct, especially in determining the SDP, due to the limited timing and spatial resolution of PMTs.

2. Spatial track length

   An EAS with a shorter spatial track is likely from a remote EAS, an EAS heading toward, or an EAS fleeing from the direction of the FD telescope, which is challenging to reconstruct geometrically.

3. θ (Zenith)

   An EAS with high θ is also challenging to reconstruct geometrically due to its deeply penetrating nature. Also, SD and FD have different thresholds for the maximum θ that can reconstruct EAS with fair accuracy.

4. Minimum viewing angle (MVA)

   The minimum viewing angle indicates the angle between the reconstructed shower axis and the line of sight of the FD station at the atmospheric depth where the FD station starts observing the EAS ($\mathrm{X_{start}}$). An EAS with a small minimum viewing angle is difficult to reconstruct geometrically because a fraction of Cherenkov radiation increases in this condition. Figure 4.12 on page 72 shows a visualization of the minimum viewing angle.

5. $\mathrm{X_{max}}$ bracketing

   As their names suggest, $\mathrm{X_{start}}$ (or $\mathrm{X_{low}}$) means the atmospheric depth where the FD station starts observing the EAS and $\mathrm{X_{end}}$ (or $\mathrm{X_{high}}$) means the atmospheric depth where the FD station finishes observing the EAS. The G-H function fitting for a longitudinal reconstruction procedure has a lower success rate for accurate fitting of $\mathrm{X_{max}}$ and $\mathrm{N_{max}}$ when $\mathrm{X_{max}}$ is not in the FOV of the FD station.

6. Fiducial volume

   Since the FD stations have a limited FOV in terms of the elevation angle as described in Section 2.2.1, a bias is introduced in the observed distribution of $\mathrm{X_{max}}$ [159]. Note that this effect is enhanced by the previous item (5. $\mathrm{X_{max}}$ bracketing), which requests the $\mathrm{X_{max}}$ of the EAS to be in the FOV, as shown in Figure 4.13 on page 73. With the MC simulation study, the optimal condition to avoid this effect $\mathrm{X_{start}}$ is estimated to be lower (i.e., shallower) than 550 g/cm^2 and $\mathrm{X_{end}}$ to be higher (i.e., deeper) than 850 g/cm^2, as indicated in Figure 4.14 on page 73.

7. Reconstructed energy

   Since the MC set for the TA hybrid trigger mode is generated in the energy range of $17.0 \leq \mathrm{Log_{10}(E_{thrown}/eV)} \leq 20.0$, as explained in Table 4.1 on page 59, it is only possible to estimate the aperture of the TA hybrid trigger mode within this energy range. However, due to the resolution in the reconstruction of the primary energy of the EAS, a migration effect (a contribution to the apertures by EAS outside of the simulated energy range) should be considered.

   Therefore, a quality cut is necessary to ensure the aperture of detectors is fully understood with the migration effect by limiting the reconstructed energy range to be narrower than the actual simulated energy range.

On the one hand, at the lower energy boundary, this effect is negligible due to the energy threshold of the FD, as explained in Section 3.1. Therefore, the lower reconstructed energy boundary for the quality cut is set to be $\mathrm{Log}_{10}(\mathrm{E}_{\mathrm{rec.}}/\mathrm{eV}) = 17.5$, where the MC simulation set has enough statistics of reconstructed events.

On the other hand, this effect must be estimated at the higher energy boundary. Since the primary energy reconstruction resolution at 10^{20} eV (thrown energy) is estimated to be 4.7% for a proton UHECR and 3.5% for an iron-nucleus UHECR, the higher energy boundary for the quality cut is set to be $\mathrm{Log}_{10}(\mathrm{E}_{\mathrm{rec.}}/\mathrm{eV}) = 19.5$, which sufficiently rejects migration effect from outside the simulation energy range. The estimation of the aperture for this analysis is described in Section 4.3.

8. Border cut

   Since this analysis only uses data acquired from the Black Rock (BR) and Long Ridge (LR) sub-arrays, the EAS with a core position near the Smelter Knolls (SK) sub-array might be reconstructed with the anchor SD, which provides poor reconstruction accuracy. This inaccuracy occurs because the SK sub-array data are unavailable in this analysis. This cut ensures that the distribution of the charged particles at the ground level is well contained inside the available sub-array.

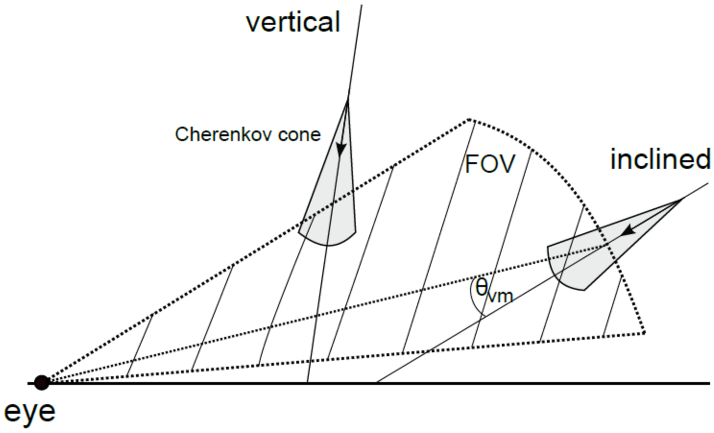

Figure 4.12: Visualization of minimum viewing angle (θ_{vm}) [53].

The EAS core position distributions for all reconstructed events passing the quality cut are plotted in Figure 4.15 (a) and (b) on page 74 for proton and iron-nucleus MC simulations, respectively. Additionally, the EAS core position distributions for three energy ranges, $17.5 \leq \mathrm{Log}_{10}(\mathrm{E}_{\mathrm{rec.}}/\mathrm{eV}) < 18.0$, $18.0 \leq \mathrm{Log}_{10}(\mathrm{E}_{\mathrm{rec.}}/\mathrm{eV}) < 19.0$, and $19.0 \leq \mathrm{Log}_{10}(\mathrm{E}_{\mathrm{rec.}}/\mathrm{eV}) < 19.5$, are plotted in Figure 4.16 on page 75. It is shown in Figure 4.15 that all EAS core positions are well contained inside the sub-arrays, following the quality cut condition described above.

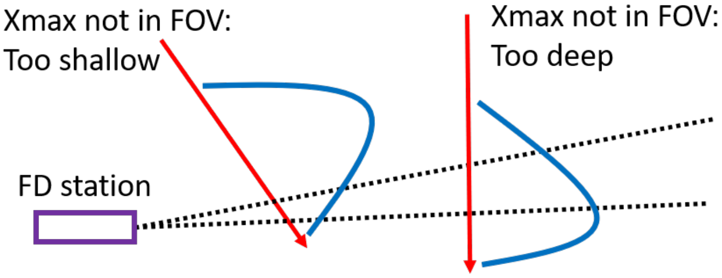

Figure 4.13: Simplified diagram explaining a bias in reconstructing X_{max} introduced by the limited FOV of an FD station. The purple rectangle represents an FD station and the two black dotted lines show its FOV. The red lines represent shower axes and the blue curves represent the longitudinal development of the EAS. The left EAS is rejected because its X_{max} is too shallow and not in the FOV. The right EAS is also rejected because its X_{max} is too deep and not in the FOV.

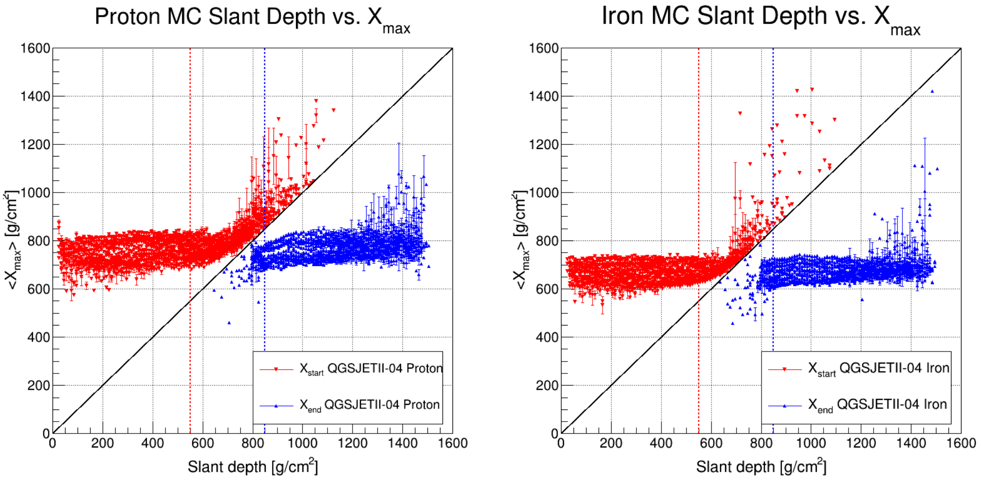

(a) Proton MC

(b) Iron-nucleus MC

Figure 4.14: (a) X_{start} vs. $<X_{\mathrm{max}}>$ and X_{end} vs. $<X_{\mathrm{max}}>$ of the proton MC events (after reconstruction and applying the quality cut except for the fiducial volume cut). The mean X_{max} values for each slant depth are plotted. The black line represents where the slant depth equals the X_{max}. Note that the X_{max} bracketing allows X_{start} to be placed only on the upper-left side of the plot and X_{end} only on the lower-right side of the plot. The two colored broken lines indicate the approximate boundaries of the region, which are affected by the limited FD FOV. The boundaries for X_{start} and X_{end} are set to be 550 g/cm^2 and 850 g/cm^2, respectively. (b) The same data as in (a), but with the iron-nucleus MC simulation. Note that the color difference here emphasizes the difference between X_{start} and X_{end}, not the mass compositions.

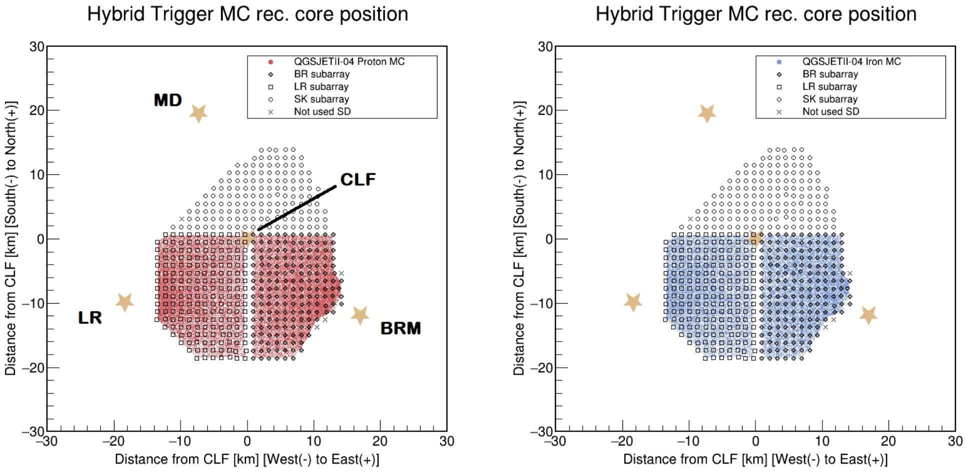

(a) Proton MC

(b) Iron-nucleus MC

Figure 4.15: (a) Distribution of EAS core positions for all reconstructed events passing the quality cut in the proton MC simulation. (b) The same data as in (a), but with the iron-nucleus MC simulation. Star markers represent the BRM, LR, or CLF.

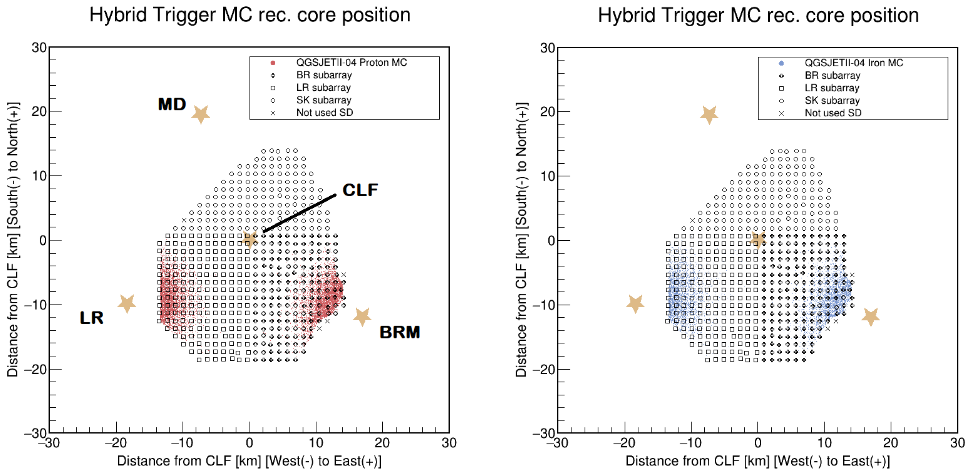

(a) Proton MC $17.5 \leq \mathrm{Log}_{10}(\mathrm{E}_{\mathrm{rec.}}/\mathrm{eV}) < 18.0$ (b) Irons MC $17.5 \leq \mathrm{Log}_{10}(\mathrm{E}_{\mathrm{rec.}}/\mathrm{eV}) < 18.0$

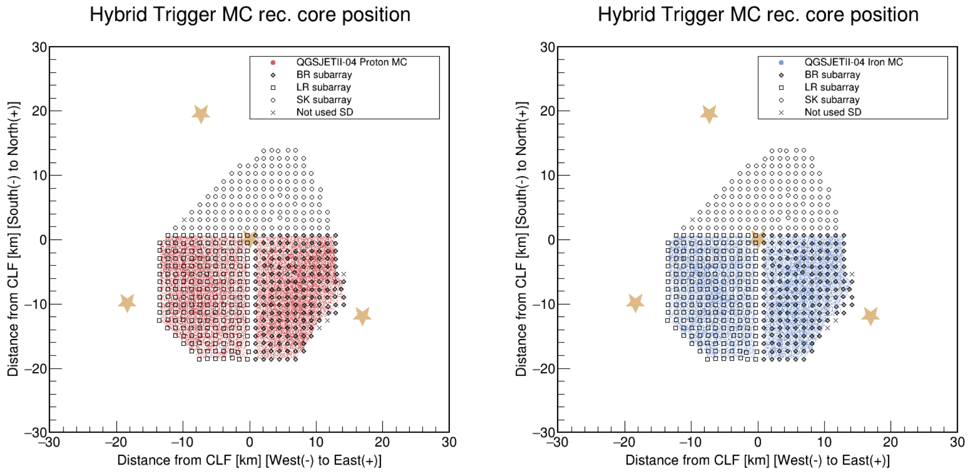

(c) Proton MC $18.0 \leq \mathrm{Log}_{10}(\mathrm{E}_{\mathrm{rec.}}/\mathrm{eV}) < 19.0$ (d) Iron MC $18.0 \leq \mathrm{Log}_{10}(\mathrm{E}_{\mathrm{rec.}}/\mathrm{eV}) < 19.0$

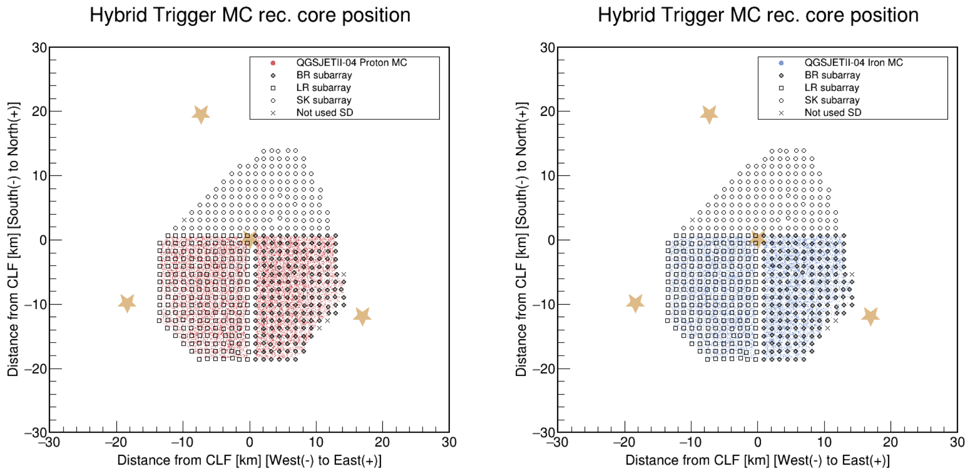

(e) Proton MC $19.0 \leq \mathrm{Log}_{10}(\mathrm{E}_{\mathrm{rec.}}/\mathrm{eV}) < 19.5$ (f) Iron MC $19.0 \leq \mathrm{Log}_{10}(\mathrm{E}_{\mathrm{rec.}}/\mathrm{eV}) < 19.5$

Figure 4.16: Distributions of EAS core positions for proton and iron-nucleus reconstructed events passing the quality cut shown on the left and right sides, respectively. The energy ranges of $17.5 < \mathrm{Log}_{10}(\mathrm{E}_{\mathrm{rec.}}/\mathrm{eV}) < 18.0$, $18.0 < \mathrm{Log}_{10}(\mathrm{E}_{\mathrm{rec.}}/\mathrm{eV}) < 19.0$, and $19.0 < \mathrm{Log}_{10}(\mathrm{E}_{\mathrm{rec.}}/\mathrm{eV}) < 19.5$ are shown.

4.3 Aperture Estimation

The aperture of the TA hybrid trigger mode is the product of an effective geometric area for EAS detection and EAS acceptance. Although the effective geometric area might be calculated analytically, analyzing a set of MC simulations is the only way to estimate the EAS acceptance. The acceptance is estimated by the ratio of the simulated to reconstructed events passing the quality cut. To estimate the ratio, the statistics of the simulated and reconstructed MC events that passed the quality cut are shown in Figure 4.17 on page 76. Note that the statistics of both simulated and reconstructed events passing the quality cut are weighted by the spectral index of -3.1, which is the typical value for the spectral index of Ultra-High-Energy Cosmic Rays (UHECR).

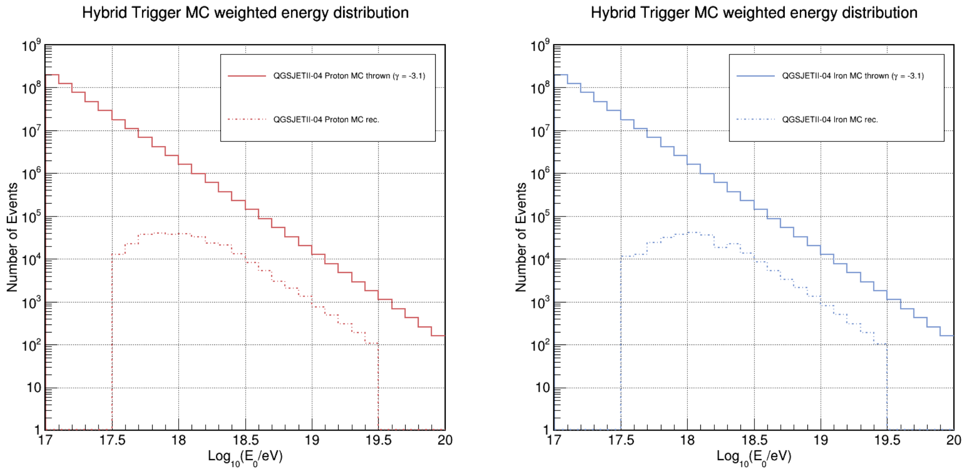

(a) Proton MC

(b) Iron-nucleus MC

Figure 4.17: (a) Weighted histograms of the number of simulated and reconstructed MC events that passed the quality cut for the proton MC simulation. (b) The same weighted histogram as in (a), but for the iron-nucleus MC simulation. All histograms are weighted by a spectral index of $\gamma = -3.1$.

From Figure 4.17 on page 76, the acceptances of the TA hybrid trigger mode for the two mass compositions are estimated as described above. The acceptances obtained here are used to estimate the aperture of the TA hybrid trigger mode. The next step is to estimate the effective geometrical area $\mathrm{A\Omega^G}$, which is formulated by the following equation:

$$\mathrm{A}\Omega^G = (\text{MC Thrown Area}) \times \int_0^{2\pi} d\phi \int_0^{\theta_{\max}} \sin\theta\cos\theta d\theta. \tag{4.11}$$

In this analysis, the MC simulation thrown area varies as a function of primary energy as shown in Table 4.3 on page 60. An asymmetric lens-shaped area for the thrown area is visualized in Figure 4.18 on page 77.

The area of the overlapping region of two circles with the radius of r and R with the distance d between two center points are calculated with Equation (4.12):

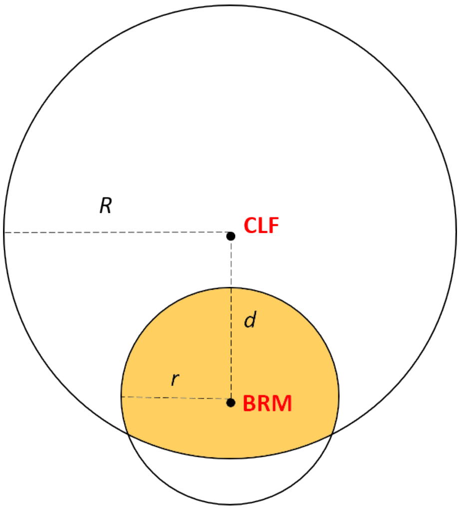

Figure 4.18: Diagram displaying the asymmetric lens-shaped thrown area of the TA hybrid trigger MC simulation. The orange-filled region indicates the thrown area of EAS core positions, which is the overlapping region of the two circles with different radii. Here, the BRM station is assumed.

$$\begin{aligned} \text{Area} = r^2 \arccos(\frac{d^2+r^2-R^2}{2dr}) \\ +R^2 \arccos(\frac{d^2+R^2-r^2}{2dR}) \\ -0.5\sqrt{(-d+r+R)(d+r-R)(d-r+R)(d+r+R)}. \end{aligned} \tag{4.12}$$

For the BRM station and the primary energy of $10^{17.4}$ eV, r is 12 km as described in Table 4.3 on page 60, R is 25 km as described in Table 4.1 on page 59, and d is 20.81 km. Then the MC thrown area is calculated to be 300.8 km^2 by Equation (4.12). Now the geometrically effective area of the solid angle is calculated using Equation (4.11) with the maximum θ of 70° as described in Table 4.1 on page 59. The geometrically effective area, in this case, is calculated to be 834.4 km^2·sr.

However, in the energy range above $10^{17.9}$ eV, the overlapping region of the two asymmetric lens-shaped areas for each FD station exists as shown in Figure 4.3 on page 60. In this case, the MC thrown area is estimated by a simplified simulation. The detail of this simplified simulation is explained below.

1. First, generate 2×10^9 points and randomly place them inside a circle of radius 25 km.
2. Next, count the number of points n that fell within the area that meets the core position conditions.
3. Then the area of the MC simulation thrown region is calculated from $\pi\times$ 25 km^2 $\times$ $\frac{n}{2\times10^9}$.
4. Finally, iterate the same simulation ten times using different random seeds to estimate the fluctuation in this method.

By using the two methods introduced above, the geometric aperture $A\Omega^{\mathrm{G}}$ as a function of energy for each FD station is estimated. Figure 4.19 on page 78

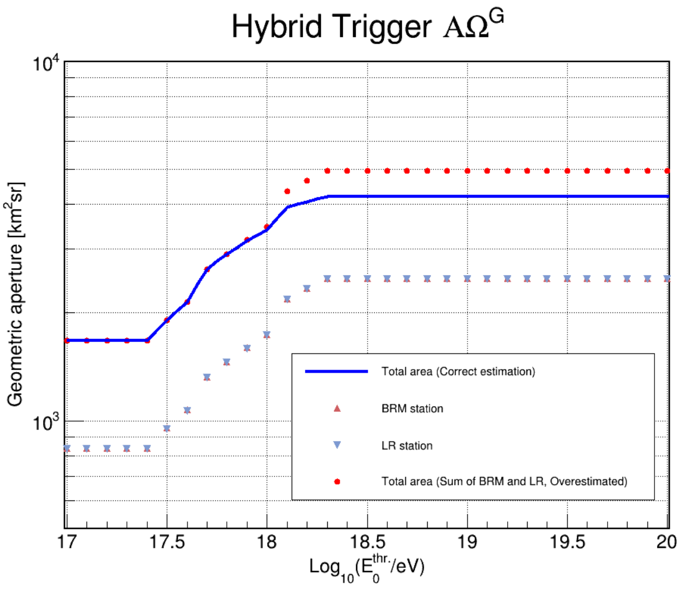

Figure 4.19: Geometric aperture $A\Omega^G$ of the BRM and LR stations, and the BRM$\bigcup$LR combined area as a function of primary energy. The solid blue line indicates the correctly combined areas and the solid red circles indicate the overestimated areas.

shows the geometric aperture for the entire energy range of the TA hybrid trigger MC simulation sets.

Now the aperture $A\Omega$ is calculated from the product of geometric aperture and the acceptance shown in Figure 4.19 on page 78 and Figure 4.17 on page 76, respectively. Then, the apertures are calculated for the BRM, LR, and BRM$\bigcup$LR stations using three types of composition models: the pure proton model, the pure iron model, and the mixed composition model.

The mixed composition model is based on the mass composition study conducted by the HiRes and HiRes/MIA experiments. This mixed composition based on the result of HiRes and HiRes/MIA experiments is also adopted in the 7-year FD monocular spectrum measurement of the TA experiment [50]. The proton fraction used in this mixed composition is indicated as a function of primary cosmic-ray energy in Figure 4.20 on page 78.

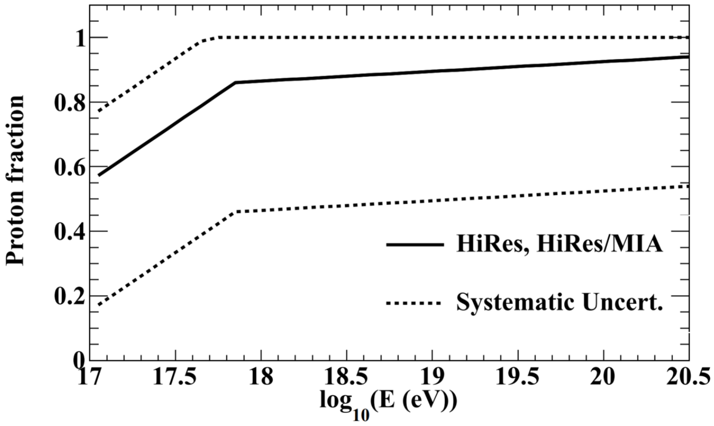

Figure 4.20: Proton fraction of UHECR measured in HiRes and HiRes/MIA experiment [50].

The aperture for the mixed composition is calculated using Equation (4.13) where f is the fraction of protons shown in Figure 4.20 on page 78 and R is $(\text{A}\Omega^{\text{IRON}}\ /\ \text{A}\Omega^{\text{PROTON}})$.

$$\text{A}\Omega^{\text{MIX}} = \text{A}\Omega^{\text{PROTON}}(R + f \times (1 - R)). \tag{4.13}$$

In this analysis, this mixed composition model is adopted to estimate the aperture of the TA hybrid trigger observation mode. The apertures of the TA hybrid trigger observation mode are shown in Figure 4.21 on page 79.

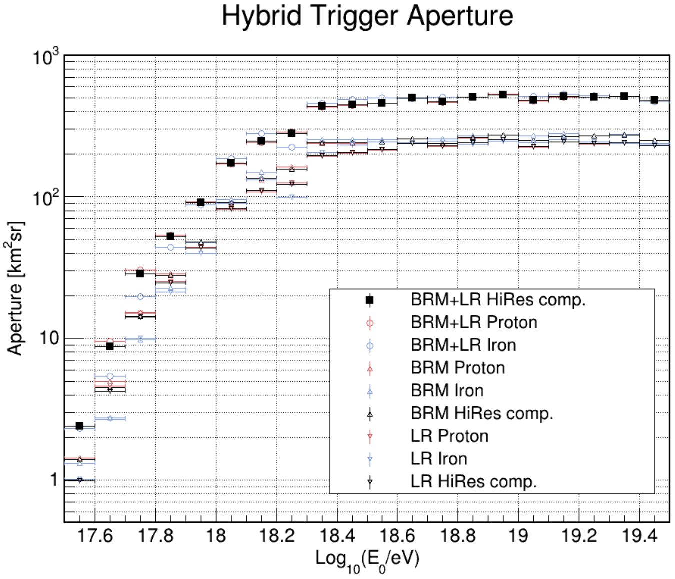

Figure 4.21: Apertures calculated for the BRM and LR stations, then BRM$\bigcup$LR combined using three types of mass compositions. The red markers indicate apertures estimated assuming pure proton UHECR. The blue markers indicate apertures estimated assuming pure iron-nucleus UHECR. The red open circles indicate the combined aperture for pure proton UHECR, and the open blue squares indicate the combined aperture for pure iron-nucleus UHECR. The black-filled squares indicate the aperture estimated using the mixed composition model.

4.4 Bias and Resolution in Reconstruction

Understanding the bias and resolution in reconstructing EAS using the TA hybrid trigger mode is important to estimate the uncertainties in reconstruction results. In this analysis, the bias and the resolution in reconstructing EAS using the TA hybrid trigger mode are estimated by comparing the value of simulated observable of an EAS with its corresponding reconstructed value for the MC events that are reconstructed and passed the quality cut.

A total of six observables are compared: θ (Zenith), ϕ (Azimuth), R_p (impact parameter), ψ, primary energy, and X_{max}. The results are shown in Figure 4.22 through 4.27 on page 80 to 85. For each comparison, a Gaussian fitting is performed on the original distribution to clarify the shape of a distribution.

From Figure 4.22 to 4.27 on page 80 to 85, it is found that some parameters do not strictly follow Gaussian distributions and show asymmetric distributions in the thrown-reconstruction comparison. This tendency is especially prominent in the reconstruction of θ and ψ for the lower energy range as shown in Figure 4.22 (a), 4.22 (b), 4.25 (a), 4.25 (b), 4.26 (a), and 4.26 (a).

A possible reason for this tendency is the contamination of Cherenkov radiation in the geometric reconstruction. As an inherent limitation of the hybrid

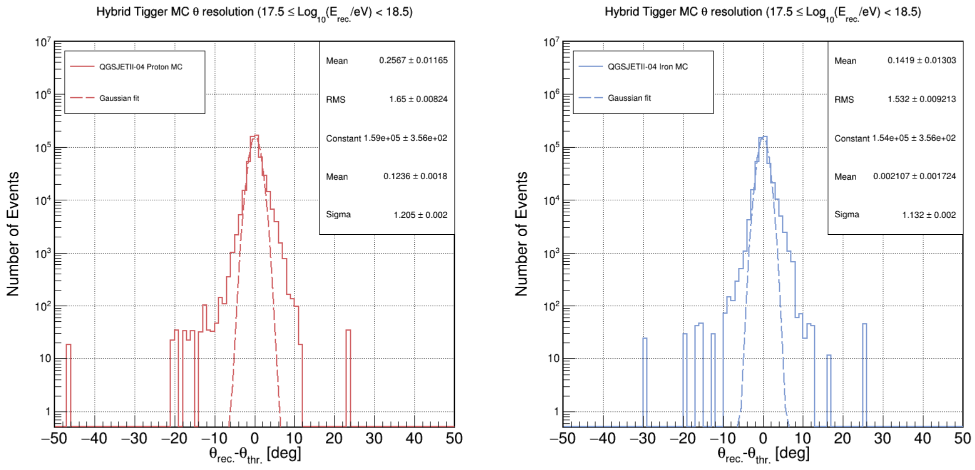

(a) Proton $17.5 \leq \mathrm{Log}_{10}(\mathrm{E}_{\mathrm{rec.}}/\mathrm{eV}) < 18.5$ (b) Iron $17.5 \leq \mathrm{Log}_{10}(\mathrm{E}_{\mathrm{rec.}}/\mathrm{eV}) < 18.5$

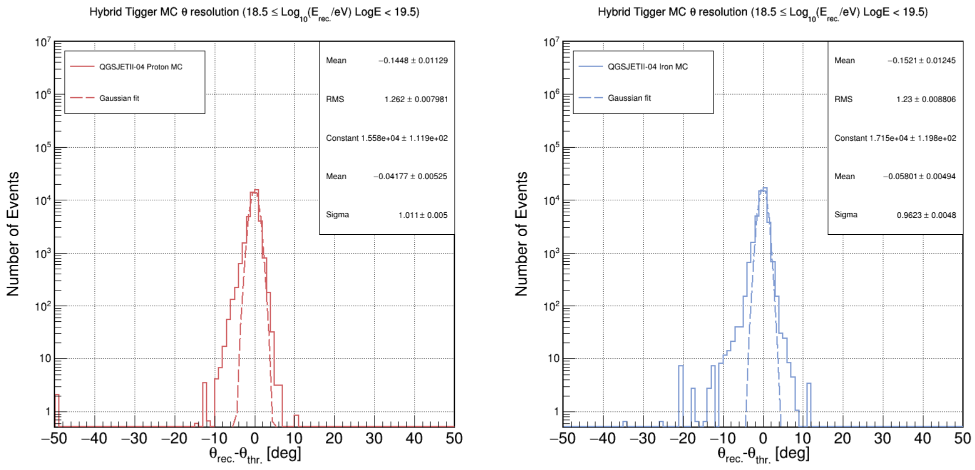

(c) Proton $18.5 \leq \mathrm{Log}_{10}(\mathrm{E}_{\mathrm{rec.}}/\mathrm{eV}) < 19.5$ (d) Iron $18.5 \leq \mathrm{Log}_{10}(\mathrm{E}_{\mathrm{rec.}}/\mathrm{eV}) < 19.5$

Figure 4.22: Bias and resolution in reconstructing θ (Zenith) estimated by $(\theta_{\mathrm{rec.}} - \theta_{\mathrm{thr.}})$ of the reconstructed events passing the quality cut. The solid lines indicate the distributions of the events and the dashed lines indicate their Gaussian fitting. The left column shows the proton MC simulation and the right column shows the iron-nucleus MC simulation. The upper row shows the lower energy range and the lower row shows the higher energy range. The statistics box on the upper-right side indicates five values: the first two values, Mean and RMS, indicate the original distribution's mean and standard deviation; the next three values, Constant, Mean, and Sigma, indicate the fitted parameters of the Gaussian fitting.

technique, the closest possible EAS core position is limited by the distance between the FD station and its corresponding SD sub-array.

Due to this condition, EAS at lower energies are more likely to be triggered and reconstructed when they are heading toward the FD station. This results in more contamination of Cherenkov radiation in the geometric reconstruction that leads to larger θ and ψ in the reconstructed EAS.

Since there are parameters that show asymmetric distributions, the bias is set at the mean value of the original distribution and the resolution is set at the RMS value of the original distribution as the worst-case scenario. The biases and resolutions for all parameters tested above are then summarized for $17.5 \leq \mathrm{Log}_{10}(\mathrm{E}_{\mathrm{rec.}}/\mathrm{eV}) < 18.5$ and $18.5 \leq \mathrm{Log}_{10}(\mathrm{E}_{\mathrm{rec.}}/\mathrm{eV}) < 19.5$ in Table 4.7 on page 81 and Table 4.8 on page 82, respectively.

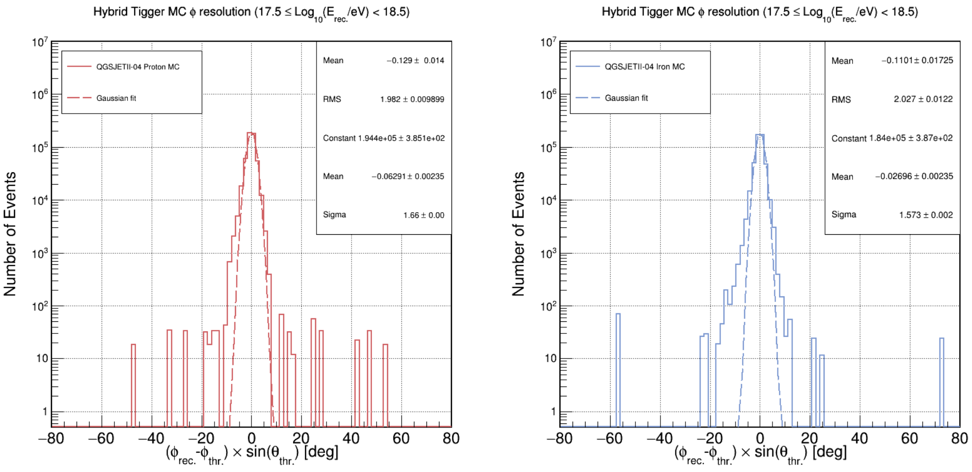

(a) Proton $17.5 \leq \mathrm{Log}_{10}(\mathrm{E}_{\mathrm{rec.}}/\mathrm{eV}) < 18.5$ (b) Iron $17.5 \leq \mathrm{Log}_{10}(\mathrm{E}_{\mathrm{rec.}}/\mathrm{eV}) < 18.5$

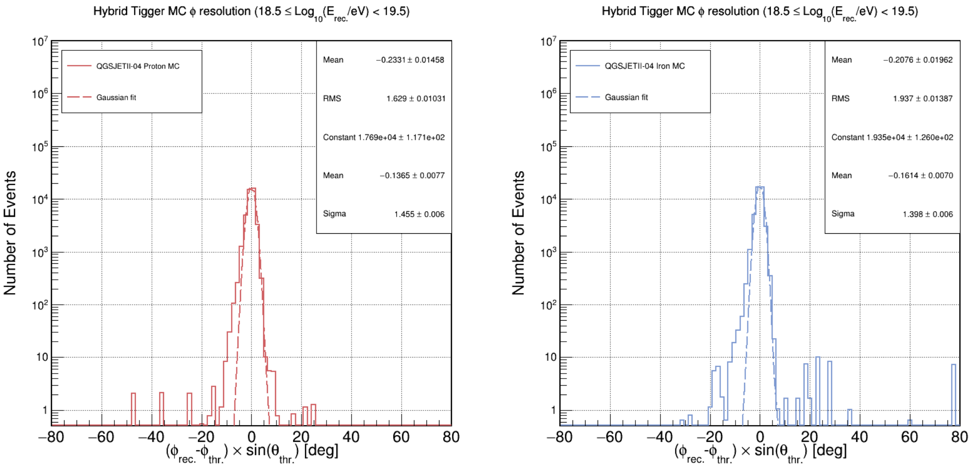

(c) Proton $18.5 \leq \mathrm{Log}_{10}(\mathrm{E}_{\mathrm{rec.}}/\mathrm{eV}) < 19.5$ (d) Iron $18.5 \leq \mathrm{Log}_{10}(\mathrm{E}_{\mathrm{rec.}}/\mathrm{eV}) < 19.5$

Figure 4.23: Bias and resolution in reconstructing ϕ (Azimuth) estimated by $(\phi_{\mathrm{rec.}} - \phi_{\mathrm{thr.}}) \times \sin\theta_{\mathrm{thr.}}$ of the reconstructed events passing the quality cut. The details are the same as in Figure 4.22.

Table 4.7: Summary of biases and resolutions in reconstructing the six parameters in the energy range of $17.5 \leq \mathrm{Log}_{10}(\mathrm{E}_{\mathrm{rec.}}/\mathrm{eV}) < 18.5$.

Parameter	Proton bias	Proton res.	Iron bias	Iron res.
θ (deg)	0.3	1.7	0.1	1.5
ϕ (deg)	-0.1	2.0	-0.1	2.0
$\mathrm{R_p}$ (%)	1.2	2.5	1.1	2.4
ψ (deg)	0.7	2.4	0.7	2.3
Primary energy (%)	12	13	-2.1	8.2
$\mathrm{X_{max}}$ (g/cm^2)	-15	31	-13	27

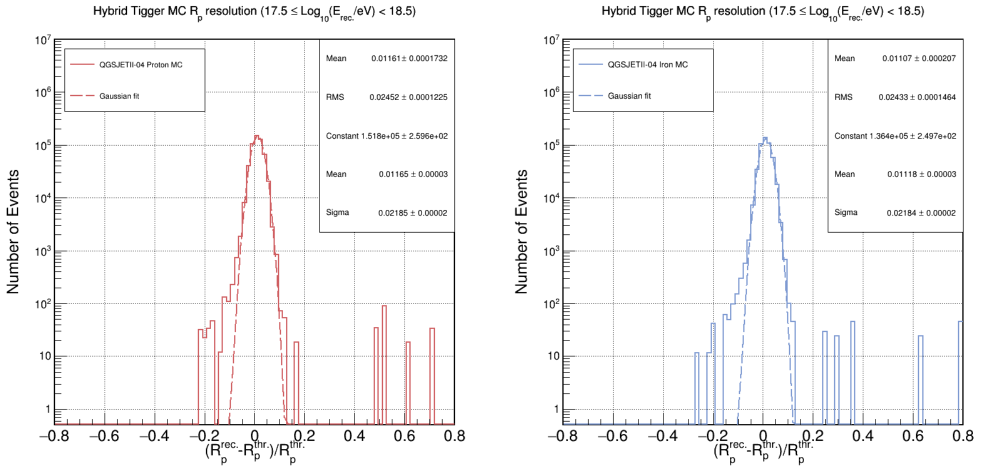

(a) Proton $17.5 \leq \mathrm{Log}_{10}(\mathrm{E}_{\mathrm{rec.}}/\mathrm{eV}) < 18.5$ (b) Iron $17.5 \leq \mathrm{Log}_{10}(\mathrm{E}_{\mathrm{rec.}}/\mathrm{eV}) < 18.5$

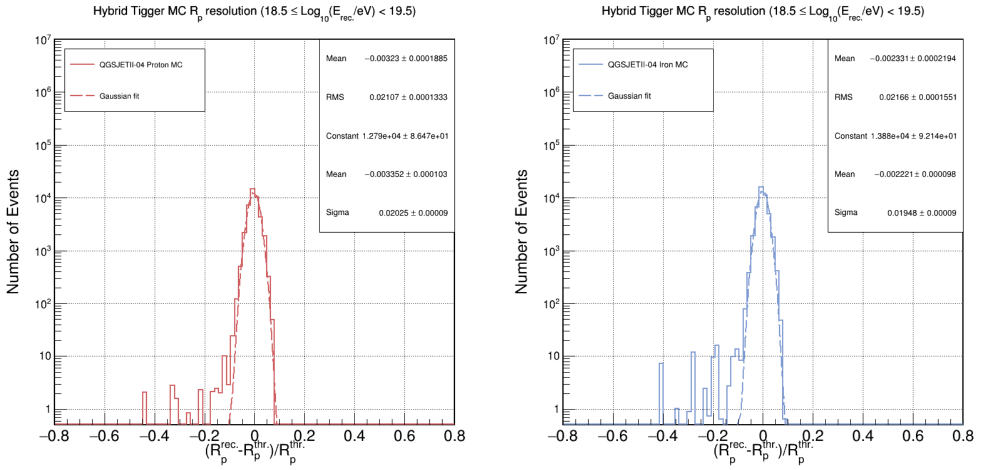

(c) Proton $18.5 \leq \mathrm{Log}_{10}(\mathrm{E}_{\mathrm{rec.}}/\mathrm{eV}) < 19.5$ (d) Iron $18.5 \leq \mathrm{Log}_{10}(\mathrm{E}_{\mathrm{rec.}}/\mathrm{eV}) < 19.5$

Figure 4.24: Bias and resolution in reconstructing $\mathrm{R_p}$ (impact parameter) estimated by ($\mathrm{R_p^{rec.}}$ - $\mathrm{R_p^{thr.}}$) / $\mathrm{R_p^{thr.}}$ of the reconstructed events passing the quality cut. The details are the same as in Figure 4.22.

Table 4.8: Same as in Table 4.7 on page 81, but in the energy range of $18.5 \leq \mathrm{Log}_{10}(\mathrm{E}_{\mathrm{rec.}}/\mathrm{eV}) < 19.5$.

Parameter	Proton bias	Proton res.	Iron bias	Iron res.
θ (deg)	-0.1	1.3	-0.2	1.2
ϕ (deg)	-0.2	1.6	-0.2	1.9
$\mathrm{R_p}$ (%)	-0.3	2.1	-0.2	2.2
ψ (deg)	-0.8	1.8	-0.7	2.0
Primary energy (%)	2.7	8.3	-6.3	5.5
$\mathrm{X_{max}}$ (g/cm^2)	-4.5	28	-8.4	22

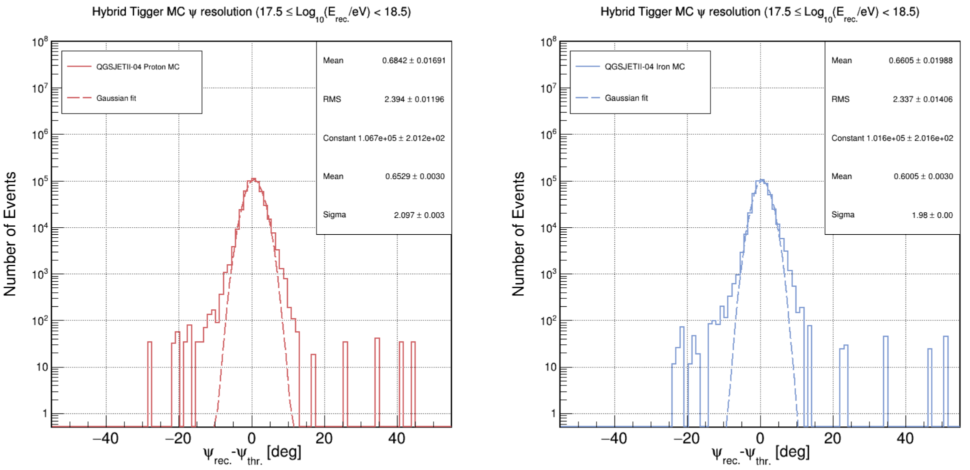

(a) Proton 17.5 $\leq$ Log$_{10}$(E$_{\text{rec.}}$/eV) $<$ 18.5

(b) Iron 17.5 $\leq$ Log$_{10}$(E$_{\text{rec.}}$/eV) $<$ 18.5

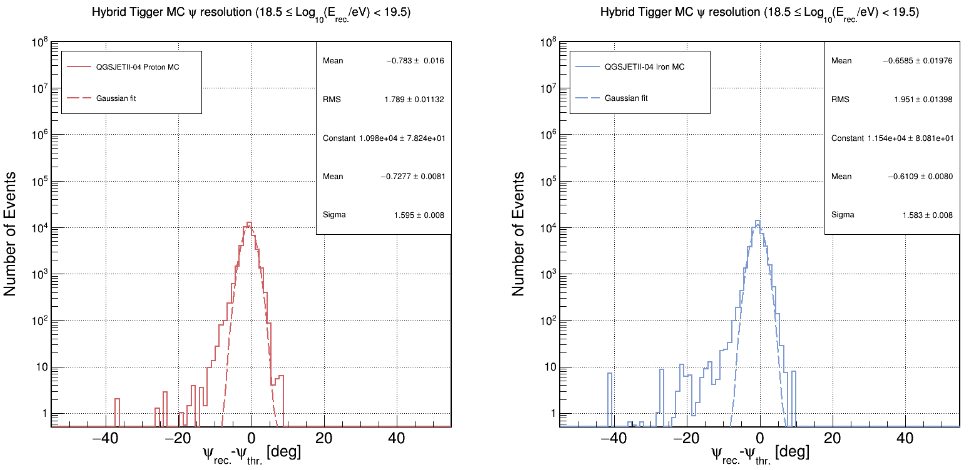

(c) Proton 18.5 $\leq$ Log$_{10}$(E$_{\text{rec.}}$/eV) $<$ 19.5

(d) Iron 18.5 $\leq$ Log$_{10}$(E$_{\text{rec.}}$/eV) $<$ 19.5

Figure 4.25: Bias and resolution in reconstructing ψ estimated by ($\psi_{\text{rec.}}$ - $\psi_{\text{thr.}}$) of the reconstructed events passing the quality cut. The details are the same as in Figure 4.22.

Table 4.7 on page 81 and Table 4.8 on page 82 show that the reconstruction resolutions of the primary energy and X$_{\text{max}}$ in the TA hybrid trigger mode are 13% and 31 g/cm^2 at the lower energy range, respectively, and 8.3% and 28 g/cm^2 at the higher energy range, respectively. These estimation results are a significant improvement compared to the typical reconstruction resolutions of the FD monocular observation mode, which is 17% for the primary energy and 72 g/cm^2 for X$_{\text{max}}$, respectively [50]. The biases and resolutions for each energy bin are also estimated for the six parameters tested above. The results are shown in Figure 4.28 on page 86 through Figure 4.30 on page 88.

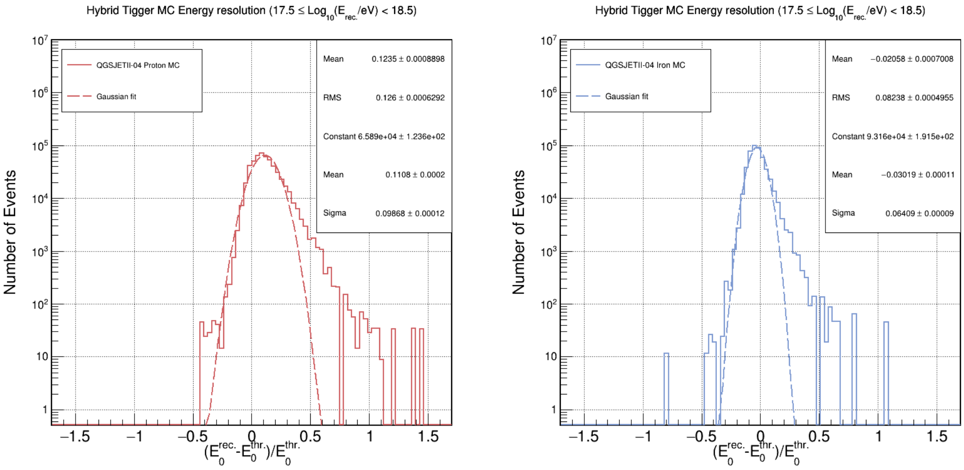

(a) Proton $17.5 \leq \mathrm{Log}_{10}(\mathrm{E}_{\mathrm{rec.}}/\mathrm{eV}) < 18.5$ (b) Iron $17.5 \leq \mathrm{Log}_{10}(\mathrm{E}_{\mathrm{rec.}}/\mathrm{eV}) < 18.5$

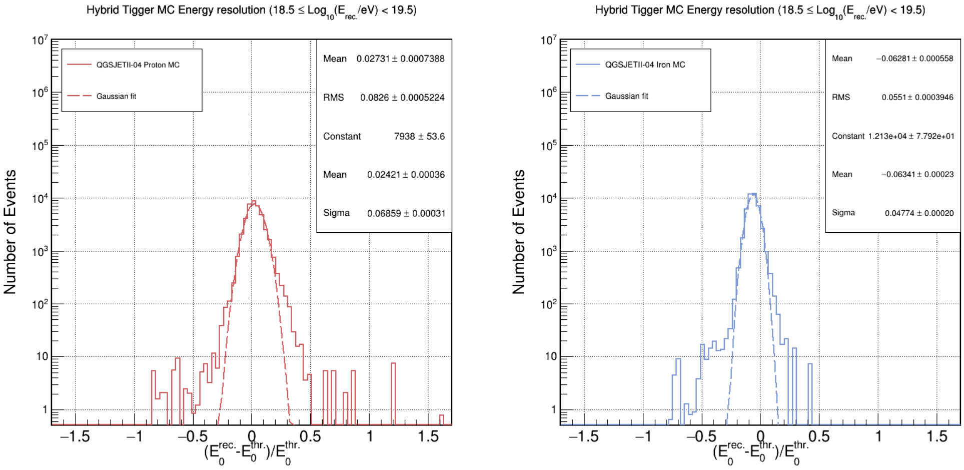

(c) Proton $18.5 \leq \mathrm{Log}_{10}(\mathrm{E}_{\mathrm{rec.}}/\mathrm{eV}) < 19.5$ (d) Iron $18.5 \leq \mathrm{Log}_{10}(\mathrm{E}_{\mathrm{rec.}}/\mathrm{eV}) < 19.5$

Figure 4.26: Bias and resolution in reconstructing primary energy estimated by $(\mathrm{E}_0^{\mathrm{rec.}} - \mathrm{E}_0^{\mathrm{thr.}}) / \mathrm{E}_0^{\mathrm{thr.}}$ of the reconstructed events passing the quality cut. The details are the same as in Figure 4.22.

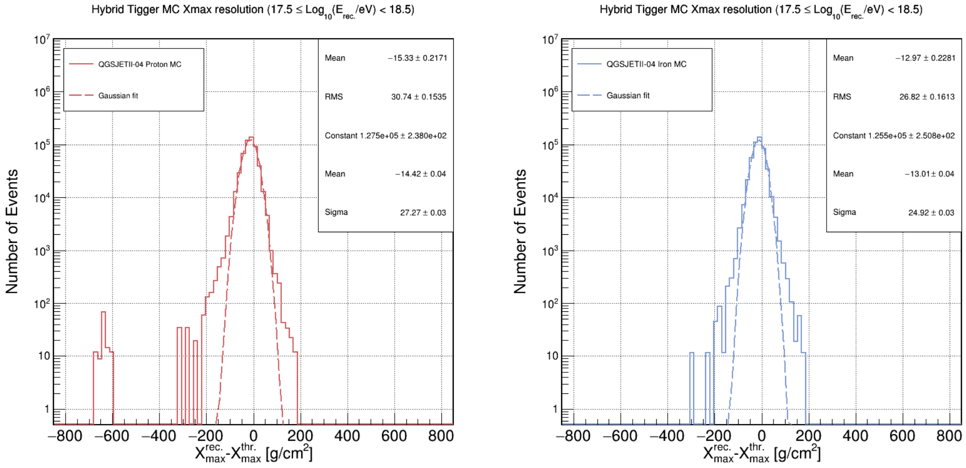

(a) Proton 17.5 $\leq$ $\mathrm{Log_{10}(E_{rec.}/eV)} < 18.5$ (b) Iron 17.5 $\leq$ $\mathrm{Log_{10}(E_{rec.}/eV)} < 18.5$

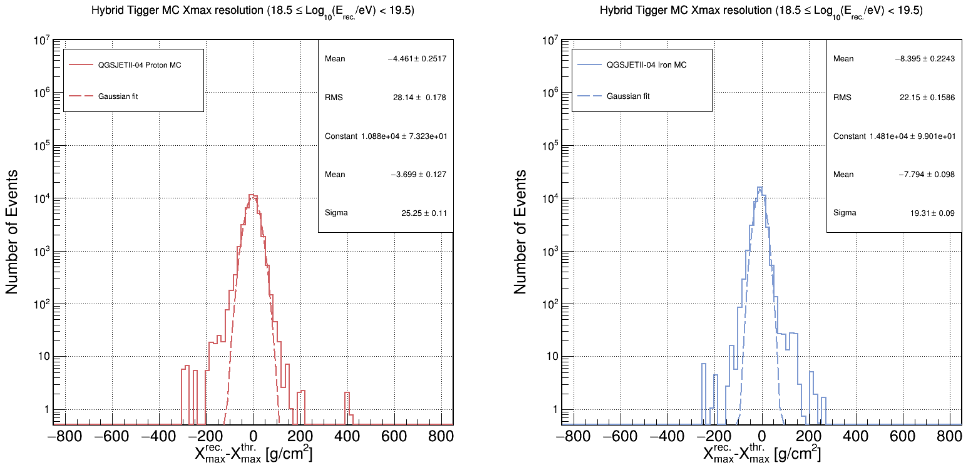

(c) Proton 18.5 $\leq$ $\mathrm{Log_{10}(E_{rec.}/eV)} < 19.5$ (d) Iron 18.5 $\leq$ $\mathrm{Log_{10}(E_{rec.}/eV)} < 19.5$

Figure 4.27: Bias and resolution in reconstructing $\mathrm{X_{max}}$ estimated by ($\mathrm{X_{max}^{rec.}}$ - $\mathrm{X_{max}^{thr.}}$) of the reconstructed events passing the quality cut. The details are the same as in Figure 4.22.

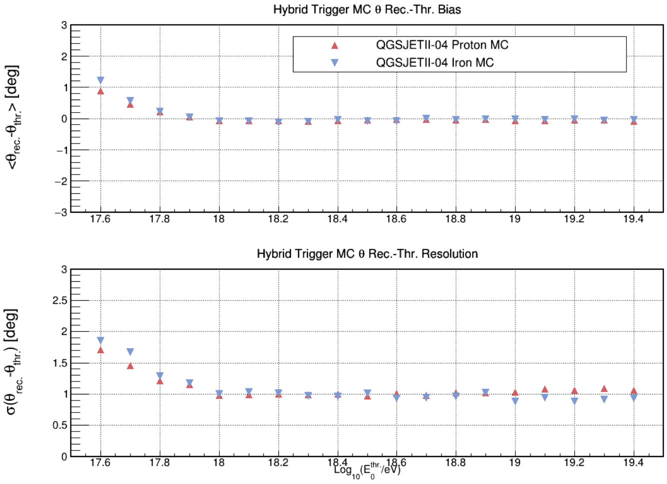

(a) θ (Zenith)

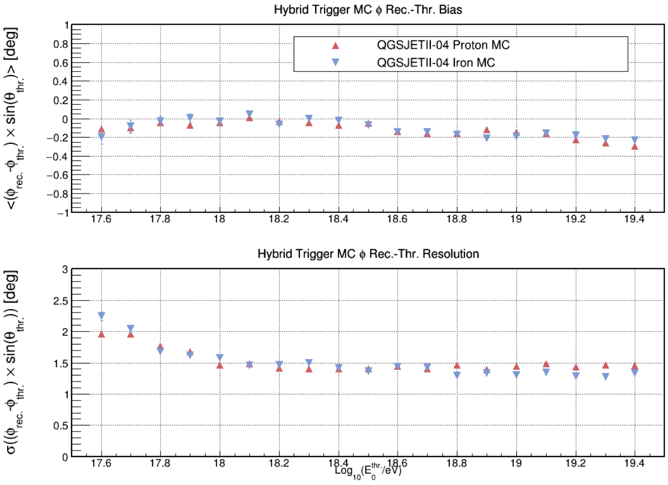

(b) ϕ (Azimuth)

Figure 4.28: (a) Bias and resolution in reconstructing θ (Zenith) for each energy bin. (b) Bias and resolution in reconstructing ϕ (Azimuth) for each energy bin. The upper panel indicates the biases. The lower panel indicates the resolutions. The horizontal axis represents the thrown energy of the simulated UHECR.

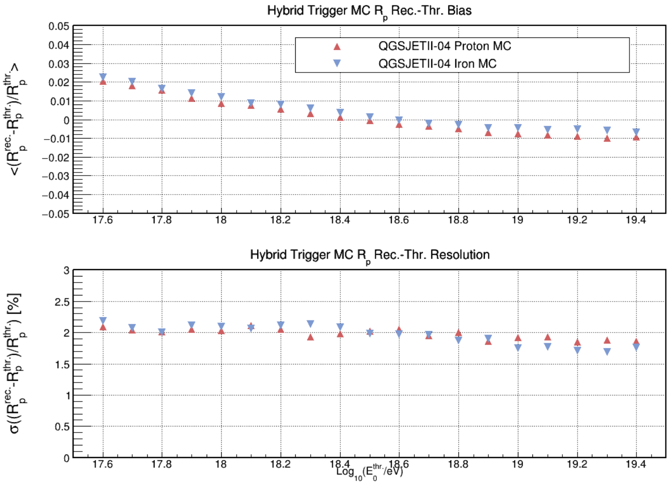

(a) $\mathrm{R_p}$ (impact parameter)

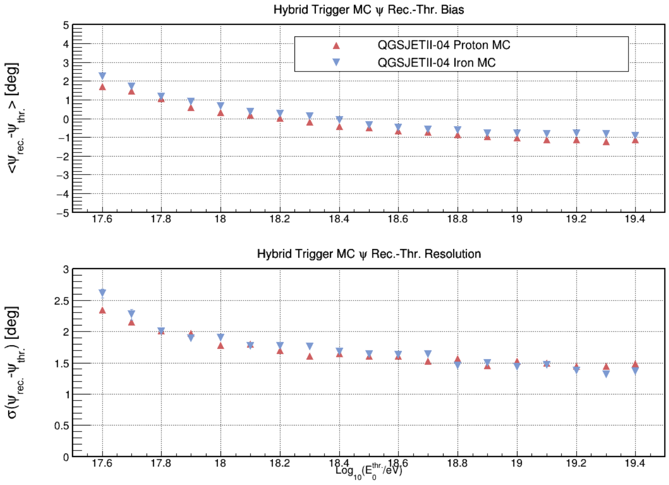

(b) ψ

Figure 4.29: (a) Bias and resolution in reconstructing $\mathrm{R_p}$ (impact parameter) for each energy bin. (b) Bias and resolution in reconstructing ψ for each energy bin. The upper panel indicates the biases. The lower panel indicates the resolutions. The horizontal axis represents the thrown energy of the simulated UHECR.

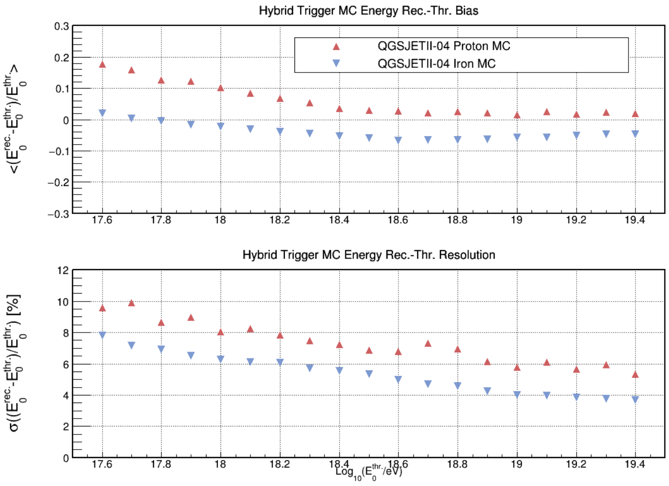

(a) Primary energy

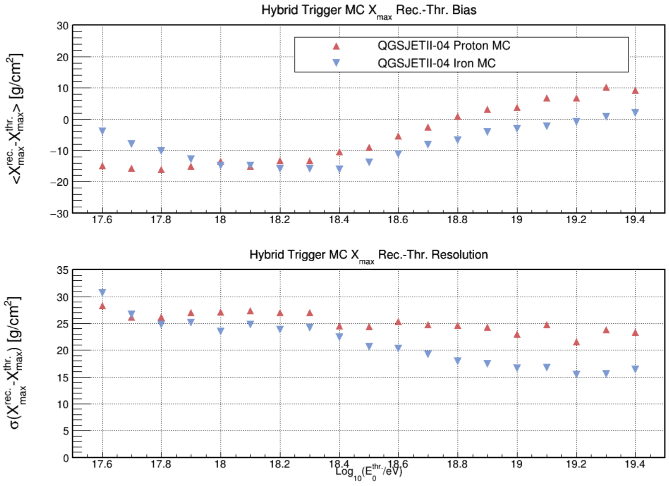

(b) $\mathrm{X}_{\mathrm{max}}$

Figure 4.30: (a) Bias and resolution in reconstructing primary energy for each energy bin. (b) Bias and resolution in reconstructing $\mathrm{X}_{\mathrm{max}}$ for each energy bin. The upper panel indicates the biases. The lower panel indicates the resolutions. The horizontal axis represents the thrown energy of the simulated UHECR.

Chapter 5

Observation Results

Chapter 5 presents a detailed analysis of the observation data acquired during the operational period of the hybrid trigger system of the Telescope Array (TA) experiment, spanning over 8.5 years from October 8th, 2010, through June 30th, 2019. This chapter will cover various aspects of the observation results, including the number of Ultra-High-Energy Cosmic Ray (UHECR) events, data/Monte Carlo (MC) comparison, combined exposure estimation, energy spectrum measurement, X_{max} measurement, systematic uncertainties, and a comparison with other measurements.

5.1 Observation Dataset

Throughout the 8.5-year observation period, the hybrid triggers were issued a total of 90,301 times, with 42,400 triggers for the Black Rock Mesa (BRM) station and 47,901 triggers for the Long Ridge (LR) station. The observation was conducted explicitly under clear weather conditions with low cloud coverage, and the selection of suitable observation periods was based on the WEAT code log data. The WEAT code, an operator-based cloud coverage log protocol, involved regular checks of cloud coverage in the North, South, East, and West directions of the sky by the Middle Drum (MD) station operator. The corresponding observation data were filtered out if cloud coverage was confirmed in both the east and south directions, as the BRM and LR stations are located East and South of the MD station, respectively.

After applying the weather selection criteria, the reconstruction principle described in Section 3.3, the pre-reconstruction steps detailed in Section 4.2.1 and 4.2.2, and the quality cut outlined in Section 4.2.4, a dataset comprising a total of 7,489 events remained. Among these events, 3,812 were recorded by the BRM station, while 3,677 were recorded by the LR station. A summary of the event statistics obtained during the 8.5-year observation period is presented in Table 5.1 on page 90.

The primary energy distribution of the 7,489 observed events is illustrated in Figure 5.1 on page 90, allowing for an examination of the energy range and distribution. Moreover, Table 5.2 on page 92 provides a detailed breakdown of the exact number of observed events within each energy bin. The Extensive Air Shower (EAS) core position distribution of the observed events is depicted in Figure 5.2 on page 91, shedding light on the spatial characteristics of the recorded events.

Table 5.1: Summary of the event statistics of the 8.5-year observations obtained by the BRM and LR stations. The ratios of passed events per stage are indicated.

Criterion	Number(BRM)	Ratio(BRM)	Number(LR)	Ratio(LR)
Total triggered	42,400	100%	47,901	100%
Geometry recon.	13,946	32.9%	12,315	25.7%
Profile recon.	13,506	31.9%	11,924	24.9%
PMT number cut	12,945	30.5%	11,255	23.5%
Track length cut	12,607	29.7%	10,939	22.8%
θ cut	11,359	26.8%	9,725	20.3%
Minimum viewing angle cut	9,184	21.7%	7,998	16.7%
$X_{\max}$ bracketing	6,970	16.4%	6,809	14.2%
Fiducial volume cut	4,544	10.7%	4,543	9.5%
Energy cut	4,487	10.6%	4,462	9.3%
Border cut	3,812	9.0%	3,677	7.7%

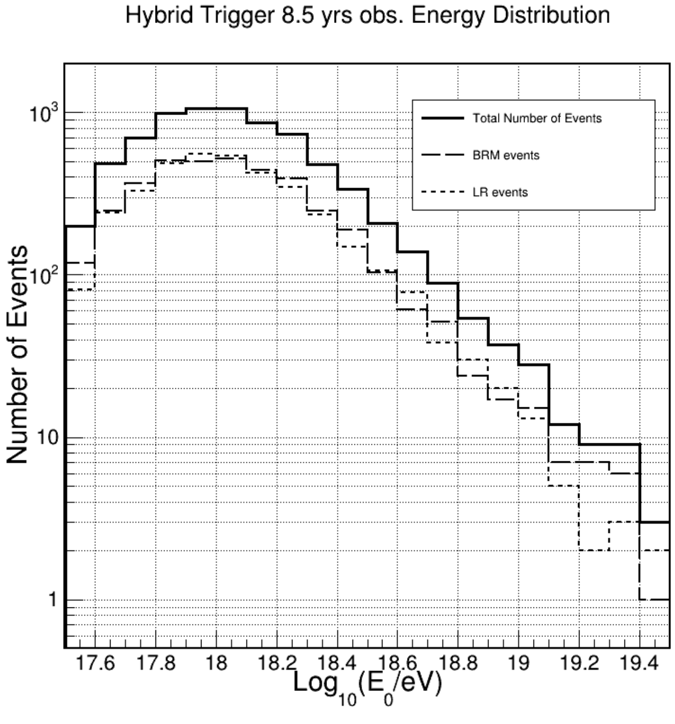

Figure 5.1: Primary energy distribution of UHECR events of the 8.5-year observation period. The solid line indicates the distribution of the events observed by both Fluorescence Detector (FD) stations. The dashed and dotted lines indicate the distributions of the events observed by the BRM and LR stations, respectively.

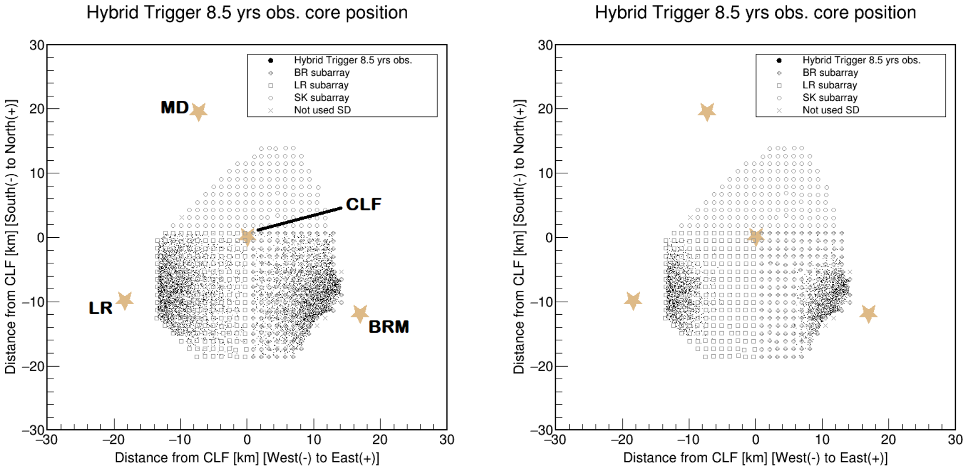

(a) Observed all energy ranges (b) Observed $17.5 \leq \mathrm{Log_{10}(E_0/eV)} < 18.0$

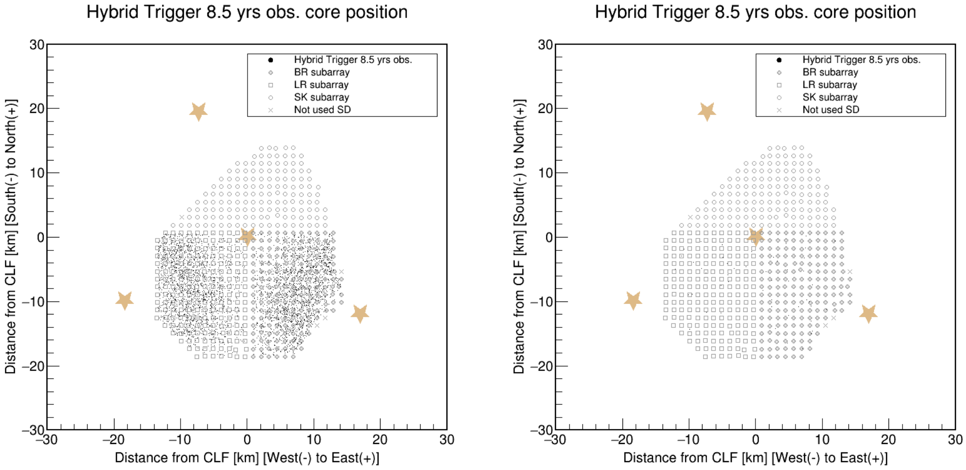

(c) Observed $18.0 \leq \mathrm{Log_{10}(E_0/eV)} < 19.0$ (d) Observed $19.0 \leq \mathrm{Log_{10}(E_0/eV)} < 19.5$

Figure 5.2: EAS core position distributions of observed UHECR events obtained in the 8.5-year observation period. The energy ranges of plots are: (a) all energies, (b) $17.5 \leq \mathrm{Log_{10}(E_0/eV)} < 18.0$, (c) $18.0 \leq \mathrm{Log_{10}(E_0/eV)} < 19.0$, and (d) $19.0 \leq \mathrm{Log_{10}(E_0/eV)} < 19.5$.

Table 5.2: Number of UHECR events per energy bin in 8.5-year observations using the TA hybrid trigger mode.

Primary Energy	Number of Events
$17.5 \leq \mathrm{Log}_{10}(\mathrm{E}_0/\mathrm{eV}) < 17.6$	199
$17.6 \leq \mathrm{Log}_{10}(\mathrm{E}_0/\mathrm{eV}) < 17.7$	475
$17.7 \leq \mathrm{Log}_{10}(\mathrm{E}_0/\mathrm{eV}) < 17.8$	706
$17.8 \leq \mathrm{Log}_{10}(\mathrm{E}_0/\mathrm{eV}) < 17.9$	985
$17.9 \leq \mathrm{Log}_{10}(\mathrm{E}_0/\mathrm{eV}) < 18.0$	1,060
$18.0 \leq \mathrm{Log}_{10}(\mathrm{E}_0/\mathrm{eV}) < 18.1$	1,055
$18.1 \leq \mathrm{Log}_{10}(\mathrm{E}_0/\mathrm{eV}) < 18.2$	858
$18.2 \leq \mathrm{Log}_{10}(\mathrm{E}_0/\mathrm{eV}) < 18.3$	743
$18.3 \leq \mathrm{Log}_{10}(\mathrm{E}_0/\mathrm{eV}) < 18.4$	478
$18.4 \leq \mathrm{Log}_{10}(\mathrm{E}_0/\mathrm{eV}) < 18.5$	341
$18.5 \leq \mathrm{Log}_{10}(\mathrm{E}_0/\mathrm{eV}) < 18.6$	209
$18.6 \leq \mathrm{Log}_{10}(\mathrm{E}_0/\mathrm{eV}) < 18.7$	138
$18.7 \leq \mathrm{Log}_{10}(\mathrm{E}_0/\mathrm{eV}) < 18.8$	90
$18.8 \leq \mathrm{Log}_{10}(\mathrm{E}_0/\mathrm{eV}) < 18.9$	54
$18.9 \leq \mathrm{Log}_{10}(\mathrm{E}_0/\mathrm{eV}) < 19.0$	37
$19.0 \leq \mathrm{Log}_{10}(\mathrm{E}_0/\mathrm{eV}) < 19.1$	28
$19.1 \leq \mathrm{Log}_{10}(\mathrm{E}_0/\mathrm{eV}) < 19.2$	12
$19.2 \leq \mathrm{Log}_{10}(\mathrm{E}_0/\mathrm{eV}) < 19.3$	9
$19.3 \leq \mathrm{Log}_{10}(\mathrm{E}_0/\mathrm{eV}) < 19.4$	9
$19.4 \leq \mathrm{Log}_{10}(\mathrm{E}_0/\mathrm{eV}) < 19.5$	3

5.2 Data/MC Comparison

A crucial step in the analysis of the TA hybrid trigger mode is the data/MC comparison, which involves comparing the distributions of various observables obtained from MC simulations with the 8.5 years of observation data. This comparison aims to ensure that the MC simulations generated in Section 4.1 accurately describe the observed events and also ensure that the simulated detectors accurately replicate the behavior of the actual detectors. To achieve this, both the MC events and observed events are processed using the same reconstruction procedure described in Section 3.3 and Section 4.2, and the identical quality cut described in Section 4.2.4 is applied.

The results of the data/MC comparison are presented in Figure 5.3 - 5.18, spanning pages 93 - 99. Each data/MC comparison plot displays three distributions of a single observable: one for proton MC events, another for iron-nucleus MC events, and the other one for the observation data. The upper part of each plot showcases the distributions of the observable. It is important to note that the distributions of the MC simulation events are normalized to the total number of observed events.

Additionally, the lower part of each plot illustrates the bin-to-bin ratios between the MC simulation events and the observation data. This ratio is obtained by dividing the number of entries in the observation data by the number of entries in the corresponding bin of the MC simulation. For example, if the MC simulation events have twice as many entries as the observation data in a specific bin, the ratio for that bin is 0.5. In the plots, the solid red lines represent the proton MC events, the solid blue lines represent the iron-nucleus MC events, and the solid black lines represent the observation data. These comparisons provide an essential validation of the MC simulations and their agreement with the observed data.

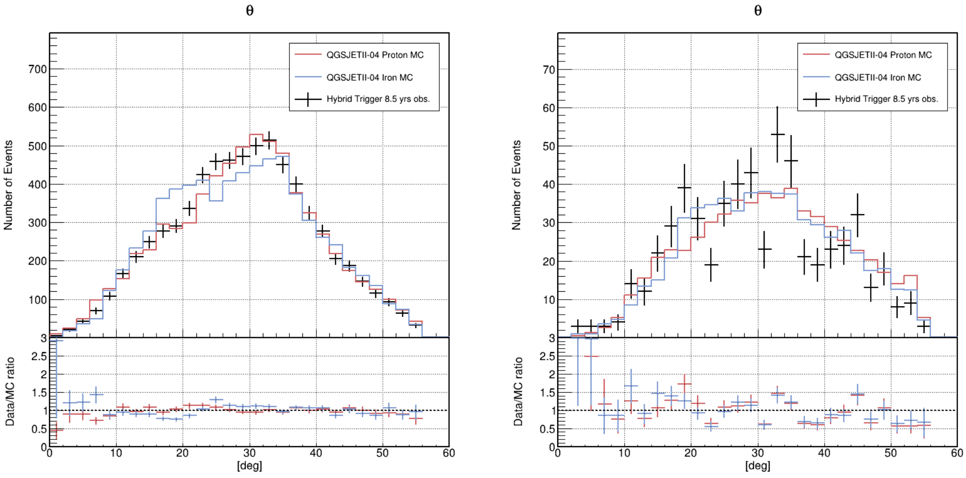

(a) $17.5 \le \mathrm{Log}_{10}(\mathrm{E}_0/\mathrm{eV}) < 18.5$ (b) $18.5 \le \mathrm{Log}_{10}(\mathrm{E}_0/\mathrm{eV}) < 19.5$

Figure 5.3: Data/MC comparison of θ (Zenith) in the energy range from (a) $10^{17.5}$ eV to $10^{18.5}$ eV and from (b) $10^{18.5}$ eV to $10^{19.5}$ eV.

The MC simulations are in fair agreement with the observation data, while an exception is found in the distribution of the number of good PMTs in Figure 5.12 (a) on page 97. The numbers of good PMTs are larger in both the proton and the iron-nucleus MC simulation sets than in the observed events. This result is the same as in that reported by the TA FD monocular analysis, which discusses the

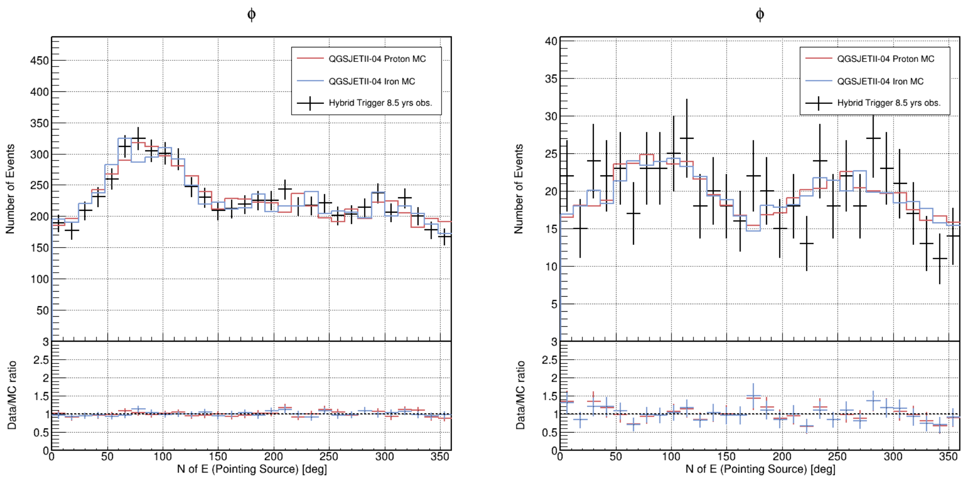

(a) $17.5 \leq \text{Log}_{10}(\text{E}_0/\text{eV}) < 18.5$ (b) $18.5 \leq \text{Log}_{10}(\text{E}_0/\text{eV}) < 19.5$

Figure 5.4: Data/MC comparison of ϕ (Azimuth). ϕ is in the North of East, pointing back to the source direction that the EAS comes. The North of East is a counter-clockwise azimuthal degree system with: East=0°, North=90°, West=180°, South=270°. For example, 90° indicates the EAS is coming from the north direction and propagating to the south direction.

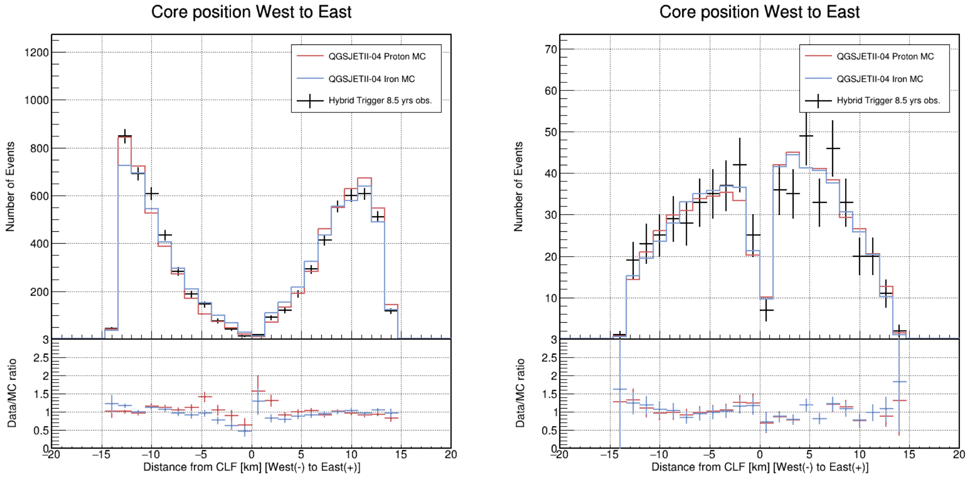

(a) $17.5 \leq \text{Log}_{10}(\text{E}_0/\text{eV}) < 18.5$ (b) $18.5 \leq \text{Log}_{10}(\text{E}_0/\text{eV}) < 19.5$

Figure 5.5: Data/MC comparison of EAS core positions (West to East) shown in two energy ranges.

discrepancy arising from the model-reality difference in the lateral development of EAS [31]. The effect of this discrepancy is estimated in Section 5.7.5 and added to the systematic uncertainties of this TA hybrid trigger analysis.

The EAS reconstruction resolutions of the TA hybrid trigger mode are presented using the MC simulations described in Section 4.4. Still, it is important to estimate the resolutions of the EAS reconstruction independently from the MC simulations. Such an estimation is possible using specific EAS events reconstructed separately by both FD stations, called stereoscopic events. Since the reconstruction procedure is performed independently by each FD station in such stereoscopic events, the difference in the reconstructed observables of the same EAS carries the information about the resolution of the EAS reconstruction in the TA hybrid trigger mode. This difference $\sigma_{\text{BRM+LR}}$ is the square root of the

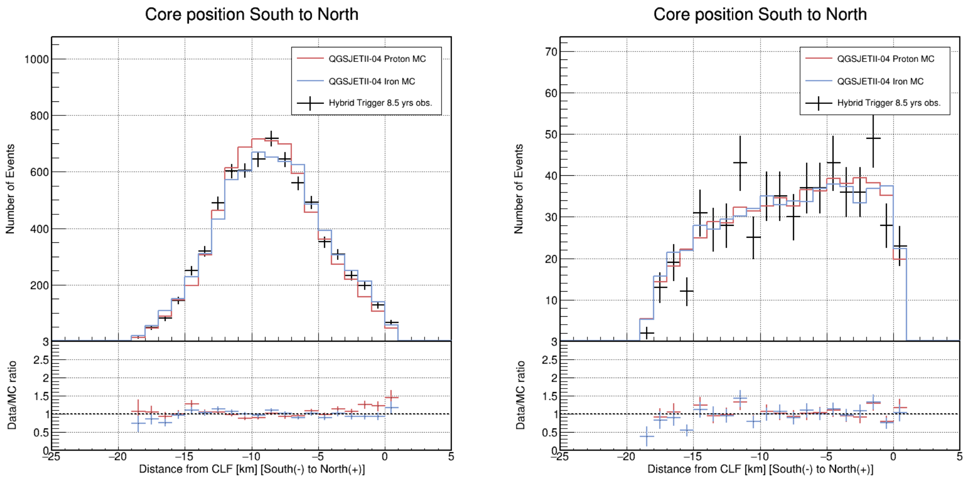

(a) $17.5 \leq \mathrm{Log}_{10}(\mathrm{E}_0/\mathrm{eV}) < 18.5$

(b) $18.5 \leq \mathrm{Log}_{10}(\mathrm{E}_0/\mathrm{eV}) < 19.5$

Figure 5.6: Data/MC comparison of EAS core positions (South to North) shown in two energy ranges.

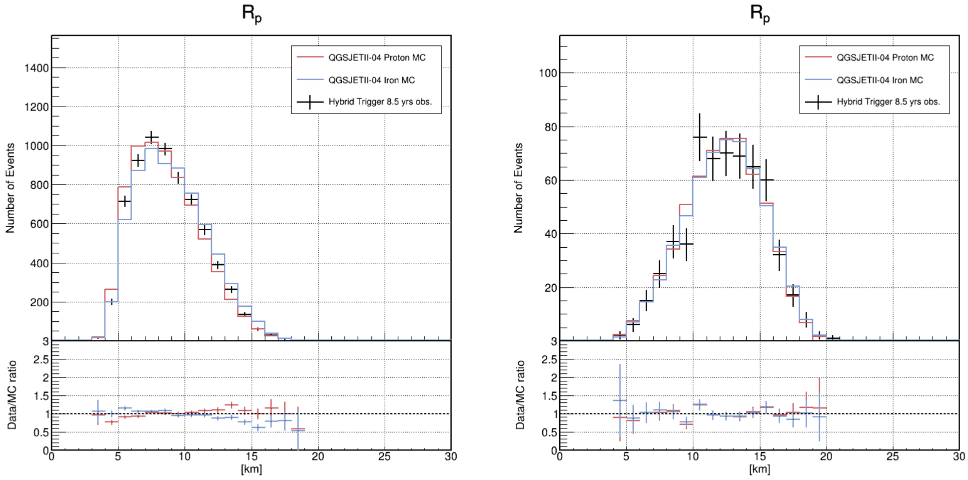

(a) $17.5 \leq \mathrm{Log}_{10}(\mathrm{E}_0/\mathrm{eV}) < 18.5$

(b) $18.5 \leq \mathrm{Log}_{10}(\mathrm{E}_0/\mathrm{eV}) < 19.5$

Figure 5.7: Data/MC comparison of $\mathrm{R_p}$ (impact parameter) shown in two energy ranges.

quadratic sum of the resolutions for each station as written in Equation (5.1):

$$\sigma_{\mathrm{BRM+LR}} = \sqrt{\sigma^2_{\mathrm{BRM}} + \sigma^2_{\mathrm{LR}}}. \tag{5.1}$$

Based on the assumption that the resolutions of reconstruction for the BRM station and the LR station are expected to be the same ($\sigma_{\mathrm{BRM}} = \sigma_{\mathrm{LR}}$) due to the identical instruments, calibration principles, and analysis procedures, the resolution of the reconstruction can be estimated as $(\sigma_{\mathrm{BRM+LR}})/\sqrt{2}$.

By comparing the pairs of reconstructed energy and $\mathrm{X_{max}}$ of 32 stereoscopic events observed over 8.5 years using the TA hybrid trigger mode, the resolution of the reconstruction is found to be 9.8% for the primary energy and 21.4 g/cm^2 for $\mathrm{X_{max}}$. However, it is important to note that this estimation method is based on a subset of the data and does not cover the entire energy range of the analysis, which spans from $10^{17.5}$ eV to $10^{19.5}$ eV.

It is seen that the higher the primary energy, the better the resolution. This

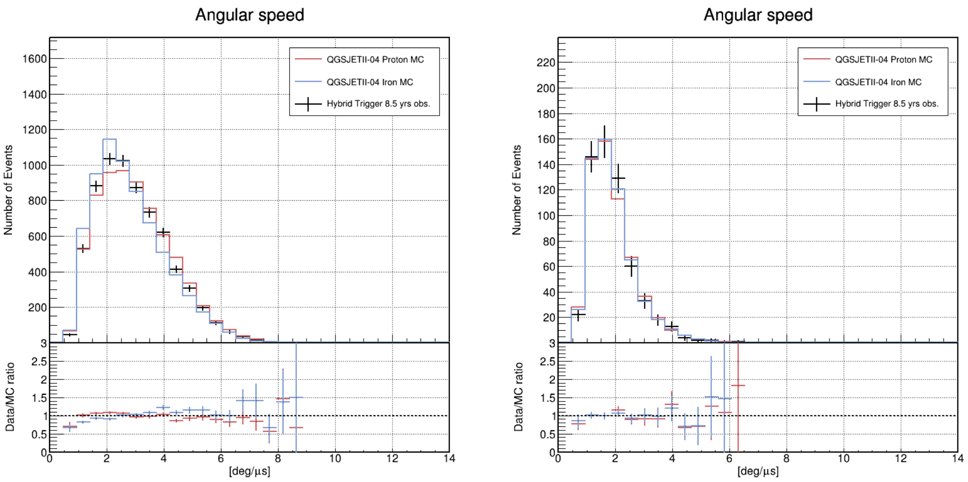

(a) $17.5 \leq \mathrm{Log}_{10}(\mathrm{E}_0/\mathrm{eV}) < 18.5$ (b) $18.5 \leq \mathrm{Log}_{10}(\mathrm{E}_0/\mathrm{eV}) < 19.5$

Figure 5.8: Data/MC comparison of angular speed shown in two energy ranges.

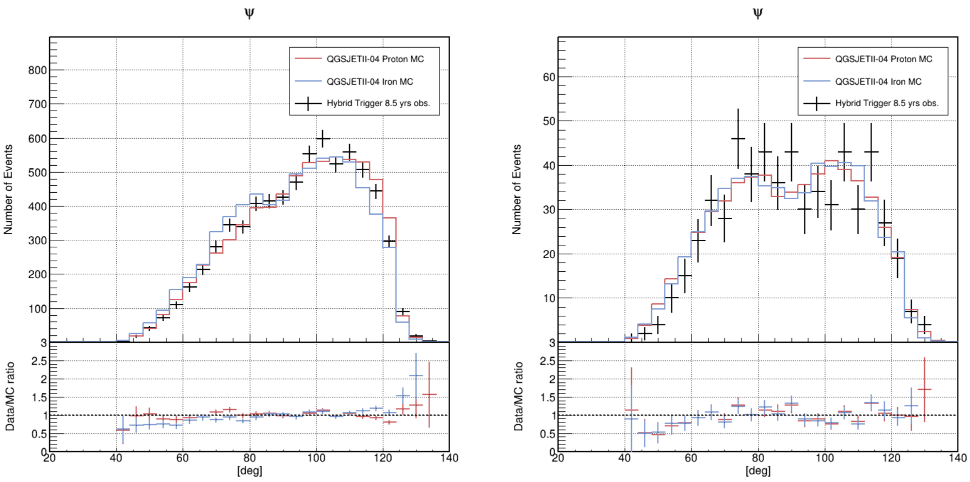

(a) $17.5 \leq \mathrm{Log}_{10}(\mathrm{E}_0/\mathrm{eV}) < 18.5$ (b) $18.5 \leq \mathrm{Log}_{10}(\mathrm{E}_0/\mathrm{eV}) < 19.5$

Figure 5.9: Data/MC comparison of ψ (SDP angle) shown in two energy ranges.

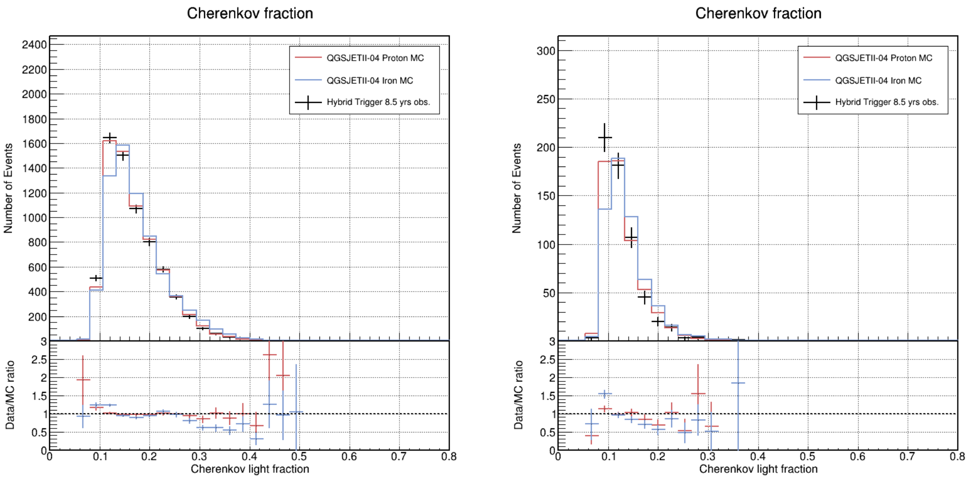

(a) $17.5 \leq \mathrm{Log}_{10}(\mathrm{E}_0/\mathrm{eV}) < 18.5$ (b) $18.5 \leq \mathrm{Log}_{10}(\mathrm{E}_0/\mathrm{eV}) < 19.5$

Figure 5.10: Data/MC comparison of Cherenkov radiation ratio shown in two energy ranges.

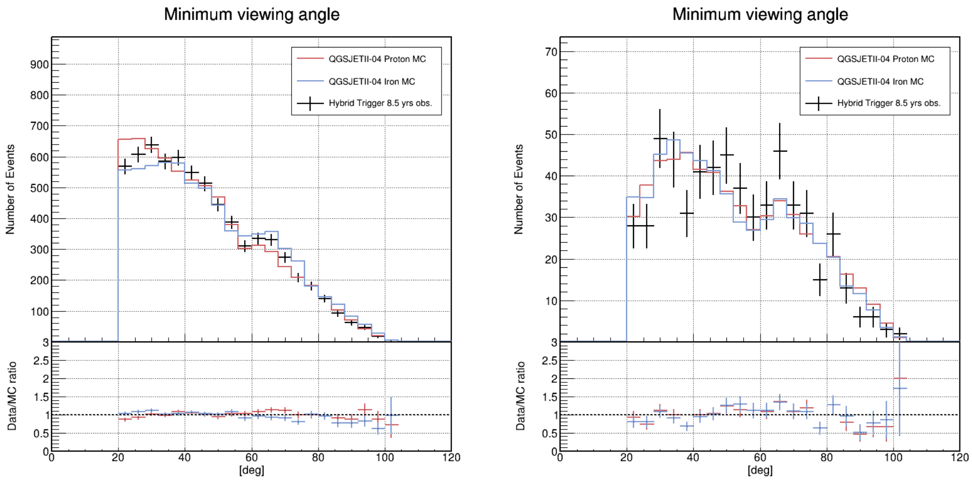

(a) $17.5 \leq \mathrm{Log}_{10}(\mathrm{E}_0/\mathrm{eV}) < 18.5$ (b) $18.5 \leq \mathrm{Log}_{10}(\mathrm{E}_0/\mathrm{eV}) < 19.5$

Figure 5.11: Data/MC comparison of the minimum viewing angle shown in two energy ranges.

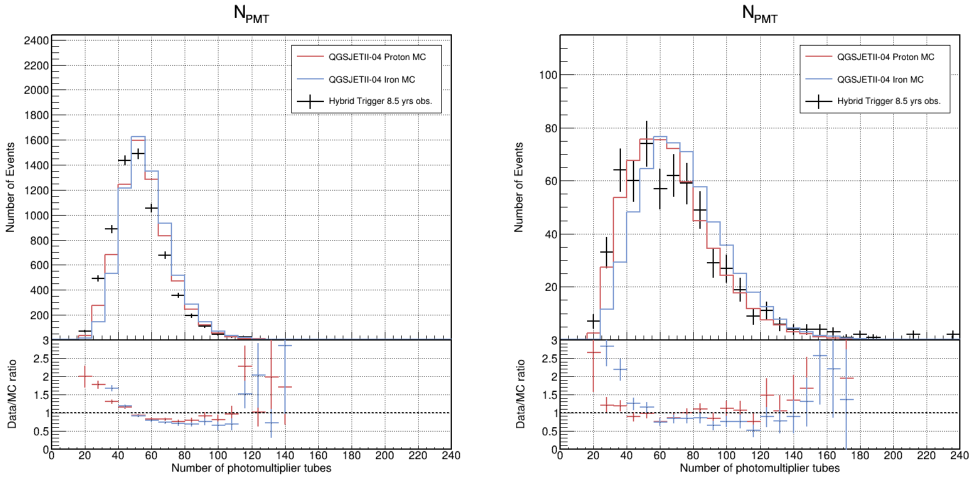

(a) $17.5 \leq \mathrm{Log}_{10}(\mathrm{E}_0/\mathrm{eV}) < 18.5$ (b) $18.5 \leq \mathrm{Log}_{10}(\mathrm{E}_0/\mathrm{eV}) < 19.5$

Figure 5.12: Data/MC comparison of the number of good PMTs shown in two energy ranges.

tendency is confirmed in Figure 4.28 through Figure 4.30 on page 86 - 88. Therefore, the resolution estimated by this method shows a similar result to the resolution estimated by the MC simulation studies in the higher energy range shown in Table 4.8 on page 82.

Besides the resolution of the EAS reconstruction, the difference in the reconstructed observables of the same EAS between the BRM and LR stations also indicates systematic uncertainties in this analysis. Figure 5.19 on page 100 shows the distributions of difference in reconstructed primary energy and X_{max}. The systematic uncertainties caused by this difference are explained in Section 5.7.6.

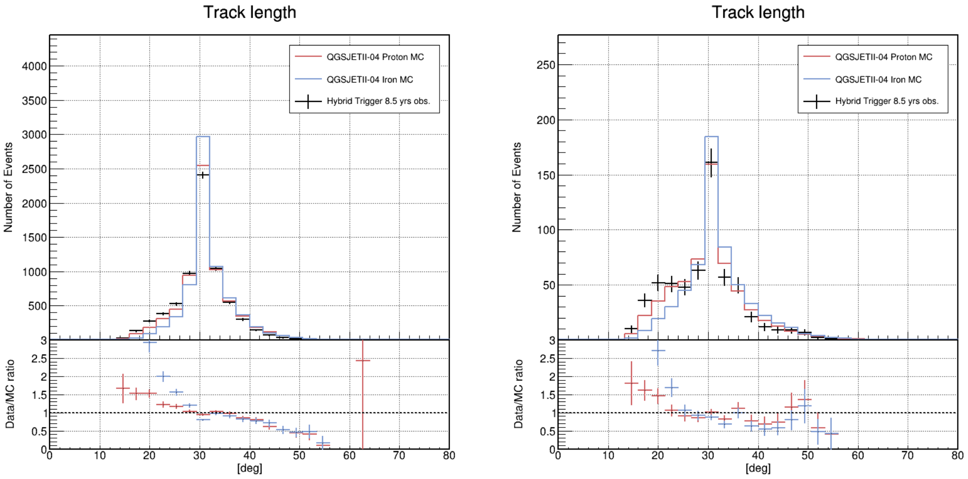

(a) $17.5 \leq \mathrm{Log}_{10}(\mathrm{E}_0/\mathrm{eV}) < 18.5$ (b) $18.5 \leq \mathrm{Log}_{10}(\mathrm{E}_0/\mathrm{eV}) < 19.5$

Figure 5.13: Data/MC comparison of the track length shown in two energy ranges.

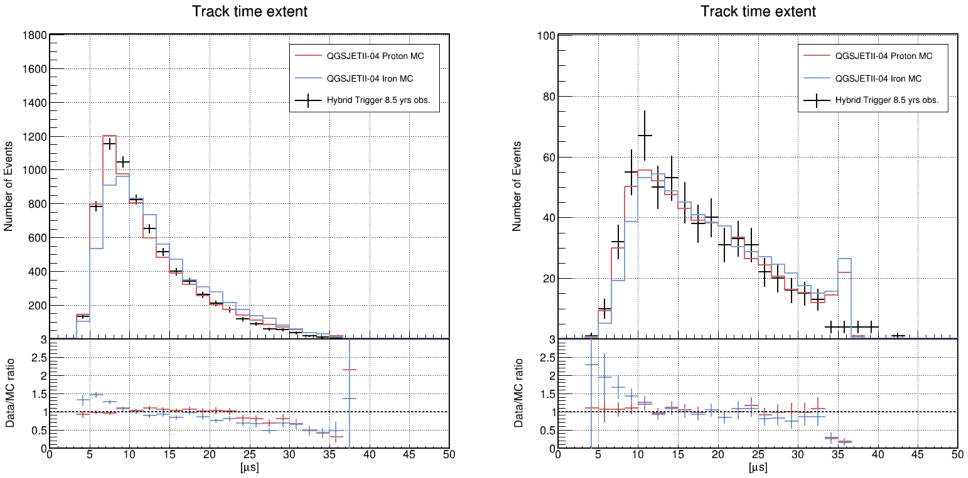

(a) $17.5 \leq \mathrm{Log}_{10}(\mathrm{E}_0/\mathrm{eV}) < 18.5$ (b) $18.5 \leq \mathrm{Log}_{10}(\mathrm{E}_0/\mathrm{eV}) < 19.5$

Figure 5.14: Data/MC comparison of the time extent shown in two energy ranges.

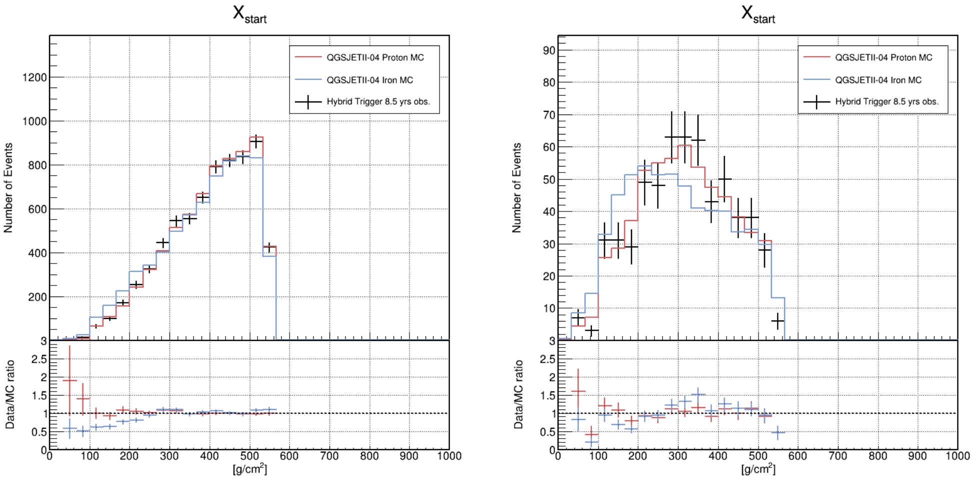

(a) $17.5 \leq \mathrm{Log}_{10}(\mathrm{E}_0/\mathrm{eV}) < 18.5$ (b) $18.5 \leq \mathrm{Log}_{10}(\mathrm{E}_0/\mathrm{eV}) < 19.5$

Figure 5.15: Data/MC comparison of $\mathrm{X}_{\mathrm{start}}$ ($\mathrm{X}_{\mathrm{low}}$) shown in two energy ranges.

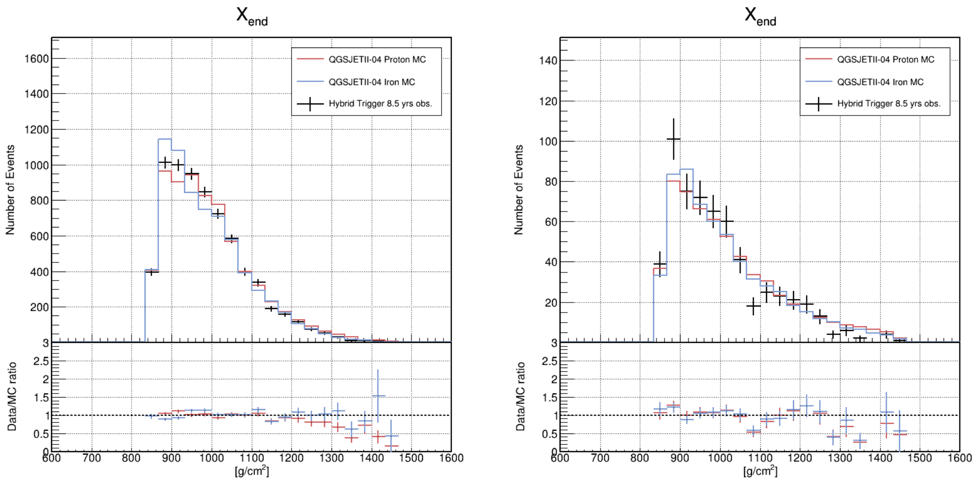

(a) $17.5 \leq \mathrm{Log}_{10}(\mathrm{E}_0/\mathrm{eV}) < 18.5$ (b) $18.5 \leq \mathrm{Log}_{10}(\mathrm{E}_0/\mathrm{eV}) < 19.5$

Figure 5.16: Data/MC comparison of $\mathrm{X}_{\mathrm{end}}$ ($\mathrm{X}_{\mathrm{high}}$) shown in two energy ranges.

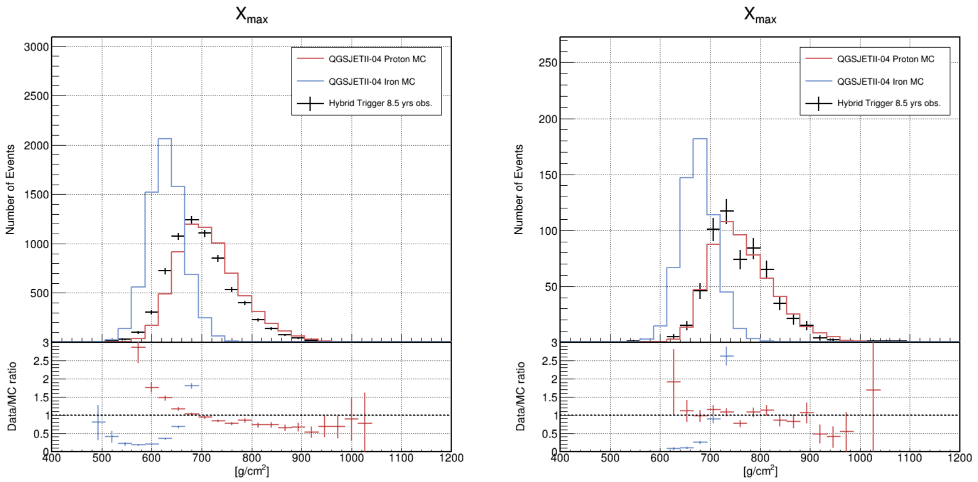

(a) $17.5 \leq \mathrm{Log}_{10}(\mathrm{E}_0/\mathrm{eV}) < 18.5$ (b) $18.5 \leq \mathrm{Log}_{10}(\mathrm{E}_0/\mathrm{eV}) < 19.5$

Figure 5.17: Data/MC comparison of $\mathrm{X}_{\mathrm{max}}$ shown in two energy ranges.

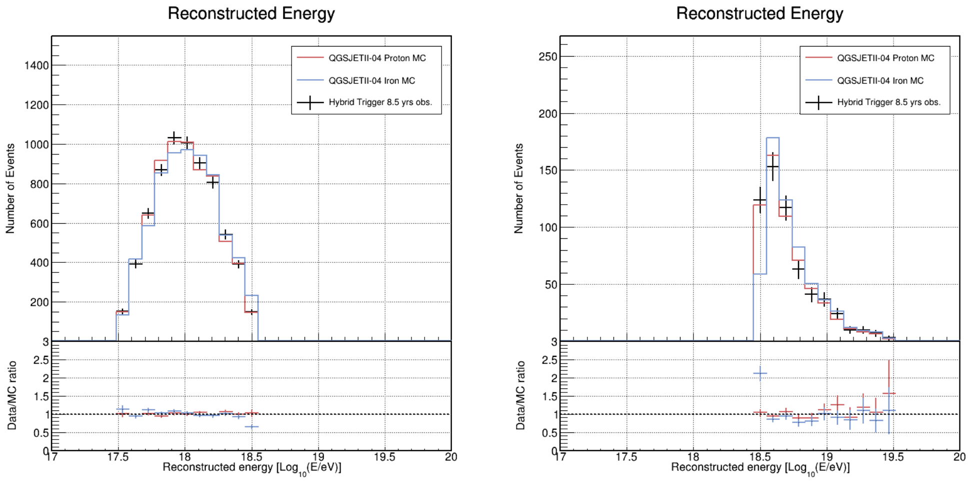

(a) $17.5 \leq \mathrm{Log}_{10}(\mathrm{E}_0/\mathrm{eV}) < 18.5$ (b) $18.5 \leq \mathrm{Log}_{10}(\mathrm{E}_0/\mathrm{eV}) < 19.5$

Figure 5.18: Data/MC comparison of reconstructed primary energy shown in two energy ranges.

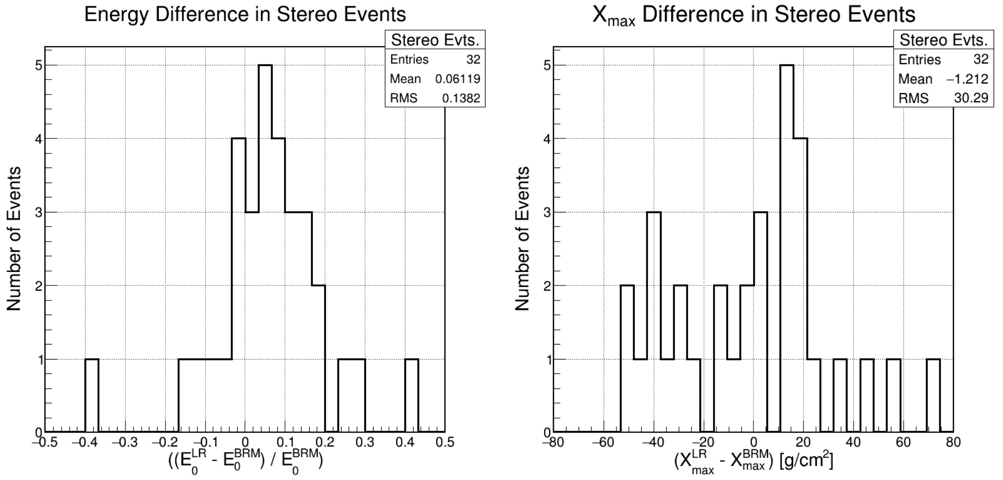

(a) Energy (b) X_{max}

Figure 5.19: Fractional differences in (a) primary energy and (b) X_{max} measured in the BRM and LR stations using 32 stereoscopic events. The upper-right box of each panel shows the mean and RMS values.

5.3 Livetime and Exposure Estimation

The estimation of livetime, which represents the total operation time used for the analysis in the TA hybrid trigger mode, involves several considerations. The following steps are taken to calculate the livetime while scrutinizing each condition:

1. Weather cut
    - The weather cut described in Section 5.1 is applied to select the periods when the observations are made under desirable weather conditions. If an operation period survives the weather cut based on the WEAT code, the on-time of the TA hybrid trigger mode is calculated using the equation: Livetime = (Total operation time - (Dead time $\bigcup$ Veto time)). Dead time refers to the insensitive period of an FD station due to the inherent structure of the FD Data AcQuisition (DAQ) electronics, as introduced in Section 2.2.1. Veto time refers to the scheduled shutdown of the TA hybrid trigger system, which was implemented to avoid disturbing the stable operation of the SD sub-arrays. Details of the veto time are provided in Section 3.2 and Figure 3.3 on page 53.
2. Exclusion of periods with technical problems
    - Operation periods with technical problems in the TA hybrid trigger system are carefully excluded from the livetime calculations. For example, periods showing subsequent features are excluded: Timeout exceptions described in Section 3.2; hybrid triggers of 0 Hz, indicating system malfunction; unstable communication status with the corresponding SD sub-array.

The cumulative livetime, representing the on-time for 8.5 years of observations using the TA hybrid trigger mode, is calculated and plotted in Figure 5.20 on page 101. This livetime information is applied to the MC simulations described

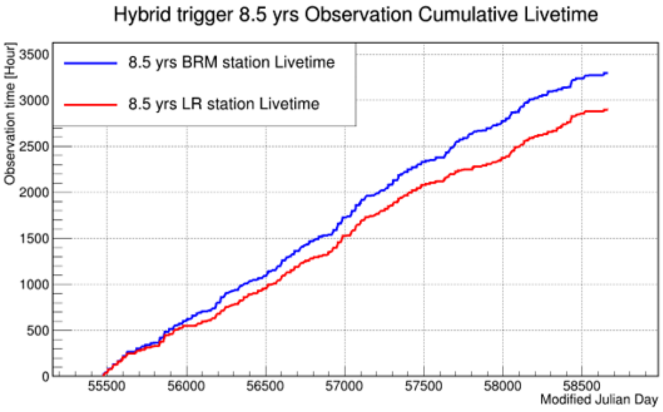

Figure 5.20: Cumulative livetime of 8.5-year observations using the TA hybrid trigger mode. The blue line indicates the cumulative livetime for the BRM station and the red line is for the LR station. The date is in Modified Julian Day (MJD): 55,477 in MJD indicates October 8th, 2010, in the Gregorian calendar and 58,664 is June 30th, 2019.

in Section 4.1 since the MC simulations require time-dependent calibration data such as PMT gains, mirror reflectances, and atmospheric parameters.

As shown in Figure 5.20 on page 101, the on-time of the BRM station is approximately 3,300 hours. For the LR station, it is approximately 2,900 hours. The difference between the two stations is consistent with the FD observation rule for the TA experiment. The LR station is supposed to terminate operation about an hour earlier than the BRM station due to the safety issue, as the LR station is facing the eastern sky where the sun rises.

Using the aperture of the TA hybrid trigger mode and the on-time of the TA hybrid trigger mode for each FD station, the combined exposure for 8.5 years of the TA hybrid trigger mode observation is estimated. Since the two FD stations are used in this analysis, the combined exposure is described by the sum of three types of exposure. The formulation of combined exposure $\omega(\mathrm{E})$ for each energy bin E is presented in Equation (5.2):

$$\begin{aligned}\omega(\mathrm{E}) = {} & \mathrm{A}\Omega^{\mathrm{BRM}}(\mathrm{E})\cdot t^{\text{BRM-LR}} \\ & + \mathrm{A}\Omega^{\mathrm{LR}}(\mathrm{E})\cdot t^{\text{LR-BRM}} \\ & + \mathrm{A}\Omega^{\mathrm{BRM}\bigcup\mathrm{LR}}(\mathrm{E})\cdot t^{\mathrm{BRM}\bigcap\mathrm{LR}},\end{aligned} \tag{5.2}$$

where $\mathrm{A}\Omega^{\mathrm{BRM}}$ means the aperture of the BRM station as a function of primary energy. $t^{\text{BRM-LR}}$ means the on-time when the BRM station is on livetime while the LR station is not. For example, when the LR station terminated observation earlier than the BRM station, only the BRM station was in operation.

$\mathrm{A}\Omega^{\mathrm{LR}}$ means the aperture of the LR station as a function of primary energy. $t^{\text{LR-BRM}}$ means the on-time when the LR station is on livetime while the BRM station is not. For example, when the BRM station halted the TA hybrid trigger system due to a Veto setting for the ELS operation or other occasions.

$\mathrm{A}\Omega^{\mathrm{BRM}\bigcup\mathrm{LR}}$ is the combined aperture of the BRM and LR stations, which is the same value shown with the black square markers in Figure 4.21 on page 79. $t^{\mathrm{BRM}\bigcap\mathrm{LR}}$ means the on-time when both the BRM and LR stations were on livetime.

Note that the UHECR composition measurement by the HiRes experiment is adopted in calculating the combined exposure $\omega(\mathrm{E})$. Refer to Section 4.3 for the details of the UHECR composition measurement by the HiRes experiment. The fraction of proton UHECR used in this calculation is shown in Figure 4.20 on page 78. Then the combined exposure $\omega(\mathrm{E})$ calculated for each energy bin is fit to a piecewise function:

$$\log_{10}\omega(\mathrm{E}) = \left\{ \begin{array}{ll} p_1\left(1-\exp\left(\frac{p_2-\log_{10}\mathrm{E}}{p_3}\right)\right), & \text{if } \mathrm{E} \leq E_{\mathrm{break}} \\ p_4, & \text{if } \mathrm{E} > E_{\mathrm{break}} \end{array} \right\} \tag{5.3}$$

where ω ($\mathrm{m}^2{\cdot}\mathrm{sr}{\cdot}\mathrm{s}$) is the combined exposure of the TA hybrid trigger mode. E_{break} (eV) is the energy where the exposure becomes flat above that point. p_n (n = 1, 2, 3, and 4) are the fit parameters. The lower energy part of the piecewise function is the exponential function, which is also adopted by fitting the apertures of the FD monocular observation mode [50]. The higher energy part of the piecewise function is a constant function representing the flat aperture caused by the size limit of the SD sub-arrays. The combined exposure for 8.5 years of observations using the TA hybrid trigger and the piecewise function fitting is shown in Figure 5.21 on page 102.

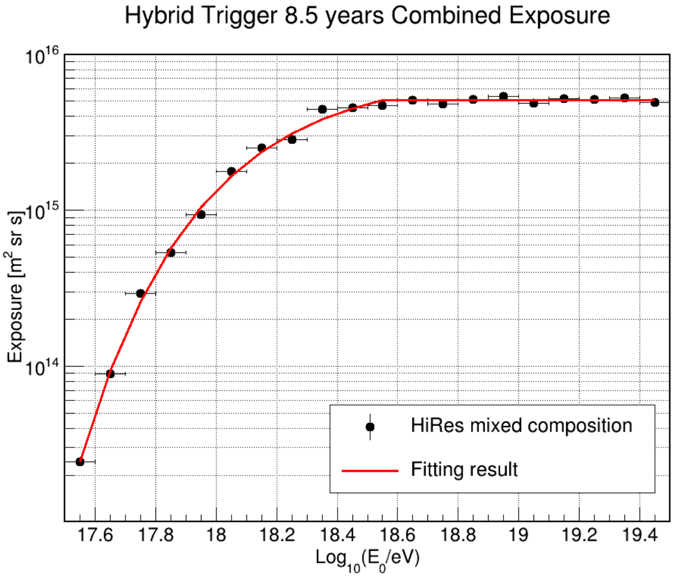

Figure 5.21: Combined exposure of 8.5-year observations using the TA hybrid trigger mode, which is calculated using Equation (5.2). The fitting result using the piecewise function is also shown. The best fit parameters are: $p_1 = 15.884$, $p_2 = 16.853$, $p_3 = 0.377$, $p_4 = 15.706$, and $\mathrm{E}_{\mathrm{break}} = 18.55$.

The fitting function is well reproduced in the combined exposure of the TA hybrid trigger mode as shown in Figure 5.21 on page 102. Therefore, this fitting result is adopted to estimate the energy spectrum described in Section 5.4.

5.4 Energy Spectrum

The energy spectrum of cosmic rays is calculated from the number of observed events, the combined exposure, and the size of a given energy bin as formulated in the following equation:

$$\mathrm{J}(\mathrm{E}) = \frac{\mathrm{N}(\mathrm{E})}{\omega(\mathrm{E}) \times \Delta\mathrm{E}}, \tag{5.4}$$

where J(E) is the flux of cosmic rays at a given energy bin E, N(E) is the number of observed events at the given energy bin E, and $\omega(\mathrm{E})$ is the combined exposure estimated in Section 5.3 using the piecewise function fit shown in Figure 5.21 on page 102. ΔE is the size of the given energy bin E. The cosmic-ray energy spectrum in the energy range from $10^{17.5}$ eV to $10^{19.5}$ eV is calculated from 8.5 years of observations using the hybrid trigger mode. The result is shown in Figure 5.22 (a) on page 103, which shows a spectral index of approximately -3.1. To show the fine structure of the energy spectrum more clearly, the flux of cosmic rays is multiplied by E^3. The result of the E^3 multiplied flux E^3J(E) is shown in Figure 5.22 (b) on page 103.

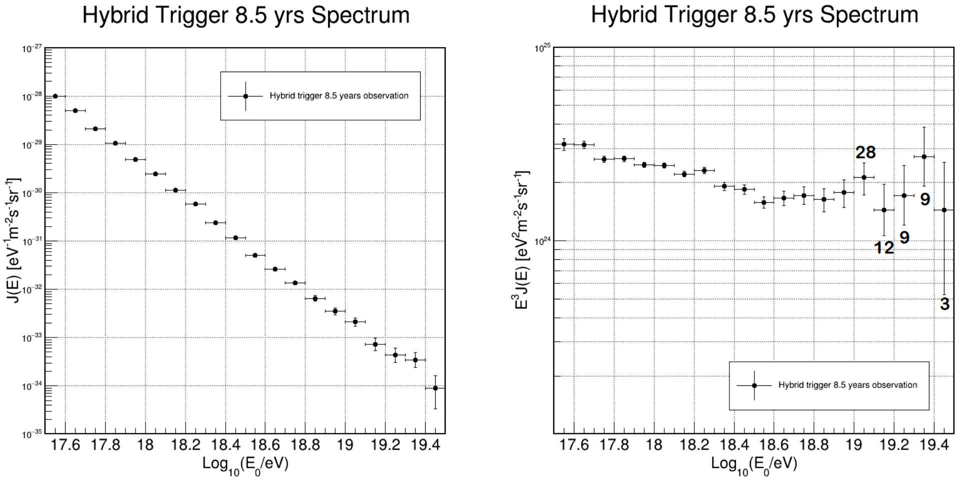

(a) Nominal

(b) Multiplied by E^3

Figure 5.22: (a) Energy spectrum of UHECR J(E) in the energy range from $10^{17.5}$ eV to $10^{19.5}$ eV, measured over 8.5-year observations in the TA hybrid trigger mode. (b) Flux J(E) multiplied by E^3 to show the structure of the spectrum. Error bars represent the statistical uncertainties in the flux, representing a 68.27% confidence interval. The confidence intervals for energy bins with fewer than 20 events are estimated by the Feldman-Cousins method [54]. The numbers of events above $10^{19.0}$ eV are indicated for each energy bin.

5.5 Depth of Maximum Shower Development

As described in Section 1.3.3, the depth of maximum shower development ($\mathrm{X}_{\mathrm{max}}$) indicates the depth in the atmosphere at which the number of secondary particles of an EAS reaches the maximum ($\mathrm{N}_{\mathrm{max}}$). This observable $\mathrm{X}_{\mathrm{max}}$ is highly important because it contains information about the primary UHECR's mass composition. To elaborate, the mean $\mathrm{X}_{\mathrm{max}}$ of the proton EAS is approximately 100 g/cm^2 deeper than that of the iron-nucleus EAS in the MC simulations in the energy range from 10^{17} eV to 10^{20} eV, as shown in the upper part of Figure 4.6 on page 63.

This difference in mean $\mathrm{X}_{\mathrm{max}}$ mainly arises from the difference in the initial energy carried by a single nucleon between a proton and an iron-nucleus UHECR. The difference in the interaction cross sections between a proton and an iron-nucleus UHECR with an atmospheric molecule also causes the difference in mean $\mathrm{X}_{\mathrm{max}}$ as described in Section 1.2.4.

The distribution width of $\mathrm{X}_{\mathrm{max}}$, $\sigma(\mathrm{X}_{\mathrm{max}})$, is also different between proton and iron-nucleus EAS. The proton EAS has a broader distribution of $\mathrm{X}_{\mathrm{max}}$ than the iron-nucleus EAS, because larger fluctuations are expected in the first interaction of proton UHECR in the atmosphere. This feature is shown in the lower part of

Figure 4.6 on page 63.

The distribution of $X_{\max}$ obtained from 8.5 years of observations using the TA hybrid trigger mode is shown in Figure 5.23 on page 104. The observed $X_{\max}$ is shown to range from 400 g/cm^2 to 1,200 g/cm^2.

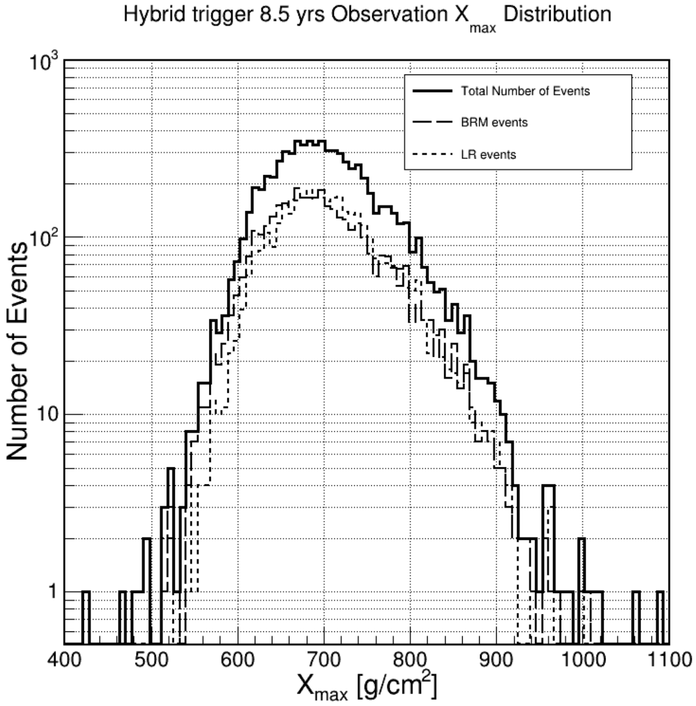

Figure 5.23: Distribution of $X_{\max}$ obtained by 8.5-year observations using the TA hybrid trigger mode. The solid line indicates the $X_{\max}$ distribution observed at both FD stations. The dashed and dotted lines indicate the $X_{\max}$ distributions observed at the BRM and LR stations, respectively.

Then the change of the mean $X_{\max}$ in the energy range from $10^{17.5}$ eV to $10^{19.5}$ eV is estimated using MC simulations. Figure 5.24 on page 105 shows $<X_{\max}>$ for proton and iron-nucleus MC simulations and $<X_{\max}>$ for the observed events. The distributions of the $X_{\max}$ width $\sigma(X_{\max})$ are also shown in the lower part of the same figure.

To visualize the change in the distributions of $X_{\max}$ as a function of primary energy, the same data plotted in Figure 5.24 on page 105 is plotted again for each 0.1-decade energy bin, showing the $X_{\max}$ distributions of all events in the proton and iron-nucleus MC simulations and the observation data for the given energy bin. The results are shown in Figure 5.25 - 5.27 on page 106 - 108. Note that the distributions of the MC simulation events are normalized to the total number of observed events.

From Figure 5.25 - 5.27 on page 106 - 108, it is confirmed that the distributions of observed $X_{\max}$ are more compatible with the results of the proton MC simulation than the results of the iron-nucleus MC simulation, especially in the energy range of $18.1 \leq \mathrm{Log}_{10}(E_0/\mathrm{eV}) < 19.0$. The observed $\sigma(X_{\max})$ result is also compatible with the $\sigma(X_{\max})$ of the proton MC simulations below $10^{19.0}$ eV.

Above $10^{19.0}$ eV, the observed $<X_{\max}>$ and $\sigma(X_{\max})$ are becoming closer to the iron-nucleus MC simulation result. However, it should be emphasized that the distributions of $X_{\max}$ do not follow a Gaussian distribution. Figure 5.27 on page 108 shows a longer tail in the distributions of $X_{\max}$ to the direction of higher $X_{\max}$.

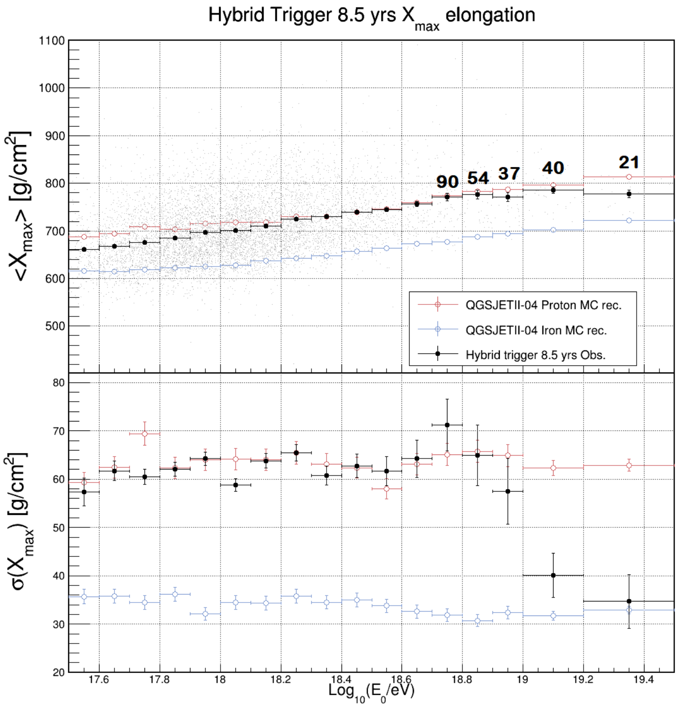

Figure 5.24: The upper part shows the X_{max} elongation rates of the proton and iron-nucleus MC simulations and the observed data plotted in 0.1-decade energy bins, except above 10^{19} eV. The red open circles, blue open circles, and black circles indicate the mean X_{max} of the proton and iron-nucleus MC simulations, and the observed data, respectively. The scatter plot of gray points indicates individual observed X_{max} values. The numbers of events are indicated if an energy bin has fewer than 100 events. The lower part shows the $\sigma(X_{max})$ of the proton and iron-nucleus MC simulations and the observed data. The markers represent the same as in the upper part.

As compared to a Gaussian distribution that has the identical mean and mode (the most frequent value), a distribution of X_{max} has the mode smaller than the mean. Therefore, it should be noted that a smaller sample size, such as 21 events, can lead to uncertain values that represent the distribution of X_{max}. The effect of a smaller sample size is examined further in Section 5.8.

As a next step to track the change in the mass composition of UHECR over a broad energy range, the mean logarithmic mass is calculated for each energy bin. The mean logarithmic mass of UHECR in the superposition model is derived using <X_{max}> of the observation data, the proton and iron-nucleus MC simulations [160]. The following calculation is performed for each energy bin, which is identical to Equation (1.1) introduced in Section 1.2.4:

$$< \ln A >= \frac{X_{max}^{obs} - X_{max}^{proton}}{X_{max}^{iron} - X_{max}^{proton}} \cdot \ln A_{iron}, \tag{5.5}$$

where <lnA> is the mean logarithmic mass of UHECR, X_{max}^{obs} is <X_{max}> of the observed data, X_{max}^{proton} is <X_{max}> of the proton MC simulations, X_{max}^{iron} is <X_{max}> of the iron-nucleus MC simulations, and $\ln(A_{iron})$ ($A_{iron} \simeq 56$) is the natural logarithm of the iron atomic mass, which is approximately 4.02. The mean logarithmic mass of UHECR measured in the TA hybrid trigger analysis is shown in Figure 5.28 on page 109.

The result of the broken line fit shown in Figure 5.28 on page 109 is summarized as below:

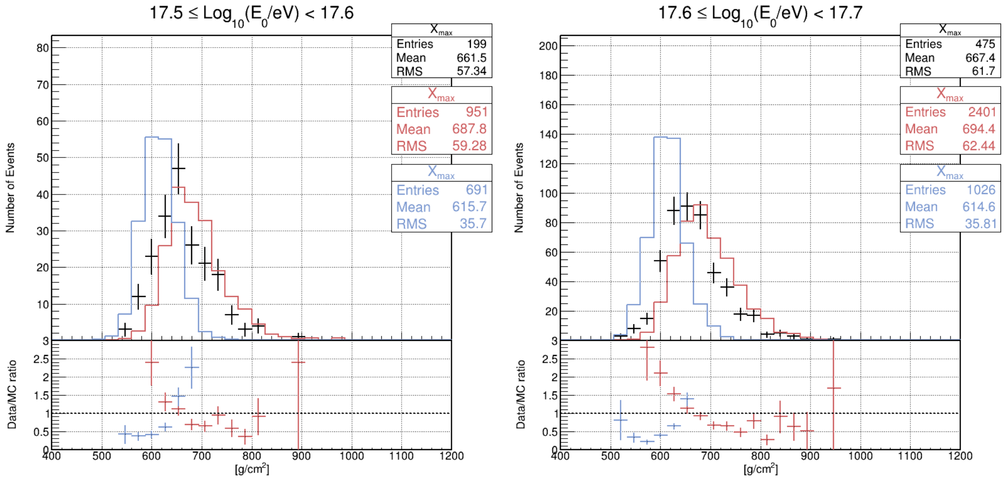

(a) $17.5 \leq \mathrm{Log}_{10}(\mathrm{E}_0/\mathrm{eV}) < 17.6$

(b) $17.6 \leq \mathrm{Log}_{10}(\mathrm{E}_0/\mathrm{eV}) < 17.7$

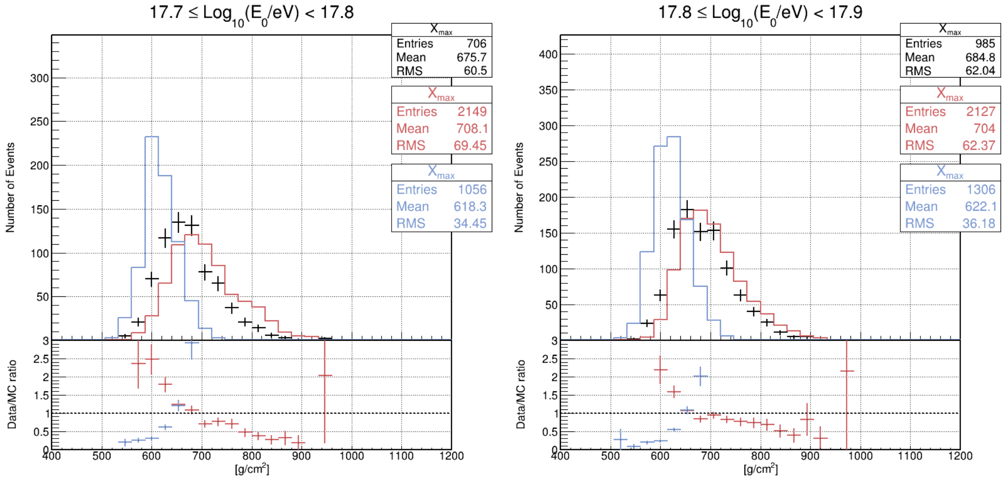

(c) $17.7 \leq \mathrm{Log}_{10}(\mathrm{E}_0/\mathrm{eV}) < 17.8$

(d) $17.8 \leq \mathrm{Log}_{10}(\mathrm{E}_0/\mathrm{eV}) < 17.9$

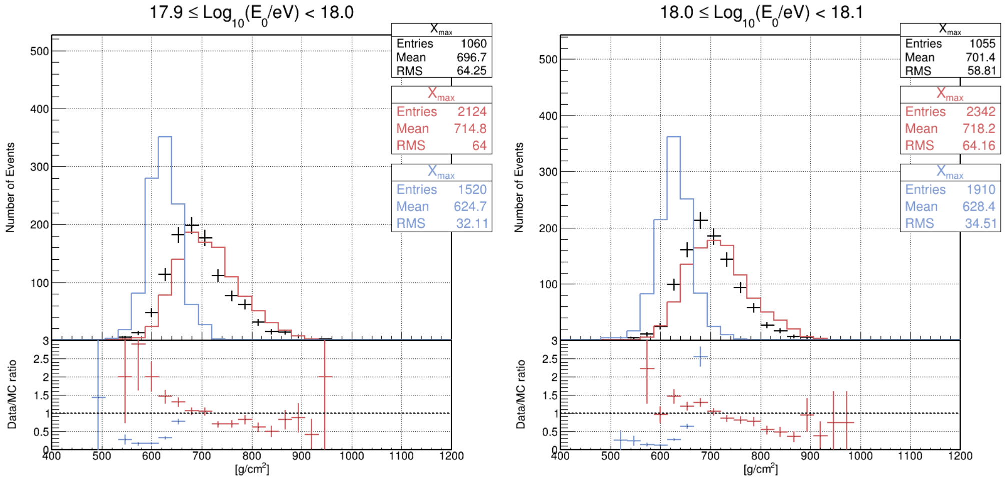

(e) $17.9 \leq \mathrm{Log}_{10}(\mathrm{E}_0/\mathrm{eV}) < 18.0$

(f) $18.0 \leq \mathrm{Log}_{10}(\mathrm{E}_0/\mathrm{eV}) < 18.1$

Figure 5.25: $\mathrm{X}_{\mathrm{max}}$ distributions of the proton and iron-nucleus MC simulations and the observed data plotted for each 0.1-decade energy bin in the energy range of $17.5 \leq \mathrm{Log}_{10}(\mathrm{E}_0/\mathrm{eV}) < 18.1$. The statistics boxes on the upper-right side indicate the mean and standard deviation of each distribution. The black, red, and blue lines indicate the observed data, the proton MC, and the iron-nucleus MC, respectively.

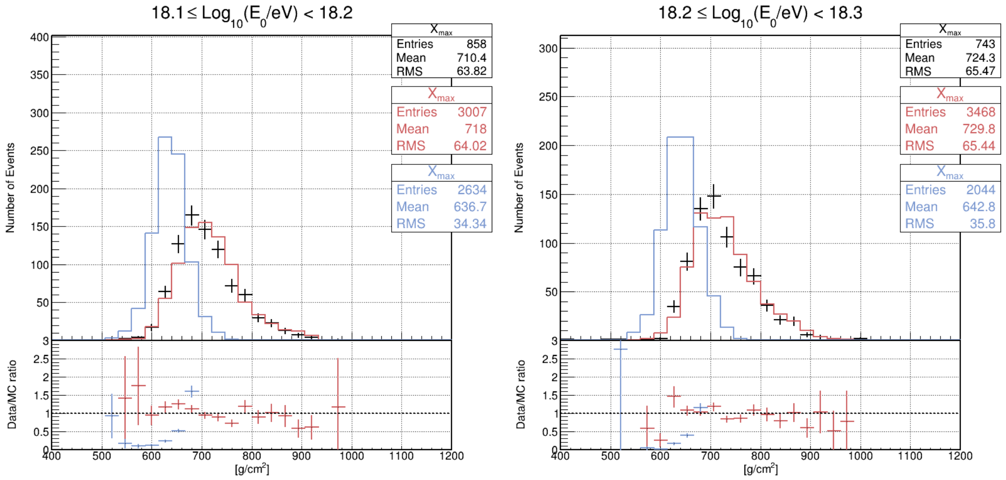

(a) $18.1 \leq \mathrm{Log}_{10}(\mathrm{E}_0/\mathrm{eV}) < 18.2$ (b) $18.2 \leq \mathrm{Log}_{10}(\mathrm{E}_0/\mathrm{eV}) < 18.3$

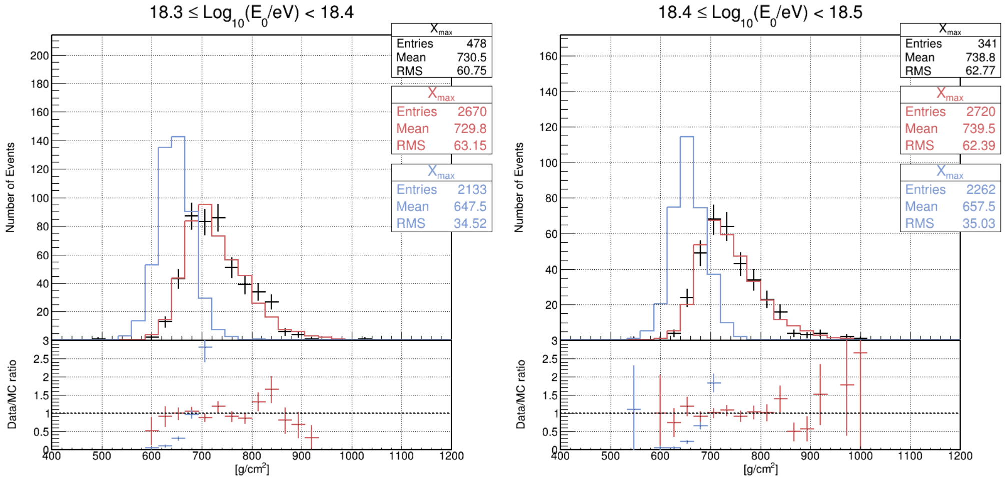

(c) $18.3 \leq \mathrm{Log}_{10}(\mathrm{E}_0/\mathrm{eV}) < 18.4$ (d) $18.4 \leq \mathrm{Log}_{10}(\mathrm{E}_0/\mathrm{eV}) < 18.5$

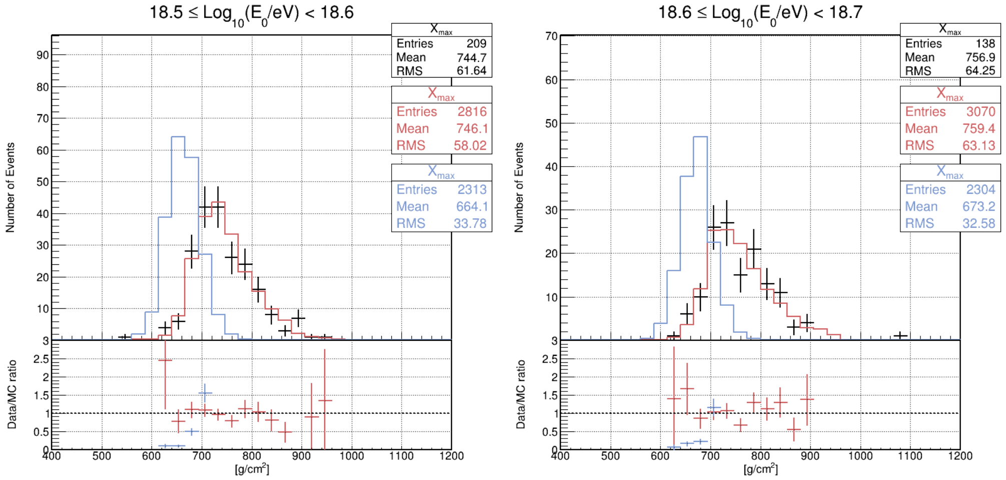

(e) $18.5 \leq \mathrm{Log}_{10}(\mathrm{E}_0/\mathrm{eV}) < 18.6$ (f) $18.6 \leq \mathrm{Log}_{10}(\mathrm{E}_0/\mathrm{eV}) < 18.7$

Figure 5.26: $\mathrm{X}_{\mathrm{max}}$ distributions of the proton and iron-nucleus MC simulations and the observed data plotted in the energy range of $18.1 \leq \mathrm{Log}_{10}(\mathrm{E}_0/\mathrm{eV}) < 18.7$.

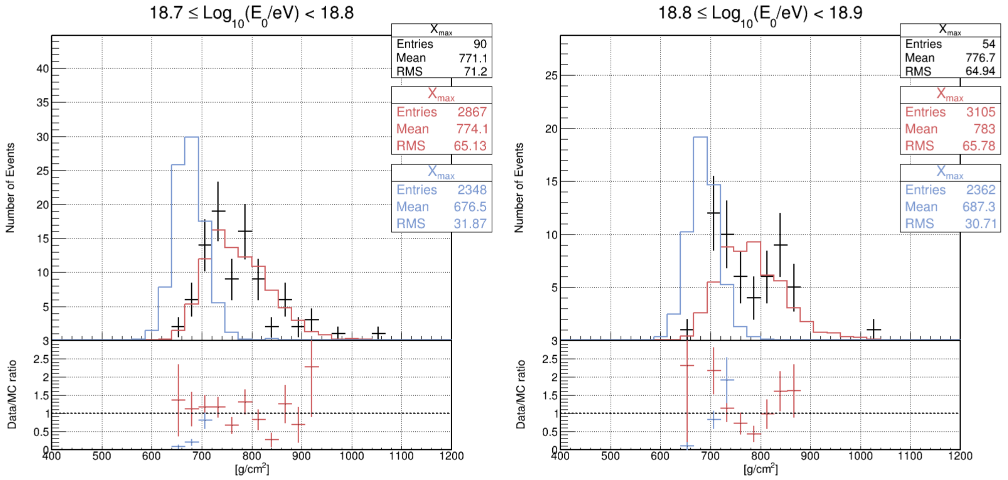

(a) $18.7 \le \mathrm{Log}_{10}(\mathrm{E}_0/\mathrm{eV}) < 18.8$ (b) $18.8 \le \mathrm{Log}_{10}(\mathrm{E}_0/\mathrm{eV}) < 18.9$

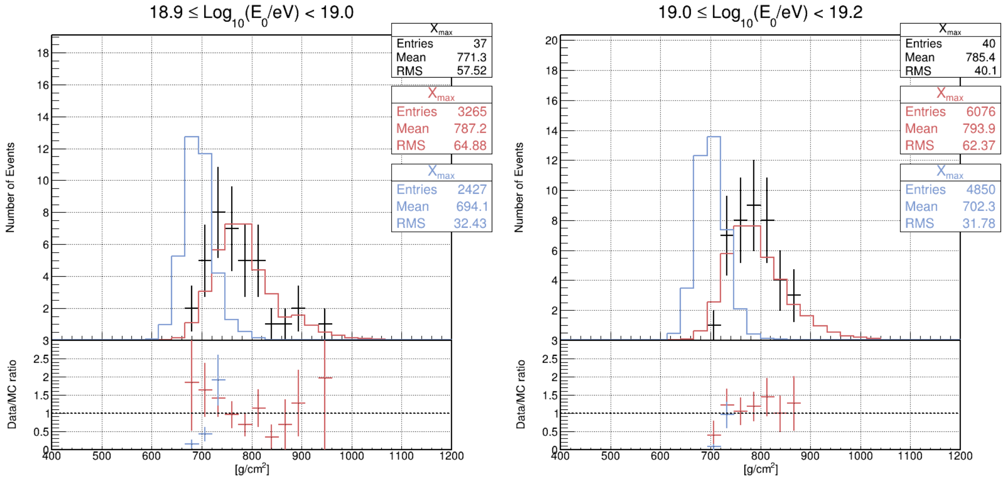

(c) $18.9 \le \mathrm{Log}_{10}(\mathrm{E}_0/\mathrm{eV}) < 19.0$ (d) $19.0 \le \mathrm{Log}_{10}(\mathrm{E}_0/\mathrm{eV}) < 19.2$

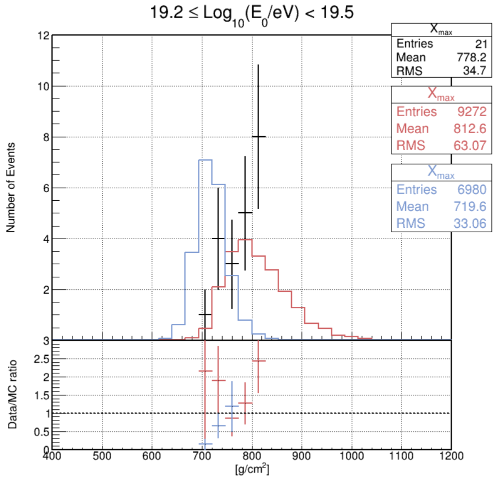

(e) $19.2 \le \mathrm{Log}_{10}(\mathrm{E}_0/\mathrm{eV}) < 19.5$

Figure 5.27: $\mathrm{X}_{\mathrm{max}}$ distributions of the proton and iron-nucleus MC simulations and the observed data plotted in the energy range of $18.7 \le \mathrm{Log}_{10}(\mathrm{E}_0/\mathrm{eV}) < 19.5$.

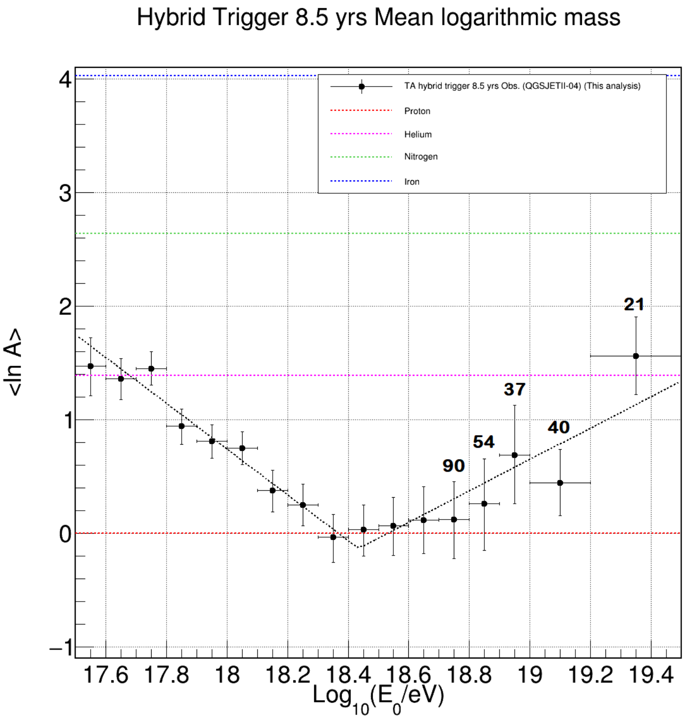

Figure 5.28: Mean logarithmic mass <lnA> of UHECR measured in the TA hybrid trigger analysis and a broken line fit. The broken line fit determined the break point at $10^{18.43\pm0.06}$ eV. The slopes below and above the break point are -2.0±0.25 $\frac{d\text{<lnA>}}{d\text{Log}_{10}(\text{E}_0/\text{eV})}$ and +1.4±0.37 $\frac{d\text{<lnA>}}{d\text{Log}_{10}(\text{E}_0/\text{eV})}$, respectively. Energy bins with fewer than 100 events are indicated with the number of events.

$$\frac{d<\text{lnA}>}{d\text{Log}_{10}(\text{E}_0/\text{eV})} = \left\{ \begin{array}{ll} -2.0 \pm 0.25, & \text{below } 10^{18.43\pm0.06}\text{eV} \\ +1.4 \pm 0.37. & \text{above } 10^{18.43\pm0.06}\text{eV} \end{array} \right\} \tag{5.6}$$

Below the energy point at $10^{18.43\pm0.06}$ eV, a negative change rate of mean logarithmic mass is indicated. This result indicates that the mass composition of UHECR becomes lighter above the energy point. In contrast, above the energy point at $10^{18.43\pm0.06}$ eV, a positive change rate of mean logarithmic mass is indicated, which means the mass composition of UHECR becomes heavier above the energy point. The difference between these change rates is +3.4 $\frac{d\text{<lnA>}}{d\text{Log}_{10}(\text{E}_0/\text{eV})}$.

Since there are only 61 observed events above $10^{19.0}$ eV in this analysis, as shown in Figure 5.24 on page 105, the statistical significance of this result should be examined by taking the event statistics into account.

The chance probability of the broken line fit exceeding the difference of the two rates +3.4 $\frac{d\text{<lnA>}}{d\text{Log}_{10}(\text{E}_0/\text{eV})}$ in pure proton composition assumption is estimated by using the QGSJET-II-04 proton MC simulation sets prepared in Section 4.1.

First, the reconstructed X_{max} of the proton MC simulation for a single energy bin is randomly sampled according to the same number of events observed in the given energy bin. Then, the mean logarithmic mass <lnA> is calculated with Equation (5.5) using the $<\text{X}_{\text{max}}^{\text{proton}}>$ of the sampled set of $\text{X}_{\text{max}}^{\text{proton}}$. This procedure is repeated 10^7 times to estimate the chance probability. The chance probability is less than 1×10^{-7} for 10^7 trials, corresponding to greater than 5.1σ.

The local significances (σ_{local}) of the slope above $\text{E}_{\text{break}}^{\text{TA}}$ (S_H), the slope below $\text{E}_{\text{break}}^{\text{TA}}$ (S_L), and the change of the two slopes (ΔS) are 3.8σ ($1.4/0.37 = 3.8\sigma$), 8σ ($|\text{-}2.0|)/0.25 = 8\sigma$), and 7.6σ ($(1.4{+}2.0)/\sqrt{(0.25^2 + 0.37^2)} = 3.4/0.447 = 7.6\sigma$), respectively.

The chance probabilities of exceeding S_H, S_L, and ΔS are 9.3×10^{-3}, $<1\times10^{-7}$, and $<1\times10^{-7}$ for 10^7 trials, respectively, which are equivalent to one-sided global significances (σ_{global}) of 2.4σ, $>5.1\sigma$, and $>5.1\sigma$.

As a next step, the reliability of this result was examined under different conditions. First, the result is examined using a different quality cut described in Section 4.2.4. In this examination, the same analysis procedure is performed to measure the mean logarithmic mass <lnA> except that the fiducial volume cut described in Table 4.6 on page 70 is not applied to both the MC and observed events. The mean logarithmic mass of UHECR measured using this condition (without the fiducial volume cut) is shown in Figure 5.29 on page 110.

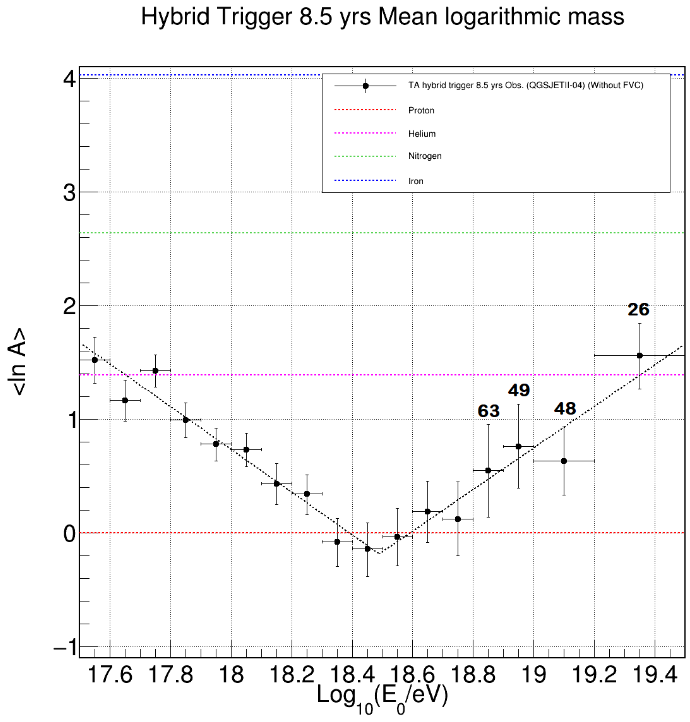

Figure 5.29: Mean logarithmic mass <lnA> of UHECR measured in the TA hybrid trigger analysis and a broken line fit without applying the fiducial volume cut. The break point is at $10^{18.49\pm0.06}$ eV. The slopes below and above the break point are -1.9±0.21 $\frac{d\text{<lnA>}}{d\text{Log}_{10}(\text{E}_0/\text{eV})}$ and +1.8±0.42 $\frac{d\text{<lnA>}}{d\text{Log}_{10}(\text{E}_0/\text{eV})}$, respectively.

Secondly, the result obtained using a different hadronic interaction model is examined. Although there is no detector MC simulation generated using the EPOS-LHC hadronic interaction model, as explained in Section 4.1, the original (thrown) X_{max} distributions of Cosmic Ray Simulations for KAscade (CORSIKA)-generated EAS with the EPOS-LHC are available as shown in Figure 4.6 on page 63.

To examine the effect of using a different hadronic interaction model in such a condition, the reconstructed QGSJET-II-04 MC events are extracted to match the EPOS-LHC thrown X_{max} distributions.

First, the weight of each CORSIKA-generated QGSJET-II-04 EAS is determined to match the thrown X_{max} distribution of EPOS-LHC CORSIKA-generated EAS. Next, each reconstructed QGSJET-II-04 MC event is weighted according to the weight of its original (thrown) CORSIKA-generated EAS determined in the previous stage. The weighted MC events estimated by this method are called EPOS-like MC events.

Using EPOS-like MC events, the same analysis procedure to measure <lnA> is performed. However, these EPOS-like MC events do not cover the entire energy range of the TA hybrid trigger analysis because the original (thrown) CORSIKA-generated EAS for the EPOS-LHC hadronic interaction model were not generated above 10^{19} eV. The mean logarithmic mass of UHECR measured using this condition (using EPOS-like MC events) is shown in Figure 5.30 on page 111.

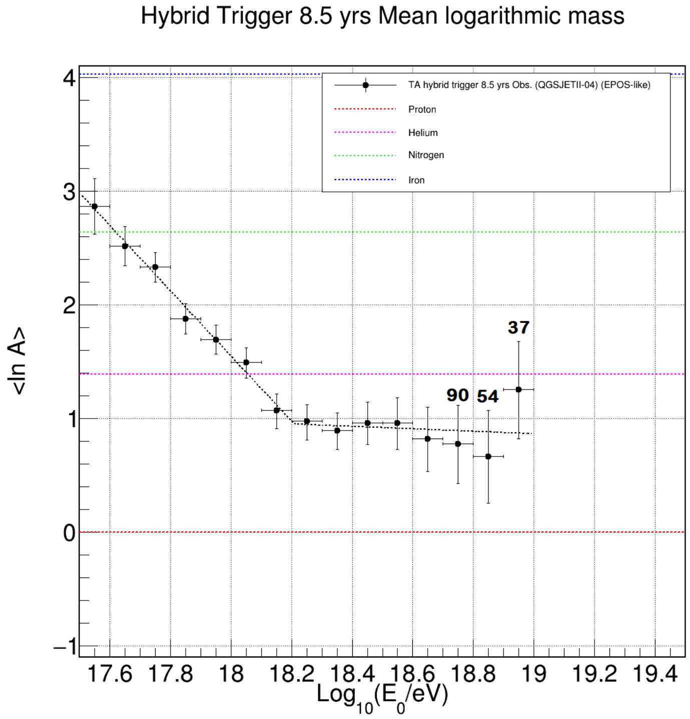

Figure 5.30: Mean logarithmic mass <lnA> of UHECR measured in the TA hybrid trigger analysis and a broken line fit using EPOS-like MC events. The broken line fit determined the break point at $10^{18.21\pm0.06}$ eV. The slopes below and above the break point are -2.8±0.32 $\frac{d\text{<lnA>}}{d\mathrm{Log}_{10}(\mathrm{E}_0/\mathrm{eV})}$ and -0.1±0.42 $\frac{d\text{<lnA>}}{d\mathrm{Log}_{10}(\mathrm{E}_0/\mathrm{eV})}$, respectively.

It is confirmed that the transition of mass composition from the 2nd Knee to the higher energy, $|S_L|>0$, also exists in both results obtained with a different quality cut and with a different hadronic interaction model. Although the $S_H>0$ obtained with the EPOS-like MC events is not evident.

In summary, the estimation of the slopes in the mean logarithmic mass of UHECR shown in Figure 5.28 on page 109 is examined to be reliable even after the change of quality cut or a hadronic interaction model.

5.6 Efficiency of SD Self-trigger

In the TA experiment, the efficiency of the SD self-trigger is estimated by the dedicated MC simulation studies. The trigger efficiencies of the TA SD self-trigger obtained by the MC simulation study are shown in Figure 5.31 on page 112.

Notably, the TA hybrid trigger mode can estimate the efficiency of the TA SD self-trigger using the observation dataset. By calculating (Number of SD self-triggered events)/(Number of all events) for each energy bin of the TA hybrid

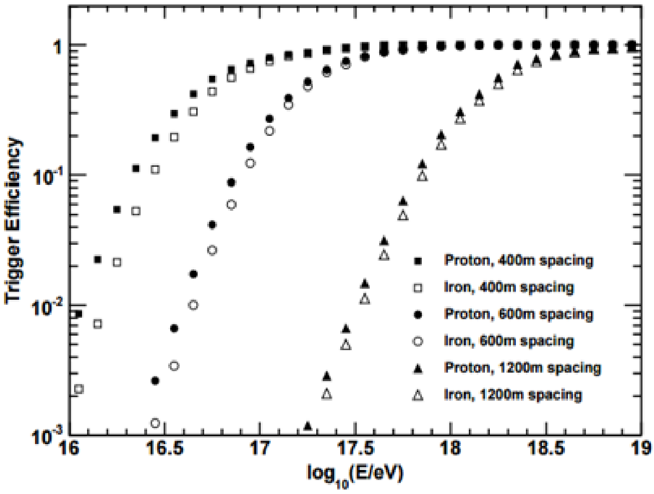

Figure 5.31: SD self-trigger efficiencies obtained by the MC simulation studies at three detector spacings for proton and iron-nucleus UHECR [49]. The triangle markers represent the trigger efficiency of the TA SD array for a given energy.

trigger dataset, the SD self-trigger efficiency is experimentally measured for the first time.

Figure 5.32 on page 112 shows the SD self-trigger efficiency estimated for each FD station. Then the SD self-trigger efficiency is estimated for both the BRM and LR stations and compared to the SD self-trigger efficiency estimated by the MC simulation study. The result is shown in Figure 5.33 on page 113.

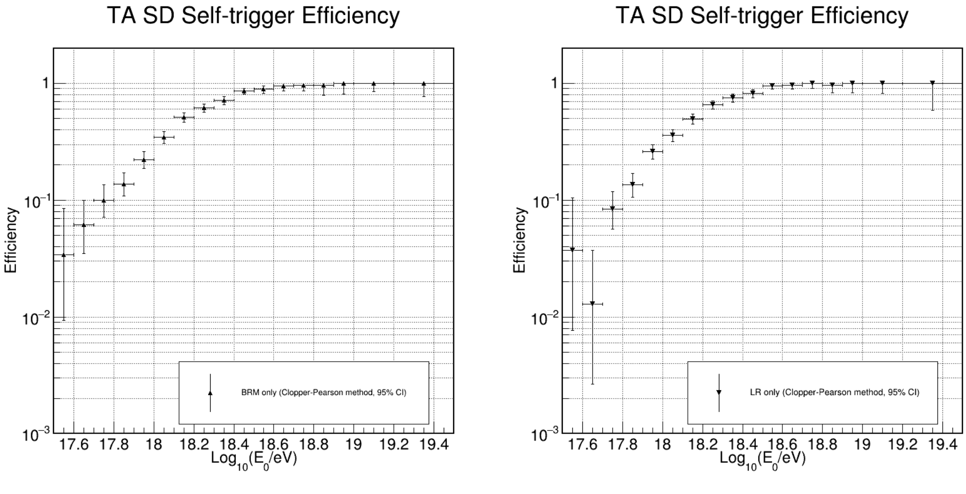

(a) BRM station

(b) LR station

Figure 5.32: (a) TA SD self-trigger efficiency estimated from the data obtained by the BRM station. (b) Same as in (a), but by the LR station. Vertical error bars indicate 95% binomial confidence intervals estimated by the Clopper-Pearson method implemented in CERN ROOT [55].

As shown in Figure 5.33 on page 113, it is confirmed that the SD self-trigger has 100% efficiency above $\sim 10^{18.7}$ eV. Furthermore, it is also shown that the SD self-trigger efficiency experimentally measured in the TA hybrid trigger mode agrees with the SD self-trigger efficiency estimated by the MC simulation study. However, this result does not estimate the effect of the quality cut.

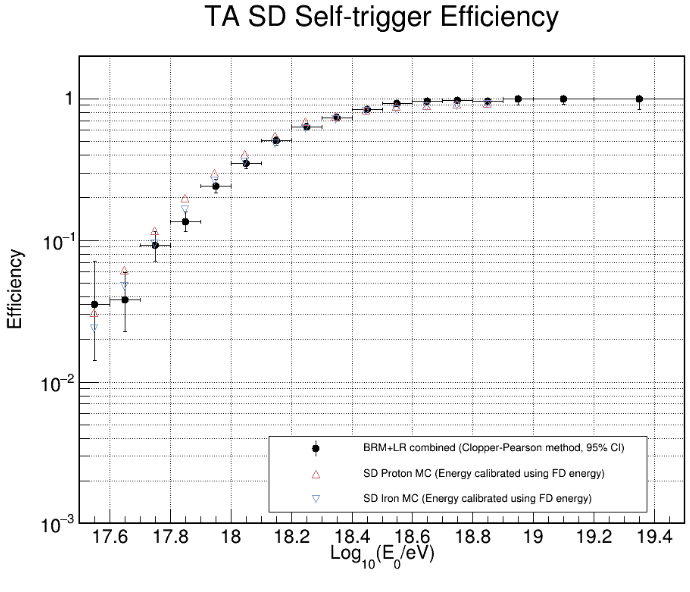

Figure 5.33: Experimentally measured efficiency of TA SD self-trigger estimated from the data obtained at both FD stations. The TA SD self-trigger efficiency obtained by the SD MC simulations is plotted together. The SD energy is calibrated using FD energy [49]. The vertical error bars are the same as in Figure 5.32 on page 112.

5.7 Systematic Uncertainties

The results of primary energy and X_{max} reconstruction in this analysis carry systematic uncertainties from multiple independent and not-fully-independent sources: the fluorescence yield model; the detector calibration; the geometry of FD telescopes; the atmospheric condition; the reconstruction procedure; the difference in the reconstruction results between two FD stations; the difference in the reconstruction results between two analysis frameworks. Each source is examined and explained in this section.

5.7.1 Fluorescence Yield

To measure air fluorescence from EAS, as described in Section 1.3.4, multiple models of fluorescence yield have been developed. In this analysis, the differential spectrum measured in the FLuorescence in Air from SHowers (FLASH) experiment and the total yield measured in the Kakimoto model are adopted [56][61]. The comparison of multiple fluorescence yield models is shown in Figure 5.34 on page 114.

Around the height of 10 km, the model showing the most significant discrepancy with the Kakimoto model is the Nagano model. The difference in total photon yield between these two models is approximately 14%. This value is adopted as the systematic uncertainty caused by the fluorescence yield model in reconstructing the primary energy of EAS.

In this analysis, it is considered that the fluorescence yield model does not affect the systematic uncertainty in reconstructing X_{max} independently from the energy scale. Therefore, the systematic uncertainty in X_{max} arising from the fluorescence yield model is a secondary effect of 14% of uncertainty in primary energy.

Using the MC simulation sets prepared in Section 4.1, it is estimated that 14% of uncertainty in primary energy is translated into 5.6 g/cm^2 of uncertainty

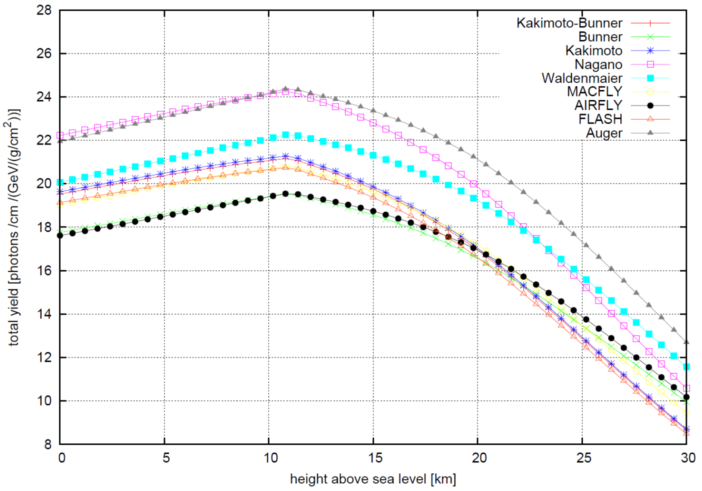

Figure 5.34: Comparison of multiple fluorescence models. The total photon yields were obtained using US standard atmosphere [31]. The plot includes the Kakimoto model [56], Bunner model [57], Nagano model [58], Waldenmaier model [59], Measurement of Air Cherenkov and Fluorescence Light Yield (MACFLY) model [60], FLASH model [61], and AIR FLuorescence Yield (AIRFLY) model [62]. Kakimoto-Bunner in the plot indicates the Bunner model scaled by the absolute yield of the Kakimoto model. Auger in the plot indicates the AIRFLY model scaled by the absolute yield of the Nagano model.

in X_{max}. This value is adopted as the systematic uncertainty caused by the fluorescence yield model in reconstructing X_{max}.

5.7.2 Detector Calibration

On detector calibration, the quadratic addition of the systematic uncertainties of all sources yields 12.2% and 4.9 g/cm^2 in reconstructing primary energy and X_{max}, respectively. The uncertainties from individual sources are described below.

CRAYS and PMT Gain Drifting

The Calibration using RAYleigh Scattering (CRAYS), which is described in Section 2.2.1, contributes a systematic uncertainty of 7.2% in reconstructing primary energy due to the uncertainty in the energy probe and 3.7% from systematic gain drifts caused by PMT transportation to the experiment site [38].

The aging of PMTs is tracked using a radioactive light source Yttrium Aluminum Perovskite (YAP). The uncertainty in reconstructing primary energy caused by PMT aging is estimated to be 7.5% over the 8.5-year observations [39].

Mirror and Optical filter

Uncertainties in reconstructing primary energy arise from measuring the FD mirror reflectance (5%) and the optical filter transmittance (1%). An additional 1% uncertainty is considered for the aging effect in the transmittance of the optical filter [52].

SD-FD Timing Difference

Synchronizing timing information between FD stations and SDs is crucial for EAS reconstruction using the hybrid technique. While the clocks are expected to be synchronized within the Global Positioning System (GPS) module's precision (14 ns for M12+; Motorola) [161], there are inherent timing offsets due to differences in each FD and SD DAQ electronics. In this analysis, uncertainties arising from the SD-FD timing difference of ±50 ns are assumed. This difference corresponds to 0.2% uncertainty in primary energy and 1 g/cm^2 uncertainty in X$_{\mathrm{max}}$ reconstruction.

5.7.3 Telescope Geometry

Uncertainties in the FD telescope's direction (0.01°) and each PMT's direction (0.1°) contribute to systematic uncertainties of 4% and 9 g/cm^2 in reconstructing primary energy and X$_{\mathrm{max}}$, respectively [31].

5.7.4 Atmosphere

The atmospheric parameters used in the analysis are based on the Global Data Assimilation System (GDAS) data and a typical Vertical Aerosol Optical Depth (VAOD) value of 0.034. A previous study comparing different atmospheric parameter sets reported uncertainties of 11.2% in energy reconstruction and 12.4 g/cm^2 in X$_{\mathrm{max}}$ reconstruction [162]. Since GDAS parameters are not significantly different from the radiosonde measurements at Elko, these values are adopted as systematic uncertainties from the atmosphere [163].

5.7.5 Reconstruction

There are sources of systematic uncertainties in the reconstruction procedure itself. Each of them is examined below.

Missing Energy

The choice of the missing energy correction curve, estimated by the QGSJET-II-04 proton MC simulations, introduces uncertainty related to the mass composition. This uncertainty can reach up to 7% at a primary energy of $10^{17.5}$ eV for iron-nucleus primaries, corresponding to a 3 g/cm^2 of uncertainty in reconstructing X$_{\mathrm{max}}$ reconstruction.

Data/MC Difference

The data/MC comparison results shown in Section 5.2 indicate the discrepancy in the distribution of the number of good PMTs between MC simulations and observed data. As shown in Figure 5.12 (a) on page 97, the number of good PMTs is larger in the MC simulations than in the observed data. This discrepancy implies that the Nishimura-Kamata-Greisen (NKG) function used to simulate the lateral distribution of EAS in this analysis results in a wider lateral distribution than the observed EAS [31].

The uncertainty from the lateral distribution of the EAS is estimated by comparing the nominal reconstruction results and the reconstruction results without considering the lateral extent of the EAS. It is found that this effect contributes to 0.3% of systematic uncertainty in energy reconstruction and 1.4 g/cm^2 of systematic uncertainty in X$_{\mathrm{max}}$ reconstruction.

5.7.6 Systematic Uncertainties Between Different Analyses in the TA Experiment

Some sources of systematic uncertainties are not-fully-independent. For example, the differences in the reconstruction results between the BRM and LR stations and the differences in the reconstruction results between the two analysis frameworks developed independently in the TA collaboration are classified as not-fully-independent.

For the difference between the two stations, the difference in primary energy and X_{max} are shown in Figure 5.19 on page 100. Here, the difference in reconstruction results from 32 stereoscopic events is indicated. The difference in the energy and X_{max} reconstruction results are 6.1% and 1.2 g/cm^2, respectively.

For the difference between the two analysis frameworks, it is estimated to be 5.4% in energy reconstruction and 5.1 g/cm^2 in X_{max} reconstruction.

A linear sum of these two sources is used as a conservative estimate instead of a quadratic sum. The total uncertainties from not-fully-independent sources are estimated to be 11.5% for primary energy and 6.3 g/cm^2 for X_{max}.

5.7.7 Total Systematic Uncertainties

Table 5.3 on page 116 lists all sources of systematic uncertainties described in previous subsections. The total systematic uncertainties in reconstructing primary energy and X_{max} are calculated from the square root of the quadratic sum of all independent and non-fully-independent items, adopting the method used in the conventional TA hybrid analysis [22]. The total systematic uncertainties of primary energy and X_{max} are estimated to be 25.8% and 18.5 g/cm^2, respectively.

Table 5.3: Summary of independent and not-fully-independent sources of systematic uncertainties in reconstructing primary energy and X_{max} using the TA hybrid trigger mode. The contributions of each source are estimated and the total systematic uncertainties are calculated.

Items	Energy	X_{max}
Independent sources		
Fluorescence yield	14%	5.6 g/cm^2
Detector	12.2%	5 g/cm^2
FD geometry	4.0%	9 g/cm^2
Atmosphere	11.2%	12.4 g/cm^2
Reconstruction	7.0%	3.3 g/cm^2
Quadratic sum	23.1%	17.4 g/cm^2
Not-fully-independent sources		
BRM-LR difference	6.1%	1.2 g/cm^2
Framework difference	5.4%	5.1 g/cm^2
Linear sum	11.5%	6.3 g/cm^2
Total	25.8%	18.5 g/cm^2

Since the systematic uncertainties in primary energy are estimated, the energy spectrum of UHECR shown in Figure 5.22 (b) on page 103 is plotted to show the corresponding systematic uncertainties. The systematic uncertainties in the flux J are dominated by the uncertainty of the energy scale σE/E, which is propagated to the flux J by the following equation [49]:

$$\frac{\sigma \mathrm{J}}{\mathrm{J}} = (|\gamma| - 1)\frac{\sigma \mathrm{E}}{E}, \tag{5.7}$$

where the flux J is described as J $\propto$ E^{γ}. γ is the spectral index. This analysis adopts a spectral index of -3.1 to estimate the uncertainties in the energy range from $10^{17.5}$ eV to $10^{19.5}$ eV. The energy spectrum $\mathrm{E}^3\mathrm{J(E)}$ of UHECR with systematic uncertainties is plotted in Figure 5.35 on page 117.

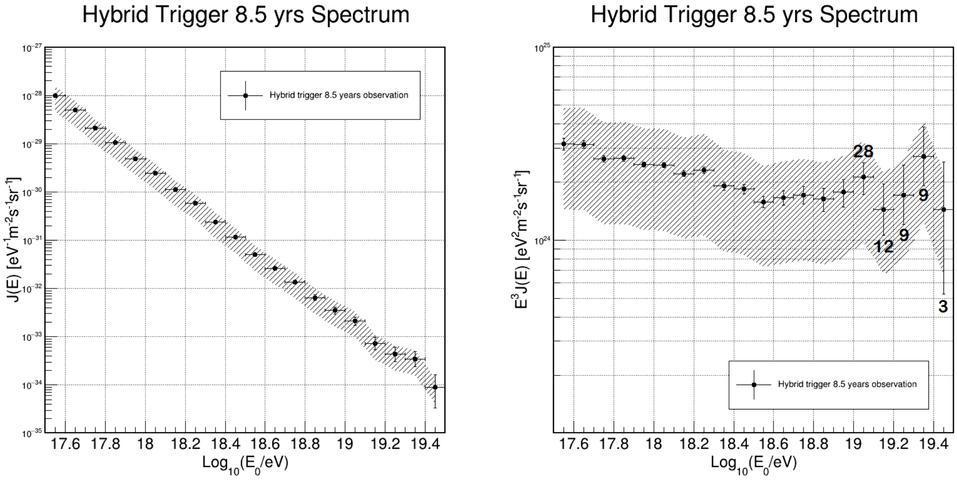

(a) Nominal

(b) Multiplied by E^3

Figure 5.35: (a) Measured energy spectrum J(E). (b) $\mathrm{E}^3\mathrm{J(E)}$. The shaded areas indicate the corresponding systematic errors. The numbers of events in energy bins above $10^{19.0}$ eV are indicated.

Next, the $\mathrm{X}_{\mathrm{max}}$ elongation rate shown in Figure 5.24 on page 105 is plotted again with its corresponding systematic uncertainties. The result is shown in Figure 5.36 on page 118.

Finally, the mean logarithmic mass (<lnA>) of UHECR shown in Figure 5.28 on page 109 is plotted to show the corresponding systematic uncertainties. The result is shown in Figure 5.37 on page 118.

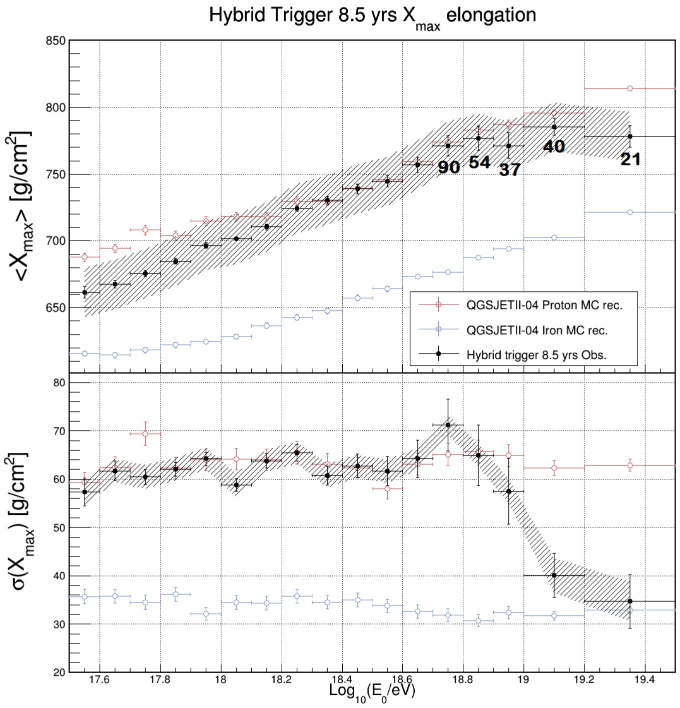

Figure 5.36: X_{max} elongation rate and $\sigma(X_{\mathrm{max}})$. The shaded areas indicate the corresponding systematic errors. The systematic uncertainties in $\sigma(X_{\mathrm{max}})$ are taken from the previous TA hybrid analysis [22].

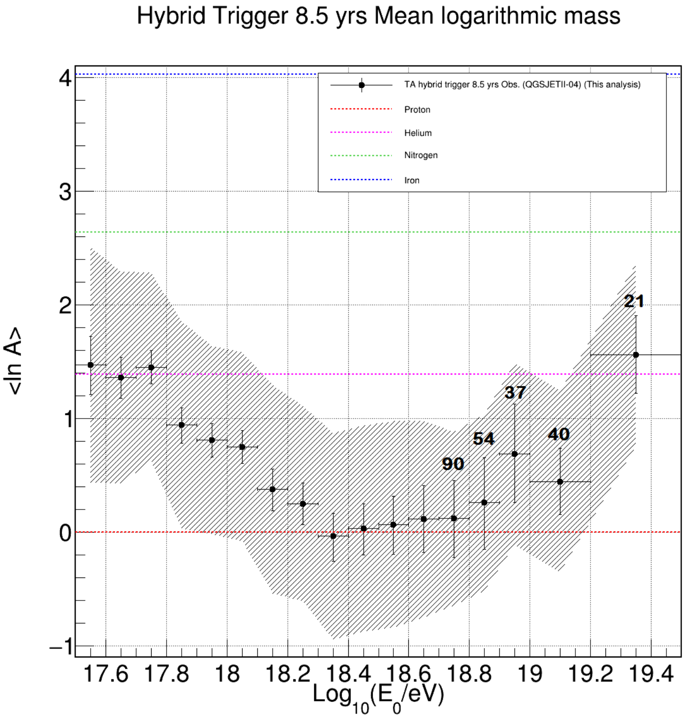

Figure 5.37: Mean logarithmic mass <lnA> of UHECR measured in the TA hybrid trigger analysis. The shaded areas indicate the corresponding systematic uncertainties. In addition, the logarithmic masses of proton, helium, nitrogen, and iron are indicated.

5.8 X_{max} Bivariate Analysis

For further studies on the mass composition of UHECR using the $<X_{max}>$ and $\sigma(X_{max})$ measurements shown in Figure 5.36 on page 118, a bivariate analysis is performed. The motivation of this analysis is that $<X_{max}>$ and $\sigma(X_{max})$ measurements show a disagreement especially for primary energies above 10^{19} eV.

In this energy region, the observed $<X_{max}>$ is more compatible with proton MC simulations within systematic uncertainties, but the observed $\sigma(X_{max})$ is more compatible with the iron-nucleus MC simulation within systematic uncertainties. To perform an analysis that also considers the low statistics of events in this energy range, the following bivariate analysis method from the previous study is adopted [22].

First, the reconstructed X_{max} of a single mass composition of the MC simulation for an energy bin is randomly sampled according to the number of observed events in the given energy bin. Then $<X_{max}>$ and $\sigma(X_{max})$ of the sampled MC events are calculated. This procedure is repeated 5,000 times to build a cloud of 5,000 data points in a $<X_{max}>$ vs. $\sigma(X_{max})$ plot. Next, three confidence ellipses are estimated using 5,000 data points representing 68%, 90%, and 95% confidence intervals.

Finally, the above procedures are performed for all energy bins of the proton and iron-nucleus MC simulations. The results of this analysis are plotted in Figure 5.38 - 5.40 on page 120 - 122.

Figure 5.38 - 5.40 on page 120 - 122 reveal that the observed data fall inside 95% confidence ellipses of the proton MC simulation sets for almost all energy bins with their corresponding systematic uncertainties. This includes the energy range above 10^{19} eV, where the $\sigma(X_{max})$ measurement showed the iron-like mass composition in Figure 5.35 on page 117.

The statistical effect is shown by a larger area of the confidence ellipse as the number of events in the energy bin decreases. It is indicated that the lower event statistics lead to an overlap between the confidence intervals of $\sigma(X_{max})$ of the proton and iron-nucleus MC simulations. This result implies that the measurement of $\sigma(X_{max})$ loses the ability to distinguish proton UHECR from iron-nucleus UHECR when an energy bin has smaller event statistics such as 21 events.

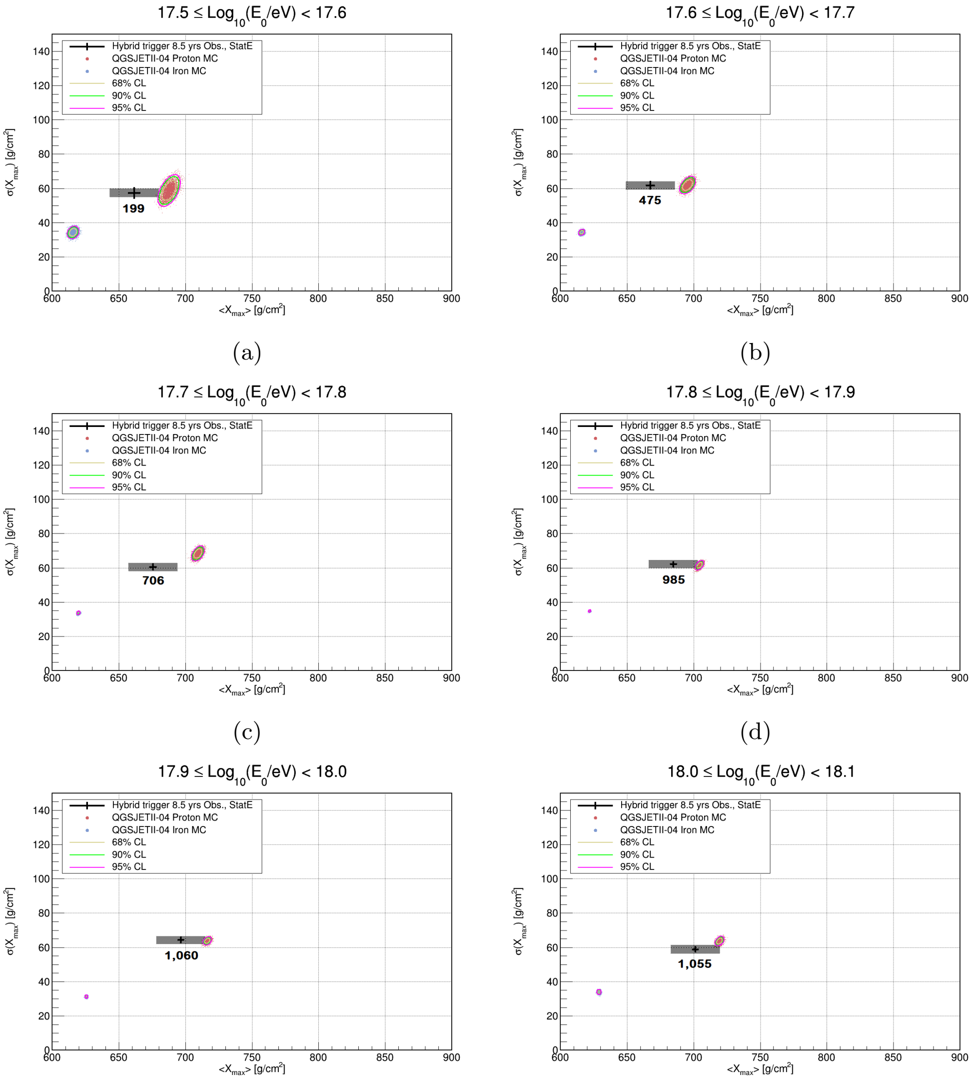

(a) (b)

(c) (d)

(e) (f)

Figure 5.38: Bivariate analysis in the energy range of $17.5 \leq \mathrm{Log}_{10}(\mathrm{E}_0/\mathrm{eV}) < 18.1$. The black crosses indicate the observed data with statistical errors. The shaded rectangles indicate systematic uncertainties in the observation data. Each set of 5,000 points indicated by a cloud of red dots is calculated from the proton MC, while a cloud of blue dots is from the iron-nucleus MC. The 68%, 90%, and 95% confidence ellipses are shown in yellow, green, and magenta, respectively. The numbers of observed events are indicated.

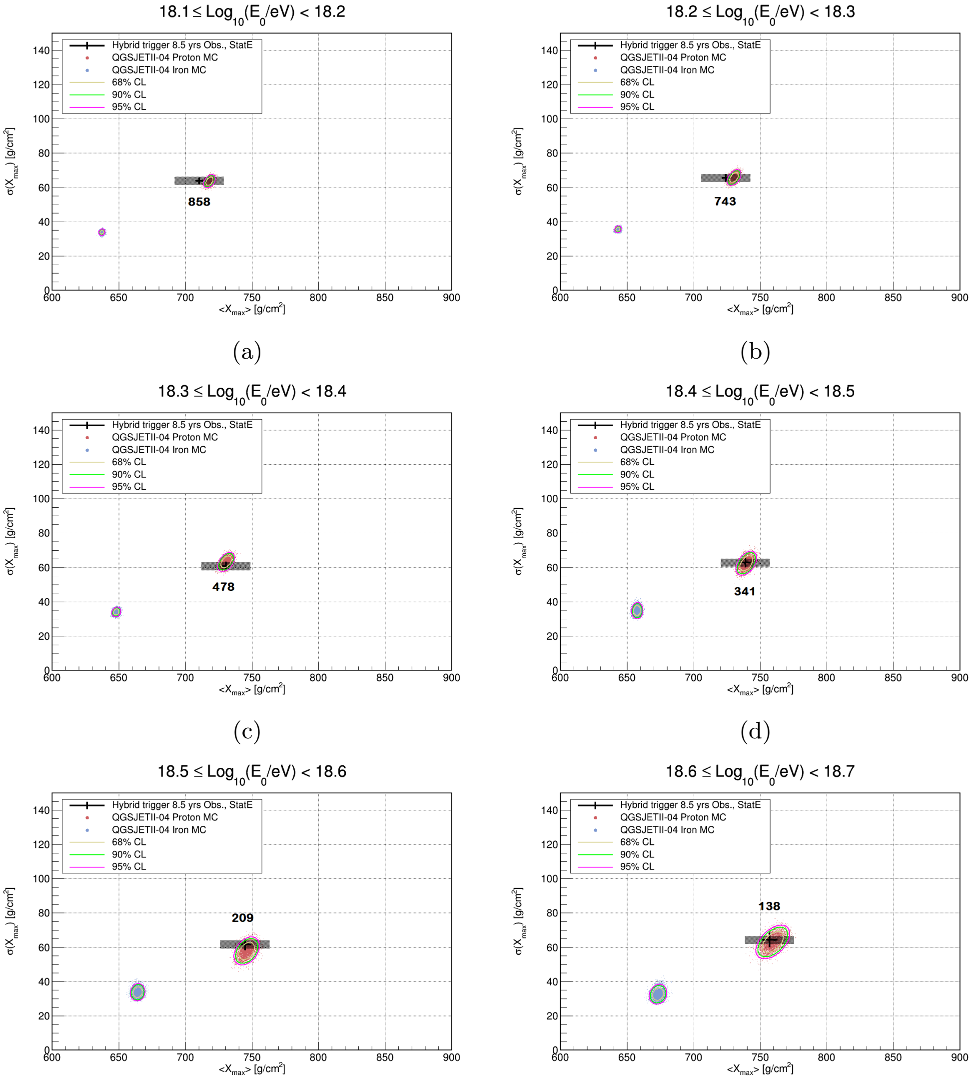

(a) (b)

(c) (d)

(e) (f)

Figure 5.39: Bivariate analysis in the energy range of $18.1 \leq \mathrm{Log}_{10}(\mathrm{E}_0/\mathrm{eV}) < 18.7$. The legends are the same as in Figure 5.38.

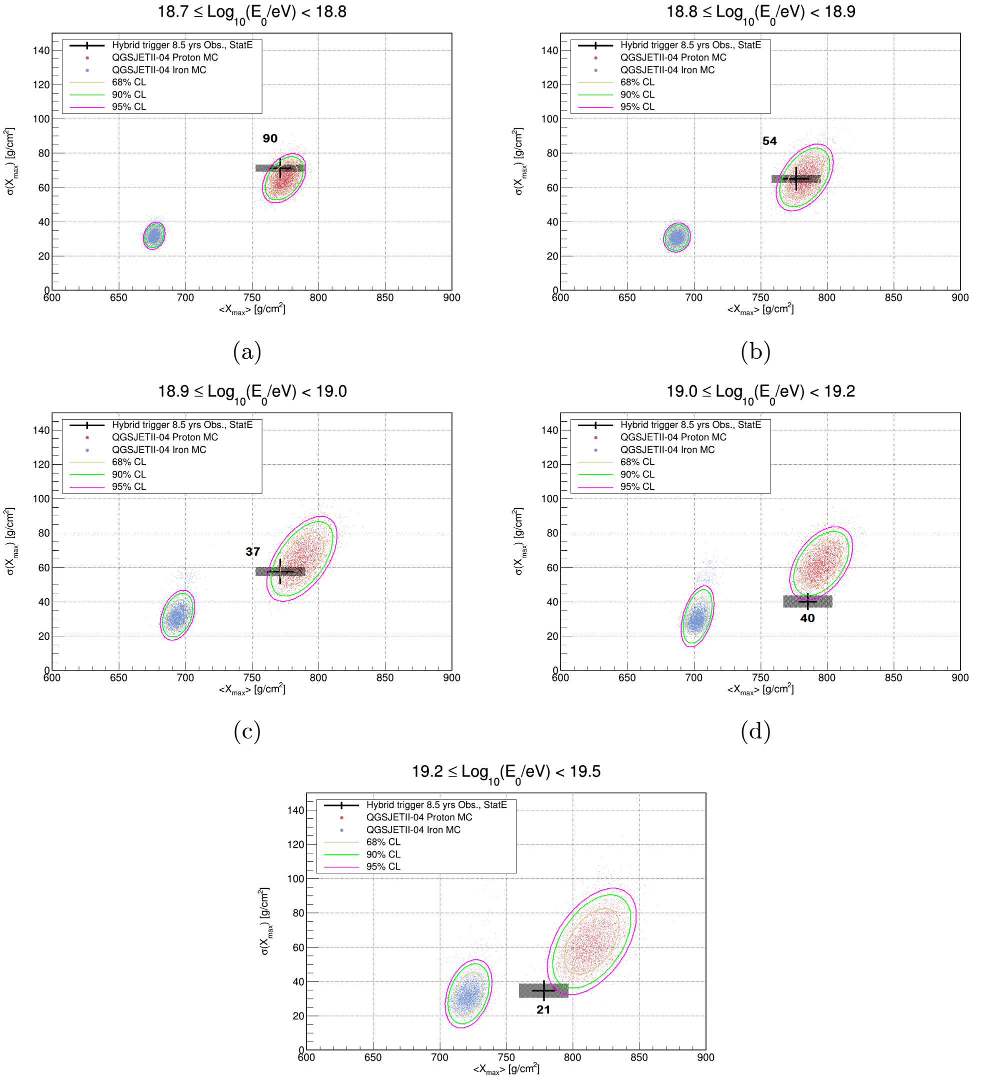

(a) (b)

(c) (d)

(e)

Figure 5.40: Bivariate analysis in the energy range of $18.7 \leq \mathrm{Log}_{10}(\mathrm{E}_0/\mathrm{eV}) < 19.5$. The legends are the same as in Figure 5.38.

5.9 Comparison with Other Measurements

5.9.1 Energy Spectrum

First, the energy spectrum of UHECR measured in the TA hybrid trigger analysis (this analysis) is compared to the result of the conventional BRM/LR hybrid mode of the TA experiment [63]. Since the two results are obtained by the same BRM and LR stations, using the identical atmospheric condition and fluorescence yield model, the two results are expected to be consistent within statistical uncertainties. The comparisons of energy spectra and event statistics are shown in Figure 5.41 on page 123.

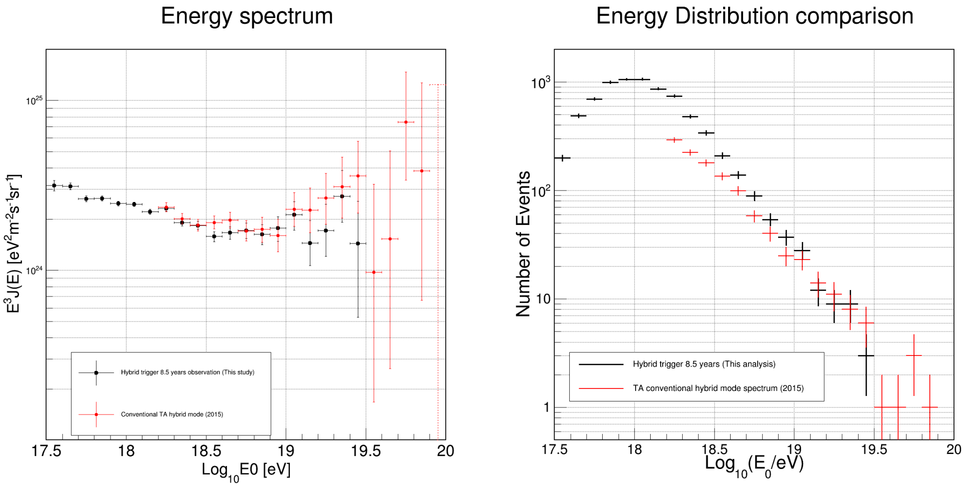

(a) E^3 multiplied spectrum

(b) Energy distribution

Figure 5.41: (a) Comparison of energy spectra between the TA hybrid trigger analysis and the conventional TA BRM/LR hybrid analysis. Since the TA hybrid trigger analysis adopted the energy range cut, the upper limit of the energy spectrum is $10^{19.5}$ eV. (b) Comparison of primary energy distributions between the TA hybrid trigger analysis and the TA BRM/LR conventional hybrid analysis [63].

Figure 5.41 (a) on page 123 shows that the energy spectra of UHECR measured in the TA hybrid trigger analysis (black markers) and the conventional TA hybrid analysis (red markers) are consistent in the overlapping energy region. It also shows that the TA hybrid trigger analysis extended the energy spectrum measured in the hybrid technique from $10^{18.2}$ eV to $10^{17.5}$ eV. Figure 5.41 (b) shows that the TA hybrid trigger analysis presents more event statistics at energies lower than 10^{19} eV.

Secondly, the energy spectrum of UHECR measured in the TA hybrid trigger analysis is compared to energy spectra measured in the other observation modes of the TA experiment: the TALE monocular mode (red) [90], the TALE hybrid mode (magenta) [21], the TA BRM/LR FD monocular mode (blue) [50], the TA conventional BRM/LR hybrid mode (ocher) [63], and the TA SD mode (green) [164]. The results are shown in Figure 5.42 (a) on page 124.

Lastly, the energy spectrum of UHECR measured in the TA hybrid trigger mode is compared to energy spectra measured in the other experiments: the IceTop [10] (blue), the Yakutsk experiment (red) [8], the Tunka experiment (brown) [5], the KASCADE-Grande (green) [4], and the Pierre Auger Observatory (PAO) (gray) [165]. The result is shown in Figure 5.42 (b) on page 124.

Figure 5.42 (a) shows that the energy spectrum of UHECR measured in the TA hybrid trigger analysis is consistent with the results obtained by the other

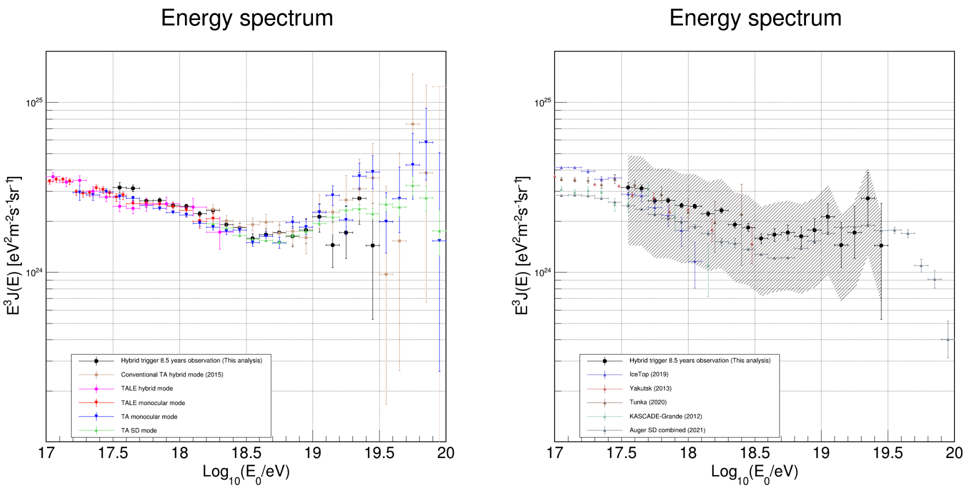

(a) Comparison with the TA results (b) Comparison with the other experiments

Figure 5.42: (a) Comparison of energy spectra between this analysis and the other five observation modes in the TA experiment. The black circles represent the results of this analysis. (b) Comparison of energy spectra between this analysis and the other five experiments. The shaded areas indicate the systematic uncertainties of this analysis.

observation modes of the TA experiment. Figure 5.42 (b) shows that the energy spectrum reported by the PAO is the only result that covers the entire energy range of the TA hybrid trigger analysis. While all results are within systematic uncertainties of the TA hybrid trigger analysis, the flux reported by the PAO is lower than that of the energy spectrum measured in the TA hybrid trigger analysis. The discrepancy could be explained by the difference in energy scales (9%) of two experiments described in Section 1.2.4.

5.9.2 Mass Composition

First, the X_{max} elongation rate measured in the TA hybrid trigger analysis is compared to the X_{max} elongation rates measured in the other TA observation modes: the TALE monocular mode (red) [145], the TALE hybrid mode (magenta) [21] and the conventional TA hybrid mode (green) [22]. The result is shown in Figure 5.43 (a) on page 125.

Secondly, the X_{max} elongation rate measured in the TA hybrid trigger analysis is compared to the X_{max} elongation rates measured in the other experiments as well: the Yakutsk experiment (red) [7], the Tunka experiment (magenta) [6], the HiRes/MIA experiment (green) [166], and the PAO (blue) [14]. The result is shown in Figure 5.43 (b) on page 125. Note that the X_{max} elongation rates (both thrown and reconstructed) of MC simulation sets for the TA hybrid trigger analysis are also plotted to show biases in the reconstruction of X_{max}.

Before interpreting the result shown in Figure 5.43 on page 125, it must be understood that the X_{max} elongation rates reported by various experiments and the other TA observation modes cannot be compared with each other and with the X_{max} elongation rates measured in the TA hybrid trigger analysis. This property arises from the innately different amount of biases in reconstructing X_{max} caused by different MC simulations, instruments, and analysis methods.

Although the results shown here cannot be compared easily, Figure 5.43 (a) on page 125 shows that the TA hybrid trigger analysis (black markers) statistically improved the result reported by the TALE observation modes (red and magenta

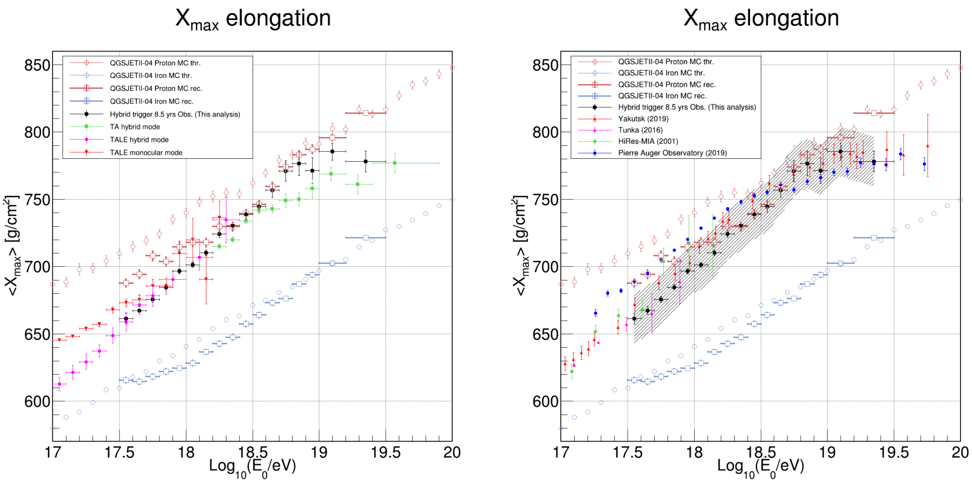

(a) Comparison with the TA results

(b) Comparison with the other experiments

Figure 5.43: (a) Comparison of $\mathrm{X_{max}}$ elongation rates between the TA hybrid trigger analysis and the other three observation modes of the TA experiment. The black circles represent the results of this analysis. (b) Comparison of $\mathrm{X_{max}}$ elongation rates between this analysis and the other four experiments. The shaded areas indicate the systematic uncertainties of this analysis.

markers) in the energy range from $10^{17.6}$ eV to $10^{18.2}$ eV.

Another point to discuss is that the PAO reported a change of the $\mathrm{X_{max}}$ elongation rate (change of the slope of $\mathrm{X_{max}}$ as a function of energy) at $10^{18.32\pm0.03}$ eV. This feature indicates that the mass composition of UHECR becomes the lightest at this energy. Therefore, such a feature can be interpreted that the transition from the heavy composition to the light composition ends at this energy point ($10^{18.32\pm0.03}$ eV) as the energy increases from the 2nd Knee. Nevertheless, the $\mathrm{X_{max}}$ elongation rate alone is not enough to estimate the mass composition of UHECR using the TA hybrid trigger analysis since the bias in reconstructing $\mathrm{X_{max}}$ is not corrected in the TA hybrid trigger analysis.

To compare the mass composition of UHECR further with experiments other than the TA experiment, which utilize different instruments and analysis methods, the mean logarithmic mass <lnA> is adopted. The mean logarithmic mass measured in the TA hybrid trigger mode is compared to the mean logarithmic mass measured in the other TA observation modes: the TALE hybrid mode (blue) [21] and the conventional TA hybrid mode (red) [22]. The result is shown in Figure 5.44 (a) on page 126.

Then the mean logarithmic mass measured in the TA hybrid trigger analysis is compared to the mean logarithmic mass reported by the other experiments: the IceTop (dark red) [10], the Tunka experiment (brown) [6], the Yakutsk experiment (red) [7], and the PAO (blue) [14]. The result is shown in Figure 5.44 (b) on page 126.

As shown in Figure 5.44 (b) on page 126, the mean logarithmic mass measured in the TA hybrid trigger mode (black markers) is consistent with the results of other experiments within systematic uncertainties, except the IceTop result (dark red). The result from the IceTop shows heavier composition between nitrogen and iron at lower energies. This difference might be caused by the muon puzzle described in Section 1.2.4 since the IceTop measures the muon multiplicity of EAS to estimate the mass composition of UHECR, unlike the other experiments that adopted the analysis of $\mathrm{X_{max}}$.

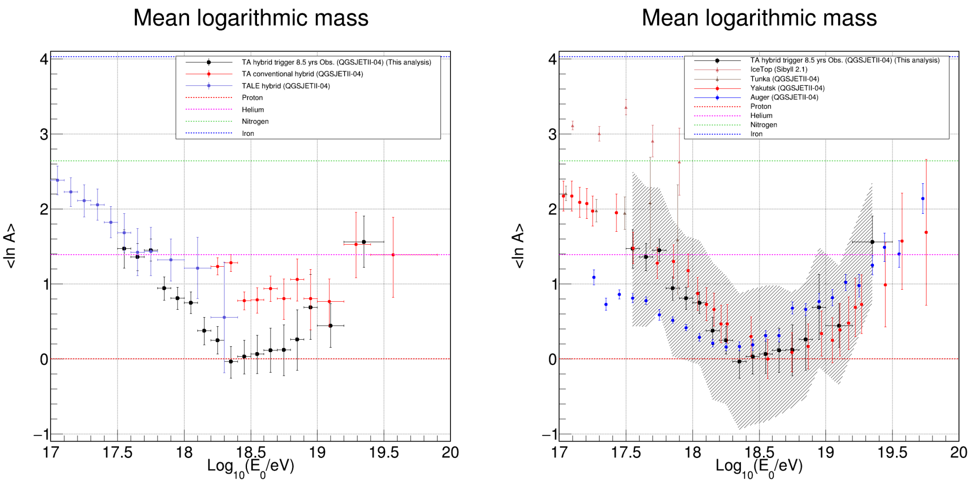

(a) Comparison with the TA results (b) Comparison with the other experiments

Figure 5.44: (a) Comparison of mean logarithmic mass (<lnA>) between this analysis and the other two observation modes in the TA experiment. The black circles represent the results of this analysis. (b) Comparison of <lnA> between this analysis and the other four experiments. The shaded areas indicate the systematic uncertainties of this analysis.

Another point to discuss in Figure 5.44 (b) on page 126 is that the <lnA> results from the TA hybrid trigger analysis (black), the PAO (blue), and the Yakutsk experiment (red) show a similar change in the UHECR mass composition. The mass composition of UHECR measured in the PAO and the Yakutsk experiment becomes lighter as energy increases from the 2nd Knee to the energy range from $10^{18.3}$ eV to $10^{18.6}$ eV. For the TA hybrid trigger analysis, the break energy is determined to be $10^{18.43\pm0.06}$ eV, where the transition of mass composition is completed. This result is comparable to $10^{18.32\pm0.03}$ eV determined by the PAO and $\sim10^{18.55}$ eV in the result of the Yakutsk experiment. However, the Yakutsk experiment did not determine the break point with the corresponding error.

On the other hand, as shown in Figure 5.44 (a) on page 126, such a trend (break feature) seems to exist from the two former results. However, it should be noted that the energy range from $10^{18.3}$ eV to $10^{18.6}$ eV is at the transition between the two conventional observation modes (up to $10^{18.4}$ eV for the TALE hybrid analysis and down to $10^{18.2}$ eV for the conventional TA hybrid analysis). Since the TA hybrid trigger analysis covers the energy range from $10^{17.5}$ eV to $10^{19.5}$ eV, the energy range of $10^{18.3-18.6}$ eV is investigated.

As the summary of the studies of the slopes and break in <lnA> as a function of primary energy, it is shown that the TALE hybrid and conventional TA hybrid analyses did not measure the break energy since they cover the energies below and above $\sim10^{18.2}$ eV, respectively. Furthermore, the <lnA> results from the IceTop and the Tunka experiment also did not report the break energy since they cover the energies below 10^{18} eV.

The results from the TA hybrid trigger analysis and the Yakutsk experiment, which are obtained by the Northern Hemisphere observatories, are consistent within statistical uncertainties. In contrast, the <lnA> values below $10^{18.0}$ eV from the PAO are smaller (indicating lighter mass composition) than those from the TA hybrid trigger analysis and the Yakutsk experiment.

Still, the results obtained by the TA, PAO, and Yakutsk experiment are consistent considering the systematic uncertainties of the TA hybrid trigger analysis. The Yakutsk experiment did not show the systematical uncertainties of their <lnA> result [7].

Figure 5.44 (a) on page 126 shows the discrepancy between the former result of <lnA> from the conventional TA hybrid analysis and the result from the TA hybrid trigger analysis. The difference between the two observation modes is examined to understand this discrepancy.

1. The difference in the EAS reconstruction principle

   By adopting a previously developed hybrid technique to reconstruct EAS with only one SD information [52], the geometric reconstruction procedure of the TA hybrid trigger analysis minimizes the χ^2 of PMT signal timings assisted by one anchor SD. On the other hand, the conventional TA hybrid analysis adopts a different hybrid technique to reconstruct EAS [22].

   Nevertheless, the conventional TA hybrid analysis has the common systematic uncertainties in reconstructing X_{max} with the TA hybrid trigger analysis since the two analyses are based on the FD data obtained by the same BRM and LR stations.

   On the other hand, it is estimated that ± 14.1 g/cm^2 of systematic uncertainties in X_{max} between the TA hybrid trigger analysis and the conventional TA hybrid analysis exists [22]. Figure 5.45 on page 128 shows the comparison of <lnA> measured in the TA hybrid trigger and the conventional TA hybrid analyses. It is shown that the difference in <lnA> between the two results can be understood considering the total uncertainty, which is the linear sum of statistical and systematical uncertainties.

2. The difference in event statistics

   Another difference between the two analyses is the dataset. As mentioned in Section 3.1, the TA hybrid trigger analysis (this analysis) uses only observation data acquired by the BRM station and its corresponding SD sub-array and the LR station and its corresponding SD sub-array. This fundamental principle of the TA hybrid trigger mode excludes the data obtained by the SK sub-array since the TA hybrid trigger system installed at the BRM and LR stations does not trigger the SK sub-array as described in Chapter 3.

   Therefore, the TA hybrid trigger analysis does not include the EAS events that fell on the SK sub-array. In contrast, the SD data of the EAS events that fell on any sub-array are used in the conventional TA hybrid analysis. This property implies that the aperture of the TA hybrid trigger analysis is smaller than that of the conventional TA hybrid analysis at higher energies. The difference in apertures is the main reason for the different event statistics.

In conclusion, the TA hybrid trigger analysis firstly confirmed the energy point $10^{18.43\pm0.06}$ for the TA experiment. This energy point is where the transition of UHECR mass composition from heavier to lighter above the 2nd Knee is completed. This feature is examined with the different quality cut conditions and the hadronic interaction model. The chance probabilities and significances of this result are estimated as well. It is confirmed that the result obtained by the TA hybrid trigger analysis is consistent with the results of the TALE hybrid mode of the TA experiment and the Yakutsk experiment. The TA hybrid trigger analysis result can also be understood within the existing systematic uncertainties between the TA hybrid trigger and the conventional TA hybrid analyses.

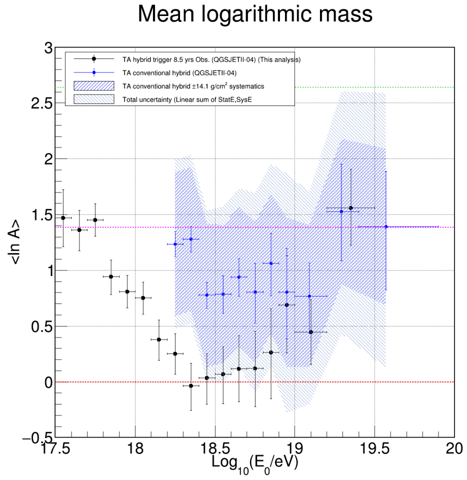

Figure 5.45: Comparison of <lnA> between the TA hybrid trigger and conventional TA hybrid analyses. The blue shaded areas indicate ±14.1 g/cm^2 of systematic uncertainties between the two observation modes. The light blue shaded areas indicate total uncertainty as the linear sum of the statistical and systematical uncertainties.

Chapter 6

Author's Contributions to the Telescope Array Hybrid Trigger Analysis

The author's contributions to the analysis of the Telescope Array (TA) hybrid trigger observation mode in this thesis are summarized as follows:

1. Examination of the analyzable period for the 8.5-year observations using the TA hybrid trigger mode:

   The author carefully examined the on-time of the TA hybrid trigger mode by considering various factors such as the weather cut, dead time of a Fluorescence Detector (FD) station, Veto time of the TA hybrid trigger system, running state of the TA hybrid trigger system, and communication status between the FD station and its corresponding Surface Detector (SD) sub-array. This step was crucial in determining the periods suitable for analysis and estimating the on-time, which is also used for generating the detector Monte Carlo (MC) simulations.

2. Generation of detector MC simulations and an observation dataset:

   The author generated a set of detector MC simulations using a library of Cosmic Ray Simulations for KAscade (CORSIKA) Extensive Air Shower (EAS) simulations and a set of Geant4 (GEometry ANd Tracking) detector models, which are prepared by collaborative efforts. The author also estimated the missing energy of CORSIKA-generated EAS using the QGSJET-II-04 hadronic interaction model. Additionally, the author prepared the observation dataset for the 8.5-year observations using the TA hybrid trigger mode based on the estimated on-time.

3. Determination of the reconstruction conditions:

   The author examined and determined the reconstruction conditions before applying the hybrid technique to analyze the TA hybrid trigger mode. This examination included evaluating the SD pre-reconstruction conditions to select SDs with EAS signals and reject background SDs. The author also determined the conditions for the quality cut in the TA hybrid trigger mode, including establishing the condition based on fiducial volume.

4. Data analysis:

   The author wrote programming codes to plot all data presented in the thesis, as well as the programming codes to analyze the results obtained by utilizing the common analysis framework of the TA experiment. These codes facilitated the analysis of the TA hybrid trigger data and the generation of relevant plots and figures.

Overall, the author's contributions encompassed the careful examination of analyzable periods, generation of MC simulations and observation dataset, determination of reconstruction conditions, and data analysis using customized programming codes.

Chapter 7

Conclusions

Cosmic rays were discovered more than a century ago and have been studied ever since. However, the origins of the highest energy cosmic rays remain a mystery. To clarify the unknown properties of Ultra-High-Energy Cosmic Rays (UHECR), the Telescope Array (TA) experiment in Utah, United States of America, started operation in 2008 as the largest UHECR observatory in the Northern Hemisphere. In addition, the Pierre Auger Observatory (PAO), the largest UHECR observatory in the world, has been operating in the Southern Hemisphere. Since the two observatories mainly cover different parts of the sky, it is essential for both observatories to confirm the physics results independently.

The three Fluorescence Detector (FD) stations and 507 Surface Detectors (SDs) allow the TA experiment to track physical signals from Extensive Air Showers (EAS) initiated by incident UHECR with two independent methods: fluorescence detection and surface detection. Since the FD monocular analysis only utilizes the information on Photomultiplier tube (PMT) timings obtained by an FD station to reconstruct EAS geometrically, the resolutions in reconstructing primary energy and X_{max} are relatively low. However, if the information on the lateral particle density and arrival time of EAS acquired by the surface detectors is provided to the FD monocular observation mode, the resolutions in reconstructing primary energy and X_{max} are improved.

Meanwhile, the difference in apertures of the FD monocular observation and SD observation modes results in approximately an order of magnitude difference in analyzable energy ranges between them ($>10^{17.2}$ eV for the FD monocular mode and $>10^{18.2}$ eV for the SD mode). For this reason, the conventional hybrid analyses of the TA experiment, which adopted a hybrid technique utilizing data obtained by the FD and SD separately, only analyzed UHECR energies above $10^{18.2}$ eV.

To lower the energy threshold of the conventional hybrid analysis of the TA experiment, a hybrid trigger system was developed. The TA hybrid trigger system implemented in the Black Rock Mesa (BRM) and Long Ridge (LR) stations has been running since October 2010. The TA hybrid trigger system is an external trigger system for the TA SD array. Whenever an FD station detects an EAS-like signal, the FD station triggers the corresponding SD sub-array to acquire the data of EAS as well. This system lowers the energy threshold of hybrid analysis to $10^{17.5}$ eV for the TA experiment.

Monte Carlo (MC) simulation studies dedicated to the TA hybrid trigger observation mode showed that the resolutions in reconstructing primary energy and X_{max} are 13% and 31 g/cm^2 in the energy range of $17.5 \leq \mathrm{Log}_{10}(\mathrm{E}_0/\mathrm{eV}) < 18.5$, respectively, and 8.3% and 28 g/cm^2 in the energy range of $18.5 \leq \mathrm{Log}_{10}(\mathrm{E}_0/\mathrm{eV}) < 19.5$, respectively. This result is a significant improvement from the typical resolutions of the FD monocular reconstruction, which are 17% for primary energy and 72 g/cm^2 for X$_{\rm max}$.

The energy spectrum of UHECR and the depths of maximum shower development (X$_{\rm max}$) of UHECR-induced EAS were measured in this analysis using data from 8.5 years of operations at the BRM and LR stations from October 2010 to June 2019 using the hybrid trigger observation mode of the TA experiment.

The energy spectrum of UHECR measured in the TA hybrid trigger analysis is consistent with previous results reported by other observation modes of the TA experiment. The lower limit of the energy spectrum measured in the conventional TA hybrid analysis was extended from $10^{18.2}$ eV to $10^{17.5}$ eV in the TA hybrid trigger analysis with higher event statistics below $10^{19.0}$ eV.

Similar to the other observation modes of the TA experiment, the result obtained by the TA hybrid trigger analysis shows higher fluxes than the result obtained by the PAO. This difference can be explained by the difference in energy scales (9%) reported by the joint working group of two collaborations.

On the mass composition of UHECR using X$_{\rm max}$ measurements, the PAO reported a change of the X$_{\rm max}$ elongation rate (the slope of X$_{\rm max}$ as a function of energy) at $10^{18.32\pm0.03}$ eV, indicating that the mass composition of UHECR is the lightest at this energy point. It can be interpreted that the transition from heavy composition to light composition ends at this energy point ($10^{18.32\pm0.03}$ eV) as energy increases above the 2nd Knee.

Due to various amounts of bias in the reconstruction of X$_{\rm max}$ in different experiments, the X$_{\rm max}$ elongation rates reported by various experiments cannot be compared simply with the X$_{\rm max}$ elongation rate measured in this analysis. For example, the PAO reported X$_{\rm max}$ elongation rates without biases, as the biases are negligible in the analysis by the PAO. Whereas the X$_{\rm max}$ elongation rates reported by the TA experiment, as well as the TA hybrid trigger analysis, include biases.

The mean logarithmic mass <lnA>, which is derived from X$_{\rm max}$ values obtained by both the MC simulations and observed data, is analyzed to estimate the mass composition. The mean logarithmic mass of UHECR measured in the TA hybrid trigger analysis confirmed the result reported by the PAO for the first time in the TA experiment. The broken line fit to the observed <lnA> values determined the break energy at $10^{18.43\pm0.06}$ eV, which is compatible with the result reported by the PAO.

The slopes of change in mass composition for QGSJET-II-04 proton MC simulations measured in the TA hybrid trigger analysis are -2.0±0.25 $\frac{d\mathrm{<lnA>}}{d\mathrm{Log}_{10}(\mathrm{E}_0/\mathrm{eV})}$ (for $\mathrm{E}_0 \leq 10^{18.43\pm0.06}$ eV) and +1.4±0.37 $\frac{d\mathrm{<lnA>}}{d\mathrm{Log}_{10}(\mathrm{E}_0/\mathrm{eV})}$ (for $\mathrm{E}_0 > 10^{18.43\pm0.06}$ eV). The local significance ($\sigma_{\rm local}$) of the change of the two slopes (ΔS = 3.4) is 7.6σ. The chance probabilities of exceeding ΔS is $<1\times10^{-7}$ for 10^7 trials, which is equivalent to a one-sided global significance ($\sigma_{\rm global}$) of $>5.1\sigma$.

The efficiency of the SD self-trigger of the TA experiment, which so far had been estimated solely from MC simulations, is measured for the first time from the experimental data of the TA hybrid trigger analysis (this analysis). The SD self-trigger efficiency measured in the TA hybrid trigger analysis is roughly consistent with that estimated by SD MC simulations, although the efficiency can depend on quality cuts. The SD self-trigger is confirmed to have an efficiency of ~100% above $10^{18.7}$ eV.

Appendix A
Data/MC Comparison by FD Station

This appendix shows each FD station's data/MC comparison results. Figures A.1 - A.16 show the comparison of proton MC simulations, iron-nucleus MC simulations, and observed data. The left and right panels show the results obtained by the BRM and LR stations, respectively. The upper and lower panels show results in the energy ranges of $17.5 \leq \mathrm{Log_{10}(E_0/eV)} < 18.5$ and $18.5 \leq \mathrm{Log_{10}(E_0/eV)} < 19.5$, respectively. Table A.1 below shows the list of observables and page numbers to find each plot.

Table A.1: The list of observables that are compared in this appendix and the page numbers of the plots.

Observable	Page
θ Zenith	134
ϕ Azimuth	135
EAS core position (West to East)	136
EAS core position (South to North)	137
$\mathrm{R_p}$	138
Angular velocity	139
ψ (SDP angle)	140
Cherenkov fraction	141
Minimum viewing angle	142
Number of good PMTs	143
Track length	144
Time extent	145
$\mathrm{X_{start}}$	146
$\mathrm{X_{end}}$	147
$\mathrm{X_{max}}$	148
Energy	149

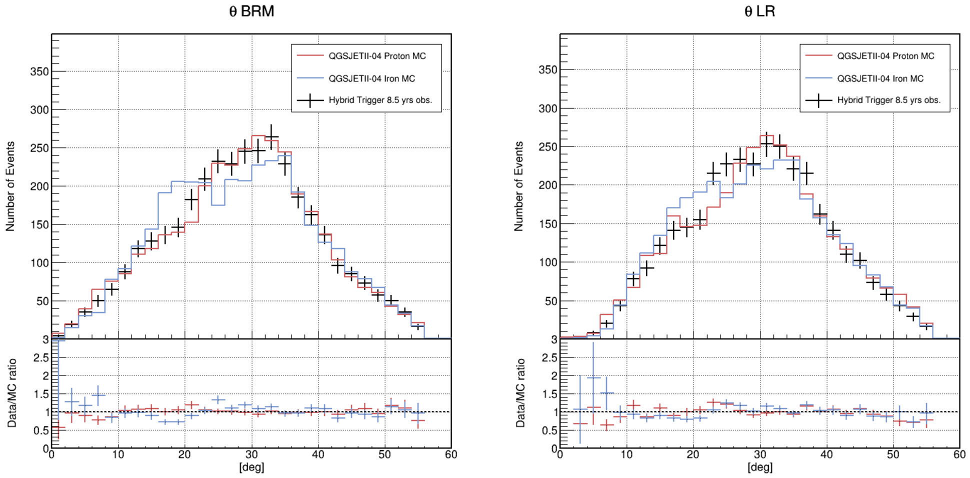

(a) BRM 17.5 ≤ $\mathrm{Log}_{10}(\mathrm{E}_0/\mathrm{eV}) < 18.5$ (b) LR 17.5 ≤ $\mathrm{Log}_{10}(\mathrm{E}_0/\mathrm{eV}) < 18.5$

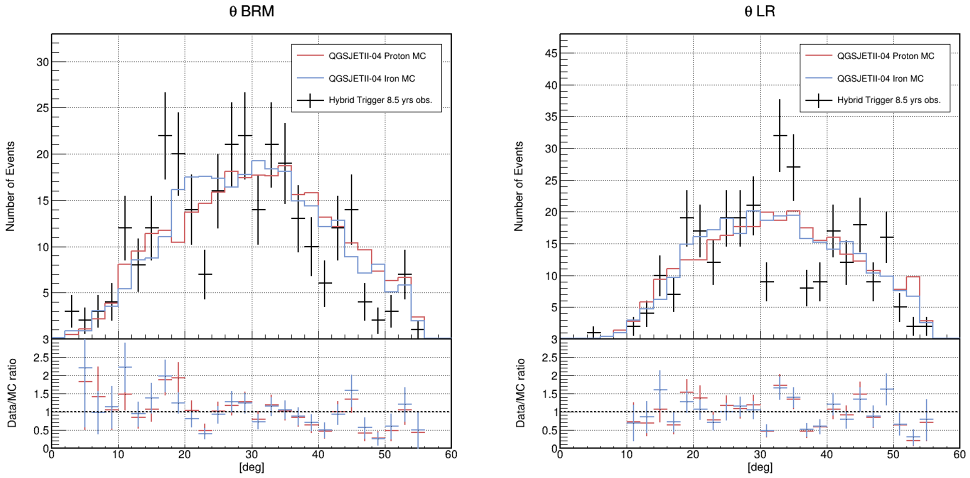

(c) BRM 18.5 ≤ $\mathrm{Log}_{10}(\mathrm{E}_0/\mathrm{eV}) < 19.5$ (d) LR 18.5 ≤ $\mathrm{Log}_{10}(\mathrm{E}_0/\mathrm{eV}) < 19.5$

Figure A.1: Data/MC comparison of θ (Zenith). The left column shows the BRM station and the right column shows the LR station. The upper row shows the energy range of 17.5 ≤ $\mathrm{Log}_{10}(\mathrm{E}_0/\mathrm{eV}) < 18.5$, and the lower row shows the energy range of 18.5 ≤ $\mathrm{Log}_{10}(\mathrm{E}_0/\mathrm{eV}) < 19.5$.

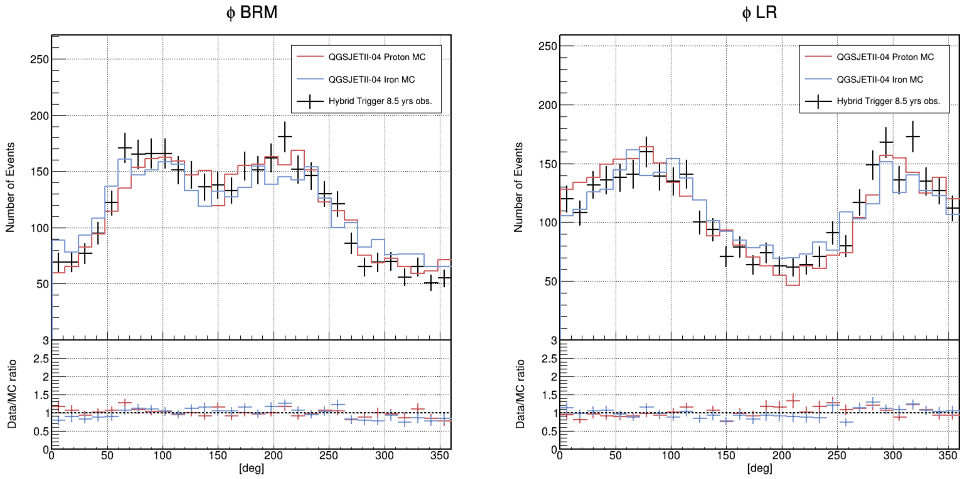

(a) BRM 17.5 $\leq$ Log$_{10}$(E$_0$/eV) $<$ 18.5 (b) LR 17.5 $\leq$ Log$_{10}$(E$_0$/eV) $<$ 18.5

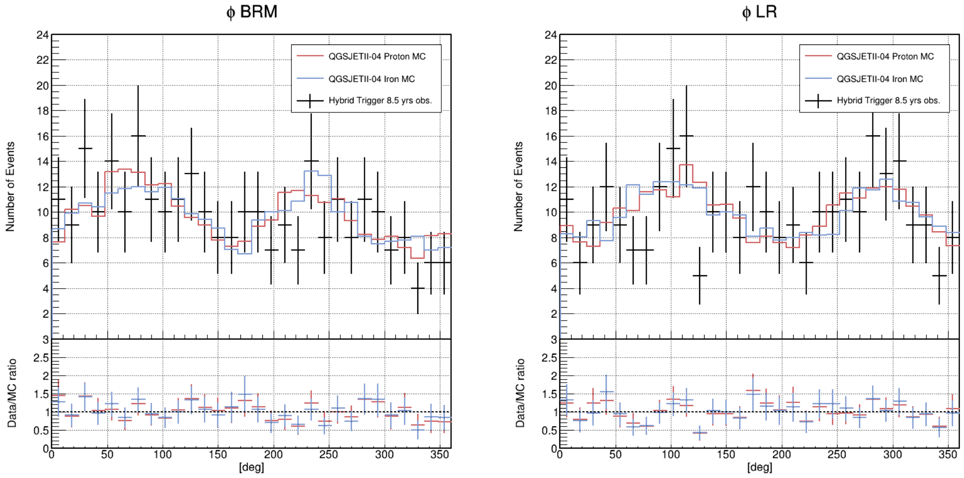

(c) BRM 18.5 $\leq$ Log$_{10}$(E$_0$/eV) $<$ 19.5 (d) LR 18.5 $\leq$ Log$_{10}$(E$_0$/eV) $<$ 19.5

Figure A.2: Data/MC comparison of ϕ (Azimuth).

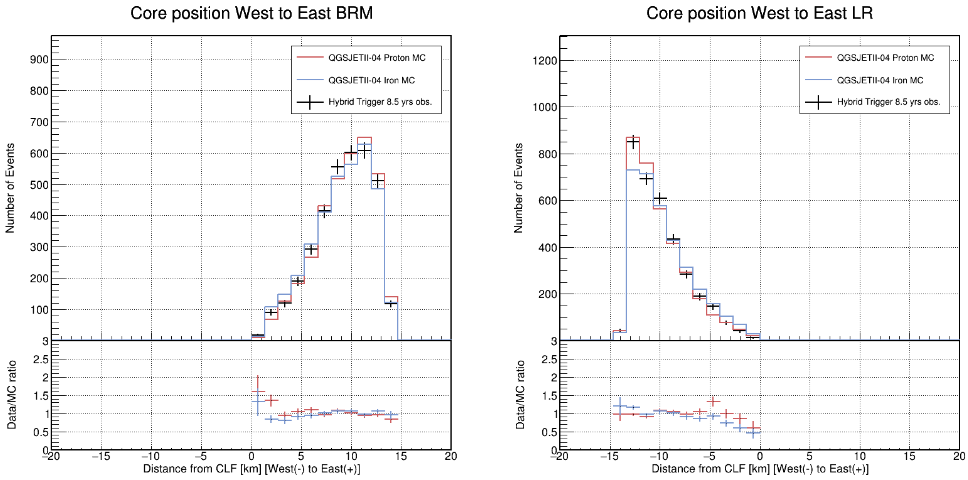

(a) BRM $17.5 \leq \mathrm{Log}_{10}(\mathrm{E}_0/\mathrm{eV}) < 18.5$ (b) LR $17.5 \leq \mathrm{Log}_{10}(\mathrm{E}_0/\mathrm{eV}) < 18.5$

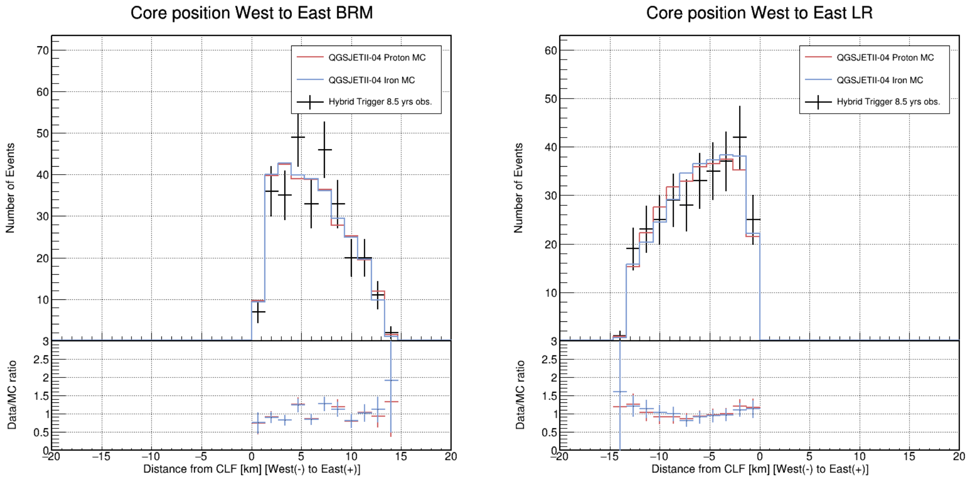

(c) BRM $18.5 \leq \mathrm{Log}_{10}(\mathrm{E}_0/\mathrm{eV}) < 19.5$ (d) LR $18.5 \leq \mathrm{Log}_{10}(\mathrm{E}_0/\mathrm{eV}) < 19.5$

Figure A.3: Data/MC comparison of EAS core positions (West to East).

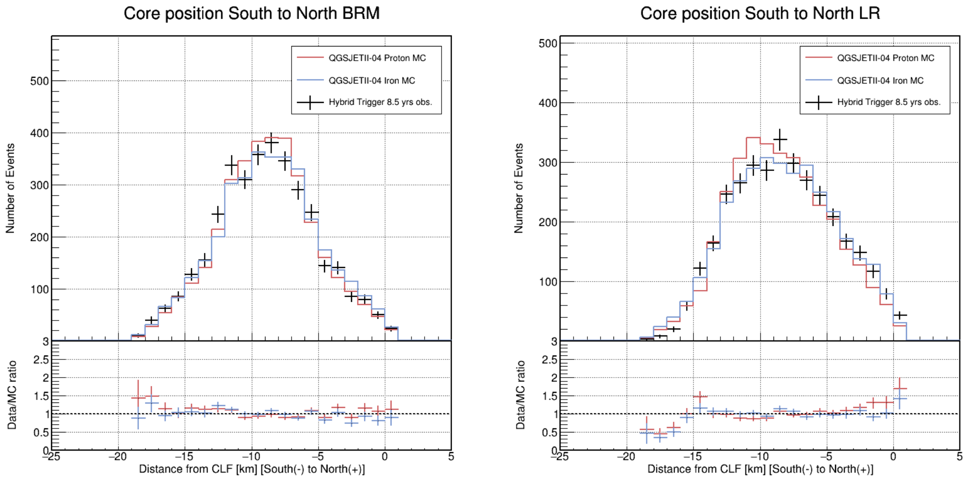

(a) BRM $17.5 \leq \mathrm{Log}_{10}(\mathrm{E}_0/\mathrm{eV}) < 18.5$ (b) LR $17.5 \leq \mathrm{Log}_{10}(\mathrm{E}_0/\mathrm{eV}) < 18.5$

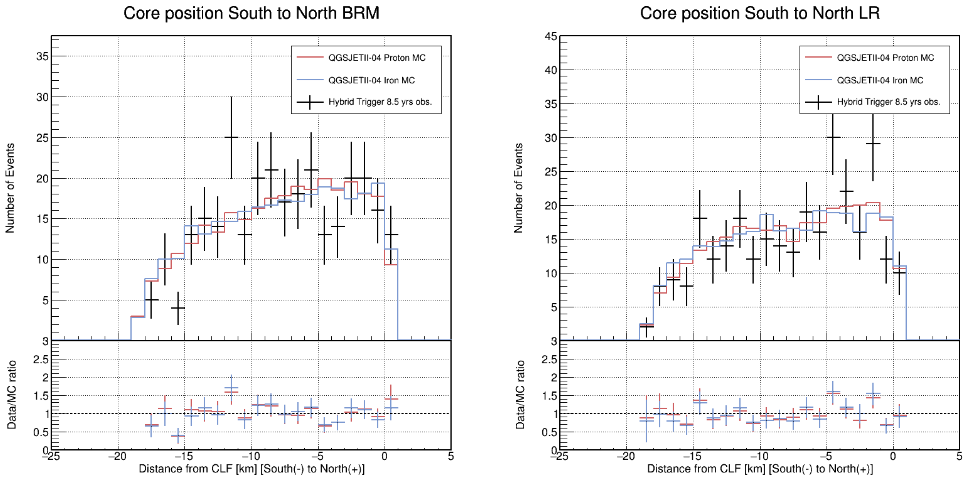

(c) BRM $18.5 \leq \mathrm{Log}_{10}(\mathrm{E}_0/\mathrm{eV}) < 19.5$ (d) LR $18.5 \leq \mathrm{Log}_{10}(\mathrm{E}_0/\mathrm{eV}) < 19.5$

Figure A.4: Data/MC comparison of EAS core positions (South to North).

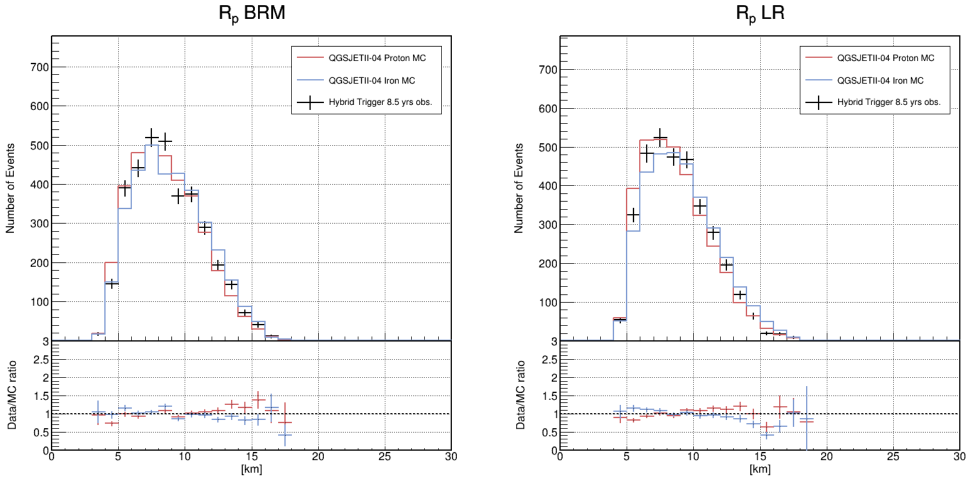

(a) BRM $17.5 \leq \mathrm{Log}_{10}(\mathrm{E}_0/\mathrm{eV}) < 18.5$

(b) LR $17.5 \leq \mathrm{Log}_{10}(\mathrm{E}_0/\mathrm{eV}) < 18.5$

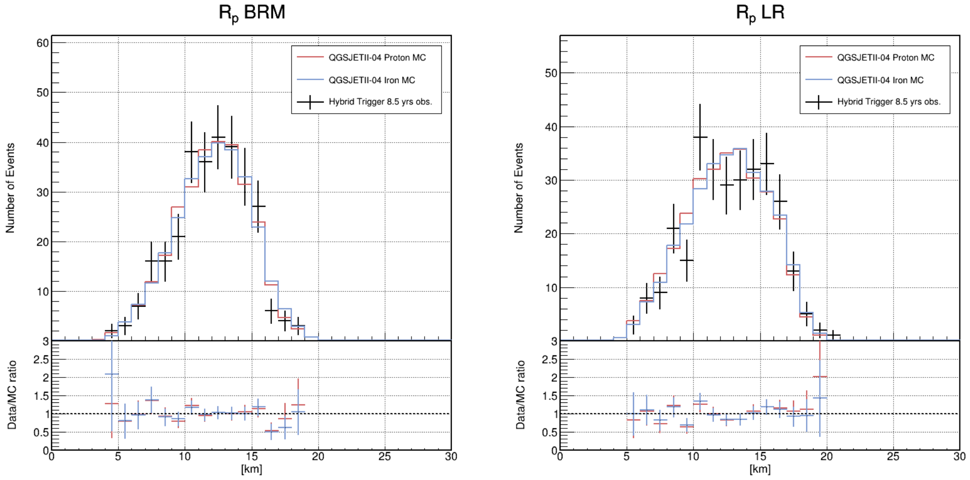

(c) BRM $18.5 \leq \mathrm{Log}_{10}(\mathrm{E}_0/\mathrm{eV}) < 19.5$

(d) LR $18.5 \leq \mathrm{Log}_{10}(\mathrm{E}_0/\mathrm{eV}) < 19.5$

Figure A.5: Data/MC comparison of $\mathrm{R_p}$ (impact parameter).

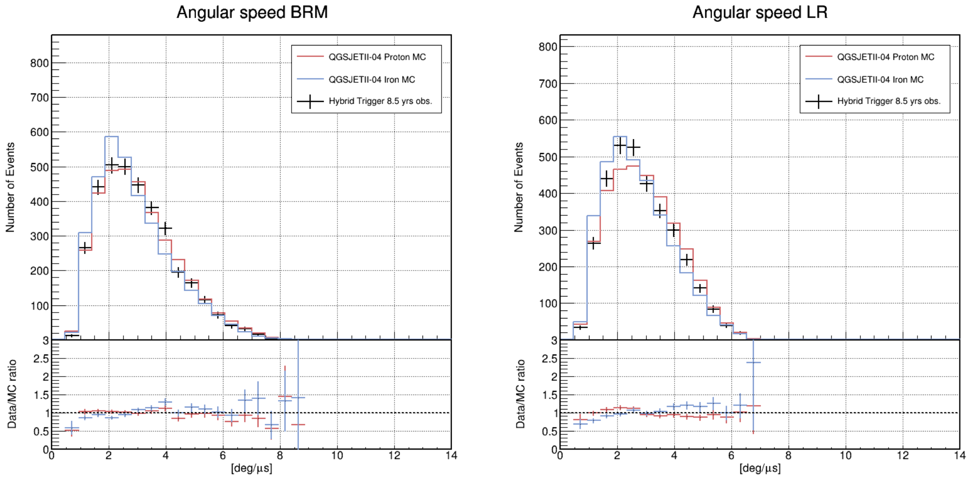

(a) BRM 17.5 ≤ $\mathrm{Log}_{10}(\mathrm{E}_0/\mathrm{eV})$ < 18.5 (b) LR 17.5 ≤ $\mathrm{Log}_{10}(\mathrm{E}_0/\mathrm{eV})$ < 18.5

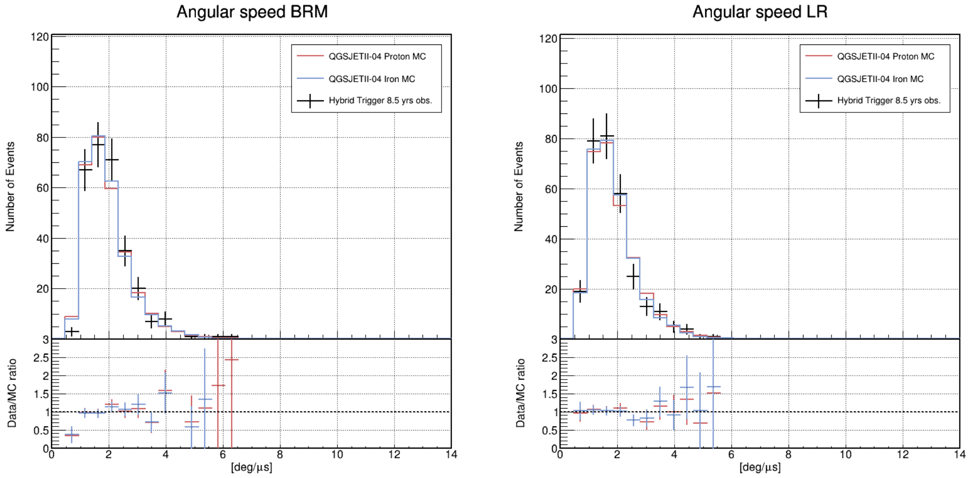

(c) BRM 18.5 ≤ $\mathrm{Log}_{10}(\mathrm{E}_0/\mathrm{eV})$ < 19.5 (d) LR 18.5 ≤ $\mathrm{Log}_{10}(\mathrm{E}_0/\mathrm{eV})$ < 19.5

Figure A.6: Data/MC comparison of angular velocity.

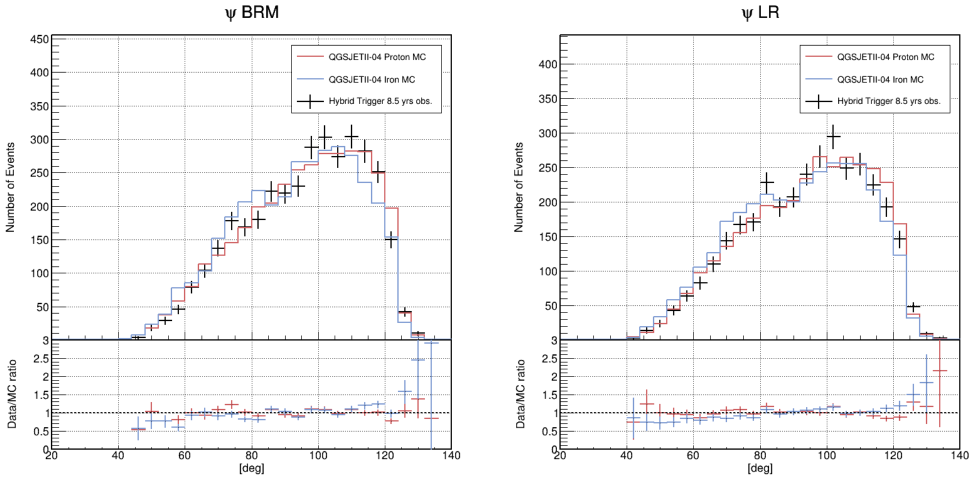

(a) BRM 17.5 ≤ $\mathrm{Log}_{10}(\mathrm{E}_0/\mathrm{eV}) < 18.5$ (b) LR 17.5 ≤ $\mathrm{Log}_{10}(\mathrm{E}_0/\mathrm{eV}) < 18.5$

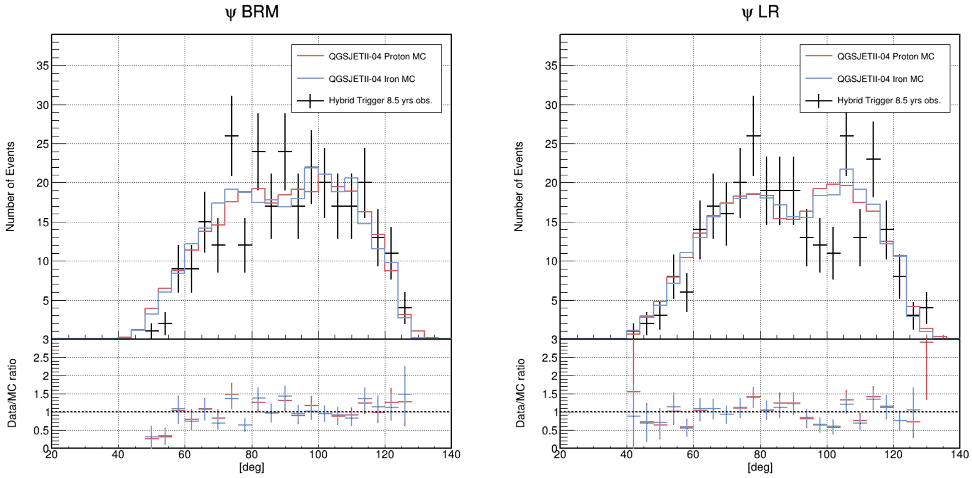

(c) BRM 18.5 ≤ $\mathrm{Log}_{10}(\mathrm{E}_0/\mathrm{eV}) < 19.5$ (d) LR 18.5 ≤ $\mathrm{Log}_{10}(\mathrm{E}_0/\mathrm{eV}) < 19.5$

Figure A.7: Data/MC comparison of ψ (SDP angle).

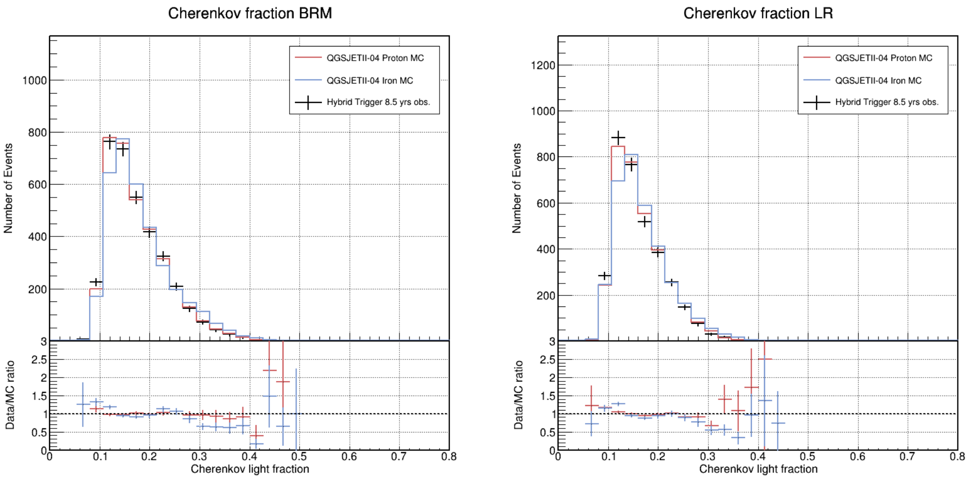

(a) BRM 17.5 ≤ $\mathrm{Log}_{10}(\mathrm{E}_0/\mathrm{eV})$ < 18.5 (b) LR 17.5 ≤ $\mathrm{Log}_{10}(\mathrm{E}_0/\mathrm{eV})$ < 18.5

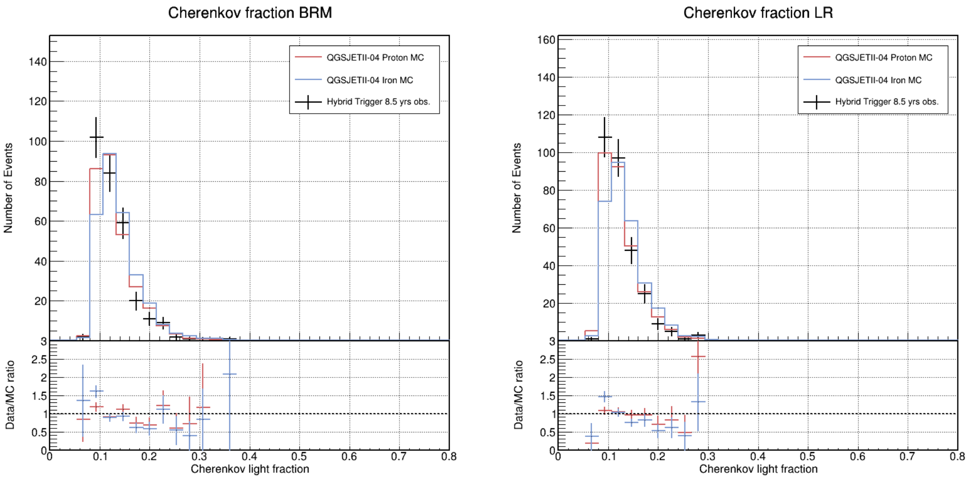

(c) BRM 18.5 ≤ $\mathrm{Log}_{10}(\mathrm{E}_0/\mathrm{eV})$ < 19.5 (d) LR 18.5 ≤ $\mathrm{Log}_{10}(\mathrm{E}_0/\mathrm{eV})$ < 19.5

Figure A.8: Data/MC comparison of the ratio of Cherenkov radiation.

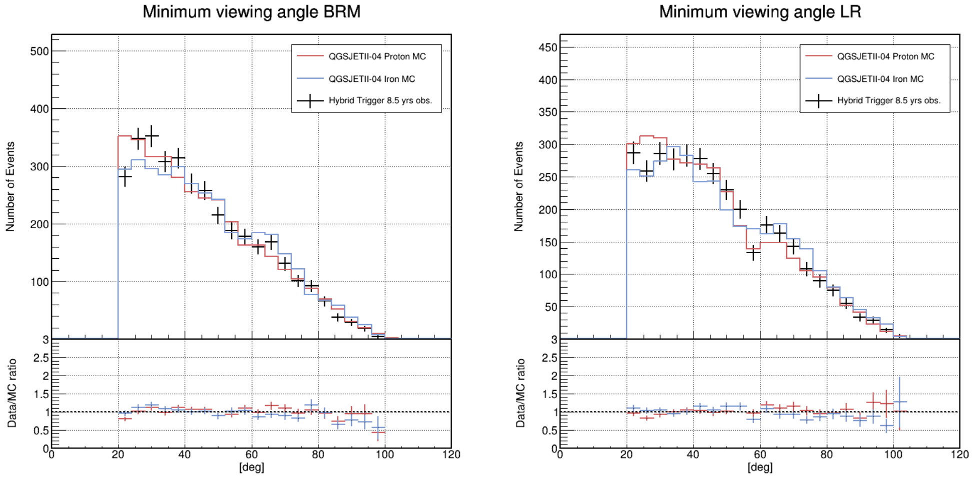

(a) BRM $17.5 \leq \mathrm{Log}_{10}(\mathrm{E}_0/\mathrm{eV}) < 18.5$ (b) LR $17.5 \leq \mathrm{Log}_{10}(\mathrm{E}_0/\mathrm{eV}) < 18.5$

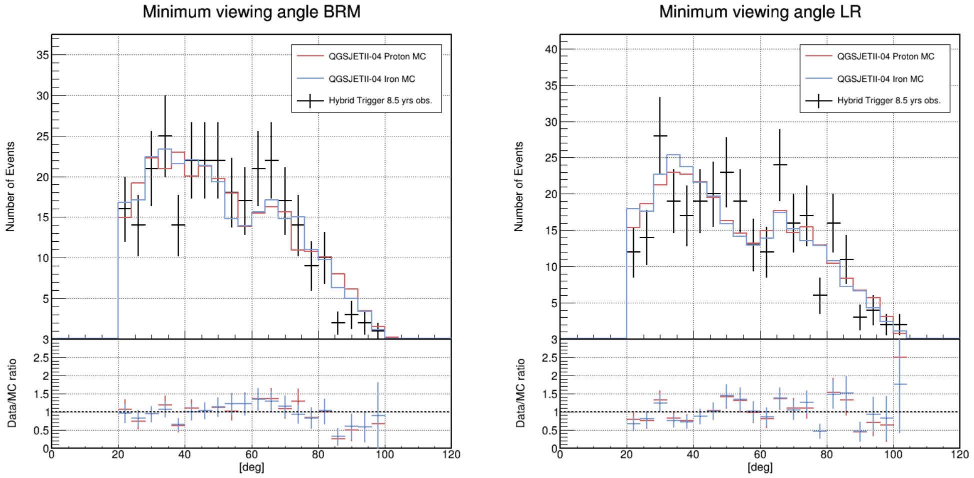

(c) BRM $18.5 \leq \mathrm{Log}_{10}(\mathrm{E}_0/\mathrm{eV}) < 19.5$ (d) LR $18.5 \leq \mathrm{Log}_{10}(\mathrm{E}_0/\mathrm{eV}) < 19.5$

Figure A.9: Data/MC comparison of minimum viewing angle.

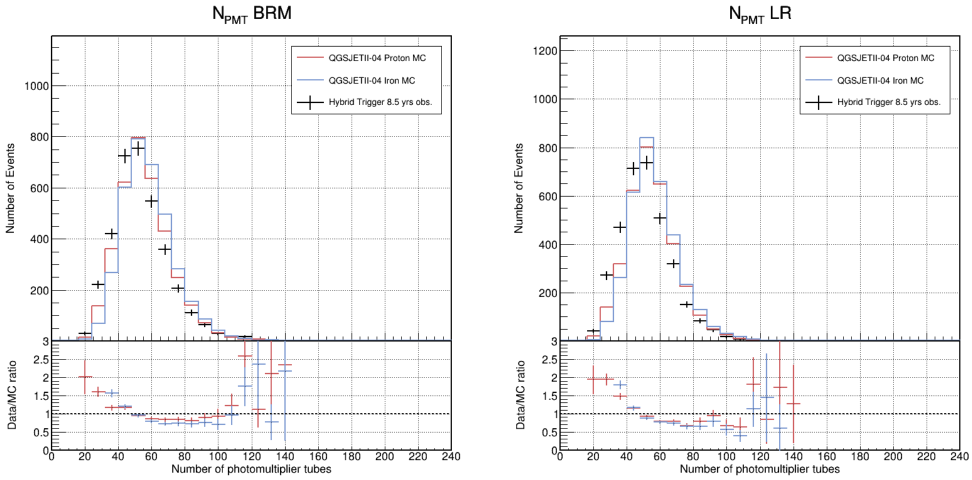

(a) BRM $17.5 \leq \mathrm{Log}_{10}(\mathrm{E}_0/\mathrm{eV}) < 18.5$ (b) LR $17.5 \leq \mathrm{Log}_{10}(\mathrm{E}_0/\mathrm{eV}) < 18.5$

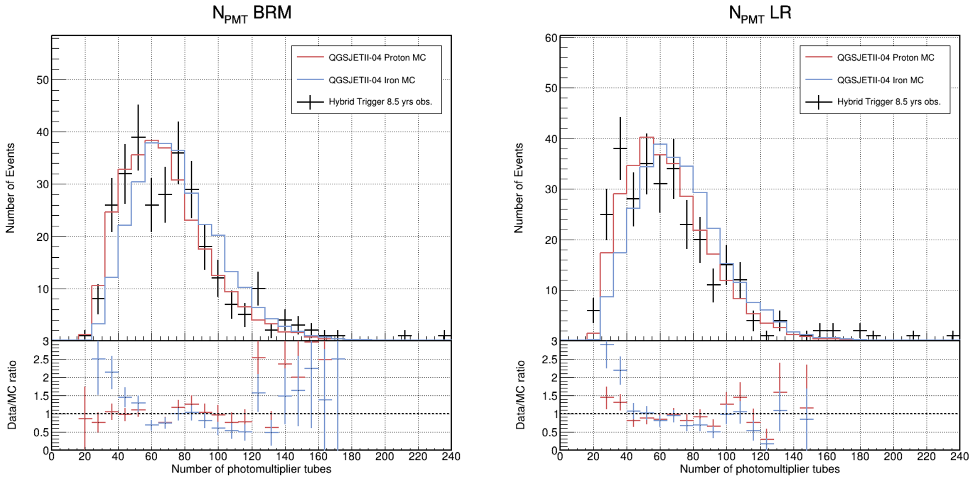

(c) BRM $18.5 \leq \mathrm{Log}_{10}(\mathrm{E}_0/\mathrm{eV}) < 19.5$ (d) LR $18.5 \leq \mathrm{Log}_{10}(\mathrm{E}_0/\mathrm{eV}) < 19.5$

Figure A.10: Data/MC comparison of the number of good PMTs.

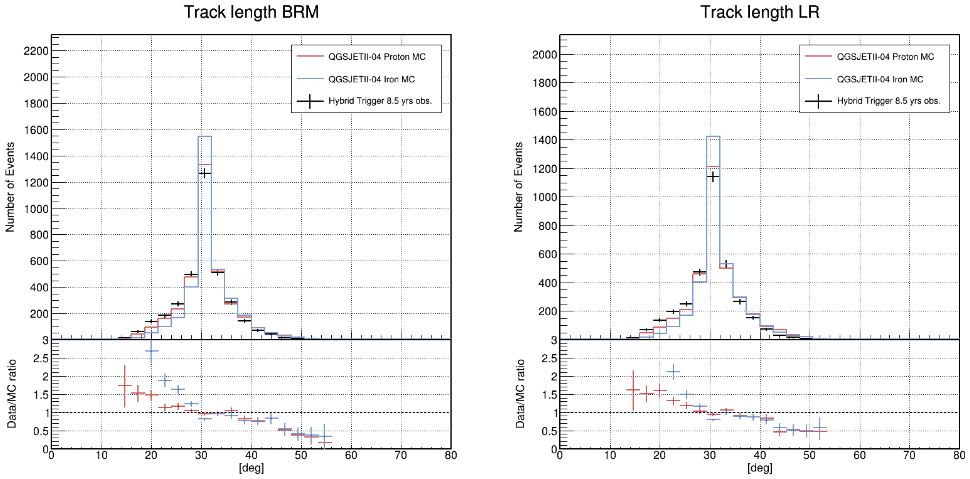

(a) BRM 17.5 $\leq$ Log$_{10}$(E$_0$/eV) $<$ 18.5

(b) LR 17.5 $\leq$ Log$_{10}$(E$_0$/eV) $<$ 18.5

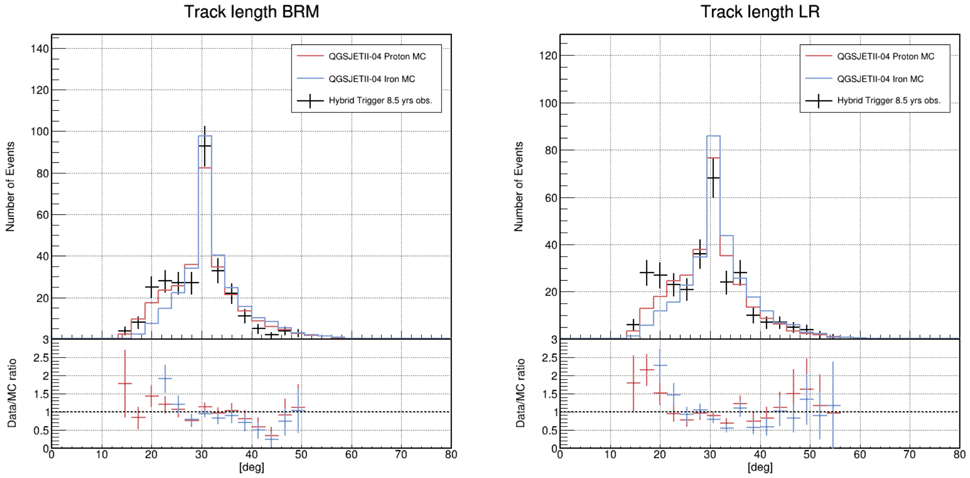

(c) BRM 18.5 $\leq$ Log$_{10}$(E$_0$/eV) $<$ 19.5

(d) LR 18.5 $\leq$ Log$_{10}$(E$_0$/eV) $<$ 19.5

Figure A.11: Data/MC comparison of track length.

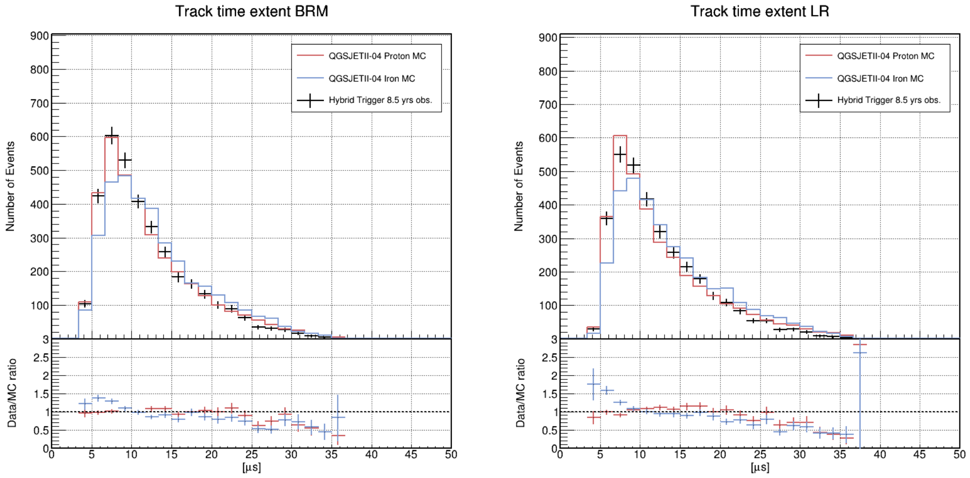

(a) BRM 17.5 $\leq$ Log$_{10}$(E$_0$/eV) $<$ 18.5

(b) LR 17.5 $\leq$ Log$_{10}$(E$_0$/eV) $<$ 18.5

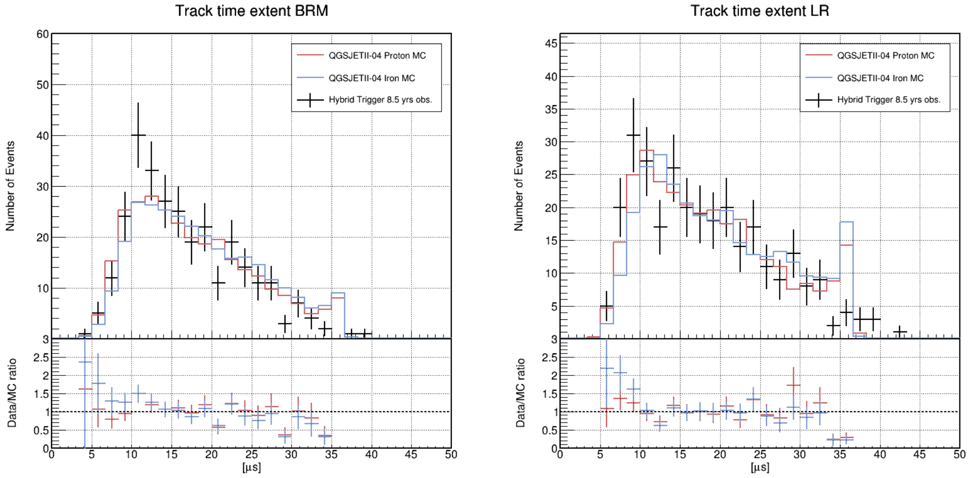

(c) BRM 18.5 $\leq$ Log$_{10}$(E$_0$/eV) $<$ 19.5

(d) LR 18.5 $\leq$ Log$_{10}$(E$_0$/eV) $<$ 19.5

Figure A.12: Data/MC comparison of time extent.

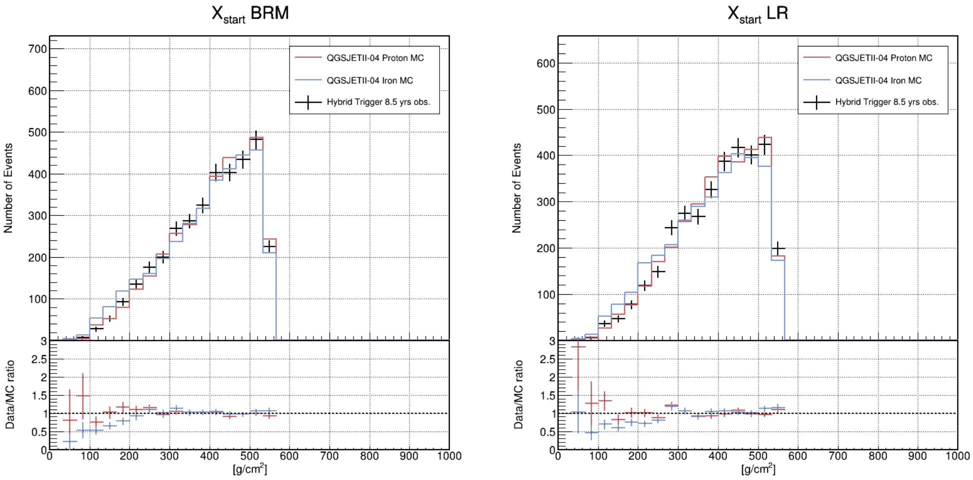

(a) BRM $17.5 \leq \mathrm{Log}_{10}(\mathrm{E}_0/\mathrm{eV}) < 18.5$

(b) LR $17.5 \leq \mathrm{Log}_{10}(\mathrm{E}_0/\mathrm{eV}) < 18.5$

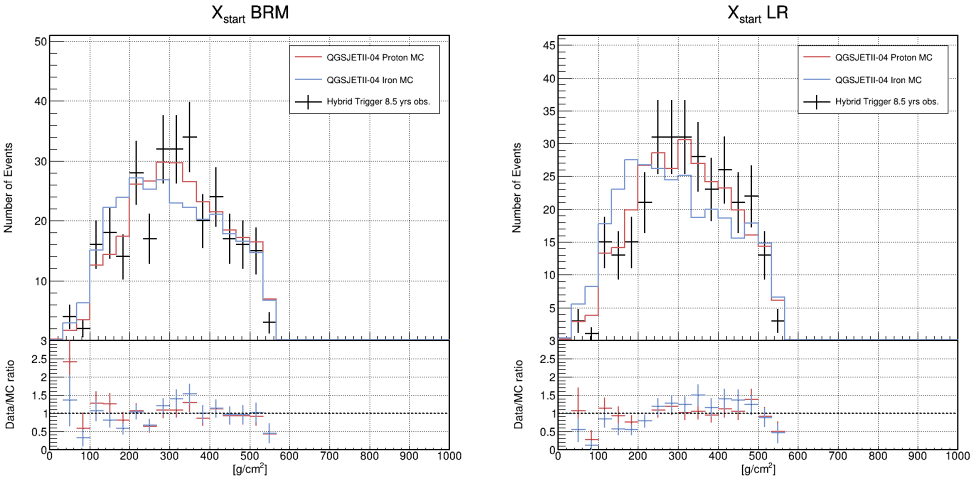

(c) BRM $18.5 \leq \mathrm{Log}_{10}(\mathrm{E}_0/\mathrm{eV}) < 19.5$

(d) LR $18.5 \leq \mathrm{Log}_{10}(\mathrm{E}_0/\mathrm{eV}) < 19.5$

Figure A.13: Data/MC comparison of $\mathrm{X}_{\mathrm{start}}$ ($\mathrm{X}_{\mathrm{low}}$).

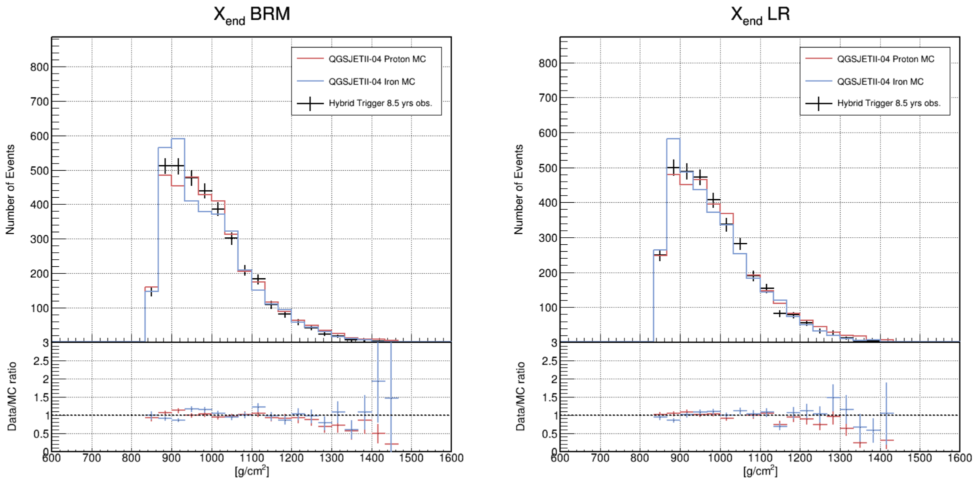

(a) BRM $17.5 \leq \mathrm{Log}_{10}(\mathrm{E}_0/\mathrm{eV}) < 18.5$ (b) LR $17.5 \leq \mathrm{Log}_{10}(\mathrm{E}_0/\mathrm{eV}) < 18.5$

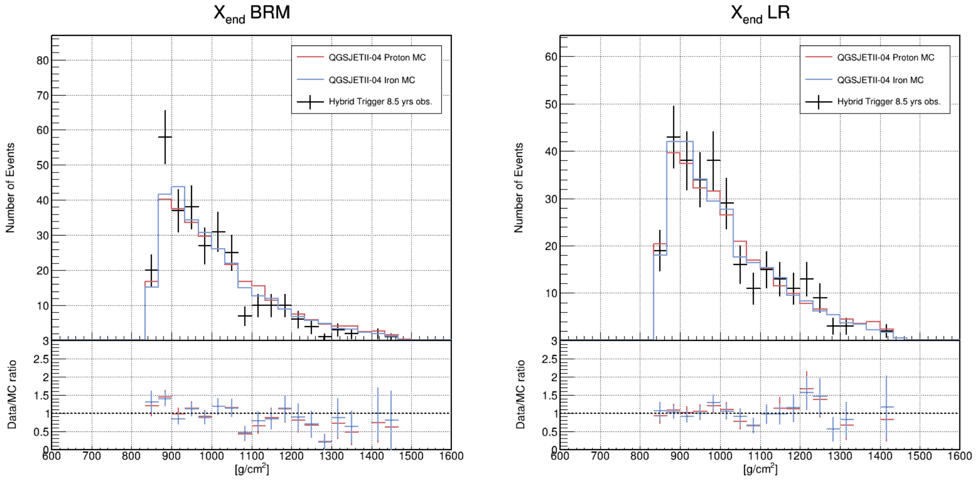

(c) BRM $18.5 \leq \mathrm{Log}_{10}(\mathrm{E}_0/\mathrm{eV}) < 19.5$ (d) LR $18.5 \leq \mathrm{Log}_{10}(\mathrm{E}_0/\mathrm{eV}) < 19.5$

Figure A.14: Data/MC comparison of $\mathrm{X}_{\mathrm{end}}$ ($\mathrm{X}_{\mathrm{high}}$).

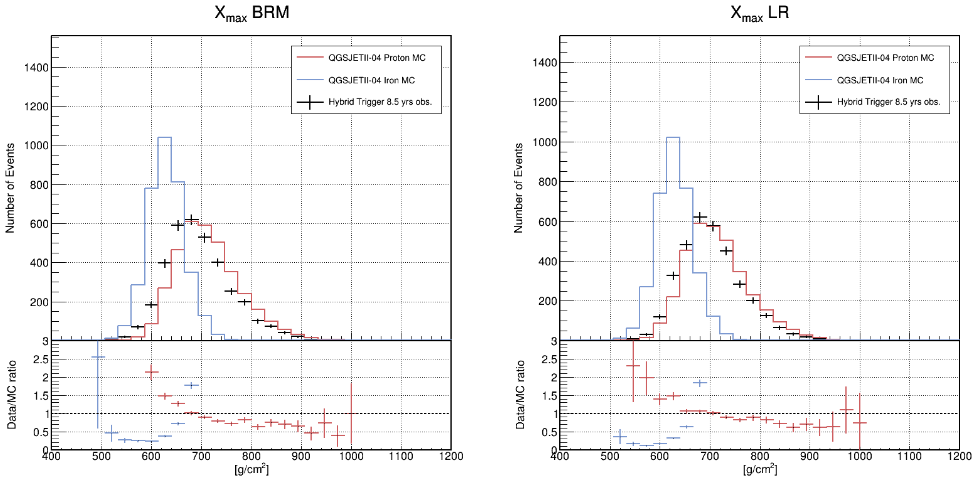

(a) BRM $17.5 \leq \mathrm{Log}_{10}(\mathrm{E}_0/\mathrm{eV}) < 18.5$

(b) LR $17.5 \leq \mathrm{Log}_{10}(\mathrm{E}_0/\mathrm{eV}) < 18.5$

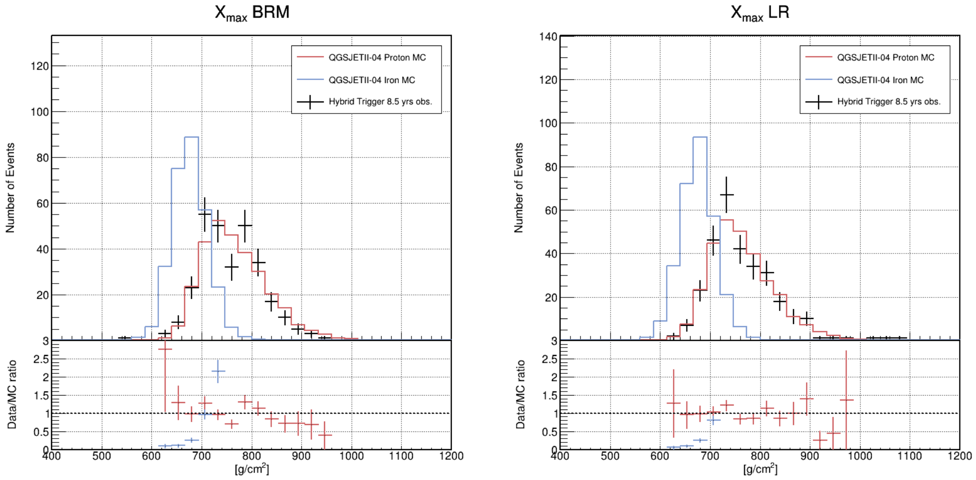

(c) BRM $18.5 \leq \mathrm{Log}_{10}(\mathrm{E}_0/\mathrm{eV}) < 19.5$

(d) LR $18.5 \leq \mathrm{Log}_{10}(\mathrm{E}_0/\mathrm{eV}) < 19.5$

Figure A.15: Data/MC comparison of $\mathrm{X}_{\mathrm{max}}$.

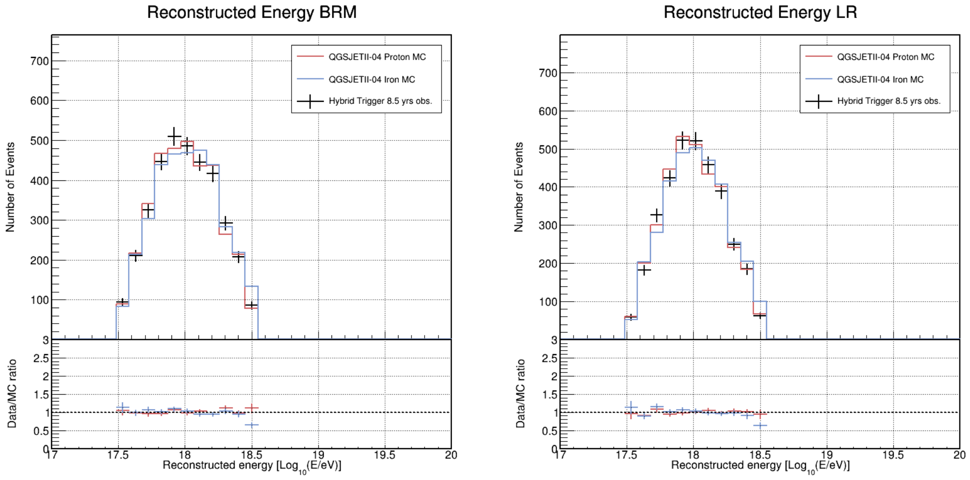

(a) BRM $17.5 \leq \mathrm{Log}_{10}(\mathrm{E}_0/\mathrm{eV}) < 18.5$ (b) LR $17.5 \leq \mathrm{Log}_{10}(\mathrm{E}_0/\mathrm{eV}) < 18.5$

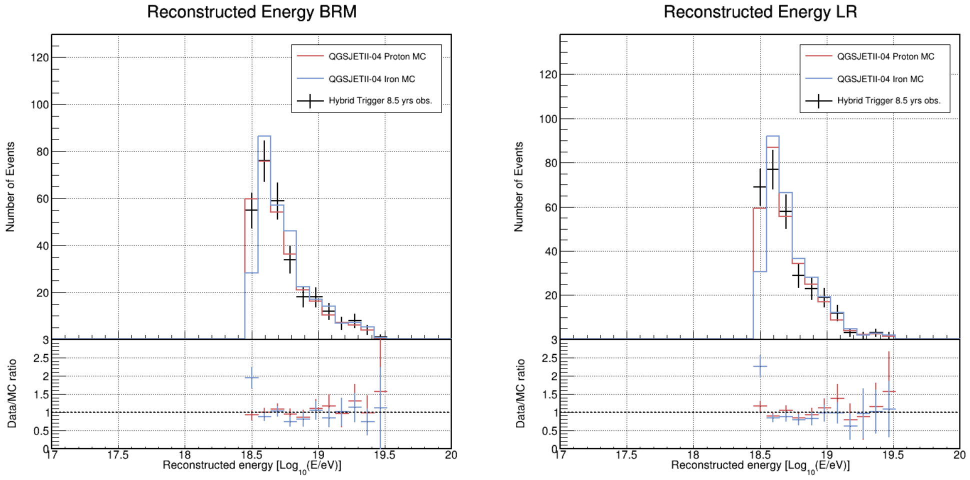

(c) BRM $18.5 \leq \mathrm{Log}_{10}(\mathrm{E}_0/\mathrm{eV}) < 19.5$ (d) LR $18.5 \leq \mathrm{Log}_{10}(\mathrm{E}_0/\mathrm{eV}) < 19.5$

Figure A.16: Data/MC comparison of reconstructed energy.

References

[1] W. Hanlon, "Cosmic Ray Spectra of Various Experiments." `https://web.physics.utah.edu/~whanlon/spectrum.html`.

[2] T. Antoni *et al.*, "The cosmic-ray experiment KASCADE," *Nuclear Instruments and Methods in Physics Research Section A: Accelerators, Spectrometers, Detectors and Associated Equipment*, vol. 513, no. 3, pp. 490–510, 2003.

[3] G. Navarra *et al.*, "KASCADE-Grande: a large acceptance, high-resolution cosmic-ray detector up to 10^{18} eV," *Nuclear Instruments and Methods in Physics Research Section A: Accelerators, Spectrometers, Detectors and Associated Equipment*, vol. 518, no. 1, pp. 207–209, 2004.

[4] A. Haungs *et al.*, "High-energy cosmic rays measured with KASCADE-Grande," *Proceedings of Science*, no. 300, 2013. ICRC2013.

[5] N. M. Budnev *et al.*, "The primary cosmic-ray energy spectrum measured with the Tunka-133 array," *Astroparticle Physics*, vol. 117, p. 102406, 2020.

[6] Prosin, V.V. *et al.*, "Results from Tunka-133 (5 years observation) and from the Tunka-HiSCORE prototype," *EPJ Web of Conferences*, vol. 121, p. 03004, 2016.

[7] S. Knurenko and I. Petrov, "Mass composition of cosmic rays above 0.1 EeV by the Yakutsk array data," *Advances in Space Research*, vol. 64, no. 12, pp. 2570–2577, 2019.

[8] S. P. KNURENKO *et al.*, "Cosmic ray spectrum in the energy range $10^{15} - 10^{18}$ eV and the second knee according to the small Cherenkov setup at the Yakutsk EAS," *Proceedings of Science*, no. 0053, 2013. ICRC2013.

[9] R. Abbasi *et al.*, "IceTop: The surface component of IceCube," *Nuclear Instruments and Methods in Physics Research Section A: Accelerators, Spectrometers, Detectors and Associated Equipment*, vol. 700, pp. 188–220, 2013.

[10] M. G. Aartsen *et al.*, "Cosmic ray spectrum and composition from PeV to EeV using 3 years of data from IceTop and IceCube," *Phys. Rev. D*, vol. 100, p. 082002, Oct 2019.

[11] A. Aab *et al.*, "The Pierre Auger Observatory Upgrade - Preliminary Design Report," 4 2016.

[12] A. Aab *et al.*, "The Pierre Auger Cosmic Ray Observatory," *Nuclear Instruments and Methods in Physics Research Section A: Accelerators, Spectrometers, Detectors and Associated Equipment*, vol. 798, pp. 172–213, 2015.

[13] V. Novotny *et al.*, "Energy spectrum of cosmic rays measured using the Pierre Auger Observatory," *Proceedings of Science*, no. 324, 2021. ICRC2021.

[14] A. Yushkov *et al.*, "Mass Composition of Cosmic Rays with Energies above $10^{17.2}$ eV from the Hybrid Data of the Pierre Auger Observatory," *Proceedings of Science*, no. 482, 2019. ICRC2019.

[15] T. Pierog, I. Karpenko, J. M. Katzy, E. Yatsenko, and K. Werner, "EPOS LHC: Test of collective hadronization with data measured at the CERN Large Hadron Collider," *Phys. Rev. C*, vol. 92, p. 034906, Sep 2015.

[16] S. Ostapchenko, "Monte Carlo treatment of hadronic interactions in enhanced Pomeron scheme: I. QGSJET-II model," *Phys. Rev. D*, vol. 83, p. 014018, 2011.

[17] F. Riehn, R. Engel, A. Fedynitch, T. K. Gaisser, and T. Stanev, "Hadronic interaction model SIBYLL 2.3d and extensive air showers," *Phys. Rev. D*, vol. 102, p. 063002, Sep 2020.

[18] R. L. Workman *et al.*, "Review of Particle Physics," *Progress of Theoretical and Experimental Physics*, vol. 2022, 08 2022.

[19] Y. Tsunesada *et al.*, "Joint analysis of the energy spectrum of ultra-high-energy cosmic rays as measured at the Pierre Auger Observatory and the Telescope Array," *Proceedings of Science*, no. 337, 2021. ICRC2021.

[20] K. H. Kampert and M. Unger, "Measurements of the cosmic ray composition with air shower experiments," *Astroparticle Physics*, vol. 35, no. 10, pp. 660–678, 2012.

[21] K. Fujita, "Cosmic Ray Energy Spectrum and Mass Composition Measurement with the Telescope Array Low energy Extension Detector in Hybrid Mode," 2021. Doctoral thesis, Osaka City University.

[22] R. U. Abbasi *et al.*, "Depth of Ultra High Energy Cosmic Ray Induced Air Shower Maxima Measured by the Telescope Array Black Rock and Long Ridge FADC Fluorescence Detectors and Surface Array in Hybrid Mode," *The Astrophysical Journal*, vol. 858, no. 2, p. 76, 2018.

[23] A. Aab *et al.*, "Observation of a large-scale anisotropy in the arrival directions of cosmic rays above 8×10^{18} eV," *Science*, vol. 357, no. 6357, pp. 1266–1270, 2017.

[24] R. U. Abbasi *et al.*, "Indications of Intermediate-Scale Anisotropy of Cosmic Rays with Energy Greater Than 57 EeV in the Northern Sky Measured with the Surface Detector of the Telescope Array Experiment," *Astrophysical Journal Letters*, vol. 790, p. 21, 2014.

[25] H. P. Dembinski, "The Muon Puzzle in High-Energy Air Showers," *Physics of Atomic Nuclei*, vol. 82, pp. 644–648, 2019.

[26] H. Dembinski, R. Engel, A. Fedynitch, T. Gaisser, F. Riehn, and T. Stanev, "Data-driven model of the cosmic-ray flux and mass composition from 10 GeV to 10^{11} GeV," *Proceedings of Science*, no. 533, 2017. ICRC2017.

[27] F. Fraschetti, “On the acceleration of Ultra-High-Energy Cosmic Rays,” *Phil. Trans. R. Soc. A*, vol. 366, pp. 4417–4428, 2008.

[28] A. Letessier-Selvon and T. Stanev, “Ultrahigh energy cosmic rays,” *Rev. Mod. Phys.*, vol. 83, p. 907, 2011.

[29] K. Yamazaki, “Search for Ultra High Energy Photons with the Hybrid Detector of the Telescope Array Experiment,” 2014. Doctoral thesis, Osaka City University.

[30] B. Keilhauer *et al.*, “Nitrogen fluorescence in air for observing extensive air showers,” *EPJ Web Conf.*, vol. 53, p. 01010, 2013.

[31] T. Fujii, “Measurements of the Energy Spectrum and the Mass Composition of Ultra-High Energy Cosmic Rays with Telescope Array Fluorescence Detectors in Monocular Mode,” 2012. Doctoral thesis, Osaka City University.

[32] `http://www.telescopearray.org/index.php/about/telescope-array`.

[33] 多米田裕一郎, “テレスコープアレイ実験における大気蛍光望遠鏡トリガーシステムの開発,” 2006. 修士論文, 東京工業大学.

[34] 石森理愛, “Telescope Array 実験におけるハイブリッドトリガーの開発,” 2010. 修士論文, 東京工業大学.

[35] 藤井俊博, “テレスコープアレイ大気蛍光望遠鏡のためのイベント再構成ソフトウェア開発と極高エネルギーニュートリノの探査,” 2009. 修士論文, 大阪市立大学.

[36] 武多昭道, “テレスコープアレイ実験大気蛍光望遠鏡電子回路の開発,” 2006. 修士論文, 東京大学.

[37] Y. Tameda *et al.*, “Trigger electronics of the new Fluorescence Detectors of the Telescope Array Experiment,” *Nucl. Instrum. Meth. A*, vol. 609, pp. 227–234, 2009.

[38] S. Kawana *et al.*, “Calibration of photomultiplier tubes for the fluorescence detector of telescope array experiment using a Rayleigh scattered laser beam,” *Nucl. Instrum. Meth. Phys. Res. A*, vol. 681, pp. 68–77, 2012.

[39] B. K. Shin, H. Tokuno, Y. Tsunesada, *et al.*, “Gain monitoring of telescope array photomultiplier cameras for the first 4 years of operation,” *Nuclear Instruments and Methods in Physics Research Section A: Accelerators, Spectrometers, Detectors and Associated Equipment*, vol. 768, pp. 96–103, 2014.

[40] 村野暢子, “TA 実験で用いる PMT カメラの 2 次元不均一性較正,” 2007. 修士論文, 東京工業大学.

[41] 中澤新, “ドローン搭載型光源を用いた大気蛍光望遠鏡の光学特性解析,” 2021. 修士論文, 信州大学.

[42] 中村智行, “TA 実験におけるエアロゾル大気透明度のモデリング,” 2022. 修士論文, 信州大学.

[43] T. Shibata *et al.*, “End-to-end absolute energy calibration of atmospheric fluorescence telescopes by an electron linear accelerator,” *Nuclear Instruments and Methods in Physics Research Section A: Accelerators, Spectrometers, Detectors and Associated Equipment*, vol. 597, no. 1, pp. 61–66, 2008.

[44] 木戸英治, “テレスコープアレイ実験による極高エネルギー宇宙線観測のための大規模地表粒子検出器の開発,” 2007. 修士論文, 東京大学.

[45] T. Abu-Zayyad *et al.*, “The surface detector array of the Telescope Array experiment,” *Nucl. Instrum. Meth. A*, vol. 689, pp. 87–97, 2012.

[46] 尾村勇吾, “Second Knee 領域における宇宙線のエネルギースペクトル及び化学組成の決定,” 2021. 博士論文, 大阪市立大学.

[47] K. Fujisue, “TAx4 surface detectors data analysis,” *EPJ Web of Conferences*, vol. 283, p. 06004, 04 2023.

[48] D. Ivanov *et al.*, “Energy Spectrum Measured by the Telescope Array,” *Proceedings of Science*, no. 298, 2019. ICRC2019.

[49] D. Ivanov, “ENERGY SPECTRUM MEASURED BY THE TELESCOPE ARRAY SURFACE DETECTOR,” 2012. Doctoral thesis, New Brunswick Rutgers, The State University of New Jersey.

[50] R. U. Abbasi *et al.*, “The Energy Spectrum of Cosmic Rays above $10^{17.2}$ eV Measured by the Fluorescence Detectors of the Telescope Array Experiment in Seven Years,” *Astroparticle Physics*, vol. 80, p. 12, 2016.

[51] 宮田孝司, “テレスコープアレイ実験における地表粒子検出器の性能評価,” 2007. 修士論文, 東京理科大学.

[52] D. Ikeda, “Hybrid analysis of ultra-high energy cosmic rays observed with the Telescope Array,” 2009. Doctoral thesis, The University of Tokyo.

[53] M. Schauer, “Analysis of the discrepancies observed in the stereo and hybrid data in the Pierre Auger Observatory,” 2015. Master’s thesis, University of Wuppertal.

[54] G. J. Feldman and R. D. Cousins, “Unified approach to the classical statistical analysis of small signals,” *Phys. Rev. D*, vol. 57, pp. 3873–3889, Apr 1998.

[55] R. Brun and F. Rademakers, “ROOT — An object oriented data analysis framework,” *Nuclear Instruments and Methods in Physics Research Section A: Accelerators, Spectrometers, Detectors and Associated Equipment*, vol. 389, no. 1, pp. 81–86, 1997.

[56] F. Kakimoto, E. C. Loh, M. Nagano, H. Okuno, M. Teshima, and S. Ueno, “A measurement of the air fluorescence yield,” *Nucl. Instrum. Meth. A*, vol. 372, pp. 527–533, 1996.

[57] A. Bunner, “Cosmic Ray Detection by Atmospheric Fluorescence,” 1967. Doctoral thesis, Cornell University.

[58] M. Nagano, K. Kobayakawa, N. Sakaki, and K. Ando, “New measurement on photon yields from air and the application to the energy estimation of primary cosmic rays,” *Astroparticle Physics*, vol. 22, pp. 235–248, 2004.

[59] T. Waldenmaier, J. Blümer, and H. Klages, “Spectral resolved measurement of the nitrogen fluorescence emissions in air induced by electrons,” *Astroparticle Physics*, vol. 29, pp. 205–222, 2008.

[60] P. Colin *et al.*, “Measurement of air and nitrogen fluorescence light yields induced by electron beam for UHECR experiments,” *Astroparticle Physics*, vol. 27, pp. 317–325, 2007.

[61] R. U. Abbasi *et al.*, “Air fluorescence measurements in the spectral range 300–420 nm using a 28.5 GeV electron beam,” *Astroparticle Physics*, vol. 29,1, pp. 77–86, 2008.

[62] M. Ave *et al.*, “A novel method for the absolute fluorescence yield measurement by AIRFLY,” *Nuclear Instruments and Methods in Physics Research Section A: Accelerators, Spectrometers, Detectors and Associated Equipment*, vol. 597, no. 1, pp. 55–60, 2008.

[63] R. U. Abbasi *et al.*, “Energy spectrum of ultra-high energy cosmic rays observed with the Telescope Array using a hybrid technique,” *Astroparticle Physics*, vol. 61, pp. 93–101, 2015.

[64] J. R. Hörandel, “Early cosmic-ray work published in German,” *AIP Conference Proceedings*, vol. 1516, no. 1, pp. 52–60, 2013.

[65] H. Geiger and W. Müller, “Elektronenzählrohr zur Messung schwächster Aktivitäten,” *Naturwissenschaften*, vol. 16, p. 617, 1928.

[66] P. Auger, “Experimental Work on Cosmic Rays Proof of the Very High Energies Carried by Some of the Primary Particles,” *Springer Netherlands*, pp. 213–218, 1985.

[67] C. D. Anderson, “The positive electron,” *Phys. Rev.*, vol. 43, pp. 491–494, 1933.

[68] J. C. Street and E. C. Stevenson, “New evidence for the existence of a particle of mass intermediate between the proton and electron,” *Phys. Rev.*, vol. 52, pp. 1003–1004, 1937.

[69] E. Fermi, “On the Origin of the Cosmic Radiation,” *Phys. Rev.*, vol. 75, pp. 1169–1174, 1949.

[70] 永野元彦, “空気シャワー観測による宇宙線研究の歴史,” *ICRR report (679 − 2014 − 5)*, 2014.

[71] P. Bassi, G. Clark, and B. Rossi, “Distribution of Arrival Times of Air Shower Particles,” *Phys. Rev.*, vol. 92, pp. 441–451, Oct 1953.

[72] G. CLARK, J. EARL, W. KRAUSHAAR, J. LINSLEY, B. ROSSI, and F. SCHERB, “An Experiment on Air Showers Produced by High-Energy Cosmic Rays,” *Nature*, vol. 180, p. 353, 1957.

[73] G. W. Clark, J. Earl, W. L. Kraushaar, J. Linsley, B. B. Rossi, F. Scherb, and D. W. Scott, “Cosmic-Ray Air Showers at Sea Level,” *Phys. Rev.*, vol. 122, pp. 637–654, Apr 1961.

[74] J. Linsley, “Evidence for a Primary Cosmic-Ray Particle with Energy 10^{20} eV,” *Phys. Rev. Lett.*, vol. 10, pp. 146–148, Feb 1963.

[75] A. M. HILLAS, "DERIVATION OF THE EAS SPECTRUM," *Conf. Proc. C*, vol. 690825, pp. 355–360, 1969.

[76] D. Newton, J. Knapp, and A. Watson, "The optimum distance at which to determine the size of a giant air shower," *Astroparticle Physics*, vol. 26, no. 6, pp. 414–419, 2007.

[77] G. Tanahashi, "Early air fluorescence work: Cornell and Japan," *AIP Conf. Proc.*, vol. 433, no. 1, pp. 54–64, 1998.

[78] A. N. Bunner, K. Greisen, and P. B. Landecker, "An imaging system for EAS optical emission," *Canadian Journal of Physics*, vol. 46, no. 10, pp. S266–S269, 1968.

[79] T. Hara, F. Ishikawa, and S. Kawaguchi, "DETECTION OF THE ATMOSPHERIC SCINTILLATION LIGHT FROM AIR SHOWERS.," *Acta Phys. Acad. Sci. Hung. 29: Suppl. 3, 369-76(1970).*, 1970.

[80] R. Baltrusaitis *et al.*, "The Utah Fly's Eye detector," *Nuclear Instruments and Methods in Physics Research Section A: Accelerators, Spectrometers, Detectors and Associated Equipment*, vol. 240, no. 2, pp. 410–428, 1985.

[81] D. Bird *et al.*, "Coincident Observation of Air Showers by the HiRes Prototype and CASA/MIA Experiments," in *23rd International Cosmic Ray Conference, Volume 4*, vol. 4 of *International Cosmic Ray Conference*, p. 283, jan 1993.

[82] H. Kawai *et al.*, "Telescope Array Experiment," *Nuclear Physics B - Proceedings Supplements*, vol. 175-176, pp. 221–226, 2008.

[83] J. Abraham *et al.*, "Properties and performance of the prototype instrument for the Pierre Auger Observatory," *Nuclear Instruments and Methods in Physics Research Section A: Accelerators, Spectrometers, Detectors and Associated Equipment*, vol. 523, no. 1, pp. 50–95, 2004.

[84] P. Blackett, "A possible contribution to the night sky from the Cerenkov radiation emitted by cosmic rays," *Proc. of Int. Conf. on the Emission Spectra of the Night Sky and Aurorae held at London*, vol. 34, 1948.

[85] W. GALBRAITH and J. V. JELLEY, "Light Pulses from the Night Sky associated with Cosmic Rays," *Nature*, vol. 171, p. 349, 1953.

[86] A. S. Krieger and H. V. Bradt, "Cerenkov Light in Extensive Air Showers and the Chemical Composition of Primary Cosmic Rays at 10^{16} eV," *Phys. Rev.*, vol. 185, pp. 1629–1635, Sep 1969.

[87] J. Jelley and N. Porter, "Cerenkov Radiation from the Night Sky, and its Application to γ-Ray Astronomy," *Quarterly Journal of the Royal Astronomical Society*, vol. 4, p. 275, 1963.

[88] M. Cawley *et al.*, "A high resolution imaging detector for TeV gamma-ray astronomy," *Experimental Astronomy*, vol. 1, pp. 173–193, 1990.

[89] J. Krizmanic, P. Bergman, D. Sokolsky, *et al.*, "The Non-Imaging CHErenkov Array (NICHE): A TA/TALE Extension to Measure the Flux and Composition of Very-High Energy Cosmic Rays," *Proceedings of Science*, no. 365, 2013. ICRC2013.

[90] R. U. Abbasi *et al.*, "The Cosmic Ray Energy Spectrum between 2 PeV and 2 EeV Observed with the TALE Detector in Monocular Mode," *Astrophysical Journal*, vol. 865, p. 74, 2018.

[91] V. Novotny, "Measurement of the energy spectrum of cosmic rays using Cherenkov-dominated data at the Pierre Auger Observatory," 2020. Doctoral thesis, Charles University.

[92] `https://www.iap.kit.edu/kascade/english/`.

[93] I. M. Kershengolts *et al.*, "THE RESULTS OF THE FIRST STAGE OBSERVATIONS AT THE YAKUTSK EAS COMPLEX ARRAY. I. THE LATERAL DISTRIBUTION AND EAS SIZE SPECTRUM AT SEA LEVEL. (TALK)," in *13th International Cosmic Ray Conference*, 1973.

[94] B. Peters, "Primary cosmic radiation and extensive air showers," *Il Nuovo Cimento (1955-1965)*, vol. 22, pp. 800–819, 1961.

[95] W. D. Apel *et al.*, "Kneelike Structure in the Spectrum of the Heavy Component of Cosmic Rays Observed with KASCADE-Grande," *Phys. Rev. Lett.*, vol. 107, p. 171104, Oct 2011.

[96] D. Bird *et al.*, "The cosmic-ray energy spectrum observed by the Fly's Eye," *The Astrophysical Journal*, vol. 424, pp. 491–502, 02 1994.

[97] V. Berezinsky, A. Gazizov, and S. Grigorieva, "On astrophysical solution to ultrahigh energy cosmic rays," *Phys. Rev. D*, vol. 74, p. 043005, Aug 2006.

[98] A. Aab *et al.*, "Evidence for a mixed mass composition at the ' ankle ' in the cosmic-ray spectrum," *Physics Letters B*, vol. 762, pp. 288–295, 2016.

[99] A. Aab *et al.*, "Features of the Energy Spectrum of Cosmic Rays above 2.5×10^{18} eV Using the Pierre Auger Observatory," *Phys. Rev. Lett.*, vol. 125, p. 121106, Sep 2020.

[100] R. U. Abbasi *et al.*, "First Observation of the Greisen-Zatsepin-Kuzmin Suppression," *Phys. Rev. Lett.*, vol. 100, p. 101101, Mar 2008.

[101] R. Aloisio, V. Berezinsky, and A. Gazizov, "Ultra high energy cosmic rays: The disappointing model," *Astroparticle Physics*, vol. 34, no. 8, pp. 620–626, 2011.

[102] D. Ivanov *et al.*, "Recent measurement of the Telescope Array energy spectrum and observation of the shoulder feature in the Northern Hemisphere," *Proceedings of Science*, no. 341, 2021. ICRC2021.

[103] P. Plotko, A. van Vliet, X. Rodrigues, and W. Winter, "Indication of a Local Source of Ultra-High-Energy Cosmic Rays in the Northern Hemisphere," `https://arxiv.org/abs/2208.12274`.

[104] T. Fujii *et al.*, "Telescope Array anisotropy summary," *Proceedings of Science*, no. 392, 2021. ICRC2021.

[105] A. Aab *et al.*, "Muons in air showers at the Pierre Auger Observatory: Mean number in highly inclined events," *Phys. Rev. D*, vol. 91, p. 032003, Feb 2015.

[106] A. Aab *et al.*, "Testing Hadronic Interactions at Ultrahigh Energies with Air Showers Measured by the Pierre Auger Observatory," *Phys. Rev. Lett.*, vol. 117, p. 192001, 2016.

[107] R. U. Abbasi *et al.*, "Study of muons from ultrahigh energy cosmic ray air showers measured with the Telescope Array experiment," *Phys. Rev. D*, vol. 98, p. 022002, Jul 2018.

[108] A. Aab *et al.*, "Measurement of the Fluctuations in the Number of Muons in Extensive Air Showers with the Pierre Auger Observatory," *Phys. Rev. Lett.*, vol. 126, p. 152002, 2021.

[109] T. J. Weiler, "Cosmic-ray neutrino annihilation on relic neutrinos revisited: a mechanism for generating air showers above the Greisen-Zatsepin-Kuzmin cutoff," *Astropart. Phys.*, vol. 11, pp. 303–316, 1999.

[110] V. Kuzmin and I. Tkachev, "Ultrahigh-energy cosmic rays, superheavy long-lived particles, and matter creation after inflation," *JETP Lett.*, vol. 68, p. 271, 1998.

[111] V. Berezinsky and A. Vilenkin, "Cosmic Necklaces and Ultrahigh Energy Cosmic Rays," *Phys. Rev. Lett.*, vol. 79, pp. 5202–5205, Dec 1997.

[112] M. Kachelriess, "The rise and fall of top-down models as main UHECR sources," in *20th Rencontres de Blois on Challenges in Particle Astrophysics*, pp. 215–224, 2008.

[113] K. Greisen, "End to the Cosmic-Ray Spectrum?," *Phys. Rev. Lett.*, vol. 16, p. 748, 1966.

[114] T. Zatsepin and V. Kuzmin, "Upper Limit of the Spectrum of Cosmic Rays," *JETP Lett.*, vol. 4, p. 178, 1966.

[115] S. Hümmer, M. Rüger, F. Spanier, and W. Winter, "SIMPLIFIED MODELS FOR PHOTOHADRONIC INTERACTIONS IN COSMIC ACCELERATORS," *The Astrophysical Journal*, vol. 721, p. 630, 08 2010.

[116] S. Yoshida and M. Teshima, "Energy Spectrum of Ultra-High Energy Cosmic Rays with Extra-Galactic Origin," *Prog. Theor. Phys.*, vol. 89, p. 833, 1993.

[117] E. Dwek and F. Krennrich, "The extragalactic background light and the gamma-ray opacity of the universe," *Astroparticle Physics*, vol. 43, pp. 112–133, 2013.

[118] R. Firestone, "The origin of the giant dipole resonance," `https://arxiv.org/abs/2009.03356`.

[119] F. W. Stecker and M. H. Salamon, "Photodisintegration of Ultra-High-Energy Cosmic Rays: A New Determination," *The Astrophysical Journal*, vol. 512, p. 521, feb 1999.

[120] H. Bethe and W. Heitler, "On the stopping of fast particles and on the creation of positive electrons," *Proc. Roy. Soc.*, vol. A146, pp. 83–112, 1934.

[121] T. Stanev, "High Energy Cosmic Rays," *Springer*, 2010.

[122] W. Heitler, "Quantum theory of radiation," *Clarendon Press*, 1954.

[123] J. Linsley, "Structure of Large Air Showers at Depth 834 G CM^{-2} Applications," *Proc. 15th ICRC, Plovdiv*, vol. 12, no. 89, 1977.

[124] T. Gaisser and A. Hillas, "Reliability of the Method of Constant Intensity Cuts for Reconstructing the Average Development of Vertical Showers," *Proc. 15th ICRC*, vol. 8, p. 353, 1977.

[125] K. Kamata and J. Nishimura, "The Lateral and the Angular Structure Functions of Electron Showers," *PTP Suppl.*, vol. 6, p. 93, 1958.

[126] K. Greisen, "Cosmic Ray Showers," *Ann. Rev. Nucl. Part. Sci.*, vol. 10, p. 63, 1960.

[127] P. A. Cerenkov, "Visible radiation produced by electrons moving in a medium with velocities exceeding that of light," *Phys. Rev.*, vol. 52, pp. 378–379, Aug 1937.

[128] T. K. Gaisser, R. Engel, and E. Resconi, "Cosmic Rays and Particle Physics," *Cambridge University Press*, 2016.

[129] H. Tokuno *et al.*, "New air fluorescence detectors employed in the Telescope Array experiment," *Nucl. Instrum. Meth. A*, vol. 676, pp. 54–65, 2012.

[130] M. Takeda *et al.*, "Extension of the Cosmic-Ray Energy Spectrum beyond the Predicted Greisen-Zatsepin-Kuz'min Cutoff," *Phys. Rev. Lett.*, vol. 81, pp. 1163–1166, Aug 1998.

[131] N. Chiba *et al.*, "Akeno Giant Air Shower Array (AGASA) covering 100 km^2 area," *Nuclear Instruments and Methods in Physics Research Section A: Accelerators, Spectrometers, Detectors and Associated Equipment*, vol. 311, no. 1, pp. 338–349, 1992.

[132] 佐野賢吾, "飛行型標準光源を用いた宇宙線望遠鏡の視野方向評価," 2020. 修士論文, 信州大学.

[133] 中村凌, "宇宙線望遠鏡実験における魚眼 CCD を用いた夜間雲量観測の実用化," 2018. 修士論文, 信州大学.

[134] S. Udo, M. Allen, R. Cady, M. Fukushima, Y. I. Ida, J. N. Matthews, J. Thomas, S. B. Thomas, and L. R. Wiencke, "The Central Laser Facility at the Telescope Array," *Proceedings of the 30th International Cosmic Ray Conference*, vol. 5, pp. 1021–1024, 2008.

[135] 山川雄一, "極高エネルギー宇宙線観測のためのテレスコープアレイ実験における大規模地表粒子検出器境界トリガーシステムの開発," 2009. 修士論文, 東京大学.

[136] G. Thomson, P. Sokolsky, C. Jui, J. Matthews, M. Fukushima, S. Ogio, H. Sagawa, *et al.*, "The Telescope Array Low Energy Extension (TALE)," *Proceedings of Science*, no. 338, 2011. ICRC2011.

[137] K. Fujita *et al.*, "Recent results from TALE and Telescope Array," *19th Rencontres du Vietnam*, Jan 2023.

[138] R. Abbasi *et al.*, "Surface detectors of the TAx4 experiment," *Nuclear Instruments and Methods in Physics Research Section A: Accelerators, Spectrometers, Detectors and Associated Equipment*, vol. 1019, p. 165726, 2021.

[139] M. Potts, C. Jui, *et al.*, "Monocular Energy Spectrum using the TAx4 Fluorescence Detector," *Proceedings of Science*, no. 343, 2021. ICRC2021.

[140] T. Abu-Zayyad *et al.*, "THE COSMIC-RAY ENERGY SPECTRUM OBSERVED WITH THE SURFACE DETECTOR OF THE TELESCOPE ARRAY EXPERIMENT," *Astrophysical Journal Letters*, vol. 768, no. 1, 2013.

[141] T. Abu-Zayyad *et al.*, "The energy spectrum of Telescope Array ' s Middle Drum detector and the direct comparison to the High Resolution Fly ' s Eye experiment," *Astroparticle Physics*, vol. 39-40, pp. 109–119, 2012.

[142] R. Abbasi *et al.*, "The hybrid energy spectrum of Telescope Array's Middle Drum Detector and surface array," *Astroparticle Physics*, vol. 68, pp. 27–44, 2015.

[143] R. Abbasi *et al.*, "Study of Ultra-High Energy Cosmic Ray composition using Telescope Array's Middle Drum detector and surface array in hybrid mode," *Astroparticle Physics*, vol. 64, pp. 49–62, 2015.

[144] T. Fujii *et al.*, "The mass composition of ultra-high energy cosmic rays measured by new fluorescence detectors in the Telescope Array experiment," *Physics Procedia*, vol. 61, pp. 418–424, 2015.

[145] R. U. Abbasi *et al.*, "The Cosmic-Ray Composition between 2 PeV and 2 EeV Observed with the TALE Detector in Monocular Mode," *The Astrophysical Journal*, pp. 909,2, 2021.

[146] T. Stroman and D. Bergman, "Telescope Array measurement of UHECR composition from stereoscopic fluorescence detection," *Proceedings of Science*, no. 538, 2017. ICRC2017.

[147] H. Tokuno, "Hybrid trigger event analysis." TA internal meeting, 2015.

[148] T. Fujii *et al.*, "An Event Reconstruction Method for the Telescope Array Fluorescence Detectors," *AIP Conference Proceedings*, vol. 1367, no. 1, pp. 149–152, 2011.

[149] D. Heck, J. Knapp, J. N. Capdevielle, G. Schatz, and T. Thouw, "CORSIKA: A Monte Carlo code to simulate extensive air showers," Tech. Rep. FZKA-6019, 1998.

[150] A. Ferrari, P. R. Sala, A. Fasso, and J. Ranft, "FLUKA: A Multi-Particle Transport Code," Dec 2005. `https://www.osti.gov/biblio/877507`.

[151] W. R. Nelson, H. Hirayama, and D. W. Rogers, "EGS4 code system," Dec 1985. `https://www.osti.gov/biblio/6137659`.

[152] P. Tanguy, "CORSIKA, Physics and Technology." ISAPP School 2018 - LHC meets Cosmic Rays, 2018.

[153] B. T. Stokes, R. Cady, D. Ivanov, J. N. Matthews, and G. B. Thomson, "Dethinning extensive air shower simulations," *Astroparticle Physics*, vol. 35,11, pp. 759–766, 2012.

[154] S. Agostinelli *et al.*, “GEANT4—A Simulation Toolkit,” *Nucl. Instrum. Meth. A*, vol. 506, pp. 250–303, 2003.

[155] ARL-NOAA, “Global Data Assimilation System (GDAS1) Archive Information,” 2004. `https://www.ready.noaa.gov/gdas1.php`.

[156] T. Tomida *et al.*, “The atmospheric transparency measured with a LIDAR system at the Telescope Array experiment,” *Nucl. Instrum. Meth. A*, vol. 654, pp. 653–660, 2011.

[157] S. Ostapchenko, “QGSJET-II: towards reliable description of very high energy hadronic interactions,” *Nuclear Physics B - Proceedings Supplements*, vol. 151, no. 1, pp. 143–146, 2006.

[158] R. O. Duda and P. E. Hart, “Use of the Hough Transformation to Detect Lines and Curves in Pictures,” *Commun. ACM*, vol. 15, p. 11–15, jan 1972.

[159] J. A. Bellido *et al.*, “Mass Composition Studies of the Highest Energy Cosmic Rays,” *Proceedings for the XXth Rencontres de Blois 2008 ”Challenges in Particle Astrophysics”*, p. 12, 2009.

[160] J. R. Höorandel, “A review of experimental results at the knee,” *Journal of Physics: Conference Series*, vol. 47, p. 41, oct 2006.

[161] 武多昭道, “テレスコープアレイ地表検出器による極限エネルギー宇宙線スペクトルの測定,” 2011. 博士論文, 東京大学.

[162] 小林友作, “Telescope Array 実験FD解析における大気の影響の評価,” 2011. 修士論文, 東京工業大学.

[163] Y. Tsunesada, “GDAS: Global Data Assimilation System.” TA internal meeting, 2015.

[164] Y. Tsunesada, T. Abu-Zayyad, D. Ivanov, G. Thomson, T. Fujii, and D. Ikeda, “Energy Spectrum of Ultra-High-Energy Cosmic Rays Measured by The Telescope Array,” *Proceedings of Science*, no. 535, 2017. ICRC2017.

[165] P. Abreu *et al.*, “The energy spectrum of cosmic rays beyond the turn-down around 10^{17} ev as measured with the surface detector of the Pierre Auger Observatory,” *The European Physical Journal C*, vol. 81, 2021.

[166] T. Abu-Zayyad *et al.*, “Measurement of the Cosmic-Ray Energy Spectrum and Composition from 10^{17} to $10^{18.3}$ eV Using a Hybrid Technique,” *Astrophysical Journal*, vol. 557, p. 686, 2001.